Droplet-based microfluidics at the femtoliter scale

Marie Leman

▶ **To cite this version:**

Marie Leman. Droplet-based microfluidics at the femtoliter scale. Mechanics [physics]. Université Pierre et Marie Curie - Paris VI, 2015. English. NNT : 2015PA066387 . tel-01273988

HAL Id: tel-01273988
https://theses.hal.science/tel-01273988

Submitted on 15 Feb 2016

HAL is a multi-disciplinary open access archive for the deposit and dissemination of scientific research documents, whether they are published or not. The documents may come from teaching and research institutions in France or abroad, or from public or private research centers.

L'archive ouverte pluridisciplinaire **HAL**, est destinée au dépôt et à la diffusion de documents scientifiques de niveau recherche, publiés ou non, émanant des établissements d'enseignement et de recherche français ou étrangers, des laboratoires publics ou privés.

Thèse de doctorat de l'Université Pierre et Marie Curie

Spécialité

Sciences mécaniques, acoustique, électronique et robotique
(ED 391)

présentée par

Marie Leman

pour obtenir le grade de

Docteur de l'Université Pierre et Marie Curie

Microfluidique en gouttes à l'échelle femtolitrique

Soutenance prévue le 18 Septembre 2015 devant le jury composé de :

M. Axel Buguin	Président
M. Andrew D. Griffiths	Co-directeur de thèse
M. Sean Kennedy	Invité
M. Huai-Zhi Li	Invité
M. Rob Nicol	Examinateur
M. Michael Ryckelynck	Rapporteur
M. Ralf Seemann	Rapporteur
M. Patrick Tabeling	Directeur de thèse

Laboratoire de Microfluidique, MEMS et Nanostructures
UMR Gulliver CNRS-ESPCI 7083

Laboratoire de biochimie
UMR Chimie Biologie Innovation- ESPCI 8231
10, rue Vauquelin
75 005 Paris

École Doctorale 391 : Sciences mécaniques, acoustique, électronique et robotique
Campus Curie - ChimieParisTech - LGGPTS
11, rue Piere et Marie Curie
75 231 Paris cedex 05

Introduction

This PhD work focuses on the miniaturization of biochemical reservoirs towards the femtoliter scale, *i.e.* reservoirs of 1-10 μm in diameter. The effort towards miniaturization is one of the constants of modern era. One of the most immediate example is the one of micro-electronics and computing. In the 1940's, one of the first electronic supercalculators, the ENIAC, occupied 160 m^2 and weighed 30 tons. The apparition of semi-conductors enabled a very fast miniaturization and the birth of micro-electronics. After the 1960's, the integration of components on circuits follows an exponential law until reaching ultra-fast processors containing 40 millions transistors and confortably fitting in an ultra-portable computer.

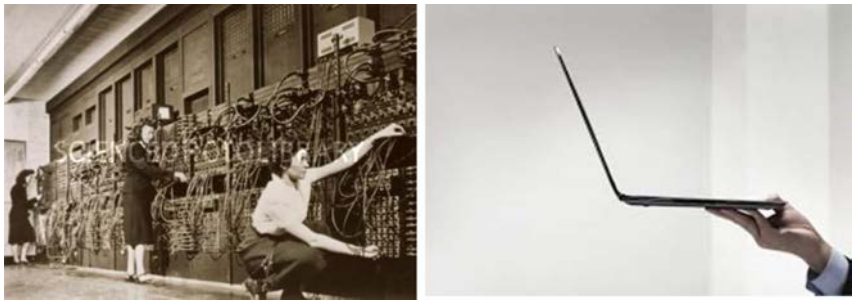

Figure 1 – Electronics were subjected to a very fast miniaturization process in the 20^{ieth} century. On the left is pictured a photo of the ENIAC, one of the first electronic calculator. It occupied a surface of 160 m^2 for an operation time on the order of the millisecond. *Adapted from Los alamos national laboratory/Science photo library.* On the right, a modern ultra portable computer. It weights 1 kg and can perform hundreds of millions of operations per second.

In the meanwhile, miniaturization also operated in chemistry and biology, though in a more humble way. Until the 1990's, most assays were realized in test tubes with volumes on the order of the mL. The apparition of microtitre plates decreased this volume to microliter scales and enabled the automation of analysis within robots. The number of assays passed from 100 per week in test tubes to more than 100 000 per day in 1536-well plates (slightly more than one per second). Further miniaturization in open reservoirs was demonstrated, with assay volumes of 1 μL in 3456-well plates[1] and of 200 nL in 9600-well plates[2] but faced considerable issues: evaporation, capillary action that could bridge the liquid between wells and result in cross-contamination, lack of reproducibility, pipetting errors[3].

The eagerness towards an increase of the analysis capacity is to be related to the inherently vast extent of biological spaces. The example of protein engineering is particularly demonstra-

tive. Protein engineering aims at improving existing proteins towards a better stability (wider conditions of use) or a better efficiency (enhanced catalytic activity of an enzyme, for instance). Protein functionality is highly coupled to its structure, which is itself determined by the amino-acid (AA) succession. There are 20 natural AA; in the case of a short polypeptide of 100 amino acids, the total number of corresponding proteins is $20^{100} \sim 10^{130}$, which is more than the number of molecules in the universe. Besides, analyzing the effect of the modification of a single AA is often inadequate; the protein structure depends on the cooperation of different AA; AA distributions cannot be studied independently, but taking into account correlations between sequence positions[4]. Combinatorial spaces are extensively broad which stimulates a constant effort towards improved throughputs.

This context encouraged the thrive of microfluidics and especially of the droplet-based microfluidics domain. Microfluidics is the science of fluids at the micrometer scale, a non-turbulent domain in which fluid flows are reversible. Microfluidics provides a platform for the robust manipulation of fluids at low cost. The use of water-in-oil droplets as biochemical reservoirs empowered a further miniaturization of volumes down to the nanoliter and picoliter scales and contributed to the improvement of the analysis capacity to 10^6 assays per day in picoliter droplet-based platforms.

In this manuscript, we demonstrate the possibility of miniaturizing droplet-based microfluidics further down to the femtoliter scale and illustrate the advantages of volume miniaturization through several biological applications.

The first part of this manuscript introduces droplet-based microfluidics and microfluidic experimental methods.

A second part focuses on the miniaturization of each elementary operation of droplet-based microfluidics to the femtoliter scale. Production on-demand, mixing, coalescence, sorting, splitting, droplet stability and biocompatibility at the femtoliter scale are investigated.

The encouraging developments of this initial stage of my PhD work stimulated the development of some biological applications. Part III focuses on the construction of a platform for the *in situ* encoding of droplets with barcodes readable per sequencing.

Last, my link with the Laboratory of Biochemistry encouraged collaborations on two other biological applications related to directed evolution. Those contributions, in which I only participated on the physics part, are gathered in a fourth part of this manuscript.

Short table of contents

This PhD work has led to the publication of an article, Droplet-Based Microfluidics At The Femtolitre Scale, that is reproduced in Appendix B and a patent, High-throughput dynamic reagent delivery system (WO 2014085802 A1). In the first months of my PhD, another article was published, Dynamics of a small number of droplets in microfluidic Hele-Shaw cell. This article focuses on preliminary work that is not directly related to my PhD subject and is reproduced in Appendix C. An article on the platform for the *in situ* encoding of droplets with barcodes readable per sequencing is under redaction.

Contents

Part I

Droplet-based microfluidics and experimental section

Chapter 1

Droplet-based microfluidics

1.1 Droplet-based microbiology before microfluidics

Long before the apparition of microfluidics, researchers had envisioned the interest of confining microorganisms and biomolecules inside droplets. This section presents the biological interest of droplets and motivates the development of droplet-based microfluidics.

1.1.1 Pure-culture

Starting from the early 1900's, researchers became aware of the necessity of isolating microorganisms to link with certainty the observable characteristic to a particular organism. They created the concept of pure-culture, meaning that all the individuals descend from the same single cell[5] and considered it a prerequisite for any investigation. Many techniques for the isolation of single microorganisms appeared thereafter [6, 7, 8]. Among them, the use of droplets as small reservoirs that isolate biological content was already envisioned. [8].

The compartimentalization of single cells into droplets demonstrated its interest immediately. In 1958, Nossal [9] isolated cells from lymph nodes of rats into droplets of a fraction of nanoliters with a glass chip represented in Figure 1.1. With a Pasteur pipette controled by the operator's mouth, droplets of cell suspensions were deposited under a film of mineral oil. Nossal obtained measurable levels of antibodies in a few hours. By stimulating the rats with two antigens, he demonstrated that cells only form one type of antibody, proving the so-called "one-cell-one-antibody rule".

However, those first compartmentalized experiments were very long and delicate and, in practice, only a few hundreds of them were performed over the following decade. The lack of digital cameras, sensitive fluorescence detection devices and modern computing methods also slowed down those advances until the late 1990s. The concept of In Vitro Compartmentalization (IVC) then prospered with favourable technological advances.

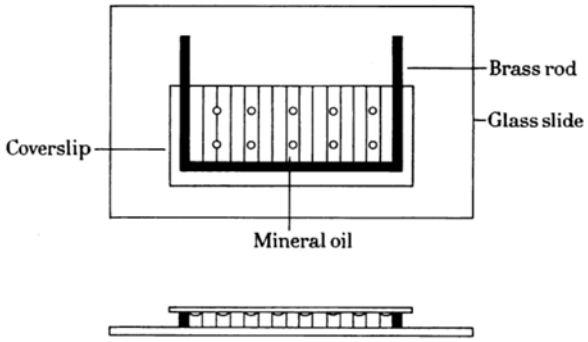

Figure 1.1 – Chip used for one of the firsts droplet-based single cell study in 1958. A glass coverslip is divided into 9 rectangles by ink lines. It is then placed on an oil chamber, which consists of three brass rods glued onto a glass slide. Mineral oil is spread on the surface of the coverslip and the operator deposits droplets of cell suspension under the mineral oil. Deposition is made with a Pasteur pipette, controled by the operator's mouth.[9]

1.1.2 In Vitro Compartmentalization (IVC)

In vitro compartmentalization envisions droplets as cell-like reservoirs in which biological assays can be performed. It applies in many biological tests, such as evolutionary studies or emulsion PCR.

Evolutionary studies Evolutionary studies ambition to understand the natural processes at play in evolution; how organisms adapt to new environments, what is the interplay between genes, does evolution happens in a slow linear way or in gradual steps are some of the questions raised. In nature, genes and their encoding molecules are compartmentalized within cells. Cellular compartmentalization is supposed to be vital for the evolution of living organims as it keeps together genes, RNAs, proteins and the products of their activities. In this perspective, the presence of the cell enables a linkage between the genotype and the phenotype. Researchers tried to use cells to co-compartmentalize genes and the proteins they encode (*In vivo compartmentalization*). However, the presence of the living cell complexifies the analysis; selection pressures are most often limited to those resulting in the survival/death of the cell. The only functions that can be studied are the ones that are essential for the survival of the cell.

Droplets appeared as a way to create artificial cell-like compartments suitable for molecular evolution studies[10]. Dan Tawfik and Andrew Griffiths demonstrated the possibility to select a desired gene inside water-in-oil droplets (Figure 1.2). First, a library of mutants of the initial gene is created and each mutant gene is linked to a substrate for the reaction being selected. The library is dispersed into droplets with less than one gene per droplet. The transcription and translation steps are performed to obtain the corresponding protein. If the protein possesses the desired enzymatic properties, the substrate is converted into a product. The encapsulation of single mutants into reservoirs enables a proper linkage between the genotype and the phenotype. Droplets containing desired genes present genes linked to the product of the enzymatic reaction

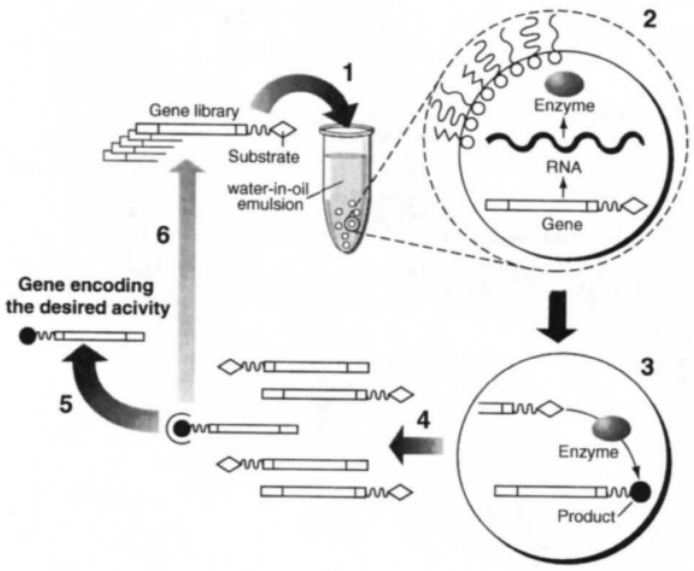

Figure 1.2 – Schematic representation of the selection procedure. Step 1: An in vitro transcription/translation reaction mixture containing a library of genes linked to a substrate for the reaction being selected is dispersed to form a water-in-oil emulsion with typically one gene per aqueous compartment. Step 2: the genes are transcribed and translated within their compartments. Step 3: proteins with enzymatic activities convert the substrate into a product that remains linked to the gene. Compartmentalization prevents the modification of genes in other compartments. Step 4: the emulsion is broken, all reactions are stopped, and the aqueous compartments are combined. Genes linked to the product are selectively enriched, amplified and characterized (step 5), or linked to the substrate and compartmentalized for further rounds of selection (step 6). Figure and caption adapted from [10]

and can be selectively enriched or compartmentalized for further rounds of selection. Droplets containing non-desired genes cannot transform the substrate into product and are not selected.

Emulsion (or digital) PCR From a commercial point of view, the most successful application of compartmentalization is emulsion Polymerase Chain Reaction (PCR). Discovered in 1986 by Kary Mullis, PCR enables the amplification of a DNA fragment via cycles of enzymatic polymerization under thermal cycling. The use of droplets to isolate DNA fragments presents multiple advantages. The PCR efficiency is known to depend notably on the characteristic of the amplified DNA; when amplifying several DNA strands in a same tube, short strands are preferentially amplified over larger ones. Another biase is the formation of DNA artifacts by recombination between compatible fragments. Those biases are particularly disturbing for the amplification of low concentrations of template DNA in which non-specific amplification products might become predominant[11, 12]. By compartmentalizing each DNA molecule in a single droplet, the PCR provides copies of a monoclonal template, suppressing mentioned biases and guaranteeing the obtention of a uniform amplification regardless of the DNA strand length[13, 14]. Additionnally, miniaturization goes along with faster thermal exchanges because of the low thermal inertia of microsystems; Wittwer & Garling[15] suggested that the specificity

and the efficiency of the PCR was improved by a fast and controlled variation of the temperature.

1.1.3 Input of microfluidics

In most industrial applications and in first research trials, the emulsification process was performed with mechanical stirring[11] or ultrasonication[12], a process that enables the creation of large volumes of emulsions but results in very bad monodispersity. In biological applications, the difference in droplets size complexifies their further analysis. The phenotype might artificially differ with the droplet volume, resulting in wrong selection steps. Polydispersity also add biases on the repartition of the biological material inside droplets, especially out of the diluted regime[16]. Last, the range of assays reachable was quite limited, as droplets could not be manipulated and no reagent could be added after the emulsification process[17, 18]. The development of microfluidics appeared as a way to produce and manipulate droplets in a much more controlled manner. Droplets can be produced at kHz rates with a very good monodispersity (typically less than 3 %), they can be merged, splitted, incubated, sorted depending on their content. The first use of microfluidic droplets for biological applications started in the years 2000 [11, 19].

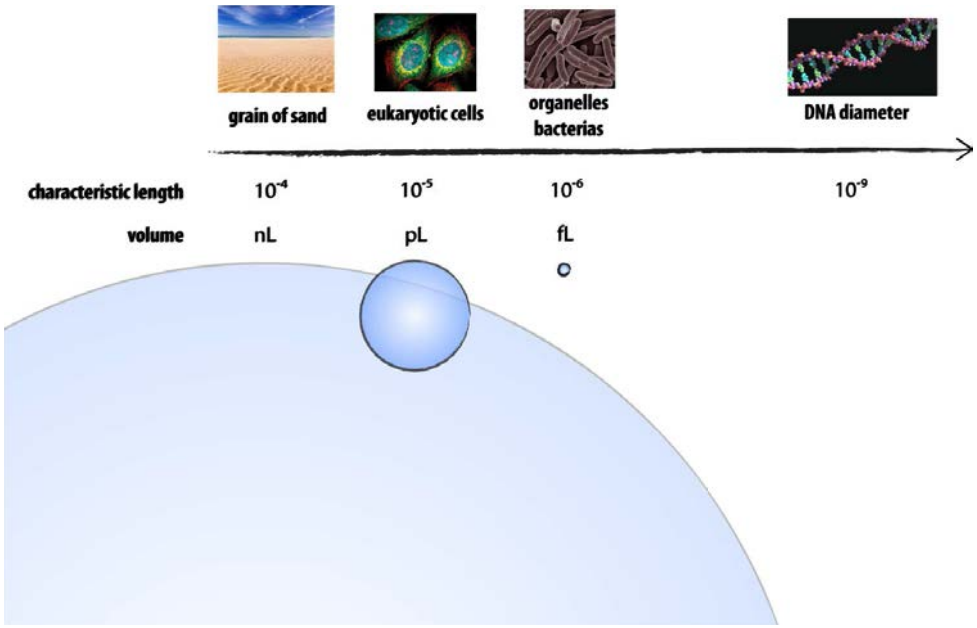

Figure 1.3 – Definition of the scales at play in this PhD manuscript. Most microfluidic devices are developped at the nL and pL scales, corresponding respectively to the size of a grain of sand, and of a eukaryotic cell. Femtoliter droplets are an order of magnitude lower in size, matching the size of bacterias.

Before entering into the details of droplet-based microfluidics, here is a scheme of the scales involved in this PhD manuscript (Figure 1.3). Most microfluidic devices are developped at the nL and pL scales, corresponding respectively to the size of a grain of sand and of a eukaryotic cell. Femtoliter droplets are an order of magnitude lower in size, matching the size of bacterias. Applications concerning cells are thus obvisouly discarded from following discussions except

when coupling picoliter and femtoliter droplets.

1.2 Droplet-based microfluidics

In this section, the main physical principles of microfluidics are first described. The basic operations of droplet-based microfluidics are then detailed: droplet production, addition of a reagent, droplet sorting, droplet splitting, incubation steps.

1.2.1 Physical principles

Continuity assumption Fluid dynamics relies on the definition of a fluid particle with continuously varying properties. At the molecular scale, the brisk variations of fluid properties prevent the definition of continuous properties of the fluid; studies on thin films have demonstrated that the molecular organization appears for thicknesses on the order of 10 molecular diameters[20]. The smaller dimensions considered in this manuscript are in the range 0.8 - 1μm and the validity of the continuity assumption is thus always verified. Similarly, most characteristic lengths (Debye length, critical radius of nucleation, capillary length, ...) are expected to become predominant below 100 nm which is beyond our miniaturization pretentions.

Our devices are in the microfluidic domain, where the only characteristic length that matters is the dimension of the system l. Consequences on the flow equations are highly beneficial, as explained in the following paragraph.

The Stokes equation The behavior of incompressible newtonian fluids is governed by the Navier-Stokes equation :

$$\rho[\frac{\partial \mathbf{u}}{\partial t} + (\mathbf{u}.\nabla)\mathbf{u}] = -\nabla p + \eta\nabla^2\mathbf{u} + \mathbf{f} \tag{1.1}$$

$$\nabla.\mathbf{u} = 0 \tag{1.2}$$

where $\mathbf{u}$ is the flow velocity, p is the pressure, ρ is the density, η the dynamic viscosity and $\mathbf{f}$ represents body forces that apply on the flow, such as gravity or electrical forces. Equation 1.2 derives from the incompressibility condition. In microfluidics, devices scales are reduced and the Navier-Stokes equation can be simplified by comparing the order of magnitude of the inertial and viscous terms. The ratio of the inertial term $\rho(\mathbf{u}.\nabla)\mathbf{u}$ over the viscous term $\eta\nabla^2\mathbf{u}$ defines the dimensionless Reynolds number:

$$Re = \frac{\rho l u}{\eta} \tag{1.3}$$

where l is the characteristic size of the system. In typical microfluidic devices, l is on the order of 10^{-6} m, u varies in the range 10^{-6} m/s to 10^{-3} m/s, corresponding to Reynolds numbers varying from 10^{-6} to 1. In such conditions, inertial terms can be neglected and the Navier-Stokes equation becomes linear. For an established flow, hydrodynamics is then governed by the Stokes equation:

$$0 = -\nabla p + \eta \nabla^2 \mathbf{u} + \mathbf{f} \tag{1.4}$$

The linearity of Stokes equation provides crucial characteristics to the flow; unicity of the solutions upon imposition of the boundary conditions, additivity of the solutions, reversibility of the flow fields. These features help a robust and predictible handling of fluids and the development of complex workflows.

Other dimensionless numbers Additionnally to the Reynolds number, several other dimensionless numbers characterize the fluid properties: the Capillary number $Ca = \eta u/\gamma$ where γ is the surface tension represents the ratio of viscous forces over surface tension forces. It is often used to characterize the disruption of a fluid into droplets or the effect of the continuous phase on droplets interface. In most microfluidic devices, the Capillary number is limited by droplets speed and varies between 10^{-5} and 10^{-2}.

Another important number is the Peclet number $Pe = \frac{ul}{D}$ where u is a characteristic speed of the flow, l the size of the system, D the diffusion coefficient. In fluid exchanges problems, it represents the relative significance of advection terms over diffusion ones. An interesting remark about the Peclet number is that it is not necessarily small in microfluidic devices, contrary to Re and Ca. Mixing can be governed by advection rather than diffusion even though scales are micrometric.

When electric fields are involved, the Bond electric number $Be = \epsilon_0 \epsilon_r l E^2/\gamma$ is used to characterize the relative importance of electrostatic forces over capillary forces. Here, ϵ_0 is the vaccuum permittivity, ϵ_r the permittivity of the fluid, E the applied electric field. Be is expected to decrease with devices miniaturization and the manipulation of very small volumes with electric forces is questionable.

In all cases, the miniaturization of droplets to the femtoliter scale does not change the main assumptions of microfluidics; Reynolds numbers and Capillary numbers remain small limiting flow description to the Stokes equation. Devices dimensions remain large enough to neglect nanofluidic phenomena. Miniaturization of droplets to the femtoliter scale is thus encouraged by the expected absence of fundamental changes in the physics of such devices. The feasibility of electrical actuation has to be assessed.

1.2.2 Basic operations of droplet-based microfluidics

We describe here the main operations of droplet-based microfluidics: droplet production, addition of a reagent, droplet sorting, droplet splitting, incubation steps.

Droplet production

Microfluidics enables the production of droplets over a wide range of volumes (nL to fL), with a high monodispersity and ultra-high throughputs (kHz - MHz). Droplets can be produced in four different configurations (Figure 1.4).

- T-junction : the T-junction was the first developped method to produce droplets in a microsystem. It consists in an intersection between a channel containing the phase to be dispersed and a channel containing the continuous phase. The phase to be dispersed fills the junction until it breaks into a droplet (Figure 1.4.a).
- Flow-focusing : the fluid to be dispersed is pinched between two streams of continuous phase. The shearing is symetrical in this geometry, contrary to the T-junction, which increases the production stability (Figure 1.4.b).
- Co-axial production : in this geometry, the droplet production is obtained through a series of concentrical capillaries. The central capillary contains the fluid to be dispersed and reaches a flux of continuous phase at the end of the central capillary. It is easy to produce multiple emulsions in this configuration, by multiplying the number of coaxial capillaries (Figure 1.4.c).
- Step-emulsification : the production of droplets in step-emulsification is inspired by the industrial membrane emulsification process. In this technique, the phase to be dispersed is separated from the continuous phase by a membrane. The phase to be dispersed is pulled through the pores of the membrane and breaks into droplets. In microfluidics systems, the membrane pore is modeled by a transition between a confined domain and a large reservoir (Figure 1.4.d).

In some cases, the production needs to be sequential rather than continuous; drop-on-demand (DoD) devices enable the sequential production of droplets. Pneumatic actuation was the first DoD method[25, 26, 27] and uses the deformation property of an elastomeric membrane to locally close a flow channel upon pressurization. This method is highly robust and enabled a large parallelization of actuators[28]. The drawback of those actuators is their response time, typically a few tens of milliseconds. In applications demanding faster throughputs, piezo-electric actuation can be envisioned, either implementing macroscopic piezo stacks[29, 30] or, more recently, using PZT films[31]. Other DoD methods exist, though more rarely used: thermally mediated droplet formation[32], laser actuation[33], hydrophobic valving[34], surface acoustic

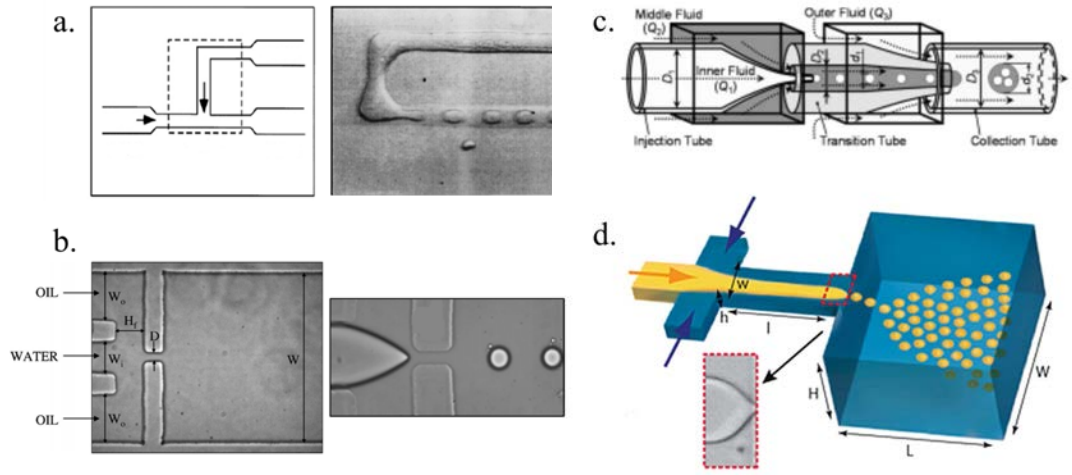

Figure 1.4 – Four types of droplet makers. a.T-junction, adapted from [21]. b. Flow-focusing, adapted from [22] c. Co-axial production, adapted from [23]. d. Step-emulsification, adapted from [24]

waves[35], magnetically modified elastomeric valves[36], electrohydrodynamic jetting at high electric fields[37].

Addition of a reagent

Addition of a reagent is necessary for most multi-step biochemical assays. It also enables a precise control over the begining of the reaction. The injection of the reagent is often performed by merging of two droplets, either by passive or active methods. Passive methods rely on geometrical or physico-chemical induction (Figure 1.5). The first coalescers leaned on the drainage of the continuous phase, allowing the droplets to enclose and merge. A variety of functional geometries can be reported, among which enlarging channels [38], sometimes with the addition of pillars that drive the droplets in the center while letting the continuous phase flow around[39]. Bremond *et al.*[40] studied the merging of droplet pairs in enlarging channels (Figure 1.5.A) and could demonstrate that the merging is induced by decompression at the outside of the enlarged area. In most above mentioned devices, droplets can merge as long as they are not initially separated by more than a few radii, which imposes a proper synchronization of droplets prior to their merging. 3D traps[41, 42] present the advantage of suppressing synchronization issues. A merging trap comprises two bypasses and side intrusions (Figure 1.5.B.a-b.). If the droplet is longer than the trap, the two bypasses are blocked when the droplet front arrives at the outlet of the trap and the droplet passes through. However, if the droplet is shorter than the trap, the continuous phase can flow through the bypasses and the droplet is locked when its front reaches the outlet of the trap. When another droplet arrives in the merging trap, the two droplets merge and, if the resulting droplet is longer than the trap, it flows out of the trap. Other passive methods can be reported such as the use of hydrophilic patches[43, 44] with the drawback of cross-contamination as droplet content contacts the channel walls, or the use of physico-chemical induction by using different surfactant concentrations[45](Figure 1.5.C) .

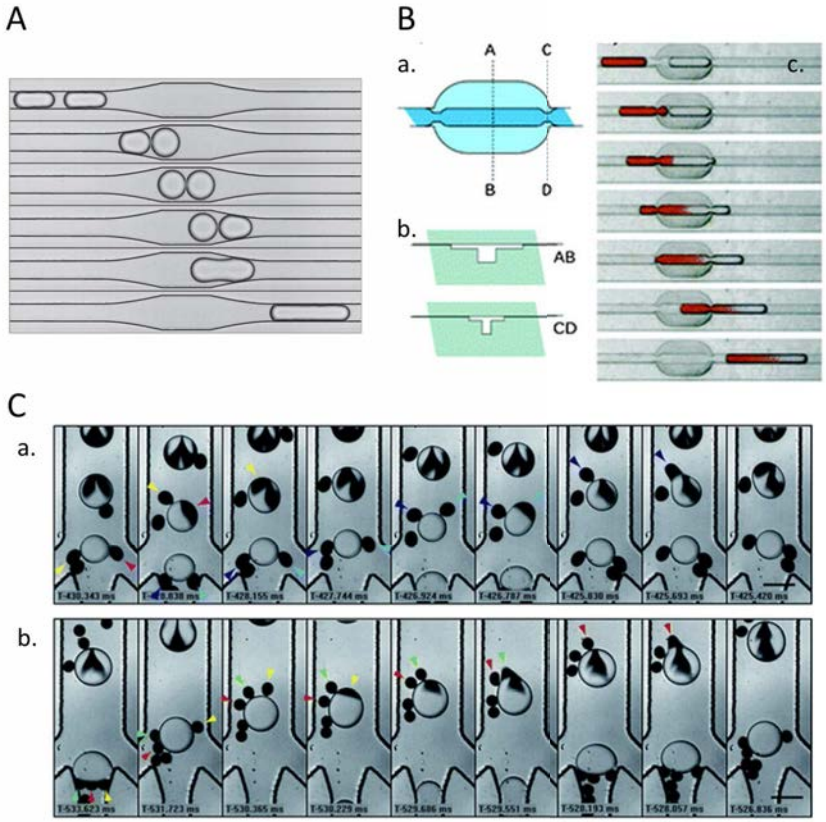

Figure 1.5 – A. Passive coalescence of droplets induced by a restriction. When the first droplet enters the restriction, it generates a pressure drop between drops that helps the interface rupture. Adapted from [40] B. Merging trap. a) Scheme of the trap from the top view. b) Scheme of the trap from a lateral view. c) When a droplet flows into a filled trap the two droplets merge. If the residual droplet is longer than the trap it completely releases the trap, while the content of the two initial droplets mixes effectively even in straight channels. The width of the straight segments of the channel is 400 μm. Adapted from [42]. C. Selective 2:1 and 3:1 passive droplet fusion. a) Time series showing a 2:1 (two-to-one) coalescence event: two reinjected droplets fuse to a single on-chip droplet. b) Time series showing a 3:1 (three-to-one) coalescence event: three reinjected droplets fuse to a single on-chip droplet. Emulsion droplets are black and on-chip generated droplets are clear. Emulsion droplets in panels a) and b) are of 5 pL and 3 pL, respectively. The arrows track droplets that coalesce. Scale bars 50 μm.

Most of those passive mergers are only suitable for non surfactant-stabilized emulsions. Active methods provide higher fusion efficiencies and are less subjected to formulation variations, at the expense of more complex equipments. The use of optical tweezers enables the manipulation of particles as long as their refraction index is higher than the one of the continuous phase [46]. This limits this method to the manipulation of water droplets in fluorinated oils. Optical tweezers can be replaced by optical vortex traps to overcome this limitation[47] but the throughputs remain very low as droplets are only handled individually (Figure 1.6.a.). It was also demonstrated that the use of a laser point between a pair of droplets can rupture the interface [33], with similar constraints in terms of throughputs (10-100 Hz) and possible degradation of DNA and proteins upon local heating (Figure 1.6.b).

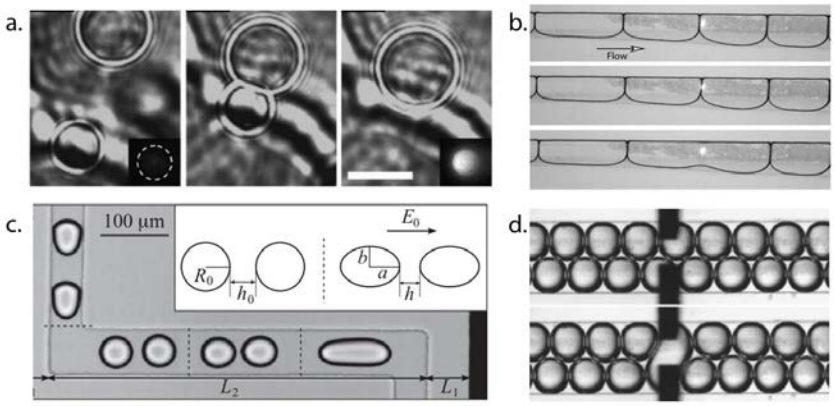

Figure 1.6 – a. Sequential images of coalescence of two aqueous droplets trapped in optical vortexes. Reproduced from [47] b. Localized fusion in a train of large drops. The drops, which flow from left to right, merge as the interface crosses the laser. Reproduced from [33]. c. Microfluidic device used for the investigation of emulsion droplet coalescence under a uniform electric field. The electric field is generated by two parallel electrodes seen on both sides of the picture. The figure shows the behavior of a droplet pair that travels along the fusion chamber. Sketch of two drops before and after being subjected to a uniform electric field E_0. Reproduced from [48]. d. Targeted electrocoalescence of droplets in a microchannel. When a low potential pulse is applied (50 - 100 ms, 1- 3 V dc), pairs of droplets coalesce at the gap between the electrodes. Reproduced from [49].

Electrical coalescers enable the manipulation of droplets at higher throughputs. Droplets may be charged with opposite sign electrostatic charges to make them merge [50], though this method is in practice hardly set up and provides side drawbacks such as the instability of the newly formed droplets. Many electrocoalescence devices have been designed since 2005 [51, 52, 53]. Depending on the application, electrodes can be directly in contact with the solution (surface electrode [49, 54] (Figure 1.6.d) or immersed platinum wires[55]), which enables the use of lower voltages, or separated by the channel walls, which suppresses cross-contamination risks [48, 51, 52, 53] (Figure 1.6.c). This latter technique is one of the most used for biochemical assays, for its robustness and compatibility with biochemical content in the AC mode.

Lastly, another way to inject a reagent is the pico-injection [56] (Figure 1.7); droplets travel though a channel containing pressurized side injectors. Under application of an electric field, the droplet membrane breaks enabling the injection of the reagent. This method does not necessitate pairing considerations and enables ultra-high throughputs (10 kHz) but cross-contamination issues may be encountered as part of the droplet diffuses towards the injector. Some studies suggest that cross-contamination issues can be weakened by increasing the injector hydrodynamic resistance[57]. The increase in hydrodynamic resistance results in an increase of the Peclet number Pe. By increasing Pe, the advective injection of the reagent is fastened while the diffusive back-flow of the droplet content is reduced. In practice, such considerations are barely taken into account in most pico-injectors, as wide channels provide a more stable meniscus and offer robustness to the injection. Cross-contamination remains a major drawback of pico-injection.

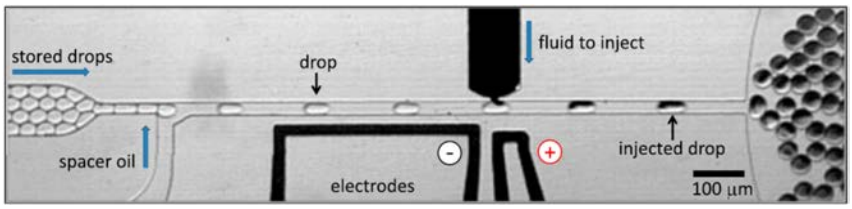

Figure 1.7 – Pico-injection device. Droplets travel though a channel containing pressurized side injectors. Under application of an electric field, the droplet membrane breaks enabling the injection of the reagent. Reproduced from [56].

Droplet sorting

Sorting of droplets is very useful to extract a population of interest out of a larger library. Efficient sorters have been described to sort droplets depending on their size and restore the monodispersity of an emulsion. Most passive sorters use asymmetric bifurcating junctions [38, 58, 59] or Pinched Flow Fractionation in which particles are focused in a pinched segment and separate depending on their size by the spreading streamlines when the channel enlarges[60, 61] (Figure 1.8.A). Other passive methods have been developed more recently such as inertial sorters[62] or sorters based on deterministic lateral displacement (DLD)[63], with an active interest directed towards the sorting of circulating tumor cells [64]. Tensiophoresis enables the sorting of droplets depending on their chemical content; subjected to an orthogonal surfactant gradient in the continuous phase, droplets migrate at a speed that depends on the concentration of proteins in the aqueous phase[65]. This method provides a passive sorting of droplets depending on their biochemical content, without labelling. Apart from this latter example, passive sorters are limited to the sorting of droplets based on their size, restricting biological applications to a few particular situations: Chabert *et al.*[66] observed that droplets containing cells were larger than the empty ones and could sort them hydrodynamically. In the case of yeast encapsulation, droplets would shrink with the cell growth and could efficiently be sorted by DLD[63].

To extract a population of droplets of interest out of a monodisperse library, active sorting methods are mandatory. Multiple actuations have been envisioned to develop active microfluidic sorters: electro-osmotic [70], mechanical [71], optical [72], magnetic [73], acoustic[68] and dielectrophoretic actuation[74]. However, for biological applications, sorting must be coupled to a droplet labelling, typically a fluorescence measurement. This leaves only a few possible actuators : electro-osmotic actuation is possible in presence of a conductive suspending phase, but is to be discarded in the case of water-in-oil droplets sorting. Mechanical and optical actuations can be envisioned, but with throughputs typically limited respectively to a few 10 Hz and a few 100 Hz. This is highly limitable for screening applications where typical libraries count 10^6 droplets. Recently, coupling of mechanical and optical methods could increase the throughputs to kHz rates; by using a pulsed laser, Wu *et al.*[67] create a cavitation vapor bubble that deflects the cell towards a collection channel at rates up to 20 kHz (Figure 1.8.B). An additional coupling to inertial chambers enabled the authors to increase the sorting purity by better controlling the particles spacing[75]. Surface Acoustic Wave (SAW) sorters can be coupled to fluorescence de-

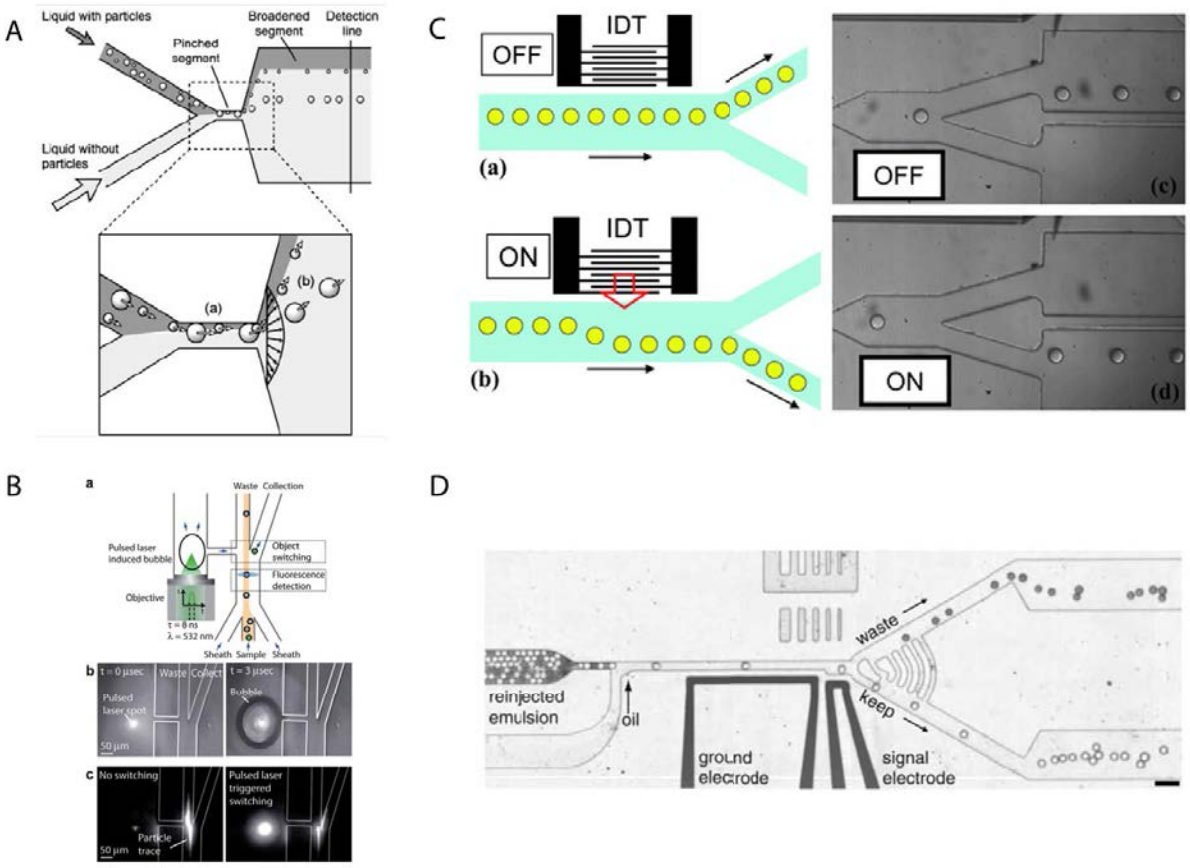

Figure 1.8 – A. Passive droplet sorting by Pinched Flow Fractionnation. Particles are focused in a narrow channel and separate according to their size at the end of the restriction by spreading of the streaming lines. Reproduced from [60]. B. Active sorting by cavitation of a vapor bubble upon a pulsed laser excitation. Reprinted from [67]. C. Active droplet sorting by Surface Acoustic Wave (SAW). a-c. Without actuation, droplets direct towards the path of minimal hydrodynamic resistance. b-d. With actuation, droplets are deflected towards the other path. Reproduced from [68]. D. Fluorescence-activated droplet sorting. Reprinted from [69].

tection and enable the sorting of droplets at a frequency up to 3 kHz [76] at a medium acoustic power (Figure 1.8.C). SAW is a promising sorting tool for the future.

For now, however, FACS remains the most powerful tool for the high-throughput sorting of single cells[77, 78, 79]. In this method, a cell suspension flows in a nozzle where cell fluorescence is analyzed by a laser excitation, cell by cell. The stream is broken into an aerosol and a charge is imposed to the cells depending on their fluorescence. Cells are deflected to different reservoirs depending on their charge at a rate up to 1.10^5 cells/s[78]. Those aerosol FACS present some major drawbacks such as the risk of contamination as the circuits are opened. The use of closed microfluidic chip efficiently suppresses this impediment; in DEP sorters, sorting results from the imposition of a non-uniform electric field that interacts with droplet dipoles and deflects them toward a collection channel[69, 80, 81] (Figure 1.8.D). Sorting rates were decreased to a few kHz in most devices, though recent advances demonstrated a 30 kHz sorting rate[82].

Droplet splitting

Droplet splitting corresponds to the division of a mother droplet into smaller daughter droplets. This operation enables the multiplexing of reactions on droplets of similar composition. In the evolutionary perspective, the splitting of droplet models the cell division and can be used to study early life processes.

Droplet splitting is usually performed by sending a droplet at high speed against an obstacle[83] or by driving the droplet against a bifurcation (typically, a T junction[84, 85]), though other methods have been reported (use of a thermic resistance [86], high electric field splitting[87]). Hydrodynamic splitting is controlled by the geometry, the viscosity ratio of the continuous and dispersed phase $\lambda = \frac{\mu_c}{\mu_d}$ and the Capillary number, defined by $Ca = \mu_c u/\gamma$. The case of the T-junction splitting was highly studied [85, 88]. It has been shown that two regimes of splitting are possible, one in which droplets occupy only a fraction of the channel width (non obstructed regime, Figure 1.9.a. - regime B), and the other in which droplets completely obstruct the channel (break up with complete obstruction of the channel (Figure 1.9.a. - regime C)). The former necessitates moderately low Ca, while the latter, being mostly controlled by the geometry, occurs almost independently of Ca (Figure 1.9.b.).

Incubation steps

Droplets are used as individual microreactors for biochemical assays that most often require incubation steps. Depending on the reaction, incubation times can vary from minutes to hours, or even days. For fast reactions, droplets are incubated on-chip, either in a single line or in deep and wide reservoirs (often called *delay-lines*). Studies demonstrated that it is possible to obtain delay-lines for incubations up to an hour with limited hydrodynamic resistance. Constrictions are added periodically to reduce the dispersion of incubation times[89]. For longer incubation periods, droplets are usually stored off-chip in a tube, covered by mineral oil or a PDMS plug to avoid evaporation issues[19, 80, 90, 91]. They can be reinjected for further analysis afterwards.

Droplet-based microfluidics provides extensive tools for the handling of droplets. A wide panel of devices permits the elaboration of complex multi-step workflows with maintaining ultra-high throughputs. Most of exposed devices focus on droplets volume ranging from the nL to the pL scale, with very few advances towards lower scales[47, 92]. In the following section, we question the interest of further miniaturization of droplets.

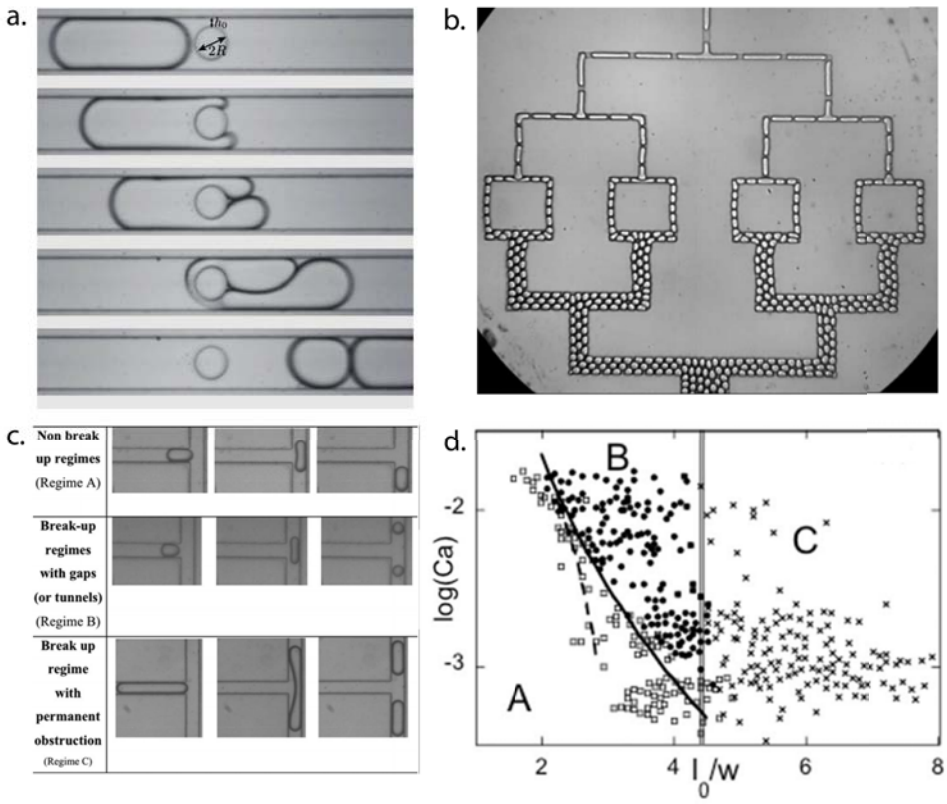

Figure 1.9 – Splitting of droplets. a. An obstacle is placed in the center of the channel. When the droplet collide the post, it splits into two daughter droplets. Reproduced from[83] b. Droplets are driven towards consecutive T-junctions and are sequentially spllitted into smaller droplets. Reproduced from[84] c. Three regimes are defined depending on the droplet length and the capillary number. A. Non breakup regime. B. Breakup without complete obstruction of the T junction. C. Breakup with permanent obstruction of the T junction. Reprinted from [88] d. Phase diagram in the case of $\lambda = 1.67$. Regime C exists at any capillary number while regime B demands a critical droplet speed. Reprinted from [88]

1.3 On the advantages and drawbacks of droplets miniaturization

Droplet-based microfluidics has demonstrated major advantages over conventional microtitre plates technologies. For instance, Agresti *et al.*[69] demonstrated a 1,000-fold increase in throughput for the directed evolution of the horseradish peroxidase enzyme, and a million fold reduction in cost that is to be related with the low volumes consumed. The screening of a typical library of 10^7 mutants takes 2 years and costs 16 million euros in microtitre plates, while it takes one day and costs 2 euros in picoliter droplet-based microfluidics.

However, miniaturization presents its own drawbacks. Despite the huge technological advances since the 1900s, further scale reduction meets the limits of technical devices. Optical sensitivity may become limiting; many assays rely on the detection of fluorescence and the downscaling limits the number of fluorophores inside each droplet. Devices miniaturization also goes along with higher hydrodynamic resistances correponding to higher working pressures. Everything is expected to go faster which raises questions of electronic automation possibilities.

The sum-up of these advantages and drawbacks sets an optimal droplet size that depends on the biological application, as recently highlighted by Rosenfeld *et al.*[16]. Similarly to those authors, we are going to study the impact of droplet size on throughput and sensitivity. We first focus on the impact of miniaturization on the throughput of workflows. Depending on the assays, the throughput can be limited by the emulsification time, by the incubation time or by the droplet interrogation/sorting time.

1.3.1 Throughput of the encapsulation step

Emulsification of a fixed volume of sample To analyze a fixed volume of sample in droplets, the first step is the emulsification process. Whatever the chosen geometry, droplet production results from the interplay between shear stresses applied by the continuous phase and the capillary tension of the interface. Two production regimes are usually defined. At low external flow rate and low flow rate ratios between the two phases, the internal fluid produces monodisperse droplets at the orifice, with a characteristic size l on the order of the orifice dimension; this regime is called *dripping*. At larger external flow rates, and keeping low flow rate ratios between the two phases, the internal fluid forms a jet that destabilizes into droplets far from the junction. This regime, so-called *jetting*, produces more polydisperse emulsions. The dripping to jetting transition depends upon the Capillary number, $Ca = \eta u/\gamma$.

To remain in the monodisperse dripping regime, the external phase flow rate is thus limited to a critical flow rate Q_{max}. The continuous phase has a maximal characteristic speed u that verifies $Q_{max} = ul^2$. The time necessary to emulsify the entire sample volume is $t_{production} \sim V_{sample}/Q_{max} \sim Q_{max}^{-1} \sim l^{-2}$. The time needed to emulsify a fixed volume of sample is thus larger for small drops. The use of femtoliter droplets is to be avoided for the emulsification of a

large volume of sample.

Encapsulation of a fixed number of molecules The above argument needs to be put in perspective; in many assays, the parameter that is fixed is the number of molecules to be encapsulated rather than the volume of sample. Encapsulation of the biological material follows a statistic distribution of uncorrelated rare events. If we denote λ the mean number of biomolecule per drop, the probability for a drop to contain k biomolecules is given by a Poisson statistic:

$$P(k) = \frac{\lambda^k e^{-\lambda}}{k!} \tag{1.5}$$

To make sure that all droplets contain one biomolecule at most, samples are very diluted ($\lambda \sim 0.1-0.2$). The expected value of λ is calculated by $\lambda = CV_d$ where C is the concentration of the biochemical sample and V_d the volume of the droplet. The miniaturization of droplets goes along with an increase of the concentration of the sample with the following scaling law: $C \sim V_d^{-1} \sim l^{-3}$. The encapsulation of a given number of biomolecules thus necessitates less droplets with their miniaturization. The time necessary to encapsulate a fixed number of biomolecules is $t_{production} \sim V_{sample}/Q_{max} \sim l^3/l^2 \sim l$. The emulsification time decreases with droplet miniaturization in the case of a fixed number of molecules.

1.3.2 Throughput of the incubation step

Thermalization of the sample Droplet incubation is often performed by thermalization of the emulsion at a favorable temperature. The establishment of thermal equilibriums is faster in miniaturized devices, with a characteristic time $\tau_{thermal} \sim \alpha l^2$. α depends upon ρ the volumic mass, C_p the specific heat ($J.kg^{-1}K^{-1}$) and K the thermal diffusivity ($W.m^{-1}K^{-1}$), and is defined as $\alpha = \rho C_p/K$. Incubation times can be limited by the use of downscaled microfluidic chambers. However, to avoid issues related to evaporation or to a poor biocompatibility of the device, emulsions are most often recovered off-chip to perform the incubation (typically, the PCR) in a conventional thermocycler. The impact of miniaturization is unclear in this later case; we want to compare the characteristic time of thermal diffusion for a fixed volume of sample, heated either in bulk or in droplets. To simplify the problem, we consider droplets as cubic elements of length l_w, surrounded by elements of oil of dimension l_o and laterally heated as represented in Figure 1.10. The macrosopic lateral dimension is L_1. If n is the number of droplets in a row, $\tau_{thermal-droplets} \sim n(\alpha_o l_o^2 + \alpha_w l_w^2) \sim n\alpha_o l_o^2$ as $\alpha_o \gg \alpha_w$. The size of the element of oil must vary depending on the temperature (thermic stirring) and is taken to l_w, the characteristic size of the droplet.

$$\tau_{thermal-droplets}/\tau_{thermal-bulk} \sim \frac{n\alpha_o l_o^2}{\alpha_w L_1^2} \sim \frac{\alpha_o}{\alpha_w}\frac{l_w}{L_1} \tag{1.6}$$

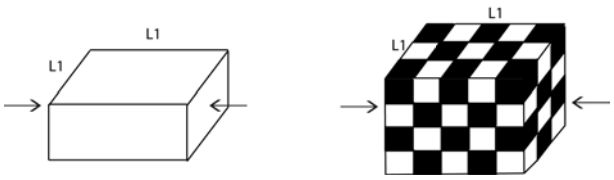

Figure 1.10 – Incubation of a fixed volume of water in a macroscopic reservoir, laterally heated. The macroscopic lateral dimension is L_1 and droplets are assimilated to small cubes of characteristic dimension l. The thermalization of a sum of individual droplets is faster than the thermalization of the bulk volume; the improvement increases with droplet miniaturization.

The incubation time of an emulsion in a conventional thermocycler is thus lower with droplet miniaturization, and lower than the thermalization of an equivalent volume of water in bulk despite the low thermal diffusivity of oil. The use of femtoliter droplets should accelerate the thermalization of samples.

Biochemical impact of droplet miniaturization In enzymatic reactions, the encapsulation of a single enzyme molecule in a small droplet increases its effective concentration; a single enzyme in a microtitre plate is very diluted ($\sim 1aM$) but by encapsulating it in a femtoliter reactor, its effective concentration is increased by 9 orders of magnitude ($\sim 1nM$). Considering the enzymatic rate k scales like the effective concentration of the enzyme[93], fluorogenic products are formed with a time scale $1/k \sim l^3$ that corresponds to a faster detectable level with droplet miniaturization. Another example of the beneficial effect of compartmentalization of biochemical reactions kinetics was recently revealed; Fallah-Araghi *et al.* demonstrated that both kinetics and thermodynamics of synthetic reactions can be enhanced by compartmentalization in micrometer-diameter droplets [94]. This process is based on an interfacial reaction-diffusion mechanism, coupling bulk and surface reactions that requires low binding energies. Droplet miniaturization is expected to increase the throughput of incubation steps from a biological point-of-view.

1.3.3 Throughput of droplet interrogation

Analysis of the droplets content is either performed in a 2D image or one drop at a time in a circulating channel.

Interrogation of a train of droplets When droplets are analyzed one-by-one, the interrogation frequency is related to droplets maximum speed and their minimal spacing. Droplets minimal spacing is set to avoid undesired interactions or coupling between droplets and can be generally fixed to a few l. The maximum droplet speed is defined either by hydrodynamic considerations, *i.e.* the maximal speed that does not induce droplet splitting, or by actuation forces limits. For instance, DEP actuation is only possible below a critical droplet speed; the maximum electric field is defined by the electrosplitting limit and sets a corresponding critical

droplet speed above which DEP forces are weaker than drag forces. More detailed analysis of the DEP sorting process can be found in Chapter 5.2. The scaling law shows that sorting frequency scales like l^{-1} in this case. When droplets speed is limited by hydrodynamic splitting, studies by Leshansky [85] defined and characterized two regimes of splitting; above a critical capillary number, droplets are splitted in a non-obstructed regime with a boundary defined by $l/w \sim Ca^{-0,21}$ where l is the droplet length, w the channel width. In the case of slower droplets, droplets split with a complete obstruction of the junction and splitting is purely governed by the junction geometry; the regime boundary is defined by $l/w \sim Ca^0$. In both cases, droplet frequency scales like $l^{-0,8}$ or l^{-1} corresponding to an increase of the interrogation frequency with droplet miniaturization.

Interrogation of a 2D chamber The interrogation of individual streaming droplets limits throughputs to a few 10 kHz in the best perspectives. Analysis of multiple droplets in large microfluidic chambers enables the improvement of the interrogation capacity. In such devices, the interrogated area is a compromise between the field of view and the collection efficiency. Increasing the observable area demands the use of low magnification objectives, that most usually have lower numerical apertures (NA). However, the NA is related with the light-gathering ability which is a highly important parameter for the fluorescence analysis of droplets. By using arrays of lenses instead of a single lens, authors could reach an interesting compromise between the field of view and the collection efficiency. On 4pL droplets, with a 1x magnification, Schonbrun *et al.*[95] demonstrated the analysis of 200 000 drops/second with a lens array. With similar techniques, the interrogation throughput was recently increased to 1.2 millions of analyzed droplets per second[96] with an improval of the sensitivity detection (2.5 μM of fluorescein). We don't pretend to discuss here the impact of miniaturization on 2D droplet interrogation, as it mostly depends on the progress of optics. Even so, the two previously depicted examples are promizing paths towards a 2D analysis of femtoliter droplets. If enabled by the resolution and sensitivity, the miniaturization of droplets at fixed field of view increases the capacity of interrogation.

Additionally, as a result of large dilution factors and of the Poisson distribution, a vast majority of droplets are empty. Using the cumulative distribution function, one can assess the percentage of empty droplets as a function of λ. For instance, to guarantee than less than 0.05 % droplets contain more than a single molecule, λ is fixed to 0.2 and 95% of droplets are empty. The percentage of empty droplets does not change with their volume at constant λ which implies that the unoccupied volume decreases with droplet miniaturization; the number of interrogated droplets of interest increases with droplet miniaturization.

1.3.4 Sensitivity

We now concentrate on the impact of miniaturization on the sensitivity of the assay. Compartimentalization in small reservoirs enables single-molecule studies but goes along with increased

adsorption issues.

Single-molecule studies, detection of rare events The compartmentalization inside individual reservoirs enables the detection of rare events; typically, in the case of emulsion PCR, all DNA templates receive a similar amplification factor in droplets while rare fragments would be hindered by predominant fragments in bulk. In the case of single-molecule studies, the compartmentalization inside reservoirs (droplets[97], microchamber arrays, lipid vesicles, virus capsids, as reviewed in [92]) is necessary to extract individual heterogeneities of a population rather than the average behavior of an ensemble. The study of enzyme kinetics demands their immobilization for long-time monitoring; the usual way to do it is by immobilizing the enzyme on a surface but this process can lead to partial inactivation, steric hindrance or disturbance of the bulk enzyme activity that are to be avoided[92]. Moreover, fluorescence assays on single-molecules face signal-to-noise issues. Background contributions may originate from elastic and inelastic scattering of light by the surrounding medium and have been shown to decrease linearly with the excited volume while the signal of a fluorophore is constant[98]. This is typically used in confocal epifluorescence microscopy experiments where the excitation laser beam is focused on a diffraction limited spot and enables the detection of single-molecule fluorescence[98]. The miniaturization of droplets enables single-molecule studies (spacial localization of biomolecules without hindering, improved fluorescence assay) and the detection of rare events.

Adsorption of biomolecules at the droplet interface With droplet miniaturization, the surface to volume ratio increases drastically and adsorption issues might become predominant. An important parameter in analyzing adsorption is the ratio of the maximum surface coverage Γ_{max} of the biomolecule over its initial concentration inside the droplet C_0. Depending on Γ_{max}/C_0, adsorption happens in presence of an excess of biomolecule or in presence of an excess of surface. This corresponds to an adsorption limited either by the area of the interface or by the quantity of biomolecule inside the droplet. Several models have been developped to study adsorption kinetics. The rate of adsorption of biomolecules can be limited by the diffusion toward the interface[99] or by the time of adsorption[100]. The miniaturization accelerates adsorption when the rate is limited by the diffusion toward the interface but should not affect adsorption kinetics in the second case. In all cases, adsorption of biomolecules must be hindered in droplets which demands the formulation of surfactants that properly protect the interface. The miniaturization of droplets enhances adsorption issues and a proper formulation must be chosen.

To summarize above discussions, most of mentioned scaling laws are in favor of miniaturization. Decreasing droplet size provides a faster encapsulation of a fixed number of biomolecules, faster incubation steps (both thermically and biologically), faster droplet interrogation - both in 2D, at the expense of a sufficient optical sensitivity, and in a train of droplets, at the expense of acceptable electronic performances -. The relevance and sensitivity of assays increases

with droplet miniaturization opening access to single-molecule studies and enhancing surface to noise ratio of fluorescence assays. Among considered phenomena, only two scaling laws are unfavourable to miniaturization: the production of large volumes of emulsions is laborious and the adsorption of biomolecules (DNA, proteins) on the interface might be detrimental to the assay sensitivity.

The initial aim of this PhD work was the investigation of the possibility of miniaturizing droplet-based microfluidics down to the femtoliter scale. As explained above, this project was encouraged by the expected absence of fundamental changes in the physics of miniaturized devices and by the wide perspectives that would provide a robust handling of femtoliter biological reservoirs. Before entering into the details of my research projects, experimental procedures are described in the following chapter.

Chapter 2

Experimental techniques

This chapter describes the experimental techniques that are common to all following chapters: femtoliter emulsification process, fabrication of the microchips and of macroscopic pieces, fabrication of pneumatic valves, biological assays.

2.1 Emulsification process

This section concentrates on the emulsification process. The production of water-in-oil femtoliter droplets is carried out by a step-emulsification device. Formulation choices are made to provide stability to the emulsions and match the envisioned biological applications.

2.1.1 Step-emulsification

Several production geometries have been introduced in Chapter 1.2.2: T-junction, flow-focusing, co-axial production, step-emulsification. In this PhD work, most emulsions have been formed using step-emulsification geometries and we will detail the principles and mechanisms at play in this particular geometry. Step-emulsification has interesting characteristics: droplets size is mostly governed by the geometry, with a weak dependence on flow conditions, production throughputs are high and monodispersivities in the range of the %.

Step-emulsification devices combine a 2D-like Hele-Shaw cell [1] with a step outlet to a deep and wide reservoir. In the Hele-Shaw cell, the phase to be dispersed is either in a T-junction conformation (Figure 2.1.a.) or pinched between two continuous phase flows (Figure 2.1.b.). In a third conformation, the phase to be dispersed simply flows through an array of holes and fells into a wide, deep reservoir of continuous phase[102]. This latter geometry is discarded from the discussion as it presents larger polydispersities (typically 5%).

1. A Hele-Shaw cell is a channel with a height h much smaller than other dimensions, considered two dimensional.

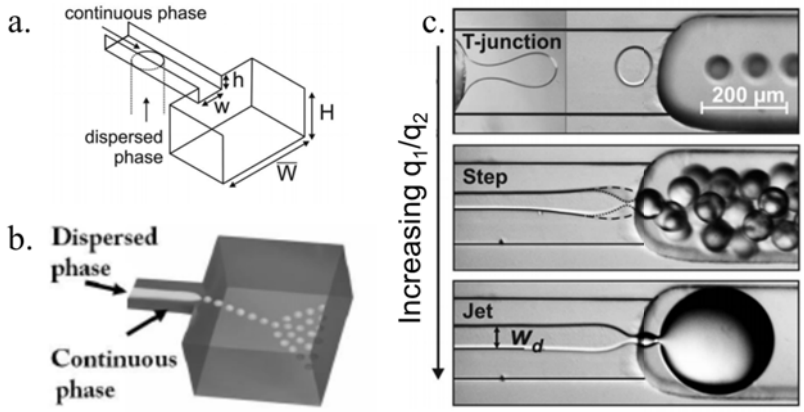

Figure 2.1 – Step-emulsification device. The shallow Hele-Shaw cell either contains a T-junction (a.) or a flow-focusing conformation (b.). c. Three regimes can be defined depending on the flow rates of the dispersed and continuous phase (q_1 and q_2 respectively). At low flow rate ratio, droplets are formed at the junction in a dripping mode. At large flow rate ratio, the dispersed phase forms large balloons at the step, similarly to a jetting mode. At intermediate values of the flow rate ratio, droplets are formed at the step by step-emulsification. a. and c. are reproduced from [101].

Three regimes can be defined depending on the flow rates of the dispersed and continuous phase (q_1 and q_2 respectively). At low flow rate ratio q_1/q_2, droplets are formed at the junction in a dripping mode (Figure 2.1.c, upper picture). At large flow rate ratio, the dispersed phase forms large balloons at the step, similarly to a jetting mode (Figure 2.1.c, lower picture). At intermediate values of the flow rate ratio, droplets are formed at the step by step-emulsification (Figure 2.1.c, middle picture).

Several models have been proposed to describe the step-emulsification regime. In a slightly different conformation where the confined section falls into a less-confined area, Dangla *et al.* use geometric arguments to explain that the growth of a droplet in the less confined area results in a necking in the confined area, eventually producing a droplet. This theory successfully describes the formation of droplets at a step but fails to distinguish the transition to jetting condition. Recent studies have demonstrated that there is a critical capillary number characterizing the transition between step-emulsification and the balloon regime[103]. If we define the capillary number Ca,

$$Ca = \frac{\mu_1 q_1}{\gamma b w} \tag{2.1}$$

With w the Hele-Shaw cell width, b its height, γ the surface tension, μ_1 the dispersed phase viscosity, q_1 its flow rate, Li *et al.* demonstrated that $Ca_*(w/b)$ is a constant; the capillary number that defines the step to jetting transition only depends on the Hele-Shaw cell aspect ratio. This model is consistent with experimental observations: Figure 2.2.a-b. represent phase diagrams of a step-emulsification device for two Hele-Shaw aspect ratios (a. $w/b = 8.8$, b. $w/b = 32.6$). The void symbols correspond to the step emulsification regime and the filled

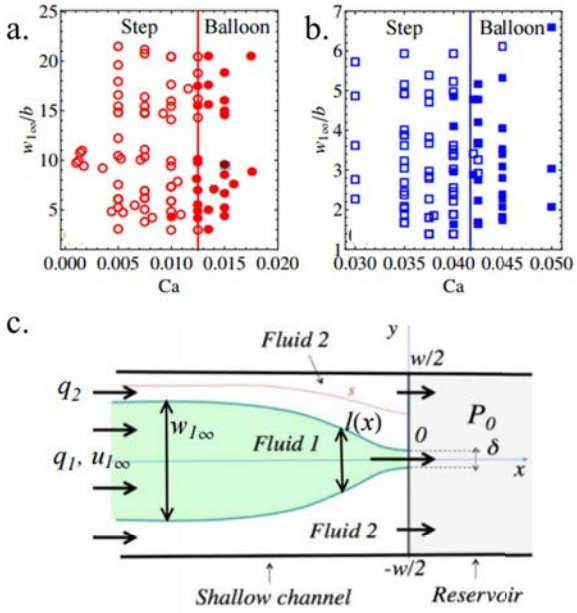

Figure 2.2 – a-b. Phase diagrams of a step-emulsification device defining the step to balloon regime transition for two Hele-Shaw aspect ratios (a) $w/b = 8.8$, (b) $w/b = 32.6$. The void symbols correspond to the step emulsification regime and the filled symbols to the balloon regime. Depicted capillary numbers are the same as defined in Equation 2.1 at the expense of a numerical value (12). The step to balloon transition occurs at constant capillary number for a given geometry. c. The phase to be dispersed (in green) is pinched between two flows of continuous phase in a Hele-Shaw cell and reaches a step to a deep reservoir. The quasi-steady shape of the tongue is represented. Reproduced from [103]

symbols to the balloon regime. Transition occurs at a constant Capillary number for a given geometry, in agreement with Equation 2.1. Li *et al.* model also provides a prediction of the droplet size, that barely depends on the flow rates and is in the order of $3b$.

All femtoliter emulsions were produced in the step-emulsification regime. Droplets size is tuned by changing the Hele-Shaw cell height and by setting it to a third of the aimed droplet diameter.

2.1.2 Emulsion stabilization

The use of droplets as microreservoirs suitable for biochemistry demands certain constraints in terms of formulation; droplets need to be stable enough to go through incubation steps without coalescing, leakage issues between droplets must be avoided, the biological material needs to be fully available for further analysis, regardless of adsorption issues. In this section, we introduce some basic knowledge on surfactant science and explain the formulation choices that were made.

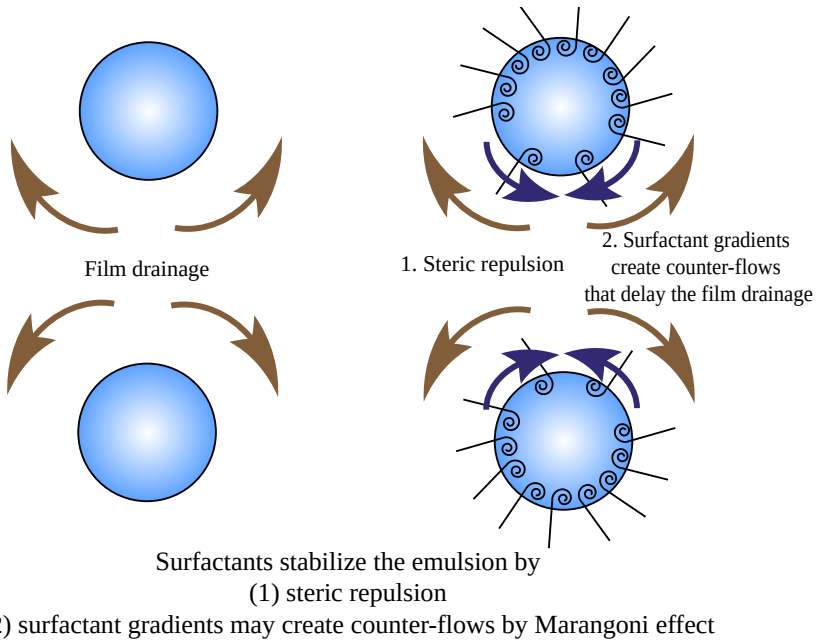

Figure 2.3 – In the absence of surfactants, droplets coalescence is governed by the film drainage dynamics. The introduction of surfactants stabilizes the emulsion by steric repulsion and may generate additionnal Marangoni flows that counteract film drainage.

What is a surfactant?

The emulsification process goes along with the creation of a large interfacial energy. To limit the interfacial energy increase, surfactants can be added. Surfactants are amphiphilic molecules, that possess a hydrophilic head linked to a hydrophobic tail. The hydrophilic part (often charged, or polar) is better solvated in aqueous medias whereas the hydrophobic tail prefers to be surrounded by oil. Surfactants are thus located at the water/oil interface and decrease the interfacial energy. Emulsion stabilization is provided by steric repulsion between the surfactant molecules (Figure 2.3). The kinetics of drainage is also slowed down by the apparition of a counter-flow governed by Marangoni effect; the drainage tends to decrease the local concentration of surfactants in between the droplets, leading to a counter-flow towards the film.

The stabilization efficiency of the surfactant is often assessed by the surface tension decrease. If we denote Γ the surfactant surface concentration, c the surfactant bulk concentration, γ the surface tension, T the temperature and R the gas constant, the decrease in surface tension is described by the Gibbs adsorption isotherm for ideal solutions (dilute regime) :

$$\Gamma = -\frac{c}{RT}\frac{d\gamma}{dc} \tag{2.2}$$

Above a certain surfactant concentration (the critical micellar concentration, or CMC), surfactant molecules tend to self-assemble and form micelles, breaking the dilute regime assumption. Above this CMC, Equation 2.2 is no further valid and the surface tension remains constant upon

addition of surfactant.

Recent studies have shown that dynamical properties are as important as thermodynamic parameters to control the emulsion stability [104]. Baret *et al.* demonstrated that the surfactant concentration has to be much higher than the CMC to efficiently stabilize droplets. In the case of a Krytox FSH - DMP surfactant introduced at 2CMC, multiple coalescence events are observed, resulting in a distribution of droplet size equal to multiple integers of the uncoalesced droplet area A_0 (Figure 2.4.a.). A concentration of 15 CMC was needed to suppress coalescence events. To better understand the dynamics of surfactants stabilization, they used a surfactant that fluoresces when it reaches the droplet interface and observed that the build up of the surfactant interfacial coverage happens on timescales on the order of the droplet manipulation (ms - s) (Figure 2.4.b). The dynamics of surfactant stabilization has to be taken into account in most experiments.

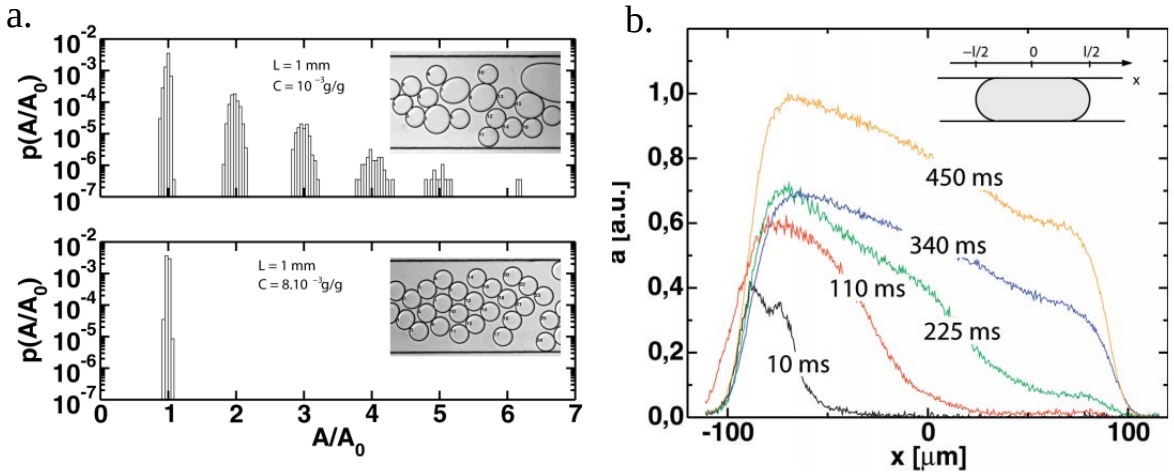

Figure 2.4 – a. Droplet stability as a function of surfactant concentration : size distribution of droplets. Droplet areas A have been rescaled by uncoalesced droplet area A_0. Upper graph : 1,9 CMC, several populations are visible, at areas equal to multiple integers of A_0. Lower graph : 15 CMC, droplets are stable. b. Fluorescent signal intensity a in arbitrary units of the surfactant as a function of the position of the droplet. The label of each curve corresponds to the droplet lifetime after generation when they are analyzed. Surfactant coverage reaches its stable value after several hundreds of milliseconds.

Aging of an emulsion

The addition of surfactants stabilizes the emulsion in a metastable state. The stability of the dispersion is governed by dynamical aging mechanisms. The first of them is the coalescence of droplets; this process is expected to be well hindered by surfactant stabilization, mainly through steric repulsion of the surfactant molecules and blocking of the continuous phase drainage by Marangoni effect in the presence of a surfactant gradient. Another aging mechanism is Ostwald ripening. In a polydisperse emulsion, small droplets have a higher Laplace pressure $P = 2\gamma/R$ (γ the surface tension, R the radius). As a consequence, small droplets diffuse spontaneously towards large droplets and the mean radius of the emulsion increases. Ostwald ripening can be

slowed down or even blocked by the addition of a solute that is not soluble in the continuous phase. Indeed, the presence of the solute creates an additionnal osmotic pressure, that retains the water inside the droplet.

Chosen formulation for our experiments

Continuous phase The continuous phase needs to satisfy two conditions : first, to enable a proper compartmentalization, solutes must be insoluble into the continuous phase. Secondly, it must be compatible with the microfluidic chip, typically made of polydimethylsiloxane (PDMS); many oils induce swelling of PDMS. Fluorinated oils satisfy those two conditions; their hydrophobicity and lipophobicity ensures a low solubility of most biological reagents and they are among the solvents that least swell the PDMS[105]. Additionnally, fluorinated oils possess a good solubility for gases, which can be useful for applications involving living organisms (cells, bacterias). We chose the HFE 7500 fluorinated oil.

Surfactant The development of surfactants to stabilize water-in-fluorocarbon emulsions is quite recent[106]. In addition of guaranteeing emulsions stability over long incubation times and wide storage conditions (typically, high temperatures), surfactants must let the encapsulated biomolecules fully accessible for further analysis, meaning they don't interact with each other. Neutral surfactants are preferred as bioreagents (DNA, RNA, proteins) are often charged and their activity might be altered by electrostatic interaction.

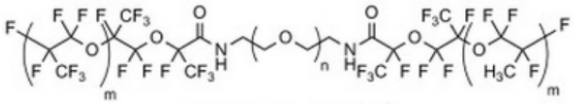

Figure 2.5 – Water-in-oil emulsions are stabilized by a PEG-di-krytox surfactant.

Holtze *et al.* developped triblock copolymers comporting a PEG block soluble to water and two long fluorinated PFPE tails that provide a good steric repulsion between droplets. They optimized the number of PEG units to lower the interaction of bioreagents, the PFPE chains length to obtain an efficient stabilization and the molecular weight of the final copolymer to maintain its ability to diffuse to the interface.

The surfactant is now provided by Raindance Technologies (EA surfactant, $M_w \sim 14000$ g/mol, CMC 0.033%, Figure 2.5). A solution of HFE 7500 containing 2% of EA surfactant (60 CMC) is used for most experiments realized in this manuscript.

To further decrease the interaction of the bioreagents with the interface, another non-ionic surfactant is added in the aqueous phase, Pluronic F-68 at a concentration ranging from 1 to 3%. (30 to 90 CMC)

Demulsifier In some biological assays, droplets need to be broken after the incubation step to analyze their content. To break the emulsion, another surfactant is added, 1H, 1H, 2H, 2H-Perfluoro-1-octanol. This surfactant possesses low stabilizing properties and is much smaller

than the EA surfactant; perfluorooctanol molecules diffuse fastly towards the interface at the expense of the EA surfactant. The emulsion stabilization is drastically reduced and droplets can be broken by vortexing.

2.2 Microfabrication techniques

This section describes basic microfabrication techniques. Microfluidic channels are built using a standard photolithography process and the Poly-dimethylsiloxane (PDMS) fast prototyping technology.

2.2.1 PDMS chips

PDMS presents many advantages: biocompatibility, porosity to gases, rapidity of prototyping, low-cost, among others. The fabrication of PDMS chips requires the following steps: first, the desired structure is designed with a CAD software, then the structure is replicated on a master mold by soft lithography. Last, PDMS counter-molds can be replicated from the master mold. Those steps are detailed in the following subsections.

Masks Masks are designed with a CAD software (Clewin5) according to the aimed application. Depending on the smallest dimension of the design, several printing methods are used. For structures down to 6 micrometers, masks are printed on flexible substrates. For smaller structures, it becomes mandatory to use chrome masks, fabricated in the UPMC microfabrication platform.

Soft lithography - standard protocol Soft lithography enables the fabrication of microstructured silica molds. The desired structures can be transferred from the mask to the mold thanks to photosensitive resists. Depending on the resist type (positive or negative), the exposed area respectively get dissolved or reticulate. A complete protocol is described thereafter in the case of the negative photoresist SU8 series and summarized in Figure 2.6 along with advice on critical steps. The wafer is dehydrated at 200 $^\circ$C for 10 minutes. This step improves the adhesion by ensuring the wafer is completely dry. The photoresist is deposited by spin-coating. The deposition thickness depends upon the spinning speed and the resist viscosity. The solvent is removed by a first baking step (soft bake) according to the manufacturer's datasheet. The resist is exposed through the mask with a UV lamp filtered at 365 nm. A catalyst is created in the exposed area. A second bake is performed to enable the exposed areas to reticulate. The non exposed areas are dissolved in SU8 developer. A hard bake is performed to improve the adhesion and the surface aspect of the resist.

In the case of positive photoresist, the resist reticulates everywhere and the exposure dissolves it locally.

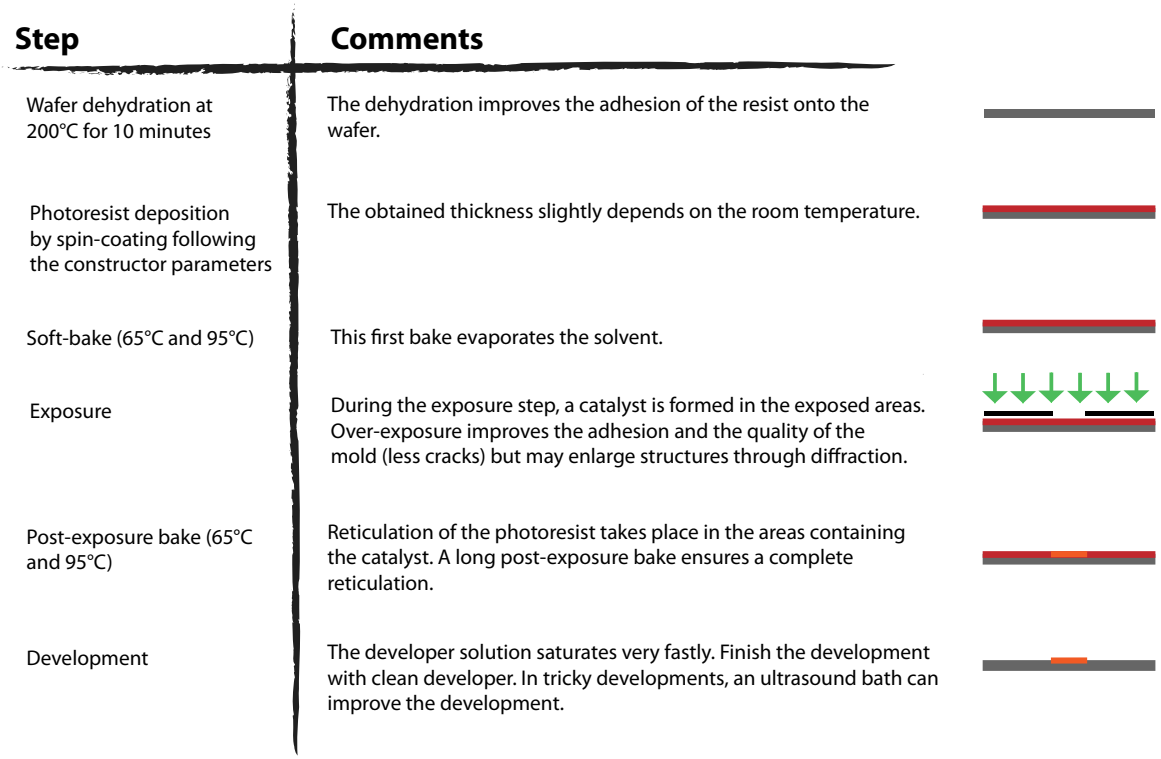

Figure 2.6 – Soft lithography steps with SU8 negative photoresist

Soft lithography - case of multiple layers To minimize the total hydrodynamic resistance in our devices, most of our molds contained several layers; local thin layers to handle femtoliter droplets and thick layers for the input channels. The multiple-layer lithography process requires alignment procedures that can be tedious and time consuming. The conventional method consists in the following steps: after the first layer construction (deposition, soft bake (SB), exposure, post-exposure bake (PEB)), the second layer is deposited and soft-baked. The wafer is then aligned with the second layer photomask, typically using a mask aligner and dedicated alignment structures. During this alignment procedure, alignment structures are hidden below the upper photoresist layer, which limits the thickness ratio between the two layers (maximum $\sim$ 1:10 before the optical contrast becomes too low to distinguish the structures), as well as the precision of the alignment, resulting from light scattering in the photoresist film. Different techniques have been used to overcome these optical limitations; one way is to create structures with higher optical contrasts independently of the SU8 mold construction, either by dry etching [107] or by using red positive resist [108]. Other methods are to add intermediate films of resist to sequentially build the desired layer, or to locally remove the resist above the alignment structure with developer [109]. However, all these methods are time consuming and add supplementary steps that either reduce the final precision of the mold, or decrease the cleanliness of the surface.

We developped a very fast and precise method to create multiple-layer wafers, in which alignment structures are fully visible whatever the thickness of the upper layers, and that does not require additional spin-coating / development steps. In our procedure, tape is used to protect

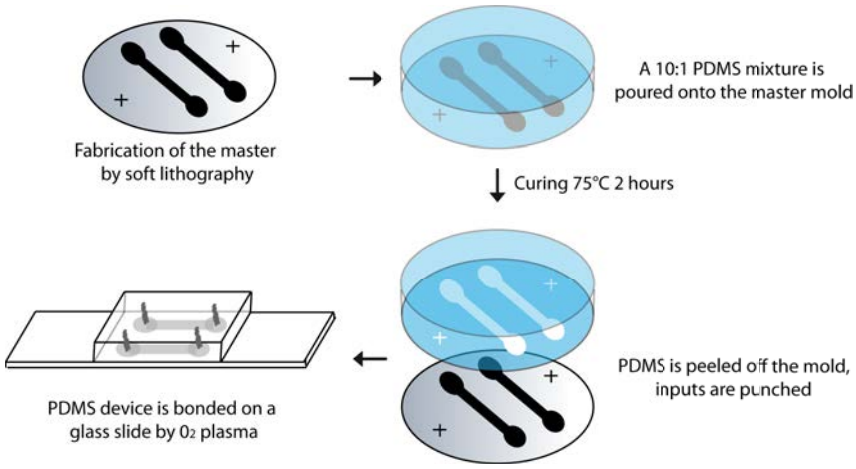

Figure 2.7 – PDMS devices are cast from the silica master by pouring a 10:1 (w/w) mixture of monomer and crosslinker onto the wafer and letting it cure at 70 ° C for 2 hours. The cured PDMS is then peeled off the master. Inlets are punched with a 0.5 mm biopsy puncher.

alignment structures from the upper layers deposition. Alignment structures are not hidden by the upper layer of photoresist, allowing to perform minute alignments, whatever the thicknesses of the different layers. With a proper design, the use of tape barely reduces the useful area of the wafer, and enables the construction of multiple layer wafers with the same alignment structures, as their complementary shapes are never constructed. Complete description and characterization of the technique can be found in Appendix A.

PDMS molding - conventional protocol with Sylgard 184 or RTV-615 PDMS PDMS devices are cast from the silica master by pouring a 10:1 (w/w) mixture of monomer and crosslinker onto the wafer, letting it degas under vaccum conditions and curing it at 70 ° C for 2 hours[110]. The cured PDMS is then peeled off the master. Inlets are punched with a 0.5 mm biopsy puncher. Two types of PDMS are used depending on the degree of elasticity wanted. When high pressures need to be applied, Sylgard PDMS is used for its higher Young modulus. Cheaper RTV is used daily, especially for the PDMS membrane of pneumatic valves described in Chapter 3.

Hard PDMS When high aspect ratios are needed (typically larger than 10), standard PDMS channels tend to collapse. In such cases, hard PDMS enables the fabrication of stiffer devices, with keeping the fast prototyping PDMS technology[111]. Its Young modulus is $\sim$ 10 MPa, ten times larger than conventional PDMS. Five reagents need to be mixed to prepare hard PDMS, with the following proportions:

VDT 731	VQM 135	modulator	SIP 6831.1	HMS 301
6.8g	1-2g	50 μL	10 μL	1g

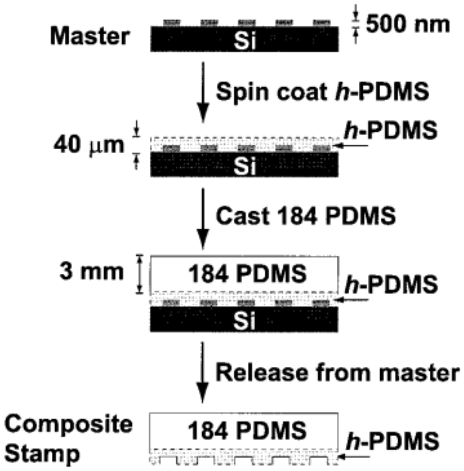

Figure 2.8 – The hard PDMS is deposited on the microstructured wafer by spin-coating (800 rpm, 30s), and baked for 30 minutes at 70 ° C. A mixture of conventional PDMS (Sylgard 184 or RTV-615) is then poured onto the hard PDMS membrane to obtain a composite chip. Reprinted from [111]

The four first reagents are mixed together and stored. An improvement of hard PDMS membrane was observed after letting the initial mix a few days in the fridge. HMS 301 is the curing agent. After its addition, the hard PDMS is deposited on the microstructured wafer by spin-coating (800 rpm, 30s), and baked for 30 minutes at 70 ° C. A mixture of conventional PDMS (Sylgard 184 or RTV-615) is then poured onto the hard PDMS membrane to obtain a composite chip.

Punching the inlets and outlets often results in fracturation of the hard-PDMS membrane. To avoid such problems, a thin flat of conventional PDMS may be deposited above the chip before punching the inlets. This enables the imposition of a pressure at the location of the biopsy puncher during its removal and suppresses fracturation issues.

2.2.2 Systems bonding and obtention of different surface properties

0_2 plasma cleaner

PDMS chips are bonded onto glass slides with an O_2 plasma cleaner. A plasma is a gaz that contains a variety of charged, highly reactive species. The surfaces to be bonded are placed in a chamber filled with O_2. Imposition of a radiofrequency electric field results in the creation of a diversity of excited species (oxygen radicals, ionized ozone, etc) that interact with most organic bonds and break them. The surfaces are oxydized, which makes them hydrophilic and reactive. Upon contact, covalent Si-O-Si links are created between the PDMS and the glass slide.

On non-bonded surfaces, the oxydation results in an increase of the density of silanol functions. Immediately after a plasma, the static contact angle measured on a flat PDMS surface is ~ 20 ° , but rearrengements in the polymeric chains and silanol condensation enable the PDMS

to go back to its native hydrophobicity after $\sim$ 15 minutes[112]. This time can be extended if the device is kept in a water reservoir[113].

All PDMS hydrophobic devices

To obtain hydrophobic devices, the first method envisioned is to create full PDMS devices; indeed, the static contact angle measured on a flat PDMS surface is $\sim 110^\circ$ C. PDMS covered glass slides are fabricated by spin-coating liquid PDMS and curing it at 70° C. The bonding is then realized by 0_2 plasma and the return to hydrophobicity is fastened by placing the chips at 90° C. Several mechanisms are envisioned to explain the progressive recovery of hydrophobicity: migration of short PDMS chains from the bulk to the surface [114], chains rearrengements inducing the internalization of SiOH functions [115], condensation of silanols into siloxane functions[112]. Experimentally, we found that the hydrophobicity recovery is enough after 12 hours at 90° C in most devices. We did not try to further characterize the partial or complete hydrophobicity recovery after this time.

Silanization

In cases where the natural hydrophobicity of PDMS is not sufficient to provide a proper wetting, a fluorinated silane can be grafted to improve the surface/fluorinated oil affinity. A vapor phase protocol was followed; surfaces are exposed to an 0_2 plasma cleaner, then deposited in a box with 20 μL of 1H,1H,2H,2H-perfluorooctyltrichlorosilane. Some silica gel is added to ensure the air is dry and avoid degradation of the silane. The box is then sealed and the surfaces are exposed to the silane vapor for 40 minutes. Bonding and silanization of the closed chamber can be performed in a row with the same plasma. A complete study of the mechanisms at play can be found in [116].

2.2.3 Microfluidic pneumatic valves

Pneumatic valves are active components that enable the controlled injection of reagents. A control channel is added above the flow channel, separated by a thin elastomeric membrane that can bulk upon pressurization of the control channel. Fabrication of pneumatic valves requires the production of two wafers, one containing the flow channels and the other one containing the control channels. On the control channel wafer, a layer of PDMS is spin-coated such as to obtain a membrane of a few micrometers above the control channels. The PDMS film is cured at 70° C for two hours. PDMS is poured onto the flow channel wafer at a thickness of $\sim$ 5 mm and cured. Devices are cut, punched and O_2 plasma bonded to the control channel wafer with a manual alignment step under a binocular. After a short bake (15 minutes at 70° C), the PDMS and the membrane can be peeled off the mold; control channels inputs are punched and devices are closed by O_2 plasma bonding on a glass slide.

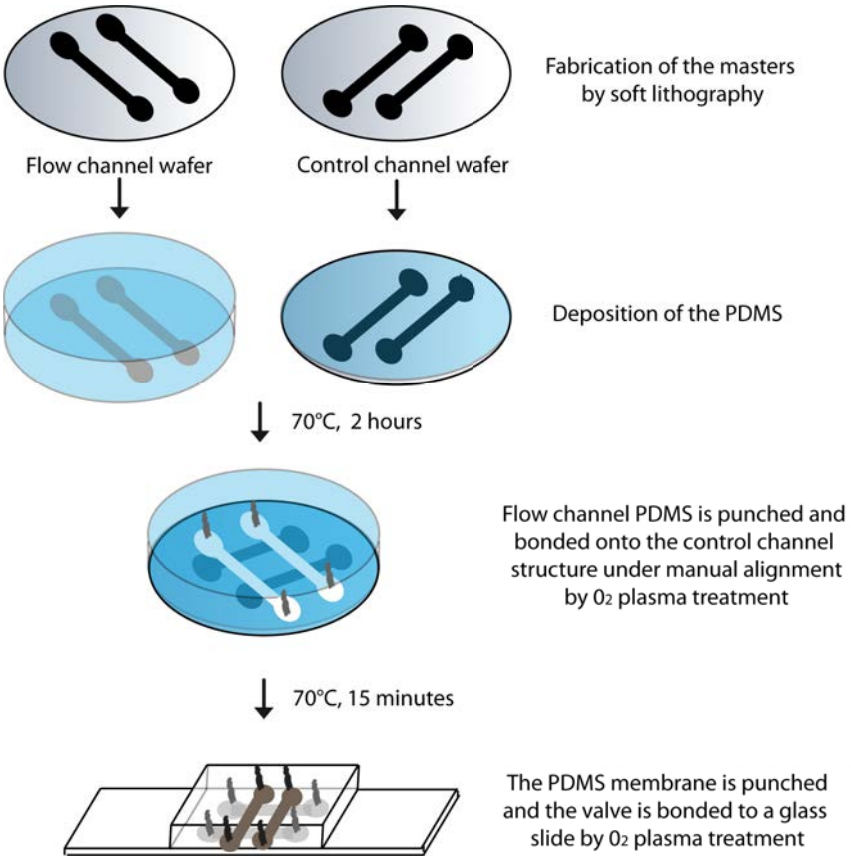

Figure 2.9 – Fabrication of pneumatic valves requires the production of two wafers, one containing the flow channels and the other one containing the control channels. On the control channel wafer, a layer of PDMS is spin-coated such as to obtain a membrane of a few micrometers above the control channels. PDMS is poured onto the flow channel wafer at a thickness of $\sim$ 5 mm and cured. Devices are cut, punched and O_2 plasma bonded to the control channel wafer with a manual alignment step under a binocular. After a short bake (15 minutes at 70 $^\circ$ C), the PDMS and the membrane can be peeled off the mold; control channels inputs are punched and devices are closed by O_2 plasma bonding on a glass slide.

Some critical steps :

- To make sure flow channels close completely upon pressurization of the control channel, it is preferable to give them a rounded profile rather than a rectangular one. Such characteristic is obtained by using positive resist for the soft-lithography process and by performing a hard bake (115 $^\circ$C). In our case, flow channels are drawn with a rectangular profile because of the very thin thickness (1 μm).
- Control channels can be placed above or below the flow channels.
- When PDMS membranes are very thin (a few μm), the punching of inputs can produce fractures that are to be avoided. Similarly to hard PDMS microfabricaiton, a thin flat of conventional PDMS may be deposited above the chip before punching the inlets. This enables the imposition of a pressure at the location of the biopsy puncher during its removal and suppresses fracturation issues.
- Structures located in the thick PDMS part tend to shrink by a few % ([117]). This effect can be neglected over short distances but is to be taken into account in the masks design for large structures.

RTV PDMS is used for the membrane to benefit from its higher elasticity.

2.2.4 Other fabrication techniques

Around microfluidic chips, macroscopic elements are needed to sustain the chips or to support the reservoirs. Two tools were used in this purpose. The 3D printer (Makerbot, The Replicator 2X) uses thermoplastic polymers to create a 3D structure previously designed on Autocad. The extrusion parameters depend on the chosen polymer; ABS is one of the most used by engineers for its strenght, machinability, high temperature resistance (softens at 90 $^\circ$C). It is soluble in acetone, a property that can be used to smooth the surface and obtain a better sealing. PLA is another thermoplastic polymer that is more rigid than ABS. This property is interesting for the construction of large pieces where the use of ABS often results in bended corners and printing errors but also means PLA structures break more easily than ABS ones. PLA softens around 50 $^\circ$C and is more complicated to machin after the 3D printing. The choice of the polymer thus depends on the aimed application. In our case, small pieces (microliter reservoir wells) were made in ABS and large pieces (chip holders, multiple reservoir) were preferently made in PLA. Another available polymer is the HIPS, that presents properties similar to the ABS with the advantage of being soluble in limonene; printing in ABS/HIPS and dissolving the HIPS afterwards enables the construction of complex structures that would not be easily accomplished without supports.

The construction of structures with a 3D printer is fast and easy but built pieces present rough surfaces and a low compliance with requested dimensions, as thermoplastics tend to shrink

during the printing. In cases where a high precision on the thickness is needed, a milling machine can be used (Charly4U) to manufacture plexiglass plates. The drill bit can be tuned in agreement with the desired structure, the smaller having a diameter of 1 mm.

2.3 Biological assays

2.3.1 Polymerase Chain Reaction

One of the most common reaction is the Polymerase Chain Reaction (PCR). PCR is the amplification of DNA by a series of thermal cycles.

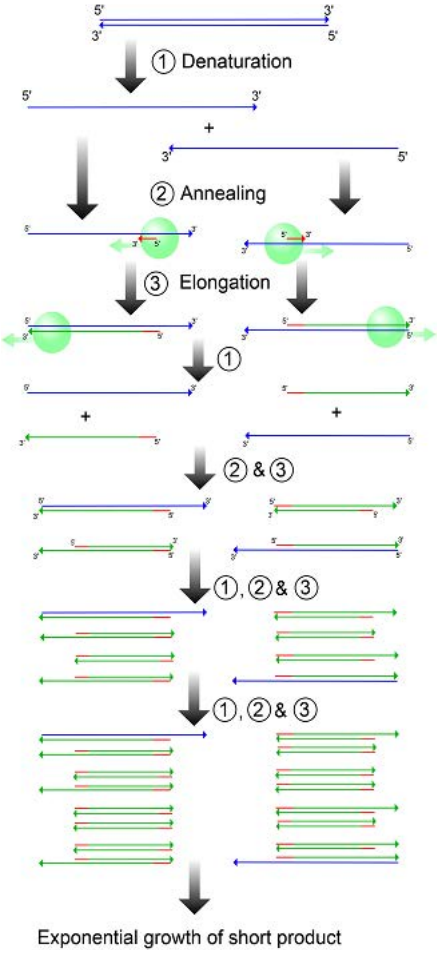

Each PCR cycle comprises 3 steps.
1. *Denaturation* The DNA is brought to high temperatures (95 $^{\circ}C$), resulting in the destabilization of hydrogen bonding in the DNA double helix, and the separation of the two DNA strands. This step is called DNA denaturation.
2. *Annealing* The temperature is lowered (around 55 to 65 $^{\circ}C$) to enable the hybridization of primers (represented by small red fragments) on the DNA. The primers will serve as binding sites for the DNA polymerase enzyme (represented by the green circle) in the third step.
3. *Elongation* The temperature is increased (72 $^{\circ}C$) to enable the DNA polymerase to synthesize the complementary DNA out of dNTPs in solution.
The cycles are repeated until complete use of the primers. After one PCR cycle, the quantity of DNA is theoretically doubled, which means that a million copies of the target DNA is obtained after 20 cycles. In practice, the amplification yield is lower; bad hybridization of the primer, poor control of the temperature, efficiency of the enzyme may affect the total yield of the PCR.

2.3.2 Agarose gel electrophoresis

An agarose gel electrophoresis corresponds to the migration of DNA in a gel under imposition of a DC electric field. The gel contains a stain (usually ethidium bromide or ®SYBR Safe) that becomes fluorescent upon intercalation in the DNA. Inside the gel, DNA molecules interact with the agarose matrix and the smaller molecules migrate faster than the larger ones; a separation

by size can be performed and the use of a ladder gives the corresponding DNA length. The fluorescence intensity is directly linked to the quantitity of DNA. The complete agarose gel electrophoresis protocol is described below.

- The gel is prepared by dissolving an agarose powder into a buffer, TBE in our case. The concentration of the gel is tuned depending on the length of the DNA strands that are to be separated. For our short DNA fragments (0.1 - 1000 bp), 2 % gels are used. The agarose solution is heated near its boiling point and poured, 2 μL of ®SYBR Safe are added. A comb is placed to create wells in the gel.
- Once the gel is reticulated, the comb is removed and the gel is placed in the electrophoresis chamber covered by TBE buffer. Samples contain the solution to be analyzed along with a loading buffer (DNA Gel Loading Dye (6X), Life technologies) that forces the solution to sink at the bottom of the well. Prepared samples can be loaded into the wells; 5 μL of ladder (GeneRuler 100bp DNA Ladder, Life Technologies) is also loaded.
- A DC voltage is applied taking into account the negatively charged DNA molecules migrate towards the anode. The voltage is chosen between 60 and 100V depending on the aimed gel quality. Migration is faster at high voltages but migration anomalies can appear such as edge effects.
- The gel is analyzed in a UV chamber.

2.3.3 DNA purification

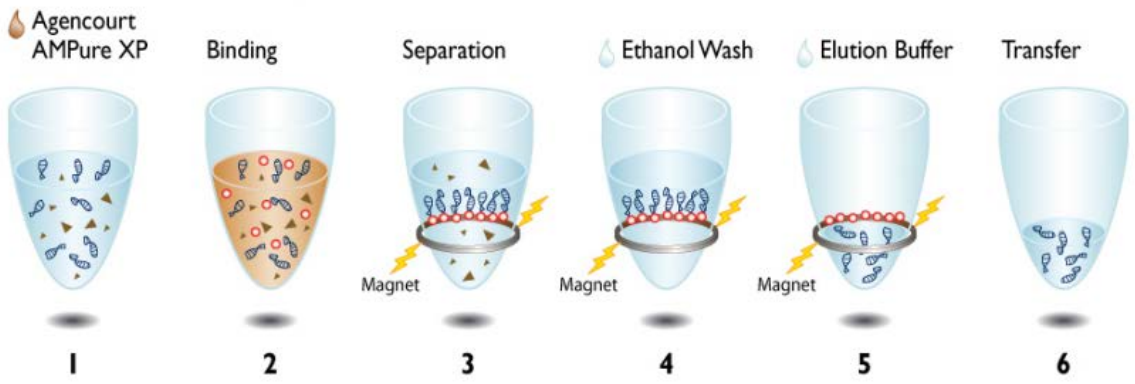

Figure 2.10 – Purification system based on magnetic separation. DNA double strands longer than 100 bp bind to the magnetic beads (step 2), enabling their separation from the sample (step 3). After several washing steps (step 4), an elution buffer is added and DNA strands are eluted from beads (step 6). Reproduced from Beckman and Coulter's Agencourt AMPure XP PCR purification Instructions for use.

AMPure kit Depending on the protocols, it is sometimes useful to remove excess primers, nucleotides, salts, enzymes in PCR experiments, or remaining short DNA strands in ligation

experiments. The Agencourt AMPure XP PCR (Beckman Coulter) purification system was used to purify samples when needed. This system relies on the use of paramagnetic beads coated with carboxyl molecules. Those particles can reversibly bind DNA in the presence of polyethylene glycol (PEG) and salt. The length of retained DNA fragments can be tuned by changing the percentage of PEG.

The protocol steps are described in Figure 2.10. The beads solution is thoroughly mixed and a volume v is added to the sample to purify. v is a function of the minimal size of DNA fragments that we wan't to recover, typically 1.6 μL per 1 μL of sample to recover >100 bp DNA strands. The solution is mixed with the pipette and binding is performed (RT, 5 minutes). The sample is placed on a magnetic rack that immobilizes the paramagnetic particles. The sample can be removed through pipetting and 2 washing steps are performed with 70 % Ethanol to remove all non-binded molecules. An elution buffer is then added, to enable the resuspension of DNA strands. The solution of purified DNA is transfered to a new reservoir.

The recovery percentage can be as high as 90 % if elution volumes and beads concentration are correctly tuned.

Part II

Miniaturization of droplet-based operations to the femtoliter scale

There is plenty of room at the bottom
Richard Feynman

This second part of this PhD manuscript focuses on the miniaturization of elementary droplet-based microfluidics operations. Each chapter concentrates on one operation: production of droplets on-demand, mixing inside droplets, operations involving electric fields (dielectrophoretic sorting and electrocoalescence), hydrodynamic splitting and incubation steps. Additional states of the arts are presented when necessary, along with theoretical interrogations on the miniaturization feasibility of such operations. Part of the exposed results can be found in the article Droplet-based microfluidics at the femtoliter scale[91] which is reproduced in Appendix B.

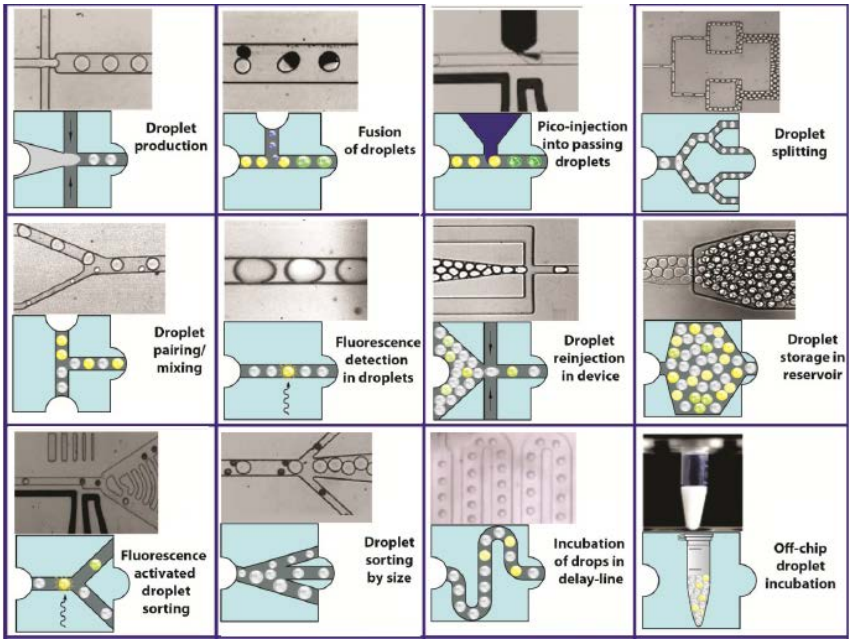

Figure 2.11 – Summary of elementary operations of droplet-based microfluidics at the nanoliter and picoliter scales. From left to right and from up to down: droplet production, coalescence of droplet pairs, pico-injection, droplet splitting, droplet pairing, fluorescence detection, emulsion reinjection, on-chip droplet storage, fluorescence-activated sorting, sorting by size, on-chip incubation, off-chip incubation. Reproduced from the PhD manuscript of Alexei Godina.

Chapter 3

Femtoliter drop-on-demand

In most biochemical assays, periodic trains of droplets are formed and manipulated at high frequencies. However, in the absence of active components, flow rates, droplet sizes and droplet production are coupled which decreases the number of controlable parameters. The use of drop-on-demand devices largely enhances the control over droplet synchronization and droplet size. Looking wider than the scope of research laboratories, drop-on-demand devices have proven their utility in our daily life, for example with the ink-jet printer.

The production of femtoliter droplets on demand is a difficult task as dead volumes need to be nearly suppressed from the entire setup. Before chosing the best strategy to produce femtoliter droplets on demand, we present concise states of the art of existing devices and discuss their miniaturization possibility. Several experimental trials were performed in agreement with these discussions: piezoinjection, miniaturization of the pico-injection, electrojetting, pneumatic actuation. Results of this initial phase are summarized thereafter.

3.1 Drop-on-demand devices

3.1.1 Pneumatic valves

Pneumatic valves take advantage of the deformation property of an elastomer (typically PDMS) to locally close flow channels (see Chapter 2.2.3). Actuators contain a control channel that is separated from the flow channel by a thin elastomeric membrane; upon pressurization of the control channel, the membrane bulks until closing the flow channel (Figure 3.1). Pneumatic valves have low internal volumes (typically a few nL), fast response times (a few milliseconds) and can be extensively parallelized [28].

Miniaturizing such devices raises several questions. Goulpeau *et al.* established predictive rules for the design of pneumatic valves from comparison between experimental data and an equivalent electrical circuit model[118]. They predicted that multiplying the characteristic di-

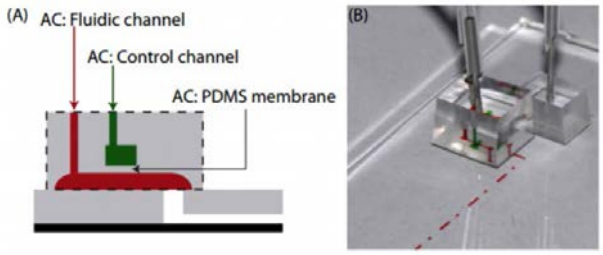

Figure 3.1 – Scheme of a pneumatic valve. The flow channel is separated from the control channel by a thin PDMS membrane. Under pressurization of the control channel, the membrane bulks and closes the flow channel. Reproduced from [26]

mensions of the pump by a factor λ would demand an operating pressure $P_{op} \propto \lambda^{-1}$. This model predicts operating pressures of 10 bars for 500 fL volume valves, and 40 bars for 10 fL valves, a range not achievable in PDMS/glass microfluidic chips. Those considerations led us to give up on this method in a first step.

3.1.2 Electrohydrodynamic jetting

Electrohydrodynamic (EHD) jetting relies on the competition between electrostatic pressure and surface tension which relative strenght is defined by the dimensionless Bond electric number, $Be = \epsilon_0 \epsilon_r E^2 l/\gamma$ with ϵ_0 the vaccuum permittivity, ϵ_r the fluid permittivity, E the electric field and l the characteristic dimension of the fluid. Above a critical electric field, electrostatic stresses are too large to maintain the interface stability; the interface deforms and a droplet is ejected. EHD jetting is usually used to print droplets on flat substrates[119, 120, 121] and create complex patterns but microfluidic versions of such devices have been developped[37].

The inspection of Be dependence with device scale shows that the miniaturization of EHD jetting systems demands the imposition of larger voltages and its feasibility needs to be demonstrated. However, this method raises few technical questions regarding the implementation of a miniaturized version of existing device and was one of the first envisioned to produce fL droplets.

3.1.3 Pico-injection

Pico-injection is widely used in multi-step droplet-based microfluidics assays as it allows the injection of a precise picolitric volume of reagent inside droplets without synchronization issues. Perpendicularly to the main flow channel, an injection channel is added and pressurized to obtain a stable meniscus of the fluid to be injected. When a droplet flows, upon imposition of an electric field, the meniscus can break and the injected volume depends on the contact time between the droplet and the reagent, and on the injection channel pressure. One of its major drawback is the cross-contamination induced by the contact between the droplet and the injection channel. The following injected droplet may receive part of the material of the preceding droplet.

Miniaturization of the pico-injection raises few technical questions. The injected volume varies with the contact time between the droplet and the injection channel and with the pressure of the injector; the minimal injected volume is on the order of the nozzle dimension. The reduction of the injected volume should be possible by decreasing the nozzle dimension and increasing electric fields to maintain a high-enough Be.

3.1.4 Piezoelectric actuation

A piezoelectric material is a material that converts an electric input into a mechanical displacement. Piezo stacks allow microsecond response times and low deflections (1-100 μm). Implementation of such actuators in microfluidic chips is usually made by positionning the piezo stack above a large reservoir, separated by a thin PDMS membrane[29, 30]. In this configuration, the deflection of the stack is directly transfered to the fluidic reservoir and the stroke volume corresponds to the product of the actuator extension times its diameter[30]; corresponding volumes are in the range of 100 pL - 100 nL and could hardly be miniaturized considering the macroscopic size of actuators. This objection might change in the years to come as PZT thin films were recently integrated into microfluidic chip, enabling the creation of micropumps actuated at low voltage[31]. This could open up new miniaturization possibilities.

In the absence of availability of such techniques in our lab, the ultra-fast response time of piezo stacks led us to look for new geometries that minimize the injected volumes with keeping macroscopic stacks.

3.1.5 Other active actuators in microfluidics

Other drop-on-demand methods exist, such as surface acoustic wave generation[35], thermally mediated droplet formation[32], hydrophobic valving[34] or magnetically modified elastomeric valves[36]. Magnetic and thermomechanical actuation were envisioned at first but are discarded from the manuscript for their lack of interesting results. Other methods were not investigated for lack of time.

3.2 Experimental part

This section presents the results of preliminary experiments. In agreement with above considerations, electrical actuation was the first envisioned (EHD jetting and femto-injection). Piezoelectric actuation was tested for its ultra-fast response time with a modified implementation to reduce injected volumes. Pneumatic actuation was tested for its ease of implementation, despite unfavorable theoretical considerations.

3.2.1 EHD jetting

EHD jetting was the first envisioned for its ease of implementation and encouraging scaling laws.

Protocol O'donovan *et al.* recently demonstrated the possibility of removing the side electrodes of a picoinjection device by directly charging the fluid to inject[122]. In agreement with this observation, two configurations were tested: one in which the electrodes are placed around the injection channel separated by a PDMS wall (Figure 3.2.a.) and another one in which the fluid to be injected is directly charged through an immersed Pt electrode (Figure 3.2.b.).

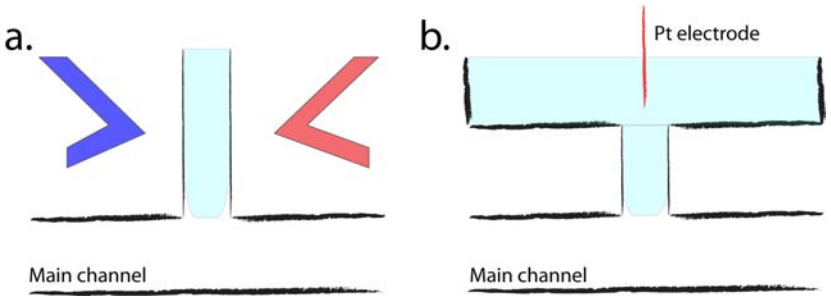

Figure 3.2 – Electrojetting femtoliter DOD devices. Electrodes may be located around the injection channel (a.) or the fluid may be directly electrified (b.)

Injectors comprise a thin channel (1 μm thick) that is connected to the thick main flow channel (25 μm). To limit the total hydrodynamic resistance, the thin part of the injector is limited to a length of $\sim 50\mu m$ and is fed by a thick reservoir (25 μm). In the side electrodes configuration, an enlarging region was added in the injector to ease the obtention of a stable meniscus (Figure 3.3.a). This provides a higher stability as a result of the high curvature between the reagent and the oil[56].

Electric voltages were produced by an AM300 generator (R&S) and amplified by a BOP1000M amplifier (KEPCO) with a gain of 100. The electric field was applied to the microfluidic device by an Electrowell (Fluigent) through Pt electrodes (Ø 300 μm) plunged into a conductive buffer. In the first configuration, side channels were filled with a solution of NaCl (189 g/mol) to create electrodes; in the second configuration, the Electrowell Pt electrode directly plunged into the solution to inject (DI water + F-68 pluronic at 1%).

Fluorinated oil is injected into the main channel using an MFCS pressure controller and injection channels are pressurized such as to obtain a stable meniscus before imposing any electric field.

Results and discussion Electrohydrodynamic jetting successfully enabled us to produce femtoliter droplets on demand, as pictured in Figure 3.3. Figure 3.3.a. shows the injection of a droplet of 16 fL, indicated by a white arrow, by imposition of a pulse of 75 ms in the first configuration. Figure 3.3.b. demonstrates the production of a droplet of 180 fL by imposition of

a pulse of 10 ms in the second configuration. Respective values of the applied voltage are 900V and 1000V, at a frequency of 1.5 kHz.

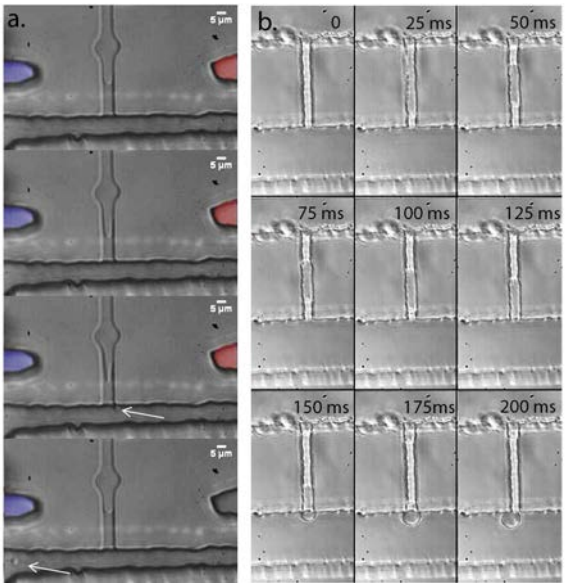

Figure 3.3 – Electrojetting femtoliter DOD. The imposition of an electric field generates a femtoliter droplet. a. Electrodes are located around the injection channel. 900V, 75 ms pulse every 500 ms, AC field. Electrodes are artificially colored (blue for the ground electrode, red for the charged AC electrode). The droplet, indicated by a white arrow, is ejected and remains trapped in the electric field until it is turned off. b. The fluid to be injected can be directly electrified. 1000V, 10 ms pulse every second, AC field.

Figure 3.4.a. depicts the evolution of the injected volume as a function of the injection number in the case of a device with side electrodes (configuration 1, 900V, pulse of 75 ms every 500 ms, dark cyan circles) and in the case of a device without electrodes (configuration 2, 1000V, pulse of 10 ms every 1s, orange circles). Injected volumes are much higher in configuration 2 and vary around the mean injected volume with a standard variation of 17 fL in configuration 2 and 4 fL in configuration 1.

Figure 3.4.b. shows the variations of the injected volume as a function of the electric pulse duration in configuration 1. There is a global increase of the injected volume. In this configuration, no volume is injected for actuation times lower than 50 ms.

Despite these encouraging results, we observed a very bad predictability of the devices behavior; depending on the device, the imposition of the electric field would either eject a droplet or repel the aqueous phase meniscus. We assume this contradictory behavior comes from the electrostrictive properties of PDMS[123, 124, 125]. When compliant electrodes are placed around a dielectric membrane, they exerce an electrostatic pressure that compresses the membrane. To conserve the volume, the membrane expands orthogonally to the field direction, as pictured in Figure 3.5. Many experiments were carried out changing the PDMS type (RTV/Sylgard), the curing agent ratio or the curing time but we could not relate those parameters to the presence or absence of electrostrictive effects.

3.2.2 Femto-injection

Protocol To miniaturize volumes injected by pico-injection, a two-layer design was envisioned, consisting of a thick main flow channel (33 μm thick) and thin side-way injectors (1.6 μm thick).

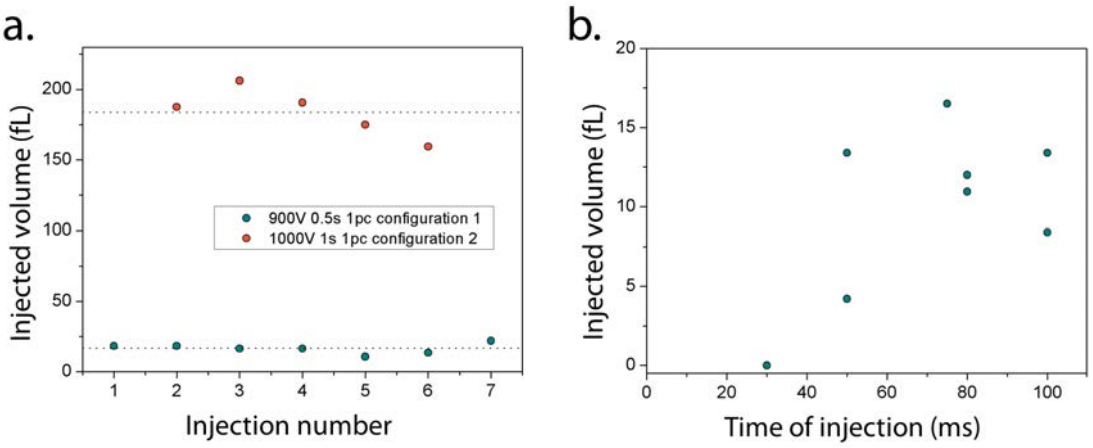

Figure 3.4 – a. Variation of injected volume as a function of the injection number in the case of side electrodes (configuration 1, dark cyan circles) and charged fluid (configuration 2, orange circles). Injected volumes are higher in the second configuration and vary around the mean injected volume with a standard variation of 17 fL. The standard variation is of 4 fL in configuration 1. b. Evolution of the injected volume with the electric pulse duration (ms) in configuration 1. There is a global increase of the injected volume. A minimum of 50 ms actuation is needed to inject water.

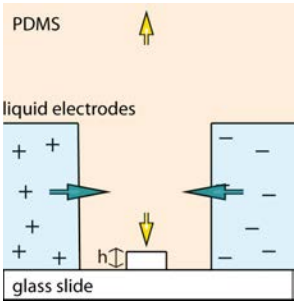

Figure 3.5 – Scheme of the electrojetting device. Compliant liquid electrodes are highly electrified. Because of the characteristic height of the channel ($h \sim 1\mu m$), even very low electrostrictive properties can produce detectable effects.

Electrodes were added in front of the injector, similarly to a conventional pico-injector, and filled with a conductive buffer charged by an Electrowell.

Fluorinated oil is injected into the main channel using an MFCS pressure controller and injection channels are pressurized such as to obtain a stable meniscus before imposing any electric field.

Results and discussion Figure 3.6.a. is a timelapse of an injection sequence, in which the injected fluid is concentrated fluorescein; fluorescence is inhibited by auto-quenching effects. Upon injection of the reagent into the droplet, the concentration decreases and there is apparition of fluorescence. Figure 3.6.b. represents the gray scale profile inside the circulating channel in presence of the electric field (pink curve) and without electric field (gray curve). The injection channel location is indicated by a dotted line. Before the injector, droplets interface are visible thanks to the difference in optical index between water and oil. After the injector, droplets become fluorescent with application of the electric field while they remain dark without electric field. Attempts to measure the injected volume were carried out (Figure 3.6.c.) but variations

are within the data analysis uncertainties.

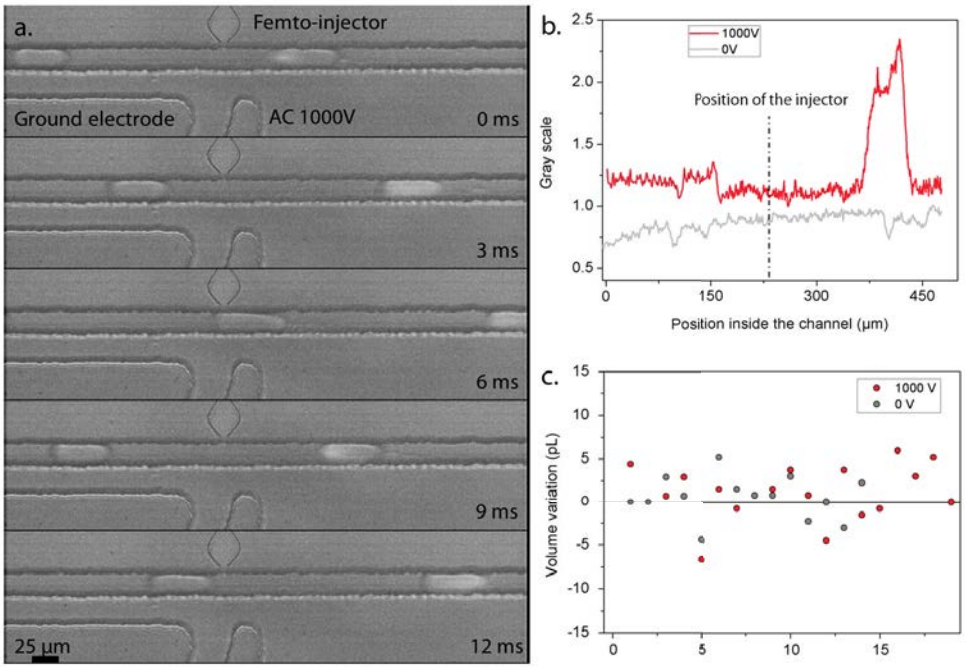

Figure 3.6 – Miniaturization of the pico-injection to the femtoliter scale. a. Time scale of an injection in the case of 50 pL droplets. The injected reagent is concentrated fluorescein. Upon release inside the droplet, the concentration decreases and the aweakening of auto-quenching effect results in the apparition of fluorescence inside the pL droplet. b. Gray scale profile inside the circulating channel in presence of the electric field (pink curve) and without electric field (gray curve). Femto-injected droplets become fluorescent. c. Attempts to measure the variation of volume were carried out but are within the data uncertainties

Similarly to the electrojetting, robustness issues were encountered with the femto-injector. Imposition of the electric field sometimes results in the repelling of the injector's phase. The lack of reproductibility led us to give up on this method.

3.2.3 Piezoelectric actuation

Protocol As explained earlier, the coupling of a macroscopic piezostack and a fluidic reservoir limits volumes in a range 100 pL - 100 nL despite the low displacements allowed by the piezoelectricity. To overcome this limitation, we imagined the system presented in Figure 3.7 in which the piezo stack is coupled to an integrated valve: pressurized fingers embrace the femtoliter injector, preventing droplets injection. The piezo deflection is imposed to the pressurized monitoring chamber, slightly increasing its total volume and releasing the injection channel. To generate the monitoring chamber, a PDMS membrane is created by pouring the PDMS over a custom insert designed on a CharlyRobot, that defines a PDMS membrane of chosen thickness (300 μm) and diameter (1-3mm). This thin membrane enables the precise positioning of the piezo actuator, and total transmition of the deflection to the monitoring chamber.

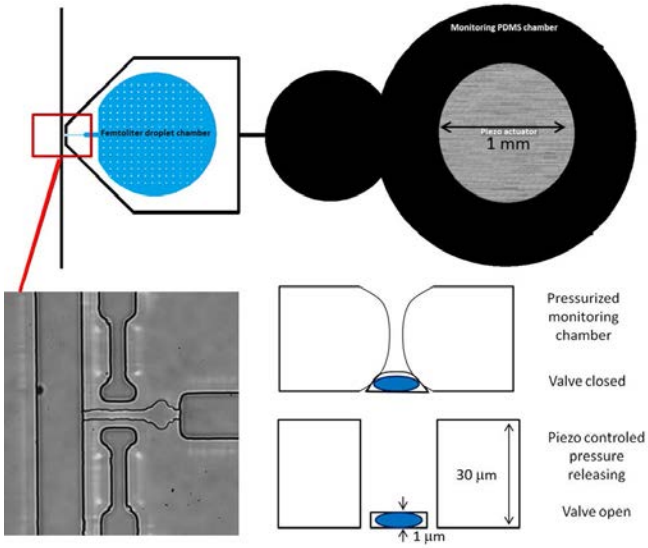

Figure 3.7 – Piezoelectric femtoliter DOD. The device comprises a thin femtoliter chamber and a large monitoring chamber. Pressurized fingers embrace the femtoliter injector, preventing droplets injection. By increasing the volume of the monitoring chamber with the piezo actuator, the release of a femtoliter droplet was expected. Even at high pressures (5bars), the injection channel is not obstructed, as depicted in the lower left image.

Results Those preliminary experiments turned out to be very tedious and did not enable a successful control of the droplet production. Lateral control channels could not efficiently close the injection channel, even at the highest reachable pressure in PDMS-glass devices (5 bars).

3.2.4 Pneumatic actuation

Considering the lack of reproductibility obtained with preliminary experiments, pneumatic actuation was tried out despite the unfavorable theoretical predictions.

Protocol In order to minimize the injected volume, the channel dimensions were decreased; the height was 1 μm and the width 6 μm. This aspect ratio was too large to be easily closed, we thus added an enlarged area (20 μm) near the main flow channel (Figure 3.8.a-b). The enlarged area helped the channel closing at reasonable working pressure (2-3 bars) with preventing the rest of the channel from collapsing. Before an experiment, control channels were filled with DI water, sometimes dyed with Brilliant Blue, and the corresponding air input was plugged on the filled channel. This step suppressed issues related to the high compressibility of air and avoided diffusion of air towards flow channels through porous PDMS.

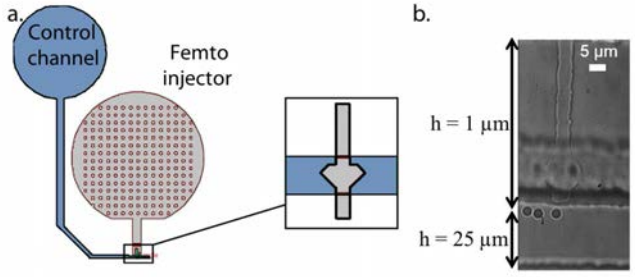

Figure 3.8 – Miniaturization of pneumatic valves. a. Scheme of the design. The injection channel is locally enlarged to enable a proper closing of the valve at reasonable pressures. b. Picture of a pneumatic femto-injector. The injection channel is very low ($\sim 1\mu m$) and falls in the thick main circulation channel ($\sim 25\mu m$).

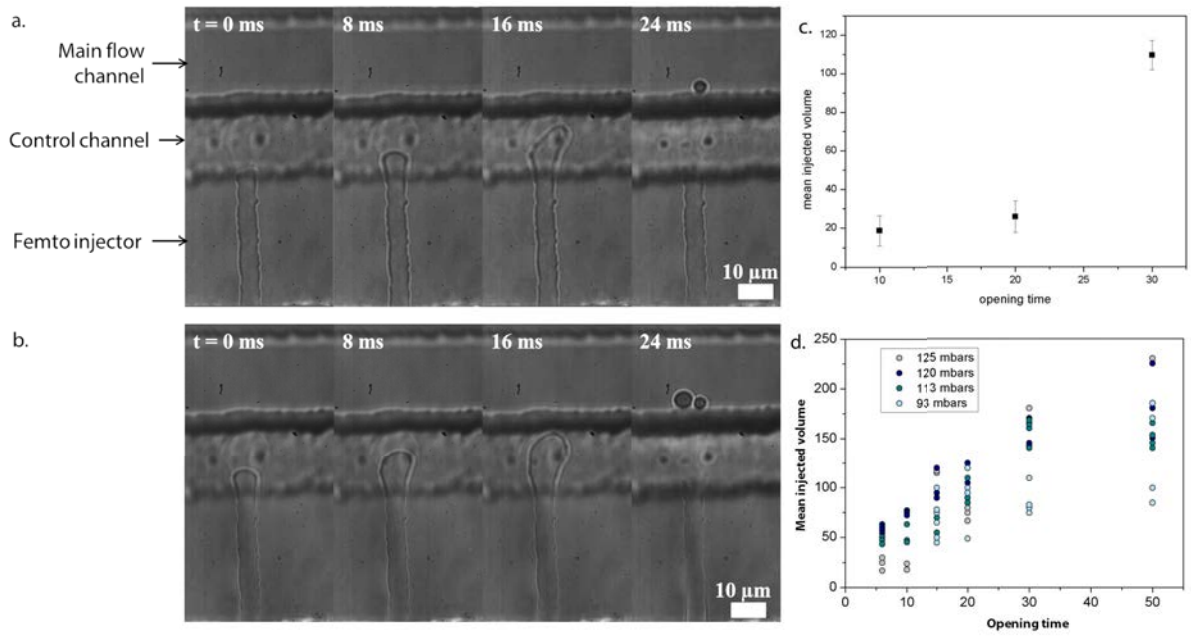

Figure 3.9 – Femto-drop on demand by pneumatic injection. a. Time lapse of the injection of a femtolitre droplet for an opening time of 10 ms. The injection channel is only partially opened during the injection process. b. Time lapse of the injection of a femtolitre droplet for an opening time of 30 ms. The injection channel opens entirely during the injection process. c. Mean injected volume as a function of the opening time, at constant pressure. The volume increases with the opening time. The increase is not linear because of the response time of the PDMS membrane. Despite this partial opening, standard variations are reasonably low between consecutive injections. d. Variation of the injected volume with the injection pressure, at different opening times.

Results and discussion With the enlarging region trick, pneumatic actuation could be successfully miniaturized down to the femtoliter scale, with a control channel pressure of 3 bars. An example is shown in Figure 3.9.a. for an opening time of 10 ms. A droplet of 16 fL is injected on demand.

Figure 3.9.c shows the mean injected volume at constant pressure (450 mbars) by increasing the opening time of the valve. Injected volumes can be as low as 16 fL at a frequency of 60 Hz. Above a critical volume, the injected phase breaks into two or more droplets by Rayleigh-Plateau instability; the total volume is represented in this graph. The increase in the injected volume is not linear, as would be expected for a completely opened valve. This must be related to the response time of the PDMS membrane. Figure 3.9.a shows that the enlarged region remains partially closed during the 10 ms injection process, whereas it completely opens above 30 ms injection times (Figure 3.9.b). At constant opening time, the dispersion in the injected volume is reasonably low (standard variation 7 fL).

The injected volume also increases with the pressure applied to the injection channel (Figure 3.9.d). By adjusting the pressure, the injected volume can be easily tuned at each injector to file down microfabrication variations.

3.3 Summary of all envisioned DoD methods

A summary of first trials can be found in the following table. Several DoD methods could be successfully miniaturized towards the femtoliter scale but the only robust device was the pneumatic actuator. Difficulties might be related to the use of PDMS and of its electrostrictive properties. Perspectives remain open for the implementation of electrical actuators in NOA or glass devices.

	Advantages	**Drawbacks**	**Perspectives**
Piezo	High actuation frequencies Low displaced volumes	Not easily implemented Hard to parallelize	Use PZT films
EHD	High actuation frequencies Ease of implementation	Need for high voltages Not reproducible because of electrostriction	Use of non-electrostrictive devices (NOA?)
Femto-I	High actuation frequencies Ease of implementation No synchronization	Need for high voltages Not reproducible because of electrostriction Cross-contamination	Use of non-electrostrictive devices (NOA?)
Pneumatic	Ease of fabrication High robustness Easy to parallelize	Low injection frequencies	Frequencies cannot be increased

Chapter 4

Mixing during the step emulsification process

Many biochemical processes exhibit fast dynamics: for instance, single-turnover kinetics of enzyme demand millisecond resolution [126]. Protein folding kinetics can happen on even shorter time scales [127]. To extract relevant parameters, mixing times must be faster than biochemical kinetics. Stopped flow and quenched flow methods have enabled the determination of some protein folding kinetics through the application of turbulent mixing under highly sheared flows. Turbulence creates multiple folds of liquids, decreasing the distance other which diffusion needs to be performed, and thus highly enhancing mixing times. However, dead volumes usually limit the time resolution to a few milliseconds in stopped-flow. Continuous-flow mixing [128, 129] enabled the reduction of dead times to a few tens of microseconds, by bringing the reagents into contact in a small mixing volume. The major drawback of such methods is the volume of samples consumed. To produce the high shear that generates turbulence, large flow rates are needed and large sample volumes are necessary. The apparition of microfluidics enabled the miniaturization of such devices and the efficient mixing of nanoliter volumes in microseconds[130].

Paradoxically, mixing in microfluidics is an inherently complicated operation. Indeed, microfluidics relies on laminarity and the absence of turbulence. Microfluidic flows most often have low Reynolds numbers ($Re \ll 100$), meaning that viscous forces dominate other inertia. Two fluids can flow side by side without mixing over long distances, with a mixing mainly governed by diffusion. A number of effective micromixers have been developped over the years, some of them based on the addition of external energy supply, and others relying on passive strategies.

In this chapter, a brief introduction on the passive mixing inside droplets is depicted before focusing on the mixing process in femtoliter droplets. Two experimental approaches were considered: the direct visualization of recirculations inside droplets during their production in step-emulsification was first envisioned. An indirect measurement of mixing times was then carried out by formation of a fluorescent product at the step.

4.1 Passive mixing inside droplets

4.1.1 Reminders on the internal recirculations of a circulating droplet

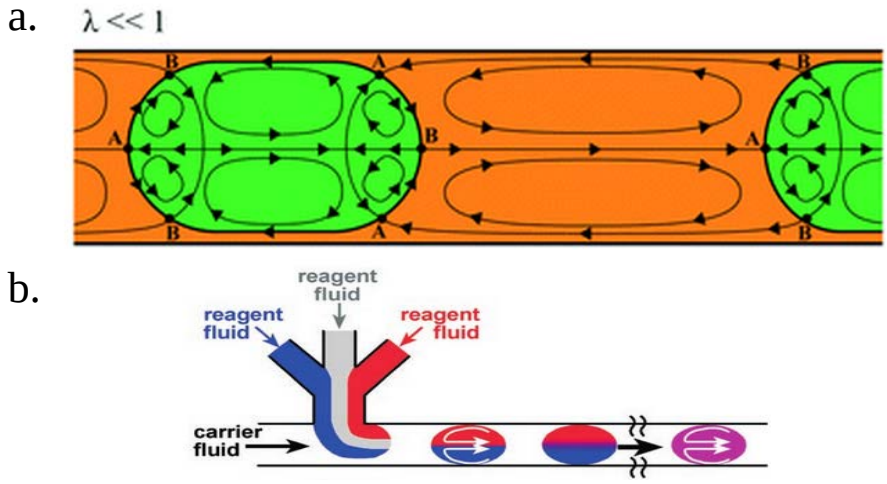

Figure 4.1 – a.Topology of the counter-rotating recirculation zones induced by the presence of the interface. The stagnation points on the interface are classified between the converging points A and diverging points B. Reproduced from [131]. b. As a consequence, mixing inside each half droplet is fast through advection in the recirculation rolls, but mixing between the two halves can only happen by molecular diffusion, resulting in long mixing times. Reproduced from [126].

When a droplet travels inside a channel, a thin film of continuous phase of uniform thickness is formed between the drop and the wall. Boundary conditions at the droplet interface induce flow fields inside the droplet. The topology of the flow is represented in Figure 4.1 in the case of a circular tube. Because of the symetry of the device, those recirculations only mix fluids in longitudinal directions but not transversally to the flow[132]. We thus need to define two mixing time scales inside a travelling droplet: in each half droplet, mixing is governed by advection whereas mixing transversally to the flow is solely governed by a much slower molecular diffusion (Figure 4.1.b). Preliminary experiments on droplets circulating in a straight microchannel showed a considerable effect of the initial distribution of fluids on the mixing time[132]. If the initial distribution was perpendicular to the flow (front-back distribution), mixing was efficient after distances corresponding to a few droplets lengths. If the distribution was longitudinal (left-right distribution), mixing was highly inefficient.

4.1.2 *La transformation du boulanger*

Mixing inside droplets can be improved by chaotic advection. The strategy is to increase the contact area between fluids to enhance molecular diffusion. In circulating droplets, an easy way to fold and stretch the fluids is by adding corners in the channel. At each corner, the recirculation rolls reorient along the channel direction, which significantly enhances the mixing efficiency[126, 133]. This stretching and folding process is often called *transformation du boulanger*, as it

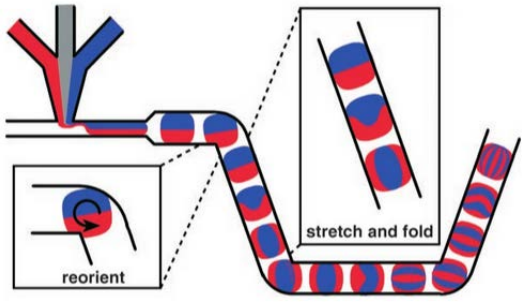

Figure 4.2 – Mixing by chaotic advection in a plug moving through a winding channel. The interfaces between the red and blue fluids are reoriented, stretched, and folded as the plug moves through the corners and straight sections of the channel. Reproduced from [126]

corresponds to the work performed by bakers to intercalate thin layers of butter to layers of paste and obtain flaky pastry. With this design, Song *et al.* decreased the mixing time inside nanoliter droplets to a few milliseconds, 1,000 times faster than diffusion mixing.

4.1.3 Diffusion times in femtoliter droplets produced in step-emulsification

Reducing the droplet size naturally decreases diffusion times. With decreasing the droplet characteristic dimension by two orders of magnitude, mixing times by pure molecular diffusion are decreased by four orders of magnitude.

$$\tau_{diffusion} \sim \frac{l^2}{D} \tag{4.1}$$

where l is the characteristic dimension other which mixing needs to be performed, D is the diffusion coefficient. As a consequence, decreasing the droplet size to a few micrometers leads to mixing times by diffusion in the order of a few milliseconds, which was the fastest reported mixing time inside droplets.

4.2 Mixing inside droplets during the step emulsification process - direct visualization

In this section, we present preliminary experiments that pretended to visualize recirculations inside droplets during their production in step-emulsification.

4.2.1 Experimental protocol

To decrease the level of complexity of the experiment, 10 pL water-in-oil droplets were produced in step-emulsification. First experiments were carried out with 100 nm fluorescent beads and a sensitive Hamamatsu Orca camera. However, the droplet production frequency and the weak fluorescence of beads could not allow us to extract workable data.

To be able to work at high acquisition frequencies, carbon black particules were added inside the water phase in a dilute regime. The solution was filtered at 1.2 μm to suppress eventual aggregates and avoid clogging issues. Droplets production was observed with a Photron fast camera.

4.2.2 Results and discussion

We could image some interesting recirculations in pL droplets, such as pictured in Figure 4.3. To make appearent particule movements, each image of Figure 4.3 is the superposition of stacks during 2 milliseconds. Particules act as passive tracers and are advected along the streamlines inside the droplet as it grows (Figure 4.3. 0ms - 12ms). As soon as the liquid bridge breaks, any advectional movement is stopped (Figure 4.3. 14 - 16 ms).

This allows us to assume that advection mixing only happens during the droplet growth and stops as soon as the droplet detaches. Though particule movements could only be imaged from the top view, recirculations are necessarily 3 dimensional, as pictured in Figure 4.4. The droplet can be divided in four advection rolls, further decreasing the distance over which molecular diffusion is expected to work.

Direct visualization of the mixing process in the droplets only brought qualitative understanding of the process. To measure a quantitative mixing time, further experiments were carried out.

4.3 Mixing inside droplets during the step emulsification process - indirect measurement

In this section, we investigate the mixing inside droplets during the step-emulsification process by an indirect measurement. An ultra-fast acid base reaction producing a fluorescent product is used to measure mixing times.

4.3.1 Experimental protocol

To further investigate the mixing process inside femtoliter droplets during their production, we used the diffusion-limited acid base reaction between fluorescein (50 mM) at pH 4 and a basic

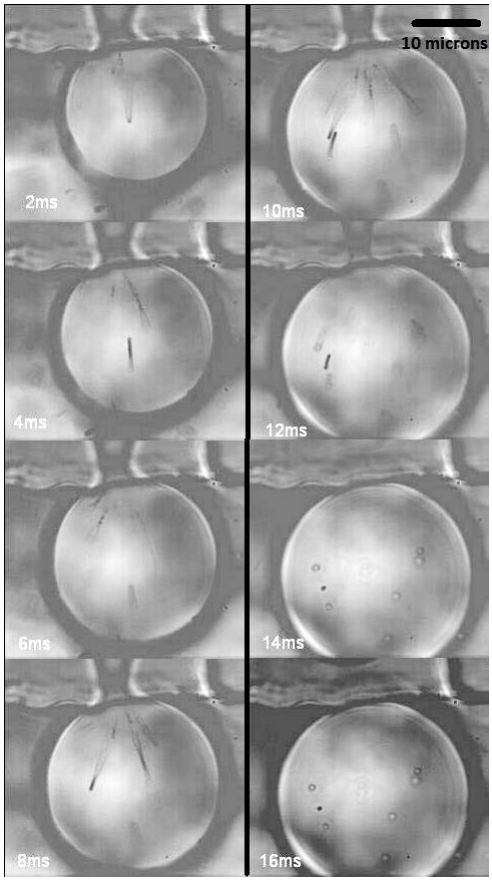

Figure 4.3 – Movement of carbon black particles inside a droplet during its production in step-emulsification.

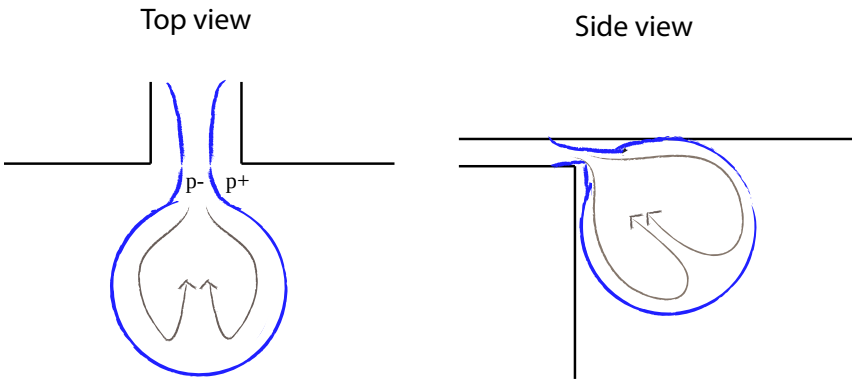

Figure 4.4 – 3D recirculations inside a droplet during its production in step-emulsification.

buffer at pH 9 (30 mM Tris-Base). This reaction is much faster than the mixing times considered hereafter. Protonated fluorescein has a very low fluorescence, while its dianionic form is highly fluorescent. An intercalating stream of acid buffer (10 mM Tris-HCl pH 4) separated the two reagents to prevent prior contact. The three laminar streams flowed side by side (Figure 4.5.a) and were pinched between two streams of fluorinated oil containing fluorosurfactant.

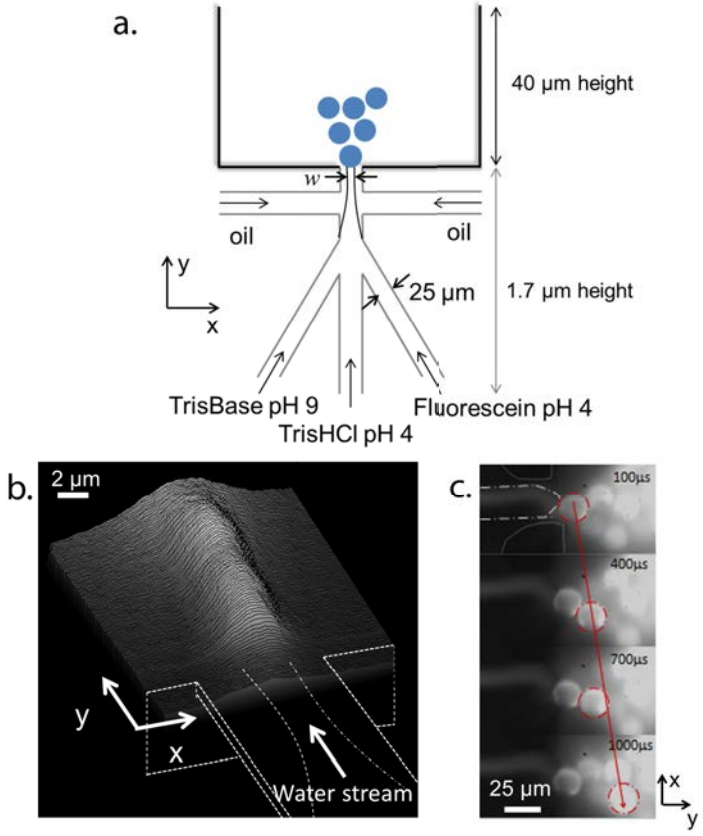

Figure 4.5 – Mixing process in femtoliter droplets. (a) Droplet production and mixing in the step emulsification regime. The increase in fluorescence resulting from fluorescein deprotonation was used to determine the mixing time. Dimensions are indicated for the fL experiments. (b) Surface profile of 75 fL droplet production, with an exposure time of 500 ms. At the step, the fluorescence emission was low then increased along the streamwise direction (y axis). (c) Example of 1 pL droplet production. The location of a selected droplet in successive images is indicated by a red circle.

Owing to the shallow geometry ($1.7\mu m$ height, $25\mu m$ width), no droplets were formed at this stage. On reaching the step, where the channel increased to $40\mu m$ in height and broadened to $100\mu m$ in width, droplet precursors began to form at the step and grew until droplets were generated. Droplets of 75 fL ($5.2\mu m$ diameter) were produced at a frequency of 10.7 kHz in the step-emulsification regime. The increase of fluorescence intensity I_f was monitored during droplet production and time-position equivalence was used to replace the position coordinate by time.

Low fluorescence emission and high speeds did not allow femtolitre droplets to be tracked individually in real time. We thus exploited image averaging to enhance the signal to noise ratio to obtain profiles like the one depicted in Figure 4.5.b, in which space has been converted to time by using the relation $t = y/U$ (with U the aqueous phase speed). Additional experiments carried out with 1.1 picolitre droplets ($13\mu m$ diameter) produced at a lower frequency (2.8 kHz) using a step emulsification regime (Figure 4.5.c) enlightened the hydrodynamics of mixing. In this case, individual droplets could be imaged and tracked after their production and the increase in

fluorescence measured by image analysis.

Before the step, the contact time $\tau_{contact}$ between the fluids was short enough to exclude the possibility of diffusive mixing as the fluids flow side by side. The contact time was 3 to 500 times smaller than the characteristic diffusion time τ_{diff} for H^+ and OH^- ions in water, calculated over the width w of the water stream (Figure 4.5.a). At infinite dilution, $D_{H^+} = 9.31.10^{-5} cm2/s$, $D_{OH^-} = 5.30.10^{-5} cm2/s$. For the 75 fL droplets: $w = 3\mu m$, $\tau_{diff} = 480\mu s$, $\tau_{contact} = 160\mu s$. For the 1.1 pL droplets: $w = 18\mu m$, $\tau_{diff} = 17ms$, $\tau_{contact} = 60\mu s$. Calculated diffusion times are overestimated as diffusion coefficients are smaller at finite dilution.

4.3.2 Results and discussion

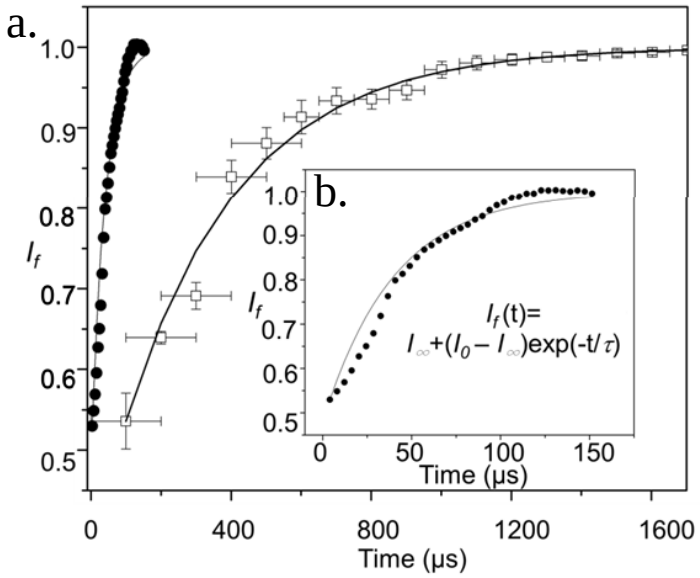

Figure 4.6 – a. pL droplet fluorescence was measured using Image J, integrating the fluorescence over the entire drop. The fluorescence intensity $I_f(t)$ (□) was renormalized and averaged over 8 droplets, then fitted to an exponential evolution to obtain the characteristic time, $\tau_{pico} = 330\mu s$. The fluorescence intensity extracted from surface profiles of 75 fL droplets production is plotted on the same graph (•). b. Average fluorescence intensity I_f of 75 fL droplets was determined as a function of the distance to the step and the time-position equivalence was used to determine the time. The fluorescence intensity was renormalized and fitted to an exponential evolution $I_f(t) = I + (I0 - I)exp(-t/\tau)$ with Matlab to obtain the characteristic time, $\tau_{femto} = 45\mu s$.

Figure 4.6.a depicts the renormalized fluorescence measurements in the femtolitre case (•) and in the picolitre case (□). Owing to the different time scales, the femtolitre fluorescence intensity measurement is replotted in Figure 4.6.b. Experimental data was fitted to an exponential evolution with Matlab (lines in Figure 4.6.a and 4.6.b). Corresponding mixing times are 330 μs in 1.1 pL droplets and 45 μs in 75 fL droplets. The latter result is the shortest time reported to date for a droplet microreactor, 35-fold smaller than fastest time previously reported (2 ms). We thus demonstrate that miniaturizing droplets to the femtolitre scale allows unprecedented fast mixing times (45 μs).

This time scale is to be compared to the droplet production time: 93 μs in the femtoliter case and 360 μs in the picoliter scale. Mixing happens on the same timescale as droplet production, allowing us to assume mixing is mostly governed by advection during the step emulsification process. An important dimensionless number for mixing issues is the Peclet number, defined as:

$$Pe = \frac{ul}{D} \tag{4.2}$$

where u is a characteristic speed of the flow, l the size of the system, D the diffusion coefficient. Pe represents the relative significance of advection terms over diffusion ones. Despite the miniaturization of our devices, the Peclet numbers are respectively of 50 and 80 in the femtoliter and picoliter cases. The predominance of advection over molecular diffusion is thus logical.

4.4 Conclusion on the mixing process during step-emulsification

In this section, we studied the mixing in picoliter and femtoliter droplets during their production in step-emulsification. Our experiments show evidence of a mixing mostly governed by advection during the droplet growing phase. Unprecedently low mixing times were observed; 45 μs in the case of 75 fL droplets. The correlation between droplets production frequency and mixing times let us envision a further reduction of mixing times. Some authors report MHz production frequencies [134], that would correspond to 1 μs mixing times if our trend is confirmed.

Mixing during the step-emulsification process

- Mixing is an inherently complicated operation in microfluidics, but should be favored by miniaturization. Diffusion times in femtoliter droplets are in the order of the millisecond.

- Direct visualization of the recirculations inside a growing droplet in the step-emulsification regime is tedious. Analysis of a scaled up devices enabled the visualization of recirculation rolls; any advectional movement stops once the liquid bridge necks and the droplet is created.

- Indirect measurement of the mixing time could be performed with an acid-base instantaneous reaction that generates a fluorescent product. Fitting to an exponential evolution indicated mixing times of 45 μs in 75 fL droplets and 333 μs in the 1.1 pL droplets.

- Experimental mixing times are comparable to production times, confirming that mixing must happen predominantly during the droplet growth by advection. Peclet numbers confirm this trend.

Chapter 5

Manipulation of droplets with electric fields

The use of electric fields to manipulate droplets has imposed itself as a highly versatile and robust method (see, for instance[50]). It presents many advantages: devices do not contain moving parts, it is posible to work under wide formulation conditions (direct or reverse emulsion, presence of surfactants, ...), actuation frequencies can be as large as 10^5 Hz, electric fields can be coupled to detection devices to trigger the actuation on demand. As explained in the introduction, two main droplet-based operations are realized by imposition of an electric field: electrocoalescence and dielectrophoretic (DEP) sorting. Electrocoalescence is the merging of droplets by imposition of an electric field. DEP sorting enables the extraction of droplets of interest out of a monodisperse droplet library by attracting them into a hydrodynamically disfavorable channel. To better understand the physics of both operations, we introduce here the electric forces in presence in such devices. We restrict ourselves to the case of water-in-oil droplets, *i.e.* to the case of conductive droplets surrounded by an insulating continuous phase. A second part of this chapter concentrates on the miniaturization of DEP sorting and electrocoalescence towards the femtoliter scale.

5.1 Impact of an electric field on water-in-oil droplets

5.1.1 Behavior of an isolated conductive droplet in an electric field

This section describes the impact of an electric field on a water-in-oil droplet. The electric field converts the droplet into a macroscopic dipole which has several consequences such as droplet deformation, modification of droplet speed or of its trajectory.

Fluid	τ **(seconds)**
DI water	10^{-4}
Fluorescein $300\mu M$	10^{-9}
DI water with 1% F-68 pluronic	10^{-7}

Figure 5.1 – Table of relaxation time constants for different aqueous phases. Characteristic times were assessed from Equation 5.1 with conductivities measured with a CDM 210 (Radiometer Analytical S.A.).

Polarization and conduction The imposition of an electric field on a water-in-oil droplet results in its polarization. Two mechanisms are at play. On very short time scales, electronic clouds rearrange (*electronic polarization*) and molecular dipoles align along the electric field (*orientation polarization*). Because of the presence of ions in the water phase, an additionnal conduction phenomena can happen depending on the excitation frequency. Ions act as free charges that can move under the imposition of a slow electric field; conductivity timescale is governed by the mobility of free charges and is most often slower than polarization.

Under the purely conducting droplet assumption, polarization and conduction processes result in the apparition of an interfacial charge distribution of opposite polarity on both poles of the droplet. The electric field inside the droplets vanishes, while it concentrates on the poles; the droplet can then be assimilated to a macroscopic dipole. The characteristic time of the apparition of charge distribution is given by[135, 136, 137]:

$$\tau_{droplet} = \frac{\epsilon_0 \epsilon_d}{\sigma_d} \tag{5.1}$$

If the excitation period is lower than $\tau_{droplet}$, free charges do not have time to move and build the interfacial distribution; in this case, droplet polarization is entirely governed by permittivities. However, aqueous solutions most often present large conductivities, corresponding to very small characteristic times. Examples are depicted in table 5.1. Even in the case of the lower conductivity purified water, the conductive assumption is valid up to an excitation frequency of 10 kHz.

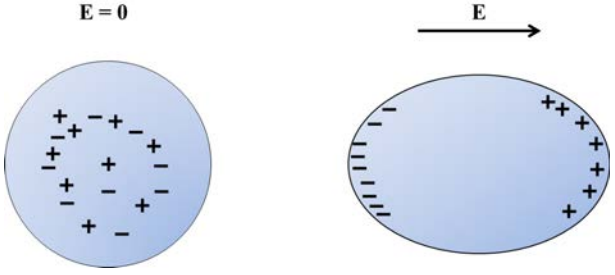

Figure 5.2 – The application of an electric field polarises the droplet, that becomes a macroscopic dipole. Charges concentrate near the interface.

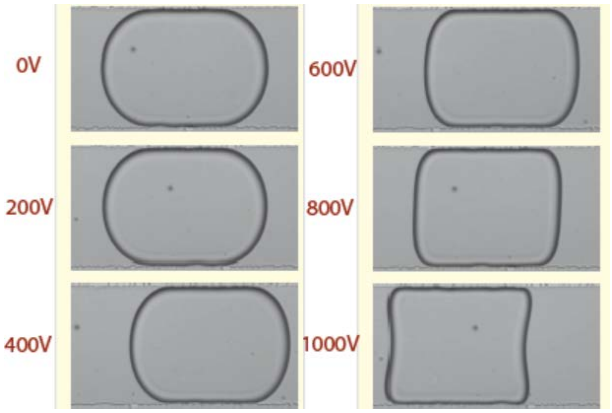

Figure 5.3 – Modification of the shape of a water + span80 droplet in hexadecane, as a function of the imposed voltage. The voltage is imposed perpendicularly to the channel. Reproduced from [138]

Deformation In presence of an electric field, the droplet is subjected to normal stresses, that can be expressed as an electrostatic pressure p_E[137].

$$p_E = 1/2\epsilon_0\epsilon_r(\mathbf{n}.\mathbf{E})^2 \tag{5.2}$$

Droplet deformation goes along with the creation of an additional interfacial area. Surface tension is thus going to generate a capillary pressure, that tends to bring back the droplet to its circular shape. The capillary pressure is given by the Laplace law:

$$p_{cap} = -2\gamma H \tag{5.3}$$

where γ is the surface tension and H is the interface curvature.

Figure 5.3 pictures the modification of the shape of a water droplet in hexadecane as a function of the imposed voltage[138]. The voltage is imposed perpendicularly to the channel. The electrostatic pressure deforms the droplet until a square shape, which is highly unfavorable from an interfacial energy point of view.

Above a critical electric field, the capillary pressure cannot overcome the electrostatic pressure; the droplet loses its integrity and splits into smaller droplets. The stability of a droplet thus depends on the ratio of the electrostatic pressure over the capillary pressure. This dimensionless number is called Bond electric number (sometimes electric Weber number).

$$Be = \epsilon_0\epsilon_r E^2 R/\gamma \tag{5.4}$$

Electrosplitting usually happens for B_e values in the range of a few units[139, 140].

Droplet speed and droplet displacement When subjected to a uniform electric field, charged droplets can move under electrophoresis effect. A droplet carrying a net charge q is subjected to a force $\mathbf{F} = q\mathbf{E}$ that either modifies its speed or deflects its trajectory depending on the field direction.

If the applied field is not uniform, droplets don't need to carry a net charge to experience an electric force; the droplet dipole interacts with the inhomogeneous electric field and generates a dielectrophoretic (DEP) force that can be expressed as[141]:

$$\mathbf{F} = (\mathbf{p}.\nabla)(E) \tag{5.5}$$

where $\mathbf{p}$ is the droplet dipolar moment and $\mathbf{E}$ is the electric field.

The dipolar moment of a spherical particule in a dielectric medium writes:

$$\mathbf{p} = v\beta\epsilon_0\epsilon_c\mathbf{E} \tag{5.6}$$

where $v = 4/3\pi R^3$ is the particle volume and β depends upon the dielectric permittivities of the phases.

β writes :

$$\beta = 3\frac{\epsilon_d - \epsilon_c}{\epsilon_d + 2\epsilon_c} \tag{5.7}$$

The DEP force is thus given by:

$$F_{DEP} = 4\pi R^3\epsilon_c\epsilon_0\beta\mathbf{E}.\nabla.\mathbf{E} \tag{5.8}$$

The direction of the DEP force depends upon the difference in dielectric constant of the dispersed phase and continuous phase $\epsilon_d - \epsilon_c$. A large permittivity droplet will be driven towards high electric field areas (*positive dielectrophoresis*) while a low permittivity droplet will direct towards low electric field areas (*negative dielectrophoresis*). Formula 5.8 shows that the DEP force is proportional to the droplet volume and to the gradient of the square electric field. Droplet miniaturization will go along with a drastic reduction of the DEP force, that might be compensated by an increase of the electric field gradient.

5.1.2 Behavior of a pair of droplets under an electric field

We consider now a pair of water-in-oil droplets. In most cases, the application of a field with an angle θ tends to reorient the droplets along the field direction, consequently we limit ourselves to the case of droplets already aligned along the electric field direction, separated by a distance

d (Figure 5.4). Under the electric field, each droplet gets polarized and can be assimilated to a macroscopic dipole. At large droplet distances ($d/R \gg 1$), droplets may be considered pointwise. The interaction between droplets is reduced to the interaction of two point dipoles localized at droplets center of mass; the resulting force is purely radial and decreases fastly with droplet separation[142]:

$$F_r = 24\pi\epsilon_0\epsilon_c E^2 \frac{R^6}{(d+2R)^4} \tag{5.9}$$

Many studies restricted themselves to this simple case with satisfying results as long as droplets remain at large separations[143, 144]. However, large discrepancies appear when droplets enclose ($d/R \sim 1$)[137, 145]. When the distance between droplets becomes on the order of their radius, a mutual induction between droplets displaces their dipolar moment. A simple correction can be implemented by a dipole-induced-dipole model[146]. Each point dipole induces an image dipole in the other droplet; by limiting themselves to the two firsts image dipoles, Yu & Wan could obtain a nice modeling of droplet-droplet interactions down to $d/R \sim 0.1$[145, 146]. When droplets are almost in contact ($d/R < 0.1$), an analytical solution is needed[147], which demands large numerical ressources. The enclosing of droplets provokes an increase of the local electric field, assessed to be roughly 14 times larger than the external field for $d/R = 0.1$[147].

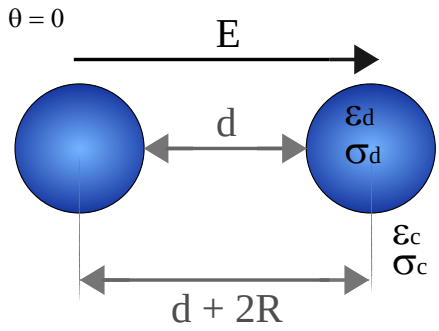

Figure 5.4 – Application of an electric field on two droplets aligned along the electric field

A pair of droplets subjected to an electric field can coalesce if the electrostatic pressure overcomes the capillary pressure. In terms of orders of magnitude, the dimensionless number that governs the electrocoalescence process is thus the same Bond electric number (Equation 5.4) that was defined for droplet electrosplitting. However, values of B_e are excepted to be much lower to enable the electrocoalescence of droplets, typically 0.2-0.4 depending on the references[48, 87]. Figure 5.5 depicts an example of the two DI water coalescence under imposition of a 1 kV/cm electric field.

Surprisingly, further increasing the electric field may inhibit droplet coalescence. Above a threshold electric field, droplets repulse each other violently after formation of a liquid bridge between them. Studies by Stone *et al.* [149] demonstrated that this instability can be explained purely geometrically. Figure 5.6 shows two configurations; in Figure 5.6.a. the droplets are almost spherical and the curvature of the neck leads to a low local liquid pressure, resulting in

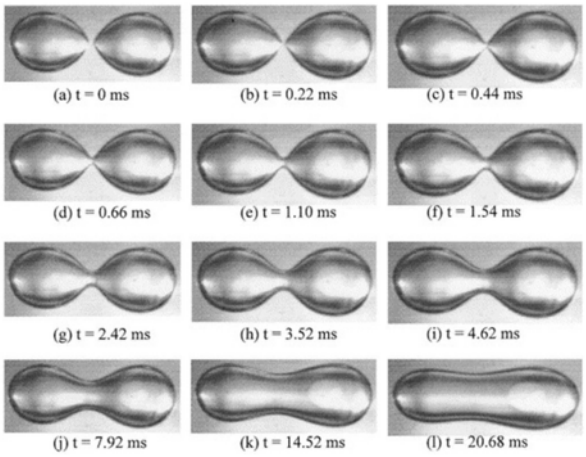

Figure 5.5 – Visualization of the attraction force between two DI water droplets at rest, under an electric field E = 1 kV/cm. [148]

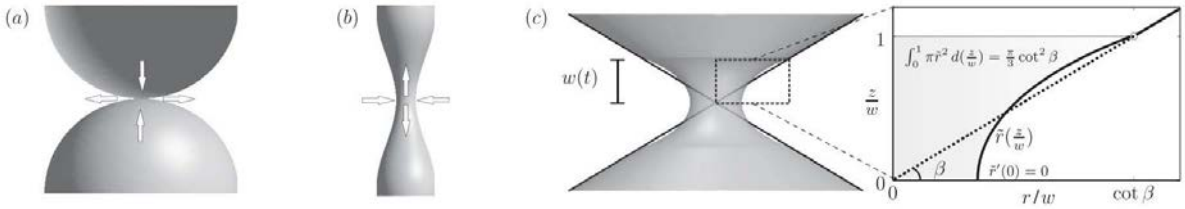

Figure 5.6 – (a) When two spherical drops contact, the curvature of the neck leads to a low local liquid pressure resulting in inward flow and coalescence. (b) The local curvature in an unstable liquid thread leads to a high pressure resulting in outward flow and pinch off. (c) The authors propose that immediately after two conical drops contact, there is a self-similar neck region, which they approximate as a volume-conserving minimal surface. They then calculate if the resulting curvature raises or lowers the local pressure, which is responsible for the resulting fluid motion. Figure and caption reproduced from [149]

inward flows as depicted by the arrows; in this configuration, droplets are about to merge. On the other hand, in the case of very elongated droplets (Figure 5.6.b.), the local curvature leads to a high pressure, and thus to an outward flow. Droplet coalescence is inhibited if the angle is larger than 30 °, that can be related to a critical electric field.

As we have seen in this chapter, the DEP force varies proportionally to the droplet volume, and the Bond electric number varies like the droplet characteristic dimension. Consequently, we may wonder whether the miniaturization of DEP sorting and electrocoalescence to femtoliter droplets are feasible.

This chapter introduced general considerations mandatory to understand the two following sections. The aim of this theoretical introduction is to discuss the physics of later studied operations (DEP sorting and electrocoalescence), but we do not pretend to quantitatively study those phenomenas. Indeed, the relevance of several approximations used in the theoretical part might be discussed, among which:

- The given DEP force expression only conserves dipolar terms. The higher order moments can not be neglected when the electric gradient are very high, which is most likely the case in our microfluidic device.

- The dependency of the DEP force with the electric field frequency has been discarded from our discussions for technological reasons; our voltage amplifier has a cut-off frequency of 2 kHz that limits our studies in a low frequency range.

- The droplet size is on the order of the distance between electrodes, which means that droplets strongly disturb the electric field. This perturbation won't be taken into account.

- Lastly, it is very difficult to predict the drainage of the film in our geometry. Indeed, droplets are completely confined, which must complexify the extraction of the continuous phase. The drainage must happen mostly in lubrication films. Drainage times won't be studied in our devices.

5.2 Dielectrophoretic sorting of femtoliter droplets

Scaling laws predict a decrease of the DEP force with droplet miniaturization. In this section, we are first going to analyze theoretically the consequences of droplet miniaturization on the sorting process. Experimental demonstration of the possibility of miniaturization of the DEP sorting to the femtoliter scale will then be performed.

5.2.1 Theoretical analysis of the sorting process

We consider a train of droplets sent towards a Y junction (Figure 5.7). Droplets completely obstruct the channel prior to the bifurcation.

In such conditions, the pressure drop across a plug is given by [131]:

$$\Delta P = R_h l u \sim \frac{\eta}{wh} l u \tag{5.10}$$

Where R_h is the fluidic resistivity, u the droplet speed (close to the flow speed U_c at low capillary numbers [131]), η the droplet viscosity, w the width of the channel, h its height, and l the plug length. The resulting force F_h that drives the plug downstream is thus given by:

$$F_h = \Delta P * S \ \eta l u \tag{5.11}$$

in which $S \sim wh$ is the droplet area (projected normally to the mean flow) on which the pressure field applies. When the obstructing droplet arrives at the junction, if the difference between the hydrodynamic resistances of the two paths is large, the droplet will be driven into the least resistive branch with, in terms of order of magnitude, the same force F_h. In the presence

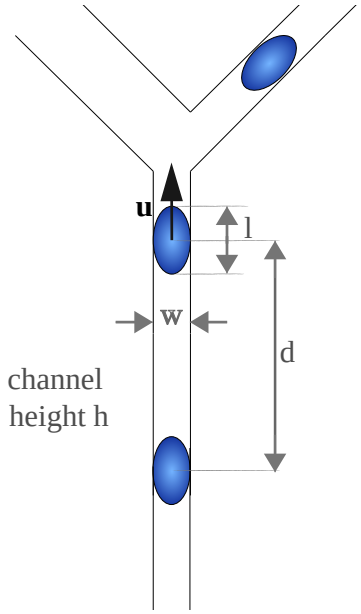

Figure 5.7 – Scheme of the sorting device. A train of droplets separated by a distance d is sent towards a Y junction. Droplets length is l, the height of the channel is h.

of a non-uniform electric field, the droplet will be attracted towards the more resistive channel by DEP forces. In order to achieve sorting, these forces must overcome F_h. As explained in section 5.1.1, the DEP force is proportional to the volume of the droplet whl and to the product of the electric field times its gradient [141]:

$$F_{DEP} \sim \epsilon_0 \epsilon_c whlE.\nabla E \tag{5.12}$$

where ϵ_0 is the vacuum permittivity, ϵ_c is the permittivity of the carrier fluid. The critical electric field E that must be applied to overcome the hydrodynamic drag is thus given by the expression:

$$\eta lu \sim \epsilon_0 \epsilon_c whlE.\nabla E \tag{5.13}$$

Equation 5.13 implies the existence of a threshold speed, $u_{thresh}(E)$, above which sorting cannot be achieved:

$$u_{thresh}(E) \sim \alpha \frac{1}{\eta} \epsilon_0 \epsilon_c whE.\nabla E \tag{5.14}$$

Where α is a numerical prefactor determined empirically. In practice, the maximum electric field E_{max} that can be applied is limited by electrosplitting [140].

$$E_{max} \sim \sqrt{\frac{\gamma}{\epsilon_0 \epsilon_c w}} \tag{5.15}$$

where γ is the surface tension. As $\nabla E \sim E/\delta$, where δ is the distance between the electrodes, combining 5.14 and 5.15, one obtains a critical droplet speed u^* above which no sorting can be achieved:

$$u^* \sim \frac{\alpha h \gamma}{\eta \delta} \tag{5.16}$$

Assuming further that the minimal distance d_{min} between consecutive droplets is in the order of a few droplet lengths l, one obtains the maximum droplet sorting frequency f_{max}, from the following relation:

$$f_{max} = \frac{u^*}{d_{min}} \sim \frac{\alpha h \gamma}{l \eta \delta} \tag{5.17}$$

This formula shows that miniaturization should favor higher sorting frequencies, since h, l and δ scale down with the same factor, implying that f_{max} is inversely proportional to the device characteristic dimension.

5.2.2 Experimental protocol

Design of the chip / COMSOL Multiphysics simulations

In conventional DEP sorting devices, electrodes are added around the circulating channel, separated by a PDMS wall that act as a dielectric barrier. To calculate the electric field corresponding to an imposed voltage at the electrodes, and check the feasibility of DEP sorting of femtoliter droplets, COMSOL Multiphysics simulations were performed. The electric field inside the channel depends on the material characteristics (permittivities), on the fluids involved and on the thickness of the PDMS wall. Using COMSOL electrostatics model, the corresponding electric potential was calculated at the Y junction. An example of obtained potential is depicted in Figure 5.8, for a 800V voltage.

Channels miniaturization goes along with an enhancement of electric fields. To obtain fields close to the electrosplitting limit ($3.1.10^6 V/m$ for 40 fL droplets [140]), PDMS walls can be as thick as 40 μm with a voltage of 1000V, a range easily reachable by standard soft lithography.

Protocol

In our experiments, embedded electrodes were added next to the Y junction during the lithographic process; this guaranteed that the electrodes were aligned with the microfluidic channel with micrometric precision, and they were close enough to generate large electric field gradients (Figure 5.9.a.). The applied AC electric fields were generated by applying between 400 and 1000 V through Pt electrodes plunged in the conductive buffer, at a frequency of 1.5 kHz. Local

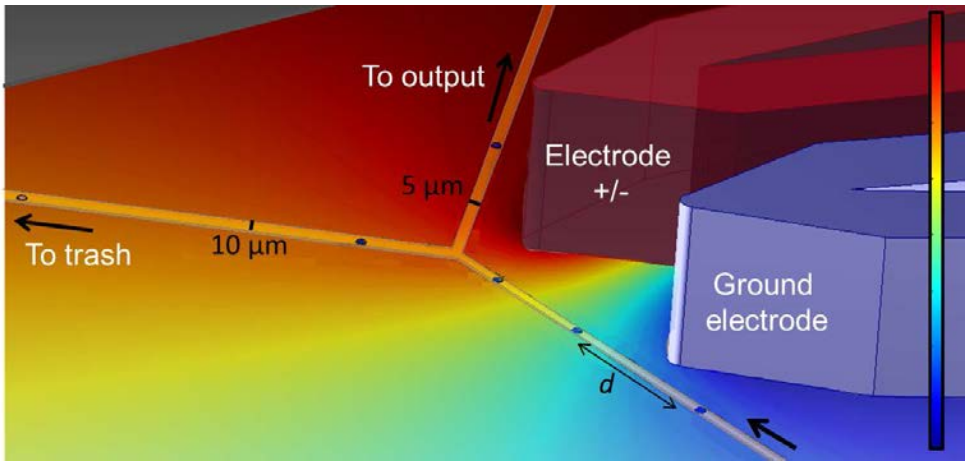

Figure 5.8 – Perspective representation of the sorting area. COMSOL calculated electric potentials are indicated.

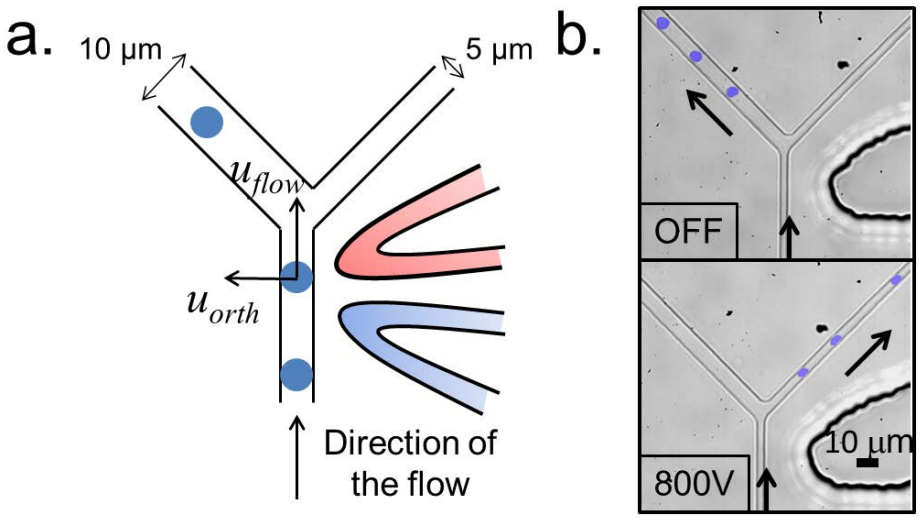

Figure 5.9 – DEP sorting. (a) Droplets are driven towards a y-shaped junction comprising two channels of unequal hydrodynamic resistance. (b) In the absence of electric field, well-separated droplets are driven towards the hydrodynamic path. In presence of a high voltage, well-separated droplets are driven towards the narrow channel.

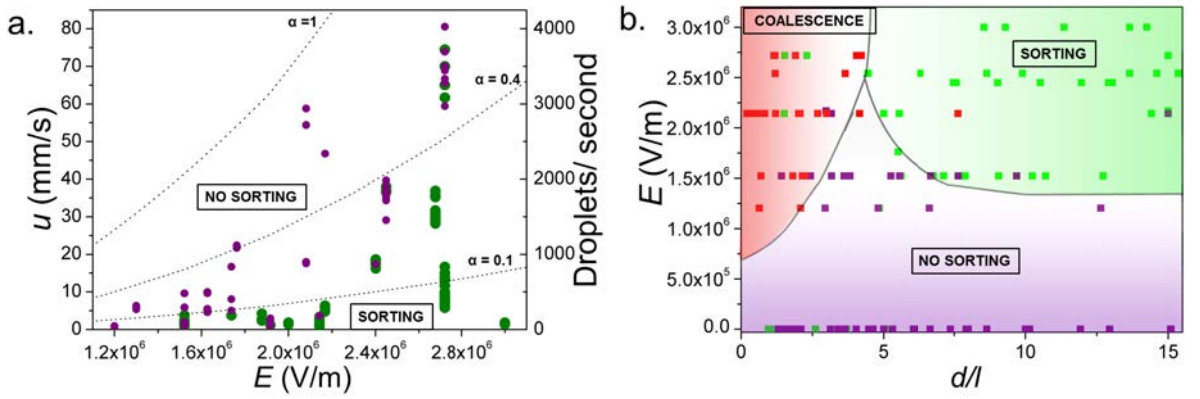

Figure 5.10 – (a) Speed of isolated droplets vs the applied electric field. Green dots: droplets directed towards the narrow channel. Purple dots: droplets directed towards the wide channel. The dotted line represents the theoretical maximum speed that enables DEP actuation calculated using Equation 5.14, with $\alpha = 0.1$, 0.4 and 1. The corresponding number of droplets per second are calculated assuming a distance of $5l$ between 20 fL consecutive droplets. (b) Phase diagram of the femtolitre DEP sorter. Green: sorted, purple: unsorted, red: undesired coalescence events. The DEP force becomes strong enough to direct droplets at applied fields larger than $1.5.10^6 V/m$. Droplets speed were limited to 0,6 - 9 mm/s. Under a critical distance $d/l = 5$, droplets coalesce in this device.

fields at the junction were found to vary from $1.1.10^6$ to $2.8.10^6 V/m$ and are close to the theoretical limit E_{max} for femtolitre droplet splitting ($3.1.10^6 V/m$ for 40 fL droplets [140]). Such fields would not be admissible for picolitre droplets, because they are above the critical field producing droplet breakup at rest ($E_{max} = 1.2.10^6 V/m$ for 15 pL ($30\mu m$ diameter) droplets).

Droplets of 20 to 50 fL volume containing deionized water with 1 % pluronic were produced on-chip with a step-emulsification process and driven towards a Y-shaped junction, with a hydrodynamic resistance ratio $R = 1.6$ between the two paths. With $R = 1.6$, the wide channel can contain up to 14 circulating droplets without substantially perturbing the main channel resistance [150]. The sorter was tested with trains of droplets travelling at velocities, u, ranging from 0.6 to 90 mm/s, varying the applied voltage V and the spacing d between the droplets. This corresponds to 8 to 9000 droplets/s, depending on u and d. Image processing was used to determine the droplet length l parallel with the flow, the distance d to the preceding droplet and the droplet trajectory.

5.2.3 Results and discussion

In the absence of an electric field, all droplets passed into the low resistance channel, but by applying a voltage to the electrodes, it was possible to direct the stream of droplets into the high resistance channel (Figure 5.9.b.). As predicted by the above theory, DEP sorting was possible only below a threshold velocity. Figure 5.10.a. shows that well spaced droplets ($d/l > 15$) were correctly driven towards the narrow channel at low speeds (green dots), but they flowed into the large channel in the presence of an electric field above a critical speed

$u_{thresh}(E)$ (purple dots). Experimentally, below $E = 1.5.10^6 V/m$, no speeds were found to enable DEP actuation, implying the threshold speed is lower than 0.6 mm/s in such conditions. The dotted lines represent the theoretical threshold speed, calculated using Equation 5.14 and electric field gradients computed with COMSOL, for $\alpha = 0.1$, 0.4 and 1. One sees that $\alpha = 0.1$ describes correctly the experimental trend at low electric fields, but $\alpha = 0.4$ better matches the experimental data at high fields. The discrepancy between theory and experiment most likely comes from the simplicity of our model; at high electric fields, droplets tend to deform, a parameter discarded from the discussion. A more accurate assessment would need to take into account the detailed shape of the droplet, its dynamical evolution during the sorting process, but also the presence of surfactants and the precise flow geometry at the junction, which is beyond the scope of this work.

Figure 5.10.b. shows an overview of the regimes of sorting found for various applied electric fields and distances between consecutive droplets, d (expressed as the ratio d/l) with $u = 0.6$ - 9 mm/s. Three regimes were observed, which are color-coded in Figure 5.10.b.: droplets passing into the wide channel (purple), droplets passing into the narrow channel (green), and droplets electrocoalescing (red). In the absence of an electric field (0V), with $d/l > 5$, all 716 analyzed droplets passed into the wide channel. In the presence of a low electric field, in agreement with the study of well spaced droplets (Figure 5.10.a.), no droplets were correctly sorted. Above $E = 1.5.10^6 V/m$, sorting was possible. In such conditions, droplets were correctly sorted as long as they were not perturbed by the preceding droplet. Figure 5.10.b. indicates that the distance between consecutive droplets has to be above $d/l \sim 5 - 6$ to enable efficient sorting, without sorting errors or coalescence events caused by the proximity of the preceding droplet.

The maximum sorting frequency obtained experimentally was 3 kHz for 20 fL droplets, which is an improvement compared to maximum sorting rates observed for picolitre droplets in this geometry (2 kHz) [69] [80]. To assess the theoretical maximum frequency at the electrosplitting limit, we assumed α was close to 0.4, and assessed the term $E.\nabla E$ in COMSOL at the theoretical limit $E_{max} = 3.5.10^6 V/m$ for 20 fL droplet splitting. Equation 5.14 then gives $u_{thresh}(E_{max}) = 203 mm/s$, and $f_{max} = 8 kHz$. It may be possible, therefore, to further improve the sorting speed by increasing the applied electric field.

We have shown that sorting of streams of femtolitre droplets under high throughput conditions is feasible. This operation is achieved by increasing the electric field, which is possible owing to the fact that electrosplitting of droplets is inhibited by miniaturization. The enhancement of the sorting frequency was limited to 3 kHz in our experiments, but theoretical frequency could be increased to 8 kHz at the electrosplitting limit.

5.3 Electrocoalescence of femtoliter droplets

Scaling laws predict that the electrocoalescence of smaller droplets demands larger electric fields. In this section, we provide some theoretical reminders on the electrocoalescence mechanism, that are helpful for the design of our miniaturized electrocoalescence chip in a second time. Experimental results are then provided.

5.3.1 Theoretical reminders

Electrocoalescence mechanism

As introduced in section 5.1.2, the interaction between a pair of droplets subjected to an electric field is very weak as long as droplets are far away. The accepted consensus is that electric forces only play a role once droplets are in close contact, while pairing is mainly governed by hydrodynamics. The attractive electrostatic force between droplets results in the drainage of the continuous phase film. The stability of films has been extensively studied[151, 152], and extented to the case of films under draining conditions[153]. Below a critical film thickness ($\sim 100nm$), intermolecular forces (typically Van der Waals forces or double-layer repulsion) become predominant and instability modes may appear, that either grow and cause the film rupture or get damped. The origin of those corrugations is usually attributed to thermal fluctuations or to mechanical perturbations.

Some studies indicate that droplets possess "natural oscillation frequencies"[154]; droplets would absorbe more energy from the applied field at certain frequencies, as assessed by observation of their oscillation amplitude. The "natural" oscillation frequency increases with droplet miniaturization, and is expected to be around 1 kHz for nL droplets excited by square electric fields[51].

Possible behaviors of a pair of droplets under an electric field

Studies on nanoliter and picoliter droplets predict the existence of three different regimes when a pair of droplets is subjected to an electric field.

Stable pair If the electric field is too low to overcome capillary pressure, or if the droplets are too distant, no coalescence happens. The pair is stable.

Coalescence If droplets are close enough to interact and if the electric field is high enough, they coalesce.

Repulsion At very high electric field, droplets repulse each other violently, after a partial coalescence and the formation of a liquid bridge. This phenomenon was presented in section 5.1.2.

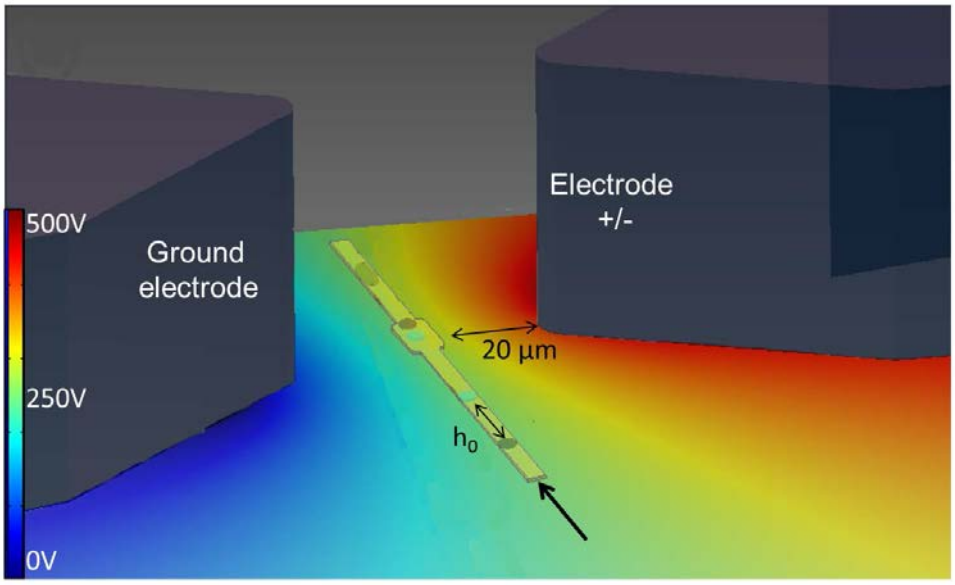

Figure 5.11 – Perspective representation of the coalescing area. COMSOL calculated electric potentials are indicated.

5.3.2 Experimental protocol

Design of the coalescence area

To help the electrocoalescence process, the design of the coalescence area was inspired by the passive coalescer geometry by Bremond *et al.*[40]. Droplets enter an enlarged area in which they are slowed down. Their slowing down is expected to both help the pairing hydrodynamically and electrically. Indeed, by increasing the time droplets are subjected to electric field, we expect the electric interaction to have more time to develop. Electrodes were positioned slightly asymetrically in order to place the field maximum at the restriction. COMSOL Multiphysics simulations were performed to predict the repartition of the voltage inside the chip (Figure 5.11).

Protocol

Two sets of 20 to 30 fL aqueous droplets were generated at 3 kHz using an on-chip step emulsification process, and brought together just upstream of the coalescence zone (Figure 5.12). Droplets entered the coalescence chamber at speeds ranging from 2 to 22 mm/s and the coalescence process was tracked by analyzing images taken with a high-speed camera. An example of coalescence of two droplets, containing brilliant black (2%) and fluorescein (1%) is shown in Figure 5.12.b. Phase diagrams were drawn for two solutions of different conductivity: deionised water with F68 pluronic (1%) and deionised water with fluorescein ($300\mu M$) (Figure 5.14). Their conductivities were, respectively, 10^{-3} S/m and 10^{-1} S/m.

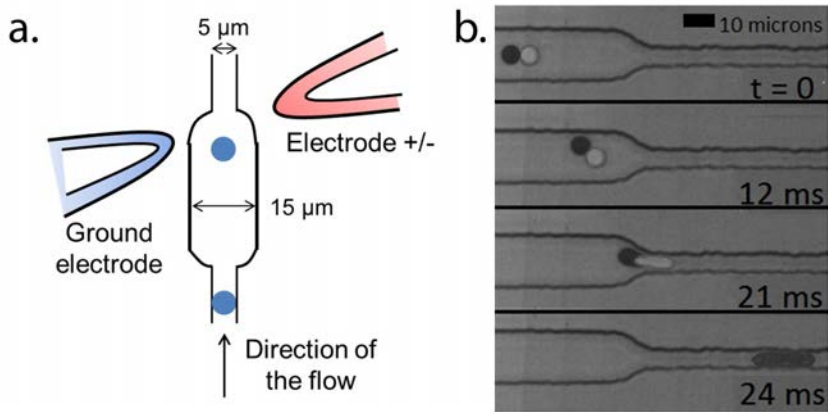

Figure 5.12 – (a) Droplet pairs are driven in an enlarged channel, surrounded by two electrodes. (b) Example of a coalescence event for 25 fL droplets colored with Brilliant Black (2%) and Fluorescein (1%), respectively. The applied voltage was 450 V. Droplets reorient along the field (t = 12ms) and then coalesce at the restriction (t = 21ms). The channel height is $1\mu m$.

We measured the radius R and the distance between paired droplets, d, at the entrance of the coalescence area. The distance between consecutive droplet pairs was maintained above $4R$ to avoid droplet-droplet interactions. Under this condition, the maximum coalescence throughput of the device was 1.1 kHz.

5.3.3 Results and discussion

Phase diagram

Similarly to picolitre droplets, three regimes were observed depending on the field strength and on the initial separation d between successive droplets: absence of coalescence (Figure 5.13.a.), droplet coalescence (Figure 5.13.b.), repulsion (Figure 5.13.c.).

Those regimes are represented on the phase diagram Figure 5.14 with the following color coding: droplet coalescence (Figure 5.14 blue area), stable droplet pairs (Figure 5.14 grey area) and repulsion between droplets (Figure 5.14 green area). No difference in behavior was observed between the two solutions of different conductivities. The phase diagram (Figure 5.14) has a structure similar to that established for picolitre droplets, with a triple point separating the three regimes. However, on analyzing in more detail the phase diagram, one sees that droplets coalesce up to an initial separation distance of 2R, compared to 0.7R usually found for picolitre droplets. This is presumably due to the geometry: droplets need to deform to enter the restriction which causes their average speed to be slowed down by 50% just before the restriction. This eases the synchronization of droplets in the coalescence area.

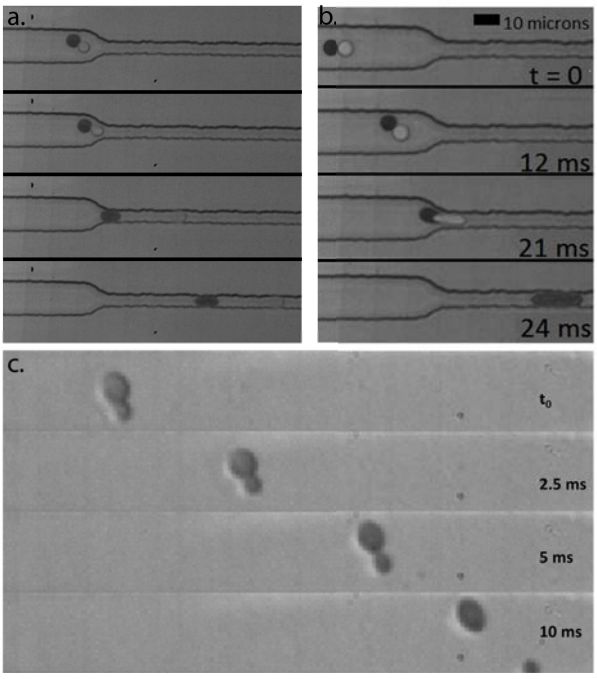

Figure 5.13 – Three behaviors are observed in our device. a. No coalescence, the pair of droplets remains stable despite the electric field. b. Coalescence of the droplet pair. c. Repulsion of the droplet pair at high fields.

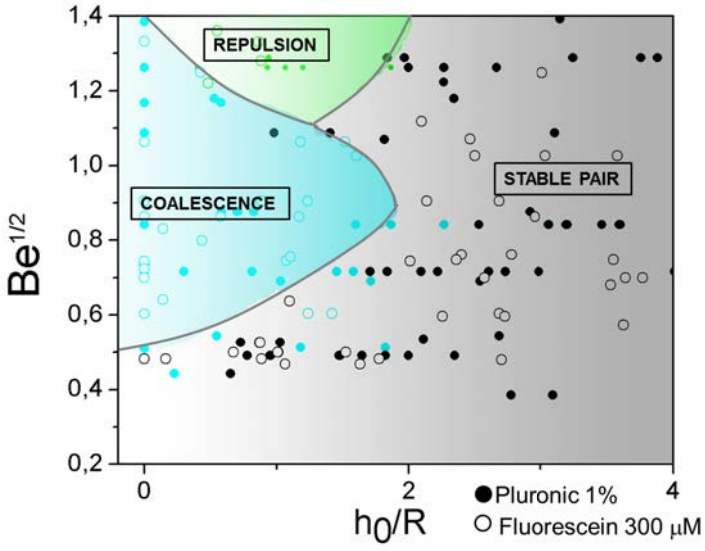

Figure 5.14 – Phase diagram of the system. Blue area: coalescence. Gray: stable pair. Green: repulsion. Experiments were carried out using droplets containing (○) 300 μM fluorescein and (●)1% Pluronic F68, without observable differences between the two solutions.

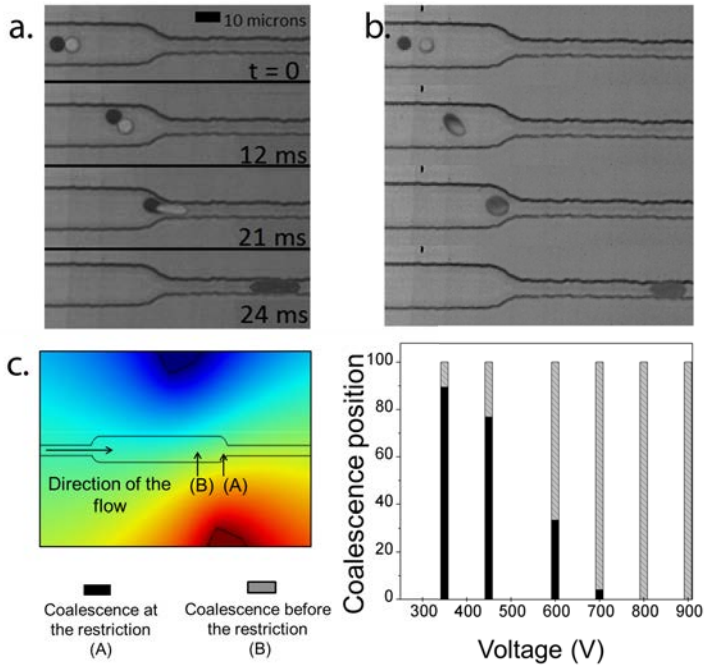

Figure 5.15 – Position of the coalescence event. (a) Example of a coalescence event at the restriction. (b) Example of a coalescence event before the restriction. (c) Repartition of the coalescence position as a function of the applied voltage.

Position of the coalescence event

Coalescence either happens at the restriction (Figure 5.15.a.) or before the restriction (Figure 5.15.b.). The position of coalescence events was highly dependent on the electric field (Figure 5.15.c-d.). Above 800V, all coalescence events happened before the constriction (Position B), whereas droplets coalesced at the restriction at lower fields (Position A). This can be explained by the fact that the mechanism of coalescence depends on the voltage: at high fields, only electric stresses are at play, whereas at lower voltages, droplet coalescence results from both electric stress and hydrodynamic decompression at the restriction.

To summarize, we demonstrate here that controlled electrocoalescence of femtolitre droplets can be achieved in a microfluidic environment, at the expense of applying larger electric fields than for picolitre droplets. The coalescence chamber design favors droplet pairing at larger initial distance and helps destabilization of the pair at the restriction.

5.4 Conclusion on the manipulation of femtoliter droplets with electric fields

We have demonstrated the possibility of sorting and merging femtoliter droplets with electric fields despite unfavorable scaling laws. Miniaturization is performed with keeping the fast PDMS

technology and remaining in standard soft-lithography resolution. Compared to the state of the art, our devices provide improved throughputs for the DEP sorting and wider initial conditions for the electrocoalescence process.

Some perspectives remain open; the DEP sorting could be further improved by triggering the electric field depending on droplets fluorescence. This would demand a setup containing a laser spot and electronic implementation to couple the electric field to droplet fluorescence and was not the main objective of this PhD work.

Manipulation of femtoliter droplets with electric fields

✧ **Theoretical reminders**

- Subjected to an electric field, droplets get polarized and can be assimilated to macroscopic dipoles.
- The dimensionless number that describes the ratio of the electrostatic pressure over the capillary pressure is the Bond electric number $Be = \epsilon_0 \epsilon_r E^2 R/\gamma$.
- Subjected to a non-uniform electric field, a dielectrophoretic force displaces the water-in-oil droplet towards the high fields area.

✧ **DEP sorting of femtoliter droplets**

- Scaling laws analysis predict a maximum sorting speed that decreases with droplets size. Fortunately, the spacing between droplets also decreases with droplet miniaturization, resulting in an increase of the sorting frequency.
- COMSOL simulations confirmed that high enough fields could be obtained with realistic PDMS walls thicknesses.
- Experiments provided values of the maximum droplet speed that still enables DEP actuation and working phase diagrams of the device.
- The maximum experimental sorting frequency was 3kHz but could be theoretically increased to 8 kHz at the electrosplitting limit.

✧ **Electrocoalescence of femtoliter droplets**

- The reduction in device scale enables the increase of electric gradients imposed.
- Three behaviors were observed, in agreement with nL droplets experiments: coalescence, stable pair or repulsion.
- Droplets can be coalesced even if initially distant of $2R$, at kHz frequencies.
- Droplets coalescence happens by pure electrocoalescence at high electric fields but by an interplay of electrical stresses and hydrodynamic induction at lower voltages.

Chapter 6

Hydrodynamic splitting

Splitting of droplets is one of the basic operations of droplet-based microfluidics; it allows the division of a mother droplet into two symetrical or asymetrical daughter droplets, enabling the multiplexing of reactions on droplets of similar composition. In the evolutionary perspective, the splitting of droplet models the cell division and can be used to study early life processes.

6.1 Reminders on droplet splitting operations

6.1.1 Significance of this operation

Several strategies can be used to split droplets, among which the application of a high electric field[87] as mentioned in Chapter 5, or the use of a thermic resistance to squeeze a large droplet [86], but we focus here on the most commonly used actuation : the hydrodynamic splitting.

6.1.2 Miniaturization considerations

The physics of droplet splitting in a T-junction was studied[84, 85, 88] and is presented in Chapter 1.2.2.

Hydrodynamic splitting is controlled by the geometry, the viscosity ratio of the continuous and dispersed phase $\lambda = \frac{\mu_c}{\mu_d}$ and the Capillary number, defined by $Ca = \mu_c u/\gamma$. It has been shown that two regimes of splitting are possible, one in which droplets occupy only a fraction of the channel width (non obstructed regime), and the other in which droplets completely obstruct the channel (break up with complete obstruction of the channel). The former necessitates moderately low Ca, while the latter, being mostly controlled by the geometry, occurs almost independently of Ca.

The miniaturization of the splitting operation can be performed by decreasing the channel section to obtain long confined droplets that split in the obstructed regime. However, the

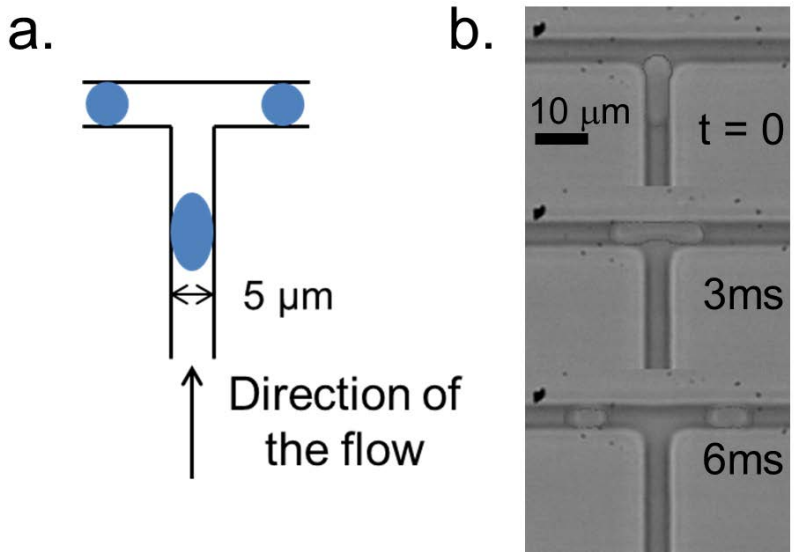

Figure 6.1 – Femtoliter droplet splitting. (a) Splitting device. Droplets flow towards a T junction. The height of the channel was 1 μm to favor obstruction and enhance the splitting process. (b) Time series of micrographs showing a 75 fL droplet splitting.

reduction of channels dimensions increases the hydrodynamic resistance and decreases droplets speed. Only low Ca will be reachable and the possibility of splitting femtoliter droplets in the non-obstructed regime is questionable.

6.2 Splitting of femtoliter droplets

6.2.1 Protocol

In our case, 25 to 135 fL droplets were generated by on-chip step emulsification and driven toward a 1 μm high, 5 μm width T-junction (Figure 6.1.a). The viscosity ratio between the oil and the water phase is $\lambda = 1.43$. Droplets were driven towards the junction and experiments were recorded by a high-speed camera. An example is reproduced on Figure 6.1.b. Droplet speeds and droplet lengths l, were measured by image analysis. The channel width w was also measured in situ, so as to take into account the PDMS deformation.

Throughout the experiments, we spanned a range of inlet pressures from 1.5 to 6 bars. Because of the geometry (long thin channels), the corresponding speeds were low - between 5 and 50 mm/s. Attempts to achieve higher flow rates were made with a neMESYS syringe pumps, but the glass slides could not withstand the corresponding applied pressures. To avoid unwanted interactions, the distance between successive droplets was kept above $4l$, limiting the frequency to 850 Hz at the maximum speed of 50 mm/s.

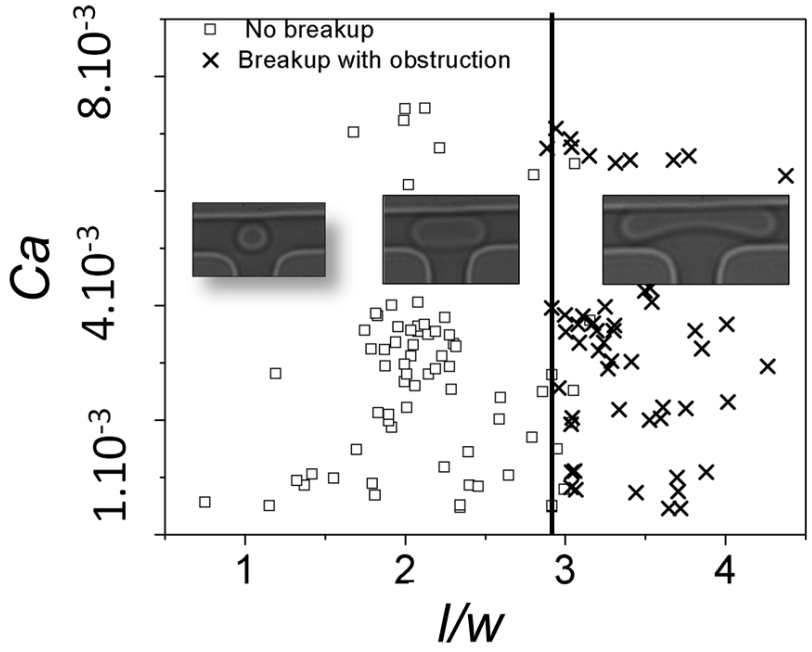

Figure 6.2 – Phase diagram of the splitting of 25 to 135 fL droplets. Only two regimes were observed: (□) non breakup, and (×) breakup with obstruction (at $l/w \sim 3$). This corresponds to a droplet volume of 75 to 130 fL in our geometry, depending on the PDMS pressure related deformation

6.2.2 Results

As expected from the low Capillary number of the system, breakup was only observed in the complete obstruction regime. Figure 6.2 shows that the critical ratio l/w upon which breakup is obtained does not depend on the Capillary number, in consistency with the theory, but is mostly controlled by the geometry. According to the model described in [155], the breakup with tunnels regime could only be achieved at capillary numbers of 10^{-2}, a range that is difficult to achieve in our device: the underlying reason is that the geometries needed to handle fL droplets result in channels with high hydrodynamic resistance, which limits droplet speeds and typically results in small Capillary numbers.

6.3 Conclusion

To summarize, we demonstrate here that femtolitre droplets splitting is achievable in T junctions in obstructed regimes, with a minimal volume of 75 fL (daughter droplets of 32 fL each) and a maximum frequency of 850 Hz. To split smaller droplets would require either smaller features, beyond the scope of standard soft-lithography techniques, or higher Capillary numbers, thereby higher pressures, which were out of reach with our device.

Splitting of femtoliter droplets

- Hydrodynamic splitting of droplets as small as 75 fL could be obtained in devices made by standard soft-lithography techniques.
- Only a narrow range of speeds was achievable experimentally because of large hydrodynamic resistances.
- As a consequence, the splitting with tunnels regime could not be observed in our devices.

Chapter 7

Droplet stability and biochemical compatibility

Droplets stability is a pre-requisite if such droplets are to be used as microreactors for biochemical reactions. When decreasing droplets size, surface effects are expected to intensify as surface to volume ratios grow (Figure 7.1): dissolution/evaporation phenomena, interaction of the biological material with the interface are potential issues of miniaturization. The impact of interfaces is actually hardly predictable; most often, part of the encapsulated material may get adsorbed and be partially not available for further biological assays, even though beneficial effects are sometimes described[94].

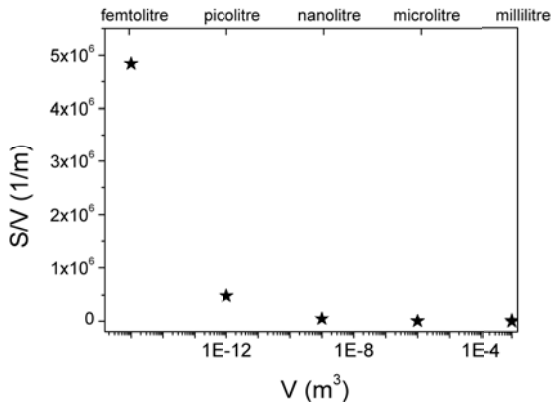

Figure 7.1 – Variation of the surface to volume ratio as a function of droplets volume. Miniaturization goes along with an intensification of surface effects.

In this chapter, we are first going to analyze the thermodynamical stability of femtoliter droplets through a theoretical approach and experimentation. The biochemical compatibility will then be assessed with one of the most common biochemical reactions, the Polymerase Chain Reaction.

7.1 Femtoliter droplet stability

7.1.1 Theoretical approach on droplet stability

The question we address here concerns the thermodynamic stability of femtolitre droplets, stability being a pre-requisite if such droplets are to be used as microreactors for chemical or biological reactions. According to the Epstein-Plesset dissolution model, established for gas bubbles in a liquid solution [156] and later extended to liquid microdroplets dissolution [157], the miniaturization increases the shrinking rate of droplets, by driving faster mass exchanges between them and the continuous phase. On the other hand, the process is known to be inhibited by the addition of solutes[158, 159, 160]. In these papers, the solutes are assumed to be insoluble in the continuous phase. Let us denote the subscripts α for the droplet and β for the surrounding phase, 1 for water, 2 for oil and 3 for the solutes. The oil reservoir is assumed to be infinite. At equilibrium, water chemical potentials in the droplet and in the surrounding phase are equal:

$$\mu_{1,\alpha}(T, P_\alpha) = \mu_{1,\beta}(T, P_\beta) \tag{7.1}$$

The equilibrium is stable under the condition[158]:

$$\lfloor \frac{\partial(\mu_{1,\alpha}(T, P_\alpha) - \mu_{1,\beta}(T, P_\beta)}{\partial R} \rfloor_{eq} > 0 \tag{7.2}$$

On the other hand, there is a relation between the fraction of water in the dispersed phase $x_{1,\alpha}$, the continuous phase $x_{1,\beta}$, and the laplacian pressure term across the droplet interface:

$$v_{m1}\frac{2\gamma}{R_{eq}} + RTln(x_{1,\alpha}) = RTln(x_{1,\beta}) \tag{7.3}$$

Where v_{m1} is the molar volume of water and R_{eq} is the radius of the droplet at equilibrium. Inside the droplet, $x_{1,\alpha} = 1 - x_{3,\alpha}$, where $x_{3,\alpha}$ is the fraction of solutes in the droplet at equilibrium; $ln(1 - x_{3,\alpha})$ can be developed at first order in the vicinity $x_{3,\alpha} << 1$. The fraction of solutes in the droplet at equilibrium $x_{3,\alpha}$ is increased by a factor $(R_0/R_{eq})^3$ as droplets shrink:

$$v_{m1}\frac{2\gamma}{RTR_{eq}} - x_{3,\alpha,0}(R_0/R_{eq})^3 = ln(x_{1,\beta}) \tag{7.4}$$

where R_0 is the initial droplet radius and $x_{3,\alpha,0}$ is the initial fraction of solutes in the droplet. The application of condition (10) to equation (12) gives the minimal fraction of solutes $x^*_{3,\alpha,0}$, and hence the minimal concentration of solutes $c^*_{3,\alpha,0}$, under which droplets are stable:

$$x_{3,\alpha,0} > (x_{3,\alpha,0})^* = \frac{2\gamma v_{m1}}{3RTR_0} \tag{7.5}$$

$$c_{3,\alpha,0} > (c_{3,\alpha,0})^* = \frac{2\gamma v_{m1}\rho_1}{3RTR_0 M_{solute}} \tag{7.6}$$

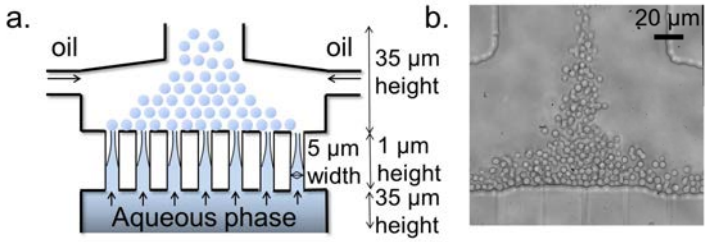

Figure 7.2 – Off-chip droplet incubation and reinjection. (a) Diagram of the parallelized femtolitre droplet maker. (b) Micrograph of a parallelized femtolitre droplet maker.

Where ρ_1 is the volumic mass of water and M_{solute} is the molar mass of the solute. With droplet miniaturization, higher solute concentrations are needed to obtain stable droplets. For a typical $M_{solute} = 300g/mol$, the minimum solute concentration as a function of droplet volume is presented in Table 1. Despite the increase in $c^*_{3,\alpha,0}$ on miniaturization, the values remain accessible experimentally, and femtolitre emulsions can easily be stabilized with proper formulation. We recall that the theory corresponds to an infinite reservoir of the continuous phase. However, in reality, the emulsion reservoir is finite, and shrinkage is expected to stop once the continuous phase is saturated with water and the chemical potentials in the droplet and in the surrounding phase are equal. In this case, the minimum initial solute concentrations required for stability, will be lower than those in Table 1.

Droplet volume	4 fL	60 fL	500 fL	5 pL
Minimum solute concentration $c^*_{3,\alpha,0}$	80 μM	28 μM	14 μM	6 μM

7.1.2 Stability of femtoliter droplets

Experimental protocol In our experiments, droplets of 65 fL volume were produced using a parallelized step-emulsification device (Figure 7.2). The aqueous phase flows through an array of 37 narrow channels (1 μm high, 5 μm wide), and falls into a deep reservoir of oil (35 μm deep), giving a total droplet production frequency of $\sim$ 10 kHz.

Results and discussion When composed of DI water ($c_{3,\alpha,0} = 0$), droplets disappeared in a few seconds (Figure 7.3.a. ○) in agreement with the theory. Droplets containing high solute concentration (for instance, PCR reagents, with $c_{3,\alpha,0}$ over $\sim$ 2 mM) demonstrated a better stability. To go deeper, we measured the droplet size distribution by injecting an emulsion comprising 65 fL droplets containing PCR reagents between two glass slides and carried out image analysis (Figure 7.3.a. ■). Just after their production, droplets shrunk slightly towards their radius of equilibrium (0.1 days). Then, the mean radius remained constant over 5 days, before increasing towards higher radii (12 days after the production). The variance in radius (Figure 7.3.b) remained small at short times (up to 2 days) and slightly increased at longer times (12 days).

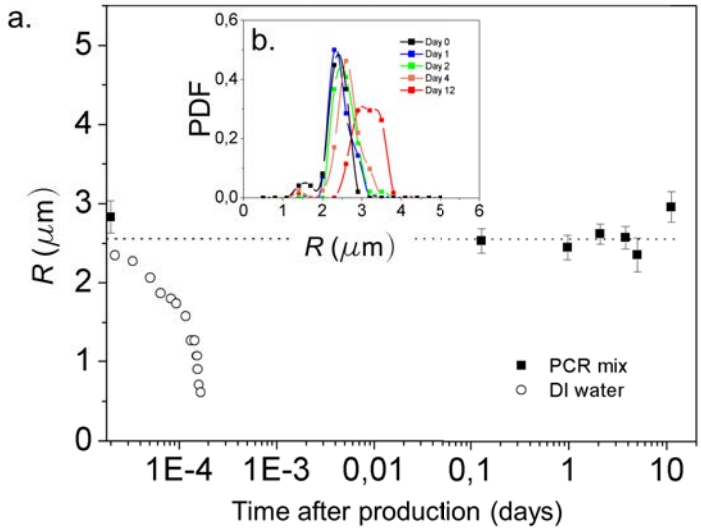

Figure 7.3 – Evolution of the average radius of 65 fL droplets containing DI water (○) or PCR reagents (■) after droplet production and during storage at room temperature under mineral oil. (d) Evolution of the probability density function (PDF). Black : day 0, dark blue: day 1, green: day 2, orange: day 4, red: day 12. The monodispersity remained high during the first two days (Coefficient of variation (CV) 0.02) and started to decrease after 4 days of incubation at room temperature (CV 0.16 at day 12).

The slight initial shrinking is most likely caused by the low but non-zero solubility of solutes in oil. In this case, size distribution depends on the diffusion rates of the solutes and is expected to decrease slightly in the case $c_{(3,\alpha,0)} \gg c^*_{(3,\alpha,0)}, c_{(3,\beta,0)} = 0$ [158]. The increase in size distribution observed at long time scales most likely results from coalescence events rather than Ostwald ripening because the average droplet volume increases.

Femtoliter droplets are stable for a few days under certain constraints on the formulation and can be used a micro-reservoirs.

7.2 Reinjection of femtoliter droplets

When performing chemical or biological reactions in droplets, many studies focus on performing incubation steps on-chip, but this is associated with a variety of technological issues, notably related to evaporation due to the porosity of PDMS. A way to avoid these issues is to recover the emulsion off-chip, incubate off-chip, and reinject the emulsion into another chip for analysis. After overnight incubation at room temperature, the 65 fL droplets containing PCR reagents were reinjected and spaced with fluorinated oil with 2% fluorosurfactant. Regular spacing of droplets demands a nozzle as narrow as the droplet diameter, to allow just one droplet to be separated by spacer oil at a time. To obtain such characteristics with 65 fL droplets, the channel height was lowered to 1 μm. The squeezed micrometric droplets have an increased effective radius and could be reinjected in a controlled way in 5 μm width channels accessible

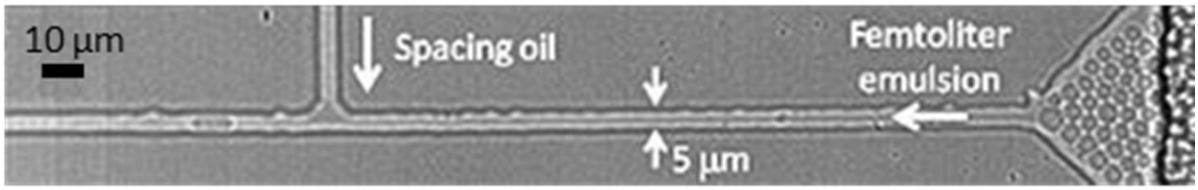

Figure 7.4 – Reinjection of a femtolitre emulsion. The channel was 1 μm high, increasing the apparent radius of droplets and enabling one-to-one injection without leaving standard soft lithography processes.

by standard soft lithography process with a chrome mask. (Figure 7.4).

7.3 Polymerase Chain Reaction (PCR)

In this section, we investigate the biocompatibility of femtoliter reservoirs through the amplfication of a plasmid DNA by PCR.

7.3.1 Experimental protocol

Droplets of 20 or 65 fL volume containing PCR reagents are produced using the parallelized step-emulsification device described above. PCR is performed on a 2660 bp pUC18 plasmid, out of which a 129 bp PCR product is amplified with M13 Forward and Reverse primers. The PCR mix is the following :

- DreamTaq enzyme green buffer (5 μL/50 μL)
- M13 Forward and Reverse primers (0,4 μM). They are the limiting reagents in the amplification
- dNTPs (200 μM)
- DreamTaq DNA polymerase (1 μL/50 μL)
- F68 pluronic (0,02%)
- drosophila total RNA (340 pg/μL)

DNA concentration is varied from 8 pg/μL to 300 pg/μL to obtain a large range of mean DNA number per droplet.

The amplification cycle comprises the following steps. Initial denaturation of DNA at 94 $^{\circ}C$ for 2 minutes, then 35 cycles consisting in:

- denaturation of DNA at 94 $^{\circ}C$ for 15 seconds

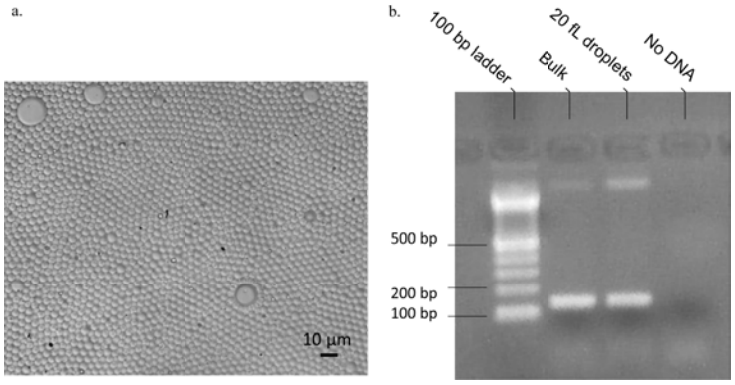

Figure 7.5 – a. Typical example of the emulsion distribution after thermocycling: there are very few coalescence events. b. Example of an agarose gel obtained in the case of $\lambda = 1,85$. Both in bulk and in droplets, complete amplification of the 129 bp target fragment was obtained.

- hybridization of primers at 62 $^{\circ}C$ for 30 seconds

- elongation of the DNA strand at 72 $^{\circ}C$ for 30 seconds

At the end of the 35 cycles, a final elongation step is performed at 72 $^{\circ}C$ for 5 minutes.

Several measures were taken to overcome adsorption issues. The reaction mixture was supplemented with 0.2% F68 Pluronic and Drosophila total RNA was added to the DNA dilutions and to the PCR mix at a final concentration of $340pg/\mu L$. Silanization of the polypropylene reservoirs was also performed, using dimethyldichlorosilane. The template DNA concentration was varied from $10pg/\mu L$ to $200pg/\mu L$ which corresponds to a mean number of template DNA molecules per 65 fL droplet, λ, ranging from 0.22 to 4.5.

After production, droplets were collected in a $200\mu L$ Eppendorf tube and covered with heavy mineral oil to avoid evaporation. PCR was then performed in a thermocycler off-chip. Figure 7.5.a. depicts a typical example of the emulsion distribution after thermocycling: the emulsions suffered very few coalescence events during the cycling. After thermocycling, the emulsion was broken by adding 30 to 60 μL of perfluorooctanol, and analyzed by agarose gel electrophoresis together with the same reaction performed in bulk (Figure 7.5.b.). Primers were the limiting reagent in this PCR reaction.

7.3.2 Results

Quantification of the number of coalescence events after thermocycling To estimate the fraction of coalescence events in a packed emulsion, we identified coalesced droplets by their size and measured the total area of coalesced droplets a_c, the total area occupied by uncoalesced droplets a_u and the total number of uncoalesced droplets n_u. The fraction of coalesced droplets is

$$C = \frac{a_c/a_u n_u}{n_u + a_c/a_u n_u} \tag{7.7}$$

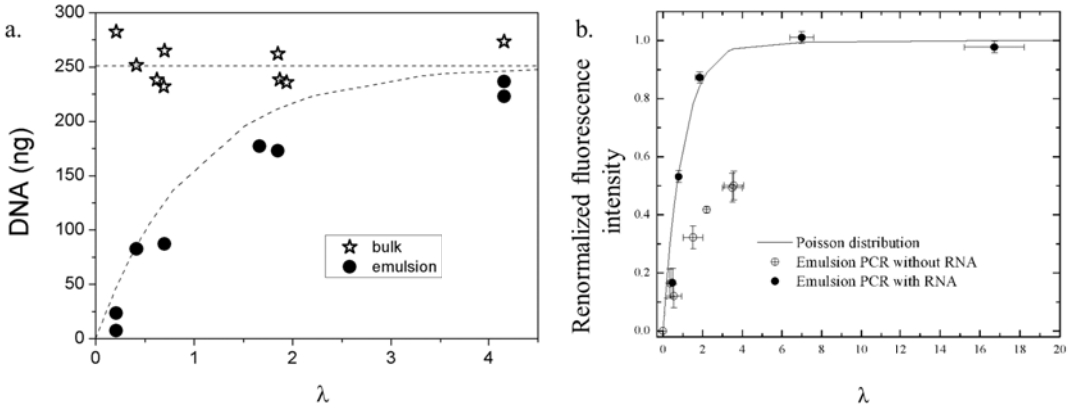

Figure 7.6 – a. In presence of total RNA, experiments were carried out varrying λ. The amplification in bulk is constant, in conformity with the use of primers as limiting reagent. In emulsion, amplification is in agreement with a Poisson distribution. b. Amplification yield (represented by the renormalized fluorescence intensity) as a function of the mean number of DNA per droplet λ. Without total RNA, the amplification is lower than expected. The addition of total RNA enabled the amplification of all the encapsulated material.

The typical fraction of coalescence events is $C = 0.3\%$, inducing a negligible biase in our experiments.

Verification of the quantitative amplification with total RNA In bulk the final yield of DNA does not depend upon the initial DNA concentration (Figure 7.6.a). In droplets, however, the final yield of DNA is expected to drop quickly when $\lambda \leq 1$. This is because the template DNA should be distributed into droplets following a Poisson distribution and when $\lambda \leq 1$ an important fraction of droplets does not contain a template DNA molecule (33% at $\lambda = 1$). The final yield of DNA should fit the curve describing the fraction of drops containing ≤ 1 template DNA molecules $f_o = 1 - e^{-\lambda}$. The yield of amplified DNA at $\lambda = 4.5$ in femtolitre droplets was similar to in bulk, but dropped off as λ decreased, closely fitting the curve described by a Poisson distribution without loss of template DNA. Initially, PCR experiments were performed without total RNA. Figure 7.6.b shows that the renormalized fluorescence intensity in droplets is lower than expected for a Poisson distribution of the biological material. Part of the template DNA was most probably adsorbed on the tubings and on the droplets interface. The introduction of total RNA saturates the interfaces, with a faster dynamics than the DNA adsorption process considering the small size of RNA molecules. The presence of residual total RNA during the PCR does not perturb its proper realization.

These results indicate that femtolitre droplets can be used for quantitative biological assays, despite the high surface to volume ratio. Some precautions are needed in terms of formulation and microfabrication, but those precautions are very similar to larger droplets'.

7.4 Conclusion on the stability of femtoliter droplets and their use as biological reactors

To summarize, aqueous femtolitre droplets are thermodynamically stable, provided the aqueous phase contains a low concentration of solute. Under these conditions femtolitre droplets can be incubated for a few days off chip and reinjected on-chip for further analysis. This stability ensures that incubation of biochemical reactions can be performed inside femtolitre droplets. The ability to perform biochemical reactions in femtolitre droplets was checked by performing PCR in the droplets: no loss of reagents was observed and the reaction was equally as efficient as in bulk, despite the high surface to volume ratio.

Droplet stability and biochemical compatibility

- Miniaturization goes along with a major increase of the surface to volume ratio. Surface effects (dissolution, evaporation, interaction with interfaces) are expected to become predominant.
- Thermodynamics predict femtoliter droplets are stable above a solute concentration of a few ten μM, that are below the typical concentrations of biochemical reactors.
- Experiments demonstrated the stability of femtoliter droplets containing a PCR mix over 4 days, while DI femtoliter droplets shrink in a few seconds.
- Reinjection of femtoliter droplets is achievable with standard soft lithography methods by reducing the channels height.
- Polymerase Chain Reaction works efficiently in femtoliter droplets at the expense of a proper protection of the interface. Total RNA and pluronic were used in our experiments, other biomolecules might be envisioned.

Conclusion on the miniaturization of droplet-based microfluidics to the femtoliter scale

We have built a femtolitre droplet toolbox of basics droplet-based microfluidic operations (Figure 7.7). Despite the small size of the droplets, we obtained a level of control comparable to that obtained for nanolitre and picolitre droplets, while still fabricating the chips using standard soft-lithography techniques and rapid PDMS technology. The ability to perform biochemical reactions in femtolitre droplets was checked by performing PCR in the droplets: no loss of reagents was observed and the reaction was equally as efficient as in bulk, despite the high surface to volume ratio. Some operations were more difficult to achieve such as splitting, which is accessible only in the obstructed regime. However, in some other cases miniaturization to femtolitre droplets offered significant advantages. Notably, mixing time was only 45 μs,the shortest reported time in a droplet microreactor. We envisage that the new capabilities to manipulate femtolitre droplets we demonstrate here will inspire the development of novel and innovative systems, able to operate under ultra high-throughput conditions using unprecedentedly low volumes of reagents (one billion times lower than in conventional microtitre-plate based systems).

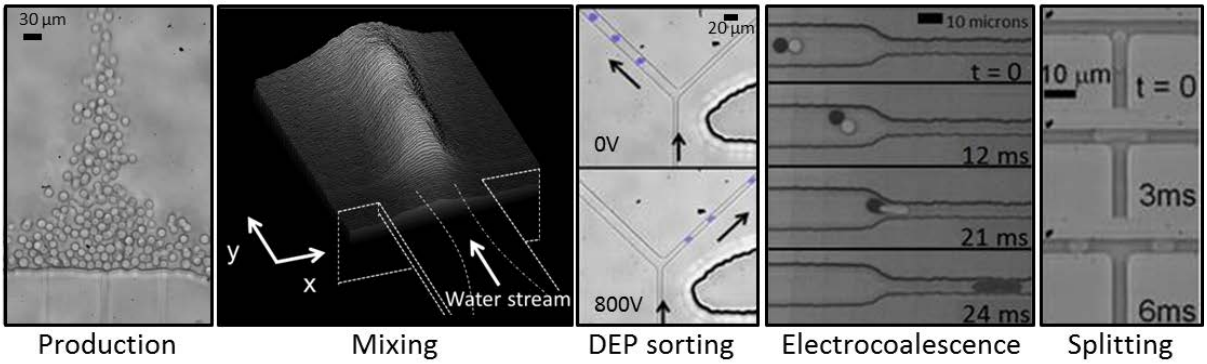

Figure 7.7 – Miniaturization of droplet-based microfluidics to the femtoliter scale. Elementary operations were successfully miniaturized down to the femtoliter scale (production, mixing, DEP sorting, electrocoalescence, splitting). Drop-on-demand and incubation steps were also miniaturized.

Part of those results were published and are reproduced in Appendix B.

Part III

Direct droplet labeling with oligobarcodes fabricated *in situ*

The encouraging developments of the initial part of my PhD encouraged the fabrication of a platform for the encoding of droplets with DNA barcodes fabricated *in situ*. This project was initiated by discussions with the Broad Institute and a patent was deposited (High-throughput dynamic reagent delivery system, WO 2014085802 A1).

We first present the interest of the platform, particularly oriented towards single-cell analysis, and state of the art on sequencing methods before introducing the work performed on the platform.

Figure 7.8 – Multiplexed platform for the in situ encoding of droplets with DNA barcodes

Chapter 8

Introduction to single-cell analysis

In the first part of this manuscript, we have demonstrated the biological interest of droplet-based microfluidics: the high-throughput manipulation of droplets opened access to the inspection of a wider area of the biological space, notably thanks to the encapsulation of single molecules/cells into droplets. Droplet interface provides a physical linkage between the genotype of the encapsulated biomaterial and its expressed phenotype. However, in many studies, the final step is the sequencing of selected biomolecules to obtain data on their genotype. Other methods to provide linkage between the selected phenotype and the genotype are to be envisioned.

This part of the manuscript introduces single-cell analysis problematics and recent methods that enabled a deeper characterization of cellular heterogeneities. Those methods require several steps, among which the isolation of the cell in a reservoir, its lysis and the sequencing of the cDNA [1]. The sequencing step demands an encoding of the cell biomaterial with barcodes readable per sequencing; the second part of my PhD focused on the developpement of an encoding platform, later on so called *droplet printer*, that provides an *in situ* encoding of droplets with oligo barcodes readable per sequencing. In this section, we present an overview of existing encoding methods and introduce the interest of our platform. The proper design of our platform demanded the inspection of hydrodynamics of droplets under different confinement conditions, that are investigated in a last part of this chapter.

8.1 Single-cell analysis

Cells of a given type can present wide expression heterogeneities even if they are kept in a homogeneous environment. Researchers feel inclined towards analysis of individual cell heterogeneities, with two main applications: first, the ability to analyze variations at the single-cell level enables the selection of better mutants in screening or directed evolution applications. An-

1. cDNA contains only the expressed genes of an organism and is produced from reverse transcription of the RNA

other application is the study of regulatory relationships between genes and pathways through single-cell transcriptomics (for instance, cells response to different stimuli [161]) that has wide implications in cancer research.

8.1.1 Screening on single-cells and directed evolution

Compartmentalization of single-cells into individual reservoirs enables the analysis of the proteins that are released or secreted by the cells and their screening. A major industrial interest is directed towards the screening of new antibodies, as expressed by the recent creation of commercial antibody-screening platforms (Hifibio), and which represents an annual market of 100 billion $. Considerable progress was done since Nossal's droplets made by the operator's mouth (Chapter 1.1.1). Cells are now co-encapsulated with magnetic beads coated by the aimed antigen; secreted antibodies bind to the beads if they are functionally active and the droplet content is analyzed, enabling the selection of interesting cells[81]. This platform presents multiple advantages such as the high-throughput analysis of cells but also the suppression of an immortalization step of the immune cells [2], as the decrease in the reactor volume enables the faster obtention of detectable levels of antibodies.

Another screening application demanding single-cell resolution is enzyme directed evolution. Directed evolution mimics the Darwinian evolution process in laboratory conditions: genetic mutations are imposed artificially, the best mutants regarding an aimed phenotype are selected and the process is cycled. This process demands the isolation of mutants into individual reservoirs to link with certainty the phenotype to the genotype of interest. Droplet-based directed evolution has demonstrated its interest, for instance in the case of Agresti *et al.*[69] who demonstrated a 1,000-fold increase in throughput for the directed evolution of the horseradish peroxidase enzyme, and a million fold reduction in cost that is to be related with the low volumes consumed.

In both cases, a final sequencing step is needed to extract the genetic information and know what mutant/cell provided the best enzyme/antibody.

8.1.2 Single-cell transcriptomics

Single-cell transcriptomics present a major interest in the study of heterogeneous tissues such as cancer cells [162, 163], in the inspection of neurologic pathologies [162] or in the study of stem cells[164]. Notably, recent studies have demonstrated that the detection of the co-occurence of several mutations within a single cell is a cancer marker and can head towards a proper treatment[165].

The analysis of single-cell transcriptomics is inherently difficult as a cell contains small amounts of biological material (a few picograms). Conventional transcriptomics techniques rely

2. The immortalization is a process that suppresses cell senescence. There are several immortalization methods, including the coupling of the cell to a cancer cell.

on an averaging over a large population of cells, typically millions, a method that fades out individual heterogeneities[161]. Transcriptomics can be performed either at the level of the protein or at the level of the RNA. Analyzing the RNA content presents the advantage of enabling an amplification by RT-PCR and the obtention of higher concentrations of material. Many protocols were developped in the years 2000, requiring complex multi-step experiments and facing the inadequation between handled volumes with standard methods (micropipeting, patch-clamp,... with volumes of 10-100 μL) and the volume of an individual cell (pL). Microfluidics appeared as an attractive tool for the analysis of single-cell transcriptomics: the reduction of volumes and the enhanced monodispersity of reactors enabled better recovery yields[166], along with higher throughputs and an improved sensitivity. Many studies were carried out on commercial systems (Fluidigm) containing hundreds of valves that can isolate cells, lyse them and assay the expression of multiple genes [166, 167, 168]. More recently, the use of water-in-oil droplets established itself as an appealing technique[169, 164]. It presents multiple advantages: the number of reservoirs can be infinitely scaled up, capture efficiencies are higher and droplets can be sorted at ultra high-throughput based on their fluorescence[82].

In all above analysis (transcriptomics, screening of antibodies, directed evolution), the use of droplets as microreactors provides a physical linkage between the genotype of the encapsulated biomolecule and its corresponding phenotype. However, the analysis of the genotype by a sequencing step after the breaking of the emulsion demands encoding strategies to maintain the link between the genotype and the phenotype.

8.2 Droplet encoding and analysis per sequencing

8.2.1 Droplet encoding

General droplet labeling methods Several encoding strategies have been developed, depending on the aimed decoding step. Optical barcodes are based on dyes or quantum dots[170], with the disadvantage of a relatively limited number of achievable barcodes (<100). Graphical barcodes[171, 172] overcome this limitation by relying on the production of patterned particles that are later injected in the droplet to be labeled. Other methods can be foreseed: spectroscopic reading[173], electronic encoding[174], physical encoding[175]. However, for applications demanding a sequencing step, above encoding methods are not convenient and other encoding methods were developped.

Droplet labeling with DNA barcodes Several sequencing-based barcoding technologies have been developped recently. The common trait in all these techniques is the construction of a large library of particles containing barcodes and their co-encapsulation with the biological material during droplet production (or in the reservoir). There are some variations around this main strategy; barcodes may be made out of elementary DNA units ligated one another, of

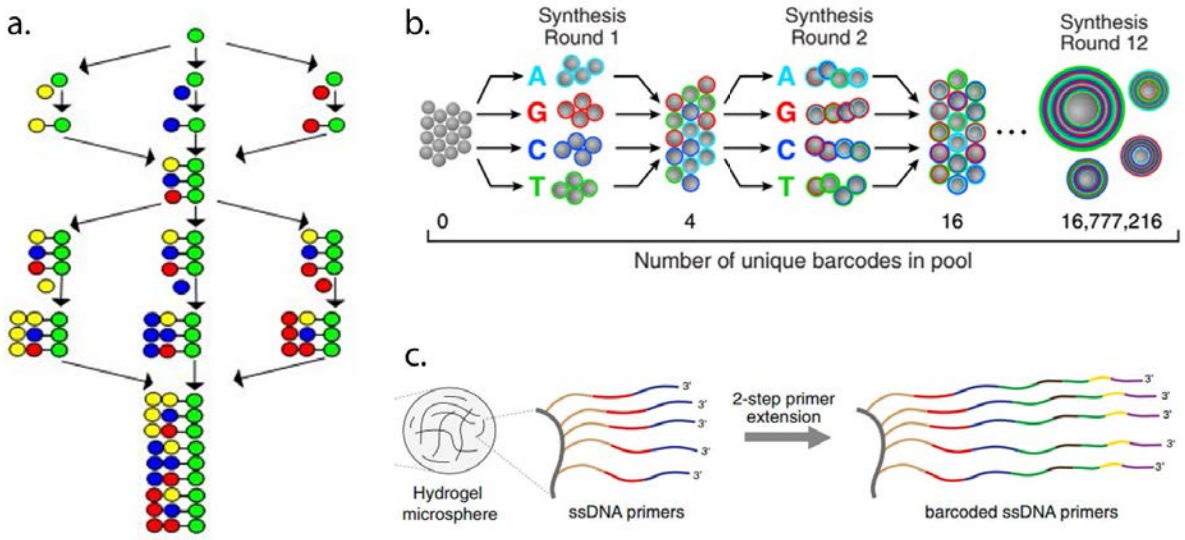

Figure 8.1 – DNA barcodes. a. Split-and-pool strategy. Particles are splitted into wells and addition of an elementary DNA unit is operated (DNA strand or nucleotide). After each addition, the particles are recovered, mixed and re-splitted into wells where the following addition of reagent is performed. If the mixing is efficient, all available barcodes are statistically obtained. Adapted from Wikipedia. b. Example of a split-and-pool strategy using coated beads as particles and nucleotides as elementary DNA unit. Reprinted from [176]. c. Example of a split-and-pool strategy using hydrogel beads as particles and hybridized DNA strands as elementary DNA units. Reprinted from [164]

DNA units hybridized and elongated by an enzyme (Figure 8.1.c) or of the four DNA bases (A, G, C, T) such as pictured in Figure 8.1.b. Particles may be beads coated with primers[176] or hydrogel microspheres[164].

The barcode library is created by split-and-pool synthesis, an approach that was developped in combinatorial chemistry and consists in several rounds of elementary units addition. Particles are distributed in wells and the first elementary unit of the barcode is added. Particles are then recovered, thoroughly mixed and re-splitted into wells where the following set of reagents is added (Figure 8.1.a.). The process is repeated multiple times until the obtention of libraries that may be as large as wanted, with typically millions of barcodes after $\sim$ 10 rounds of split-and-pool. The mixing step is decisive for the obtention of all available barcodes. As the split-and-pool synthesis relies on statistical events, the number of synthesized particles must be much larger than the number of droplets to encode to limit the risk of encoding several droplets with the same barcode. Typically, the number of synthesized particles is taken two orders of magnitude larger than the number of droplets to encode.

This encoding strategy has demonstrated its effectiveness but presents some drawbacks; notably, the construction of the barcodes library takes a day, errors can happen during the co-encapsulation of particles and biological material and few droplets contain both a particle and a cell in the diluted Poisson distribution encapsulation regime. Part of this PhD work focused on the development of a competitive barcoding strategy in which DNA barcodes are built *in situ*.

This strategy should enable a more controlled encoding with a barcoding on-demand, eventually triggered by the analysis of the droplet phenotype. The use of femtoliter droplets provides a wide multiplexing capacity, as multiple encoding droplets can be injected to the picoliter droplet to be encoded without increasing its volume.

8.2.2 Sequencing

In above described applications, the last step of the experiment is the sequencing of biomolecule variants to determine the genome sequence. The following section describes principles of main sequencing strategies.

Historical methods Sequencing methods enable the determination of the succession of nucleotides of a DNA fragment. First methods appeared in the late 1970's, in parallel in Sanger's and Gilbert's teams. Sanger's method[177] relies on the construction of the complementary DNA strand with a DNA polymerase. Four experiments are needed to build the sequence, in which the medium contains the four usual dNTPs and a modified version of one dNTP that act as replication terminator. The DNA replication thus terminates randomly with the incorporation a modified dNTP. If the modified dNTP is adequately diluted, all DNA lengths are obtained statistically. By reproducing the replication for the four different dNTPs and analyzing the results by agarose gel electrophoresis, the sequence can be directly read (Figure 8.2).

Sanger method was rapidly automatized and gels were replaced by capillary separation and laser detection of the fluorophore, empowering the apparition of high-throughput sequencing. Starting from 2000's, and especially with the foundation of the International Human Genome Sequencing Consortium whose aim is to sequence the human genome, a huge reduction in sequencing costs operated; the cost per megabase of DNA sequence followed a Moore's law from 2000 to 2007.

Next-generation sequencing With the thrive of microfluidics (emulsion PCR, microarrays), sequencing methods evolved quickly after 2007, at a pace that exceeded Moore's law by far; the cost per megabase of DNA sequence fell from 700 $ to 0.1$ in four years. Four NGS platforms exist, with their own chemistry, advantages and drawbacks. The 454 platform (Roche), the SOLiD system (Life Technologies), and Ion Torrent (Life Technologies) use emulsion PCR and are respectively renowned for long reads, short reads and its low-cost machine. The leadership is currently owned by the Illumina plateform (Illumina), that specializes in short reads and uses bridge PCR on a glass microchip (*flow cell*) as the amplification method. The Illumina plateform uses a modified version of Sanger sequencing; synthesis of the complementary DNA strand is performed with modified dNTPs that contain a fluorescently labeled terminator. Optical readout is performed, then the terminator is cleaved out to allow the incorporation of the next base. The latest Illumina MiSeq paired-end technology offers 10^7 sequence reads of up to 2*300 bp length in a single run.

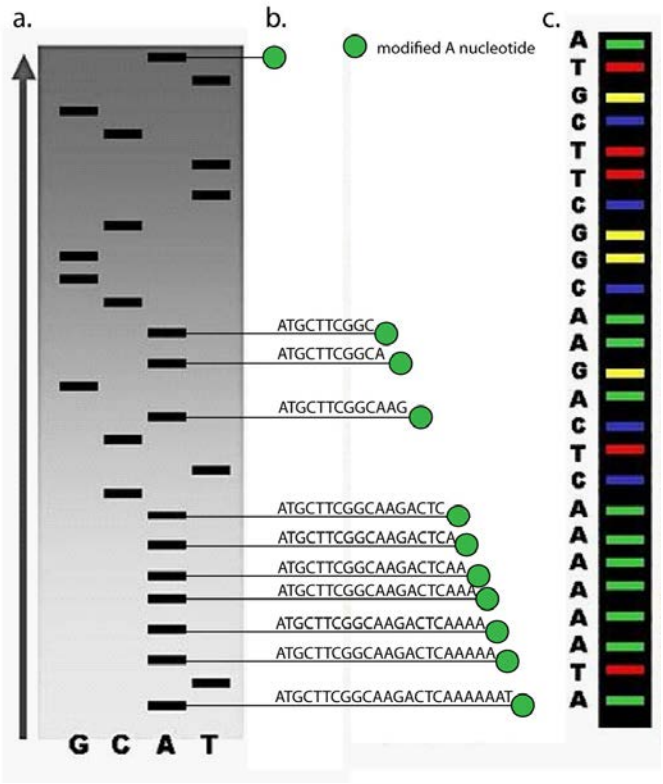

Figure 8.2 – Sanger sequencing method. a. Sequencing gel. Each lane corresponds to an elongation in the presence of a modified dNTP (G, C, A and T). b. Corresponding fragments of DNA in presence of the modified A nucleotide. c. The entire sequence can be reconstructed from the analysis of the four lanes of the gel. Part of the figure was adapted from Wikipedia.

The Illumina next-generation sequencing technology The paired read sequencing process comprises the following steps:

- The sample is prepared : DNA strands need to contain P5 and P7 primers to enable their capture on the flow cell. Tags may be added with the P7 primer to multiplex the analysis: up to 6 samples can be sequenced on the same flow cell. Samples also need to contain binding sites for the sequencing polymerase, SBS3 and SBS12.

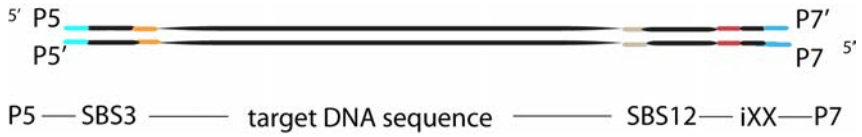

Figure 8.3 – Overview of the sample after its preparation. P5 and P7 primers will enable the sample capture on the flow cell. SBS3 and SBS12 are binding sites for the sequencing polymerase. iXX represents a tag, that can be added to the P7 end to multiplex sequencing experiments on the same flow cell.

- The sample is loaded on the flow cell. Primers hybridize to the lawn of complementary oligos on the surface of the cell. After the DNA capture, a cluster is formed by bridge amplification; similarly to PCR, a series of denaturation and extension cycles are operated on the DNA strand to obtain clusters of copies of the initial DNA strand that will enhance the optical signal. Nicely, the diffusion time of DNA strands towards the oligo lawn is slower than the bridge PCR amplification which guarantees the obtention of clusters of a monoclonal DNA strand.
- Sequencing is performed by incorporation of terminator-bound dNTPs. A first read is performed from SBS3 primer, a second read is performed from the SBS12 primer.
- Reads need to be aligned to reconstruct the genome using bioinformatics tools. A variation of analysis are possible; notably, demultiplexing of the tagged DNAs is implemented at this step.

The huge progresses in sequencing technologies enable to use such methods routinely in laboratory research and encourage the development of encoding platforms such as our droplet printer. In the droplet printer, encoding femtoliter droplets are coupled to picoliter droplets to be encoded. The correct engineering of microfluidic devices requires the understanding of droplets flow under different confinement conditions.

8.3 Hydrodynamics of droplets under different flow conditions

The coupling of droplet scales comes along with complex hydrodynamical questions; flow conditions differ depending on the degree of confinement of the droplet. The understanding of their movement and interaction requires the inspection of droplet hydrodynamics.

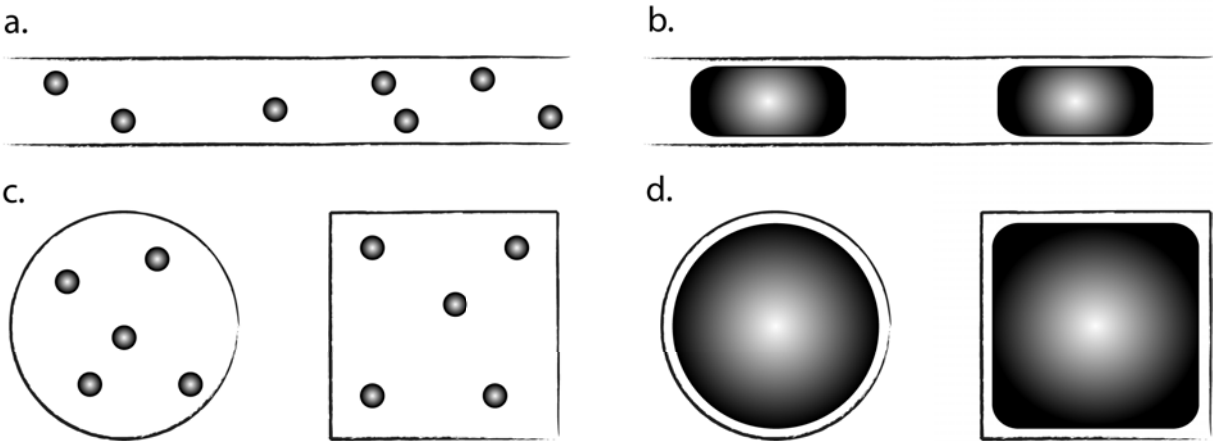

Figure 8.4 – a. Small droplets flow under bubbly conditions. b. Large droplets form slugs separated from the channel walls by a lubricating film. c. Bubbly flows are comparable in circular and square section channels. d. Slug flows vary depending on the channel cross-section because of the presence of gutters.

8.3.1 Hydrodynamics of droplets

The presence of the droplet interface goes along with specific hydrodynamic considerations, notably on boundary conditions, and on the interaction of droplets with the continuous phase flow.

Boundary conditions *Solid-fluid interface*

The presence of a wall imposes a condition of zero-velocity at the solid-fluid interface. This assumption is clear for the normal component of the fluid speed, and corresponds to the fact that the fluid cannot interpenetrate the wall. The tangential component of the fluid can be non-null depending on the slippage properties of the interface, but is considered null in most cases.

Fluid-fluid interface

In the case of multiphase flows, such as water-in-oil droplets, the presence of the droplet interface introduces interfacial tension considerations. For a curved interface, the surface tension expresses itself through a discontinuity of normal stresses at the interface. The pressure is higher inside the curved region, by a factor $\Delta p = \gamma C$ where C is the interface curvature (*Laplace law*). Tangential stresses are related to surface tension gradients along the interface, that can appear from temperature variations or non-uniform surfactant molecules concentrations. In the absence of surface tension gradient, tangential stresses are continuous through the droplet interface. The velocity is thus continuous at the droplet interface.

Droplet transport In multiphase flows, droplets are advected by the continuous phase inside the channel with formation of a lubricating film between the droplet and the channel wall. Depending on the relative size of the channel and of the droplet, several flow conditions exist.

For droplets smaller than the channel size, droplets are spherical and flow under bubbly flow conditions (Figure 8.4.a.). They are subjected to local streamlines which means, typically, that their speed is larger in the center of the channel than close to the walls.

On the contrary, if the droplet is larger than the channel size, it occupies almost all the channel section and forms a slug (Figure 8.4.b). In this case, droplets move at a speed averaged over the channel section. The slug speed slightly differs from the average speed of the continuous phase by a factor[178]:

$$\frac{v_{droplet} - v_c}{v_{droplet}} \sim -Ca_d^{-1/3} \tag{8.1}$$

in a rectangular channel, where we denote $v_{droplet}$ the droplet speed, v_c the continuous phase speed and Ca_d the capillary number based on the velocity of the droplets (Figure 8.4.d). This observation is however wrong in circular channels where slugs flow faster than the continuous phase, with a velocity difference that scales like:

$$\frac{v_{droplet} - v_c}{v_{droplet}} \sim Ca_d^{2/3} \tag{8.2}$$

The diversity of degrees of confinement and flow conditions results in a wide variety of behaviors; coupling of confined and unconfined flows result in complex hydrodynamic questions that are inspected thereafter.

8.3.2 Coupling of confined and unconfined flows

Relative speed of droplets and slugs In most devices described in the continuity of this work, small spherical droplets and large slugs flow in the same square channel. The question of their relative speeds needs to be addressed. The no-slip condition at the channel walls results in the apparition of a Poiseuille flow, with a maximum velocity at the center of the channel. In order to simplify the analysis, we assume that the channel is circular, which corresponds to neglecting the square-section gutters. The Poiseuille flow in a circular channel of radius a can be expressed as, in cylindrical coordinates:

$$v(r, \theta, z) = v(r) = v_{max}(1 - \frac{r^2}{a^2}) \tag{8.3}$$

$$v_{max} = -\nabla p \frac{a^2}{4\eta} \tag{8.4}$$

In a first approximation, the slug's speed can be assessed by the ratio of the flow rate over the channel cross-section, corresponding to a speed $v_{slug} = v_{max}/2$. The variations announced in paragraph 8.3.1 are supposed negligible, in agreement with [179][131]; in the rectangular case, variations are below 6% for typical capillary numbers $10^{-6} < Ca_d < 1$.

We denote R the droplet radius and d the position of the droplet regarding the channel center (see Figure 8.5.a.). In the polar coordinate centered at the droplet location, the flow field can be expressed like:

$$r^2 = (d + r_1 cos\theta_1)^2 + r_1^2 sin^2\theta_1 = d^2 + 2dr_1 cos\theta_1 + r_1^2 \tag{8.5}$$

$$v(r) = v(\sqrt{d^2 + 2dr_1 cos\theta_1 + r_1^2}) \tag{8.6}$$

The speed of a droplet of radius R located at a distance d from the channel center is thus:

$$v_{droplet} = \int_0^R \int_0^{2\pi} v_{max}(1 - \frac{d^2 + 2dr_1 cos\theta_1 + r_1^2}{a^2}) d\theta_1 dr_1 \tag{8.7}$$

After integration, the ratio of the droplet to the slug speeds is a function of d/a and R/a:

$$\frac{v_{droplet}}{v_{slug}} = 2[1 - (d/a)^2 - (R/a)^2] \tag{8.8}$$

Figure 8.5.b shows the variation of the speed of the droplet as a function of its distance to the center of the channel d/a extracted from equation 8.8. Each color corresponds to a different droplet size R/a. Large droplets ($R/a > 0.3$) are always faster than the slug and are expected to pair behind the preceding slug. Small droplets ($R/a < 0.3$) can be faster or slower than the slug depending on their lateral position.

Flow fields induced by the droplet interface The presence of the droplet interface modifies the typical Poiseuille flow field, by preventing the circulation of immiscible fluids through the interface. As explained earlier, the slug either flows slightly faster or slower than the continuous phase depending on the geometry (circular or rectangular). This implies that the liquid particles catch up with one of the slugs and have to change direction to avoid the slug interface. The presence of the slug interface creates recirculation zones and stagnation points.

The above discussion on liquid particles can be adapted to small droplets. Indeed, in the case ($R/a < 0.3$), if the droplet is initially faster than the slug, it catches up the slug, is deflected towards the wall by recirculation rolls and finally gets slower when feeling the local Poiseuille components near the wall. The droplet remains against the wall until reaching the following slug, that brings it back in the center of the channel etc. Figure 8.6.a. represents a timelapse

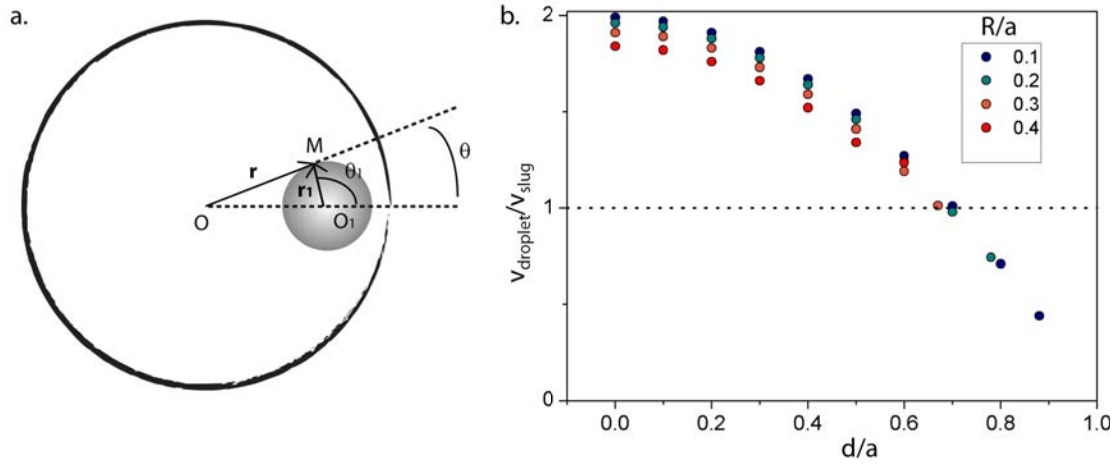

Figure 8.5 – a. Cross-sectional view of the system, with the representation of the two polar coordinates involved in our calculation. b. Variation of the speed of the droplet as a function of its distance to the center of the channel d/a extracted from equation 8.8. Each color corresponds to a different droplet size R/a. Large droplets ($R/a > 0.3$) are always faster than the slug and are expected to pair behind the preceding slug. Small droplets ($R/a < 0.3$) can be faster or slower than the slug depending on their lateral position.

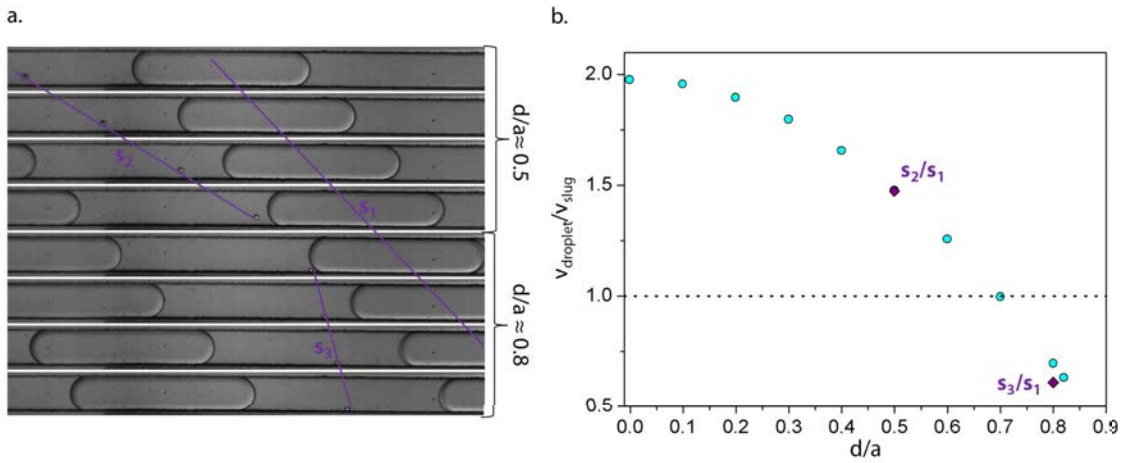

Figure 8.6 – a. Time lapse of droplet and slug co-flow. The slug flows at constant speed; the droplet is initially faster than the slug ($d/a \sim 0.5$) but is deflected by the slug interface and gets slower against the wall ($d/a \sim 0.8$). Slopes have been measured to evaluate droplet and slug speeds. b. Droplet trajectory follows the blue curve from $d/a \sim 0.5$ to $d/a \sim 0.8$. Experimental data points perfectly fit the theoretical curve.

of a droplet traveling faster than the slug, that is deflected by the slug interface and gets slower against the wall. Slopes have been represented and measured to assess droplets speeds.

Figure 8.6.b. represents the variations in d/a of the droplet; initially, the droplet is faster than the slug ($d/a \sim 0.5$) but it gets slower when enclosing the wall ($d/a \sim 0.8$). Experimental data points are represented by violet diamonds and perfectly fit the theoretical data curve.

A proper droplet pairing is thus easily achievable for large droplets ($R/a > 0.3$); large droplets are always faster than slugs and hydrodynamically pair with their preceding slug. However, if we try to limit the injected volumes and use smaller droplets ($R/a < 0.3$), pairing considerations will be more delicate.

We have presented several biological applications that benefit from droplet-based microfluidics technologies but demand an encoding of cells of interest for a final sequencing step. In the following chapter, we present a new encoding platform, so called droplet printer, that enables an encoding on demand with DNA barcodes readable per sequencing. For the development of robust devices, we used above considerations and either benefited from hydrodynamic pairing (case $R/a > 0.3$) or applied external forces to avoid complex hydrodynamical interrogations.

Chapter 9

Direct droplet labeling with oligobarcodes fabricated *in situ*

In this chapter, we introduce a method to produce on-chip DNA barcodes that can be read through sequencing. Femto-drops containing oligomers are generated on demand via pneumatic valves and combinatorially injected into the pico-drop library to create unique DNA barcodes. We first present the interest of our method compared to the state of the art. A second part of this chapter concentrates on the development of the droplet printer platform through three cornerstones: the production of multiple droplets on-demand, their pairing and their releasing in the droplet to be encoded. A last part of this chapter presents a biological proof of concept of the interest of the platform.

9.1 Interest of our method compared to the state of the art

9.1.1 State of the art

As introduced in Chapter 8.2.1, several sequencing-based barcoding technologies have been developped recently. The common trait in all these techniques is the split-and-pool construction of a large library of particles containing barcodes and their co-encapsulation with the biological material during droplet production[164, 176].

This encoding strategy has demonstrated its effectiveness but presents some drawbacks; first, the construction of the barcodes library takes an entire day, with a number of synthesized particles that is taken two orders of magnitude larger than the number of droplets to encode to ensure unicity of the barcoding. Moreover, the number of barcodes needed is artificially inflated by two factors. First, the encapsulation of biomolecules in a Poisson dilute regime results in a high percentage of empty droplets, typically 90 % and a large portion of barcode particles is thus encapsulated into empty droplets. Secondly, for most applications, the resolution of the

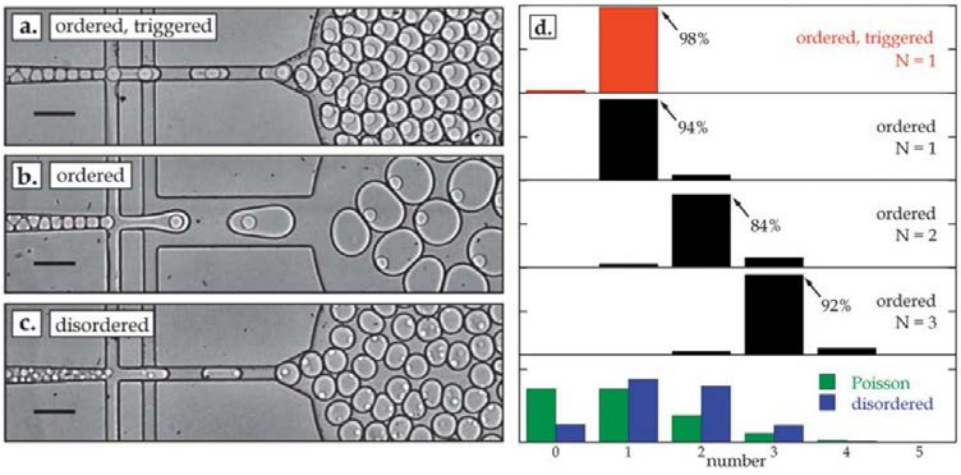

Figure 9.1 – Abate *et al.* could beat Poisson distribution by using closely packed ordering of hydrogel beads. Photomicrograph of the encapsulation process utilizing close-packed ordering and geometrical droplet triggering (a.), close-packed ordering (b.) and disordered encapsulation (c.). The scale bar is 75 μm. d. Probability distributions in the three above mentionned cases, as shown for one, two and three particles in the ordered encapsulation. Figure and caption adapted from [180]. Even in this improved version, the coupling of the encapsulation of cells in the diluted regime to the addition of barcoding particles fill only 8 % of droplets.

analysis does not need to be infinite; cells/enzymes can be gathered into bins according to their expressed phenotypes. A binning by 10 - 20 already gives a proper resolution and actually meets the limits of the number of fluorescence thresholds that can be distinguished. One can question the interest of a larger number of bins.

Researchers are investigating ways to improve the bead barcoding technology. The co-encapsulation of cells and barcodes is performed under dilute conditions for the cells and close-packed ordering for the barcode particules [180] (Figure 9.1). The close-packed ordering helps the obtention of one barcoding particule per droplet. However, even with this improvement, the co-encapsulation of a diluted solution of cells and of a barcoding particle still corresponds to only 8% of droplets containing one cell and one barcode, which means that more than 90 % of barcodes are useless. Additionnally, Figure 9.1.a-c. shows that the size of droplets varies as researchers try to obtain different encapsulation efficiencies. The coupling of encapsulation parameters and droplet size is to be avoided.

All these considerations led researchers to look for competitive encoding strategies. One of them would be the construction of DNA barcodes *in situ* by injection of elementary DNA units into an already formed droplet library. This strategy should enable a more efficient encoding and opens up new possibilities; for instance, droplet barcoding could be triggered by the analysis of the droplet phenotype, enabling a more clever encoding.

9.1.2 Interest of our method

We envision the construction of a platform that enables the *in situ* encoding of droplets by injecting elementary DNA units of the barcodes on-demand. A scheme of the *droplet printer* is represented in Figure 9.2 in the case of 8 injectors controlled by 8 valves. The library of droplets to be encoded is driven in a straight channel comprising side injectors that contain the elementary DNA units. Small droplets are injected on-demand as the droplet to be encoded passes by. Injection of the DNA units in the droplet is operated by electrocoalescence in a later part of the device.

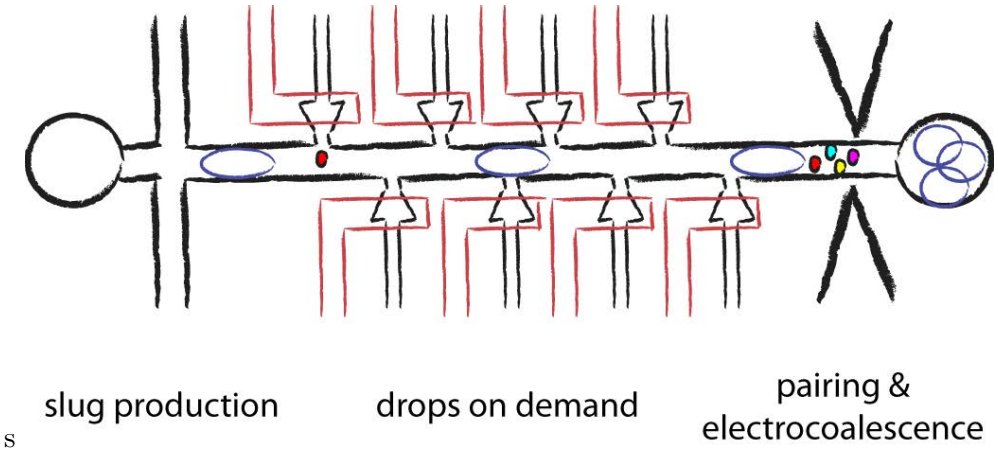

s

Figure 9.2 – Scheme of the droplet printer used thereafter.

Considering the predominance of engineering issues at the femtoliter scale, which resolving is not the aim of a PhD work, a scaled-up version of the printer was created, encoding nL slugs with pL droplets. Physical studies are performed both at the femtoliter/picoliter and picoliter/nanoliter scales but the biological proof of concept is shown in the case of 8 picoliter injectors.

The development of a robust droplet printer requires several achievements: an efficient and synchronized injection of multiple droplets containing the DNA units, their pairing with the slug library and finally, their injection into the slugs. Those three cornerstones are studied thereafter.

9.2 Injection of multiple femtoliter droplets on demand

9.2.1 Experimental protocol

Choice of the drop-on-demand method As explained in Chapter 3, several DoD techniques were successfully miniaturized to the femtoliter scale. The project was oriented towards the pneumatic actuation that had demonstrated the more robustness. With this choice, the frequency of injection is limited to a few 10 Hz, a frequency which is enough for a proof of concept but should be later engineered towards kHz rates.

The pressurization of each pneumatic actuator is monitored by a solenoid valve (LHD A0523112H, The Lee Company) controlled through a National Instrument NI-S 6008 card and a custom Labview software. The Labview software defines an array of True/False states that correspond to the open/close states of the eight solenoid valves. Every 10 ms, a 1D array containing the states of the 8 valves is sent to the NI card. The card translates this sequence into on/off voltages that are applied to the solenoid valves. Without voltage, valves are pressurized with a reference pressure P1; energized valves switch to pressure P2. The maximum pressure difference that can be applied is 2 bars. The opening and closing time of those valves are respectively of 3 and 4 ms according to the constructor, with a total actuation time faster than the software time step.

Softwares for the injection of multiple femtoliter droplets on demand Several Labview softwares were developped depending on the aimed injection procedure. For preliminary experiments, each valve state would be defined by an alternance of open and closed time steps. This monitoring strategy becomes tedious as soon as a larger number of valves needs to be controlled and synchronized. Indeed, droplets travel along the main channel at a speed u and a synchronized injection demands a delay between consecutive injectors $\tau = d_{inj}/u$ if d_{inj} is the distance between the two injectors. Another software was developped that takes as input the droplets speed and their production frequency and controls the delayed sequential injection of all available barcodes, either in a uniform distribution or in a gradually varying form (one barcode ①, two barcodes ②, three barcodes ③, etc).

9.2.2 Results

Some examples are depicted in Figure 9.3 for the synchronized injection of 2 or 3 different reagents in the upscaled pL-nL device.

Labview softwares enable a synchronized injection of droplets by taking the slug speed and the slug production frequency as input.

9.3 Pairing and releasing of multiple droplets into a slug

After the injection step, droplets and slugs are driven downstream in the main flow channel until the electrocoalescence area under different confinement conditions. In this section, we study their hydrodynamic interaction and the electrocoalescence process.

9.3.1 Design of the chip

Hydrodynamic considerations To limit the final volume of the slug despite multiple injections, droplets volume is restricted and droplet size observe the condition $R/a < 0.3$. In

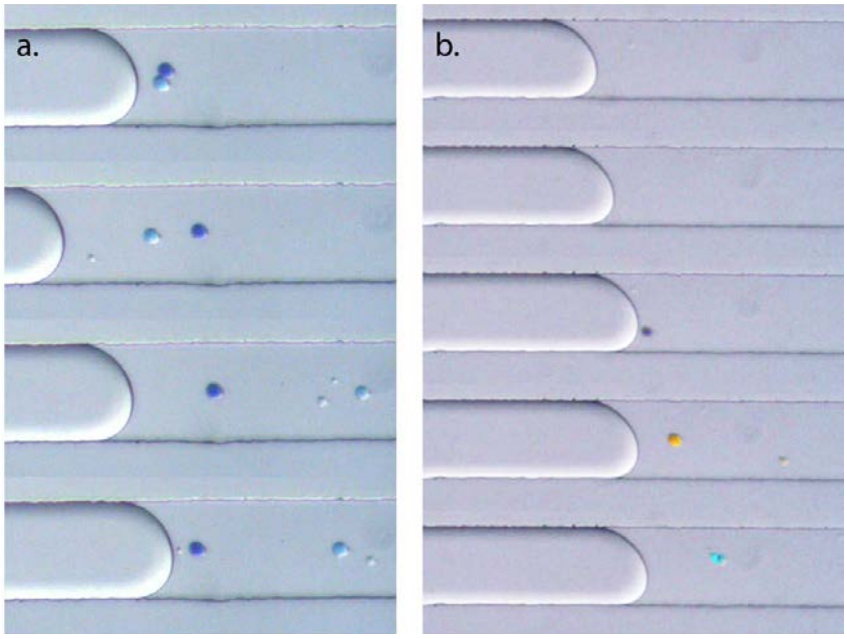

Figure 9.3 – Examples of synchronized injections of a.2 or b.3 different reagents. Each image corresponds to a different slug. The channel width is 125 μm.

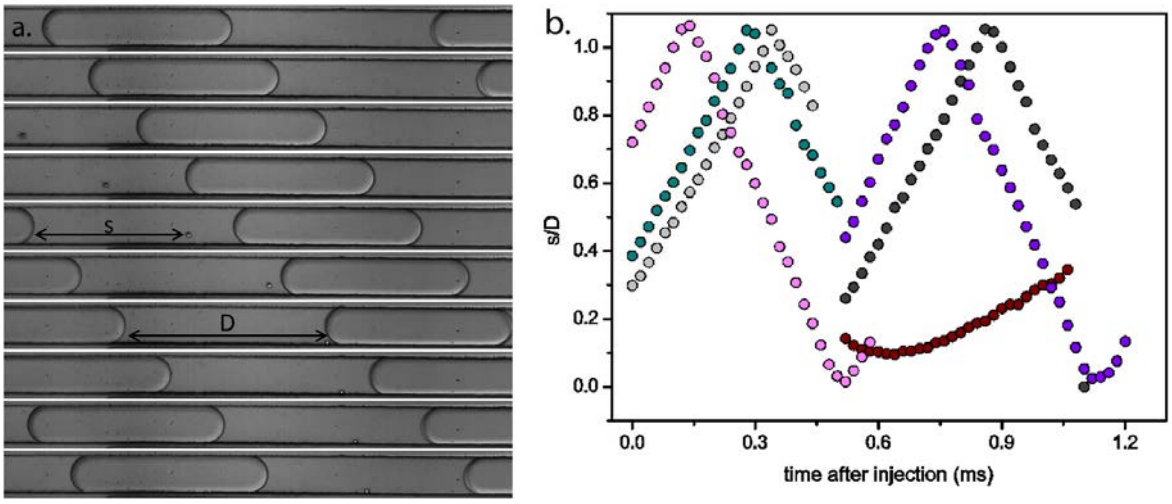

Figure 9.4 – Droplets traffic in the main flow channel. a. Time lapse of a representative example in which a barcoding droplet follows the streamlines between two consecutive slugs. The continuous phase flows from left to right. b. Evolution of the distance between the droplet and the preceding slug as a function of time. Each color represents a different droplet. s/D varies between 0 and 1, corresponding to a contact with the preceding and following slug.

agreement with chapter 8.3.2, droplets act as passive tracers and follow the streamlines between consecutive slugs. Figure 9.4.a. represents a time lapse of a barcoding droplets flowing between two slugs. The evolution of the distance between the droplet and the following slug s was measured as a function of time and is represented in Figure 9.4.b, where each color represents a different droplet. s/D varies between 0 and 1, corresponding to a contact with the preceding and following slug and hydrodynamical pairing has to be discarded from injection strategies. When multiple barcoding droplets are injected in between two consecutive slugs, collision events are observed in some experiments that temporarily modify droplets trajectory and further complexify the hydrodynamics of droplets.

The robust injection of droplets into the slug thus demanded active strategies that overcome hydrodynamic issues. As already showed in the Chapter Manipulation of droplets with electric fields (chapter 5), the presence of a non-uniform electric field deflects droplets towards high-field areas. We envisioned that the imposition of an electric field could trap barcoding droplets between electrodes, guaranteeing a proper synchronization and merging with the following slug. COMSOL simulations were performed to verify the feasibility of this pairing and releasing strategy.

COMSOL simulations 2D COMSOL simulations were performed without flow. A droplet of varying size and lateral position is placed in between the electrodes, surrounded by two slugs with s/D ranging from 0 to 1. Slugs are assumed to travel from bottom to top and the small droplet is placed slightly ahead of the electrodes to be able to assess the direction of the electric force along the flow direction. The electric potential is calculated by imposing a voltage (600-1000 V) on one electrode and neutrality to the other one. The 2D DEP force is assessed by following equations:

$$F_{DEP,x} \sim \pi \epsilon_0 \epsilon_r R^2 E_x . \nabla_x E_x \tag{9.1}$$

$$F_{DEP,y} \sim \pi \epsilon_0 \epsilon_r R^2 E_y . \nabla_y E_y \tag{9.2}$$

The resulting lateral force on the droplet is estimated by integrating $F_{DEP,x}$ over the droplet surface and the longitudinal force is estimated by integrating $F_{DEP,y}$ over the droplet surface.

Figure 9.5 represents the electric potential simulated by imposing a 600 V tension, in the case of a laterally centered droplet (Figure 9.5.a.) and of a deflected droplet (Figure 9.5.b.). The gradient of the electric potential along x is pictured by an arrow surface. The variation of the DEP force x component integrated over the droplet surface as a function of s/D is depicted in Figure 9.5.c. in the case of a droplet located against the wall (orange circles) or at the center of the channel (dark cyan circles), with $R/w = 0.1$. To avoid numerical issues related to the meshing and dielectric discontinuity at the channel wall, the droplet is located 1 μm away for the wall in the deflected case. The same graph in the case of the trapping force is represented in Figure 9.5.d.

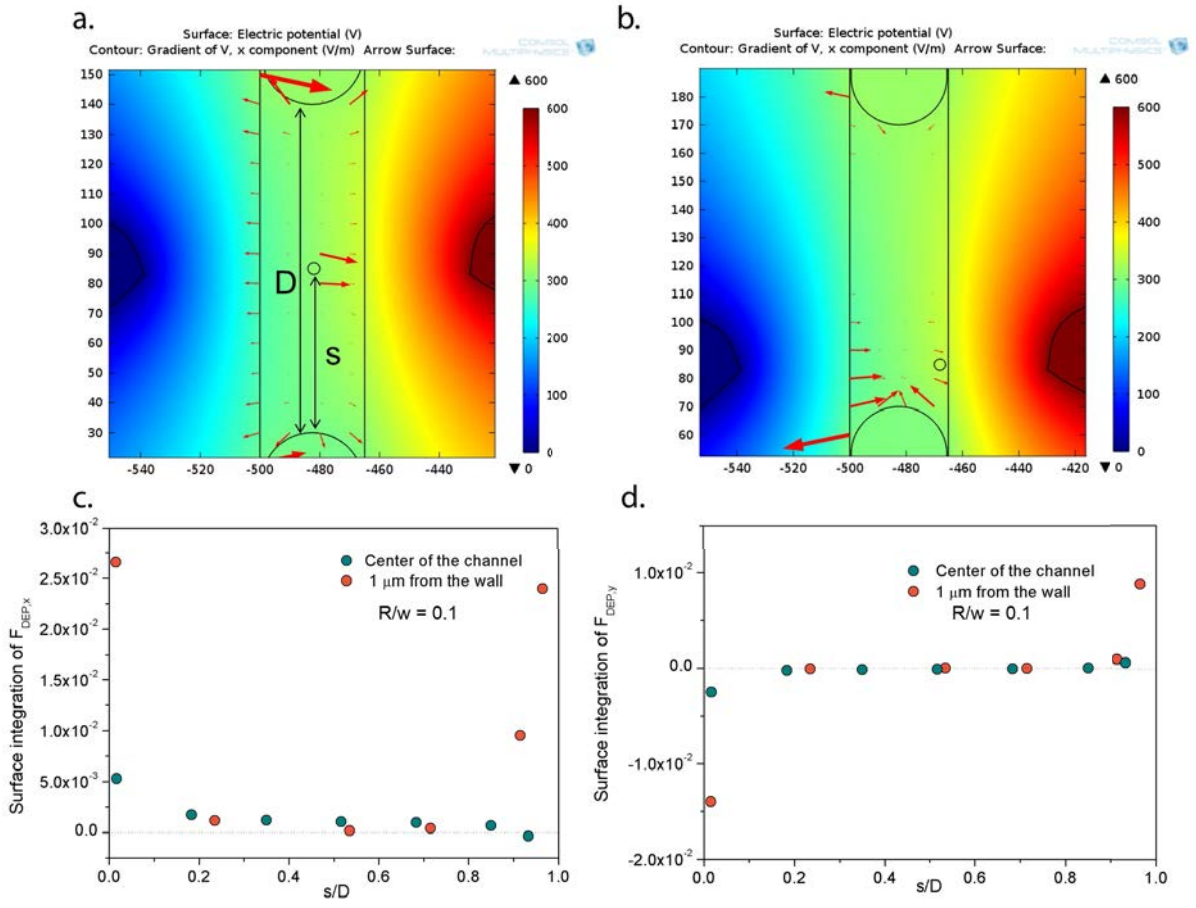

Figure 9.5 – a. Electric potential and its gradient on x for a centered droplet with $R/w = 0.1$, $s/D = 0.5$. b. Electric potential and its gradient on x for a droplet along the wall with $R/w = 0.1$, $s/D = 0.15$. c. x component of the DEP force calculated using formula 9.1 for a centered droplet (dark cyan circles) and a droplet located 1 μm from the wall (orange circles), with $R/w = 0.1$. The x component of the DEP force is always positive for a droplet against the wall and remains positive as long as $s/D < 0.9$ in the centered case. d. y component of the DEP force calculated using formula 9.2 for a centered droplet (dark cyan circles) and a droplet along the channel wall (orange circles), with $R/w = 0.1$. The y component of the DEP force is negative for $s/D < 0.8$, corresponding to a trapping effect (the droplet was positioned slightly ahead of the electrodes); coalescence errors could happen if small droplets are close to the preceding slug when entering the electrocoalescence area.

The x component of the DEP force is always positive for a droplet against the wall and remains positive as long as $s/D < 0.9$ in the centered case. Droplets are thus always deflected towards the positive electrode, with the exception of a droplet centered in the channel and very close to the preceding slug, a not much likely situation. The y component of the DEP force is negative for $s/D < 0.8$ corresponding to a trapping effect as long as $s/D < 0.8$; coalescence errors could happen if small droplets are close to the preceding slug when entering the electrocoalescence area ($s/D > 0.8$).

To assess a value of the 3D DEP force, simulated data can be multiplied by R; DEP y components are in the order of 10^{-12} to 10^{-8} N which is to be compared to the Stokes force. Reynolds numbers are in the range 10^{-5} to 10^{-3} which corresponds to $F_{Stokes} = 6\pi\eta Ru$ values in the range 10^{-14} to 10^{-12}N. The enclosing of the droplet to the wall further reduces the Stokes force by a factor 2 according to Figure 8.5. Simulations confirm the possibility of trapping droplets by dielectrophoresis.

Those simulations provided encouraging results of the possibility of trapping small droplets and releasing them in the following slug. Experiments were carried out to verify simulated results.

9.3.2 Pairing and releasing by imposition of an electric field

Experimental protocol Two electrodes are added around the main flow channel at a distance equal to the minimal resolution of the soft lithography mask (30 μm in the pL-nL device, 6 μm in the fL-pL device). Electrode channels are filled with a conductive buffer (NaCl, 189 g/L) and connected to a voltage amplifier through an Electrowell (Fluigent). Femtoliter droplets are produced on demand with a pneumatic valve. An increasing number of femtoliter droplets (1-4) is injected upon arrival of the picoliter slug. Applied voltage varries from 600 to 800V, at a frequency of 1.5 kHz.

Results and discussion Experiments confirmed expected behaviors: when barcoding droplets arrive in the electric field area, they are deflected towards the charged electrode and trapped until their merging with the following slug (Figure 9.6.a). The trapping process is not hindered by the presence of multiple droplets. Figure 9.6b-c. show different observed behaviors in the electrocoalescence area. No matter the position of droplets before their arrival in the electrodes zone, they get trapped along the AC electrode until coalescing with the following slug. Multiple droplets align into chains and merge with the slug, with (9.6.b) or without (Figure 9.6.c) merging first together.

At intermediate electric fields, we observed that the droplet trapping is sometimes perturbed by the arrival of the slug but this process is easily contained by using higher voltages (> 700 V).

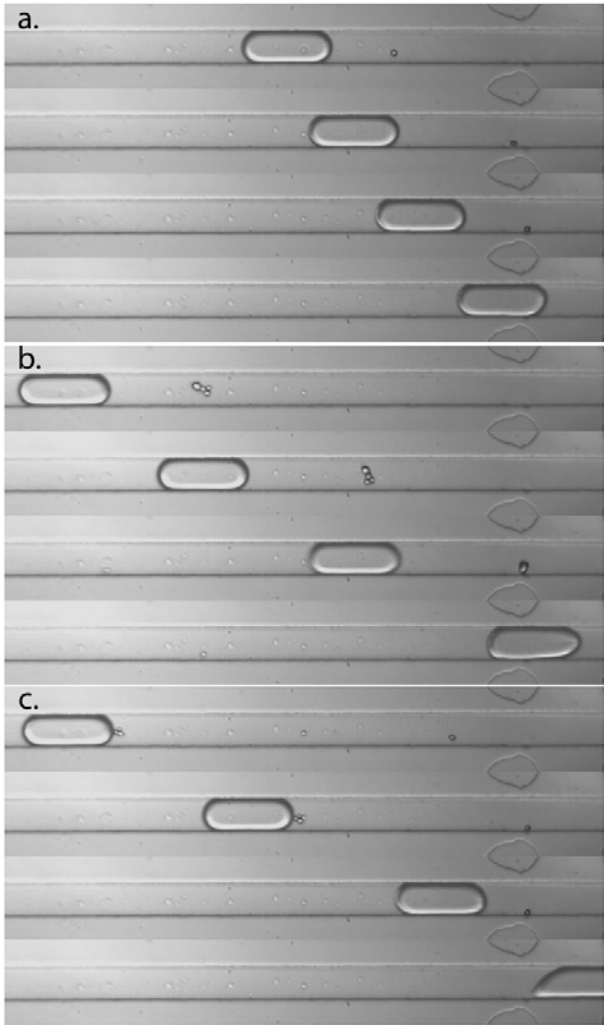

Figure 9.6 – Time lapse of different behaviors observed during the electrocoalescence process. (700V, 1.5 kHz). a. A single droplet deflects towards the AC electrode and gets trapped until coalescing with the following slug. Time step 0.2s. b. Four droplets align into chains under the AC field, then coalesce together and get trapped until coalescing with the following slug. Time step 0.4s. c. A single droplet stays trapped for $\sim$ 1 second before coalescing with the following slug. The three other droplets stay paired with the slug until coalescing under the AC field. Time step 0.4s.

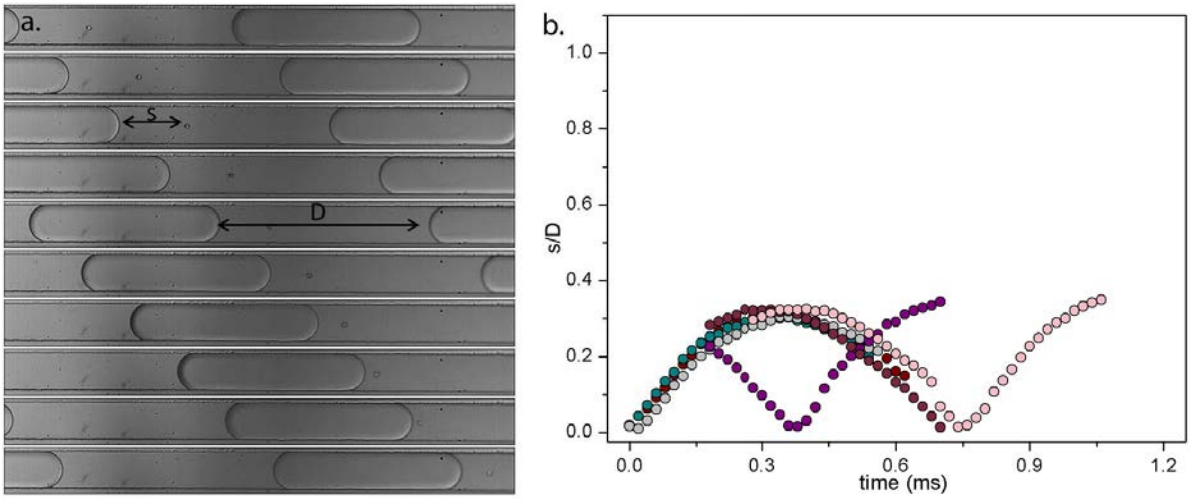

Figure 9.7 – Droplets traffic in the main flow channel after imposition of an electric field. a. Time lapse of a representative example in which a barcoding droplet follows the streamlines between two consecutive slugs. The continuous phase flows from left to right. b. Evolution of the distance between the droplet and the preceding slug as a function of time. Each color represents a different droplet. s/D varies between 0 and 0.4; the droplet remains close to the following slug.

Pairing and releasing is performed very robustly by imposition of large voltages (> 700V). All analyzed droplets were correctly injected in the following slug.

Digression - an interesting hydrodynamic behavior in presence of an electric field
The imposition of an electric field results in an alteration of above mentioned hydrodynamic considerations far upstream the electrodes area. Small droplets no longer follow the streamlines between consecutive slugs but stabilize a few radii ahead of the following slug, as pictured in Figure 9.7. s/D varies between 0 and 0.35, corresponding to a pairing of the droplet with the following slug. The interplay of attractive electrostatic forces and hydrodynamic forces sets an equilibrium position that improves the pairing of droplets with their following slug, until leading to their merging in the electrodes area.

Interestingly, electrostatic effects are observed several minutes after the field is turned off. Leaking of charges in nonpolar liquids such as the fluorinated oil is expected to be much faster than the timescales involved herein (milliseconds). However, recent studies have demonstrated that inverse micelles can become charge carriers in nonpolar liquids[181, 182]. In nonpolar liquids, free charges cannot exist because the electrostatic attraction is always higher than the kinetic energy that could separate charges and their countercharges over long times. The interplay of those two competing forces defines the Bjerrum length, $\lambda_B = |Z_1 Z_2 q_e^2/4\pi\epsilon_0\epsilon_c kT|$, where Z_1 and Z_2 are charges valencies and q_e is the elementary charge. The Bjerrum length represents the distance that must separate charges and their countercharges to avoid them from binding electrostatically irreversibly. Without surfactant, nonpolar liquids have large Bjerrum lengths which correspond to a low probability of finding free charges. The presence of surfactants

at high concentration goes along with the formation of micelles that may maintain a minimal distance between charges and their coutercharge and prolong electrostatic effects. Timescales involved in such experiments range from milliseconds to hours[183], which is compatible with our observations.

This side behavior provides further more robustness to the pairing and releasing operation as droplets are closer to their following slug and injection errors predicted by COMSOL in the case $s/D > 0.8$ are avoided. Droplets are reproducibly paired and injected into the following slug. The obtention of a robust platform encouraged the realization of a biological proof of concept of the droplet printer platform.

9.4 Construction of barcodes *in situ* on a 8 injectors / 8 valves design

The construction of barcodes *in situ* on an 8 injectors / 8 pneumatic valves design was foreseed as a proof of concept of the potentials of our platform. The experimental protocol is described along with some preliminary results. We apologize for the lack of final results as samples are currently under sequencing and analysis steps.

9.4.1 Definition of the elementary DNA units

Eight elementary double strand DNA units are used to build barcodes: A_0, A_1, B_0, B_1, C_0, C_1, D_0, D_1. Sequences of elementary units single strands are summarized in Appendix D; double stranded DNA units are built by hydridization of top and bottom single strands.

Those elementary double strand DNA units can be ligated together by a T7 ligase that is contained in the slug library to be encoded. The design of the elementary DNA units ensures that units A's can only be ligated to units B's, units B's to units C's and units C's to units D's. The final barcode is an $ABCD$ double stranded DNA assembly; there are 16 combinations with this design. Figure 9.8 represents the droplet printer in an eight injectors configuration. Slugs containing the ligase are injected with four elementary DNA units (one A, one B, one C and one D) via electrocoalescence. Ligation of the elementary units is then performed at room temperature.

9.4.2 Experimental protocol

Common protocol Barcode elementary units solutions are prepared by mixing 5 μL of $X_{y,bot}$, 5 μL of $X_{y,top}$ and 10 μL of water, at a final concentration of 400 μM. The droplet printer is initialized by filling the control channels with DI water. This step prevents air from diffusing

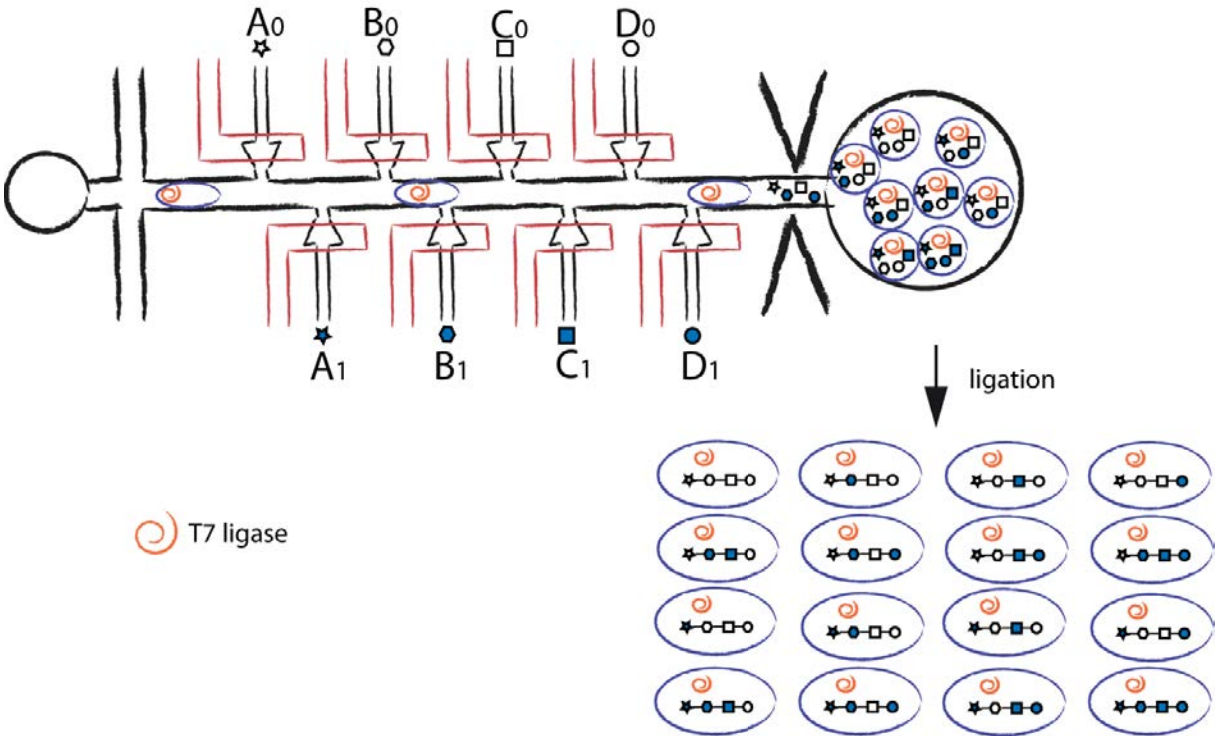

Figure 9.8 – Scheme of the droplet printer in an 8 injectors configuration. The slug library contains the ligase that can ligate elementary A, B, C, D DNA units. Each barcode is made of 4 elementary units (one A, one B, one C and one D); 16 barcodes can be produced in this configuration

through the porous PDMS membrane into the flow channels. Salt water is injected into the electrodes (AC field and ground electrode at the output). Oil is injected in the flow channel to ensure proper wetting properties, then the eight DNA elementary units are injected with open valves. The output tube is plugged to avoid later hydrodynamic resistance changes that would perturb the pressure equilibration. This does not trouble the encoding process as the AC field is not turned on at this step, and no barcode can be created without the enzyme contained in the slug library. Valves are actionated with an opening time of 10-30 ms depending on the experiment and DNA unit injectors pressures are fine-tuned to adjust the injected volume. Pictures of the setup are represented on Figure 9.9.

The slug solution is prepared and kept into ice during the entire printing process. The slug production is started and we measure the production frequency and the slug speed to implement those parameters into the Labview software and synchronize the barcodes injection. The encoding can then begin; valves are momentarilly closed, the AC field is turned on and the barcodes injection is launched. After encoding, the emulsion is kept at room temperature for 15 minutes to ensure the ligation is completed. The emulsion is then stored in the fridge until further analysis.

Composition of the slugs Two experiments were carried out; the first one aimed at verifying that barcodes were efficiently ligated in droplets (Figure 9.10). To do so without expensive

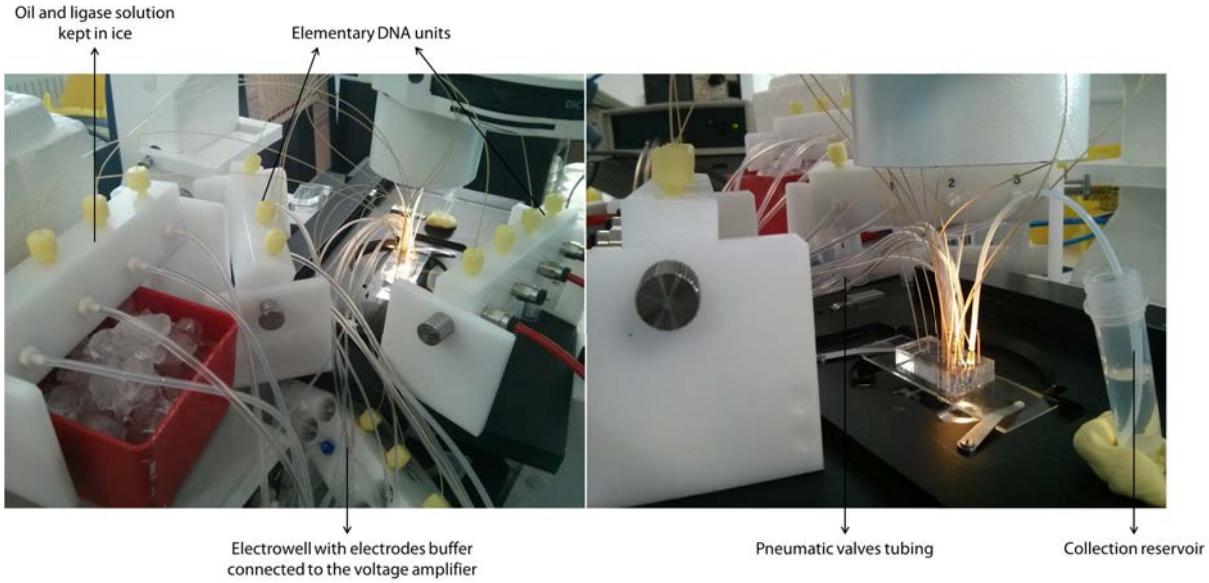

Figure 9.9 – Droplet printer setup. The ligase solution is kept in ice during the entire encoding process. Electric fields are applied through an Electrowell (*Fluigent*), a device in which Pt electrodes are immerged into a salty buffer injected in the micro-chip.

sequencing steps, an agarose gel electrophoresis analysis was envisioned. PCR primers were added to the slug solution to enable the PCR amplification of the barcode library and the obtention of concentrations suitable for the agarose gel electrophoresis experiment. The slug solution composition is, in this case: 20 μL of T7 enzyme buffer, 4 μL of SBS12 primers at 4 μM, 4 μL of SBS12as primers at 4 μM, 4 μL of SBS3 primers at 4 μM, 4 μL of SBS3as primers at 4 μM and 4 μL of T7 ligase. After droplets encoding and the ligation step, the emulsion is broken by addition of perfluoroctanol and purified on an AMPure kit as explained in the Experimental chapter. The PCR is performed with P5 and P7 primers and a Phusion 2 enzyme: initial denaturation (98 ˚C, 30”), 20 cycles of denaturation (98 ˚C, 10”), annealing (58 ˚C, 30”), elongation (72 ˚C, 30”) and the final elongation step (72 ˚C, 2’).

Latter experiments were performed without sequencing primers to be able to tag the different experiments and sequence them in a single round (Figure 9.10). The slug solution only contains 20 μL of T7 enzyme buffer, 16 μL of water and 4 μL of T7 ligase. After the encoding step, slugs are incubated 15 minutes at room temperature and the emulsion is broken. Small non-ligated DNA fragments (<100 bp) are removed by purification on an AMP Pure kit. A tagged SBS3 and the SBS12 end are ligated by a T7 ligase 30 minutes at room temperature. The sample is purified to suppress remaining tags on an AMPure kit. 6 cycles of PCR are performed to make sure we obtain detectable levels of barcodes, with the same protocol than above. The number of PCR cycles is limited to avoid the apparition of PCR artifacts.

Four encoding experiments were conducted; two providing a uniform distribution of barcodes (tags i00 and i03) and two providing a gradually increasing distribution of barcodes (tags i09 and i25).

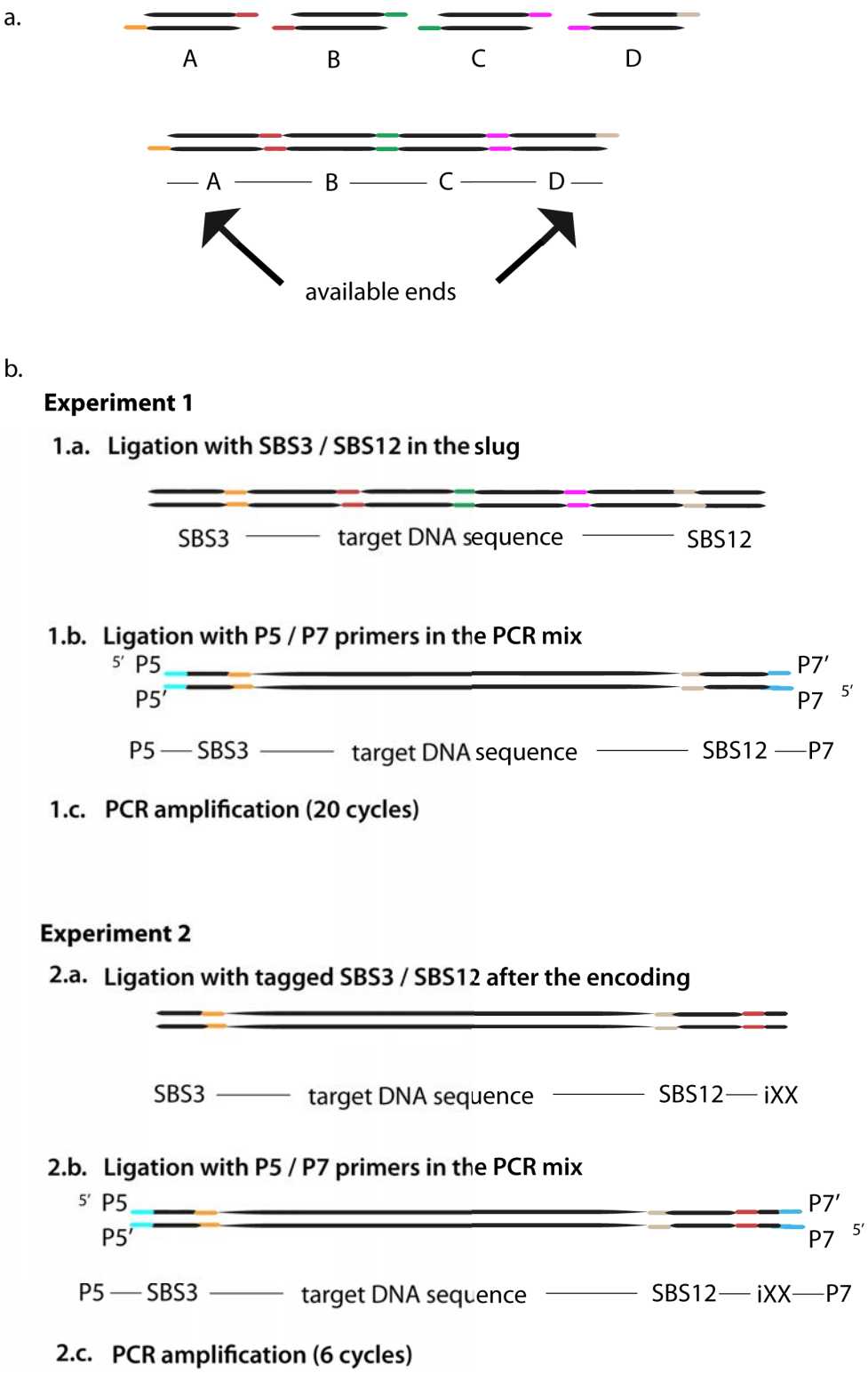

Figure 9.10 – a. Description of the barcoding strategy. Elementary A, B, C, D units can be selectively ligated by a ligase. Ends are designed to only enable A-B-C-D strands construction. A and D present ends that enable further ligation to SBS3/SBS12 primers. b. Two types of barcoding experiments were carried out. Experiment 1: to verify the efficiency of DNA ligation in droplets, SBS3/SBS12 primers were added in the slug library. They form an SBS3-ABCD-SBS12 strand that can be amplified by PCR with P5/P7 primers. Experiment 2: to analyze multiple samples in a sequencing platform, tagged primers are added after the encoding process. The slug library only contains the ligase, SBS3 / tagged SBS12 are added after the emulsion is broken. A PCR step is performed with P5/P7 primers, that will also enable barcodes capture on the sequencing flow cell.

After the PCR, DNA is quantified by a Qubit assay, following a protocol described in the experimental part. 75 ng of each sample is analyzed by agarose gel electrophoresis to verify the correct formation of barcodes and the purity of the samples before sequencing.

9.4.3 Results

Verification of the ability of constructing barcodes *in situ* Initial experiments without sequencing primers were conducted and amplified by PCR. Migration on an agarose gel showed a proper ligation of DNA elementary units and the formation of DNA barcodes of 200 bp, as depicted in Figure 9.11. A smear appears above 250bp, that may come from ligation of non-specific strands (incorporation of two C is possible even though not favorable) or from PCR artifacts (recombination of strands in bulk). Addressment of this question will be done by sequencing on latter experiments.

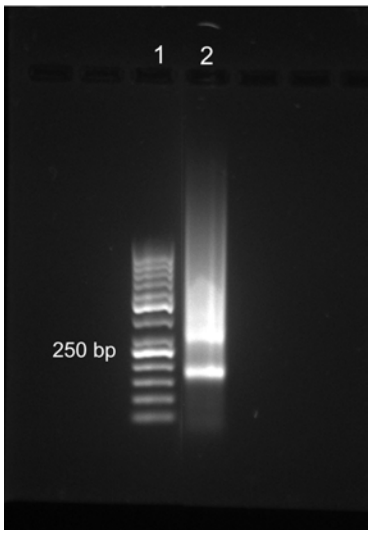

Figure 9.11 – Agarose gel electrophoresis of the broken emulsion,amplified by PCR. Lane 1: ladder 50 bp, lane 2: encoded emulsion. Barcodes of 200 bp were correctly formed in the device. The smear above 250 bp must correspond to PCR artifacts or incorporation of several elementary units, that is possible even though not favorable.

The ligation efficiently works in droplets which confirms the possibility of building DNA barcodes *in situ*.

Fabrication of four libraries of barcodes *in situ* **Results of the sequencing are not available at the time of this manuscript version. Sequencing results should be ready for the PhD defense. We apologize for the lack of a proper results and discussion section.**

a.

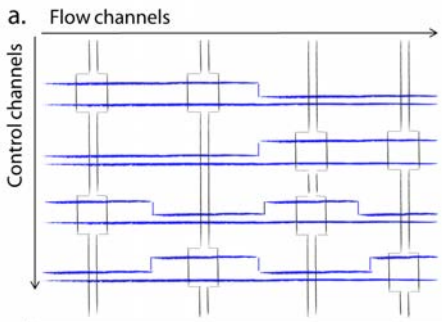

b.

Number of pressure inputs N	Number of injectors addressable	Number of barcodes
8	16	256
12	64	4e9
16	256	3.4e38

c.

Figure 9.12 – Multiplexed version of the printer.

9.5 Perspectives

9.5.1 Multiplexed version of the droplet printer

The proof of concept was performed with a device that enables the creation of 16 barcodes, a number that should be enough for most applications if coupled to a detection of fluorescence triggering, but that could seem limiting for ultra-high resolution analysis. To increase the density of injectors, a multiplexing strategy was developped using an approach already established in [25]. We take advantage of the lower deformability of narrow chambers and design injectors and control channels containing narrow and wide areas (Figure 9.12.a.). When two large areas are superimposed, the flow channel can be closed upon pressurization of the control channel. When two narrow areas are superimposed, the control channel pressure is set to a value that does not enable actuation.

If we denote N the number of control channels, the number of injectors n that can be controlled scales like $n = 2^{N/2}$. A table of the number of addressable injectors as a function of the number of pressure inputs is depicted in Figure 9.12.b. The corresponding number of barcodes is also calculated. To obtain a unique labelling of typical droplet libraries involved in directed evolution experiments ($\sim$ a million of droplets) the required number of input pressures is 12, which is tedious but feasible. Besides, more complex multiplexing strategies have been presented in the literature [184], that could further reduce the number of compulsory pressure inputs.

The increase of the density of injectors raises questions about the integration possibilities on a microchip. The inputs needed to be separated from the channel area, as represented in Figure 9.12.c. To make sure input channels do not upsurge the device hydrodynamic resistance, a three layer soft lithography process was required: a thin layer for the injectors (5 μm), an intermediate layer for the main flow channel (60 μm) and a thick layer for the input channels

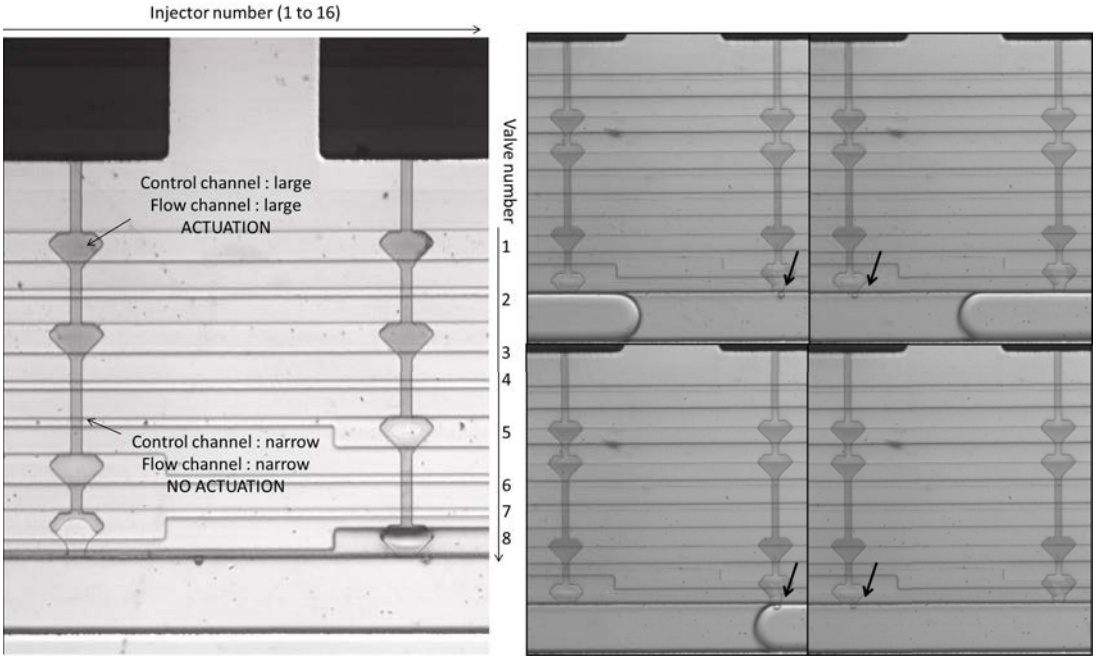

Figure 9.13 – Multiplexed version of the printer. a. On this picture, valves 1, 3, 6 are not pressurized and valves 2, 4, 5, 7 and 8 are pressurized. The release of pressure in valve 7 generates a droplet on the left injector. The absence of coupling between injectors is verified. b. Time lapse of the alternate control of two consecutive injectors. Produced droplets are indicated with a black arrow.

(300-400 μm). The case of an 8 valves / 16 injectors was successfully demonstrated. On Figure 9.13.a, valves 2, 4, 5 and 8 are always pressurized. Under release of the pressure in valves 1, 3, 6 and 7, a droplet is released on the left injector. No droplet is injected from the right injector, confirming the absence of coupling between two consecutive injectors. Figure 9.13.b is a time lapse of the alternate control of two consecutive injectors. Produced droplets are indicated with an arrow.

The large number of inputs led us to modify the PDMS microfabrication process; instead of punching all the holes, a custom insert was placed on the wafer before pouring the PDMS and maintained by magnets. A corresponding input reservoir was designed and printed with a 3D printer to minimize the number of reservoirs to pressurize.

9.5.2 Going towards higher throughputs

The pneumatic actuation restrain us to Hz frequencies, that will become limiting for large libraries. There is no possible advance with keeping the pneumatic control but going towards higher throughputs is however envisionable by using femto-injectors. As detailed in the chapter Drop-on-Demand (Chapter 3), femto-injection was demonstrated but presented robustness issues. The development of this technique is appealing for the absence of synchronization considerations and its ultra-high throughput, but would demand material engineering to suppress electrostriction phenomena. The use of rigid materials such as NOA or glass devices could solve

those issues.

9.6 Conclusion

In this chapter, we demonstrated the construction of a robust platform for the *in situ* encoding of picoliter (respectively nanoliter) droplets with femtoliter (respectively picoliter) droplets containing elementary DNA units that can be ligated one another. The use of electrodes enables a proper pairing of droplets with the following slug and release of the DNA inside the slug. The possibility of performing DNA ligation inside the slugs was verified and further proof of concepts are under sequencing analysis. Multiplexing possibilities were also demonstrated in cases where 16 level of barcoding are not sufficient.

Perspectives on this platform remain fully opened with the investigation of other injection methods that would provide higher throughputs and with the coupling of the injection to a detection of fluorescence step. This fluorescence triggering should decrease the number of necessary barcodes to a few 10-20 depending on the aimed resolution, compared to millions in existing encoding methods.

In situ encoding of droplets with DNA barcodes

✧ **Drop on demand**

- To minimize engineering considerations, pneumatic actuation was used and most experiments are performed in a scaled up nL-pL droplet printer.
- Droplet injection is controlled by a custom Labview software that takes as input the slug production frequency and the slug speed. Corresponding delays are imposed between the injectors to properly pair encoding droplets and the slug.

✧ **Pairing and electrocoalescence**

- Hydrodynamic pairing is discarded from the project but efficient trapping and releasing is obtained by imposition of an electric field.
- COMSOL simulations predict the possibility of trapping small droplets and the absence of injection errors as long as $s/D < 0.8$.
- An electrostatic effect is observed and helps the pairing of droplets with their following slug, suppressing above mentioned coalescence errors.

✧ **Proof of concept on a 8 valves design**

- The feasibility of the construction of DNA barcodes inside droplets was demonstrated.
- Uniform encoding and gradually encoding of 4 slugs library was performed. Samples are under sequencing and analysis.

✧ **Perspectives**

- Pneumatic actuation enables the multiplexing of inputs and the creation of thousands to millions of barcodes with a limited number of inputs (10 valves).
- The use of other DoD methods could increase the throughputs of encoding; femto-injection would provide kHz encoding frequencies.

Part IV

Contribution to other biological projects

This last part of the manuscript focuses on two projects I contributed to, without having the leadership. Both projects could directly take advantage of the use of femtoliter droplets, either to miniaturize a multi-step workflow and maintain high throughputs or because they needed large dilution ratios.

A first chapter introduces the biological context of those studies and particularly the study of evolutionary processes. The implementation of femtoliter droplets in both projects is performed in a second chapter.

Chapter 10

Introduction to the study of evolutionary processes

The high-throughput manipulation of droplets allows a wide range of processes and assays, some of them requiring complex, multi-step operations and opens access to the inspection of a wider area of the biological space. Notably, thanks to the LBC lab, major advances have been done in the study of evolutionary processes. Studies on the evolutionary mechanisms may seem academical at first sight, but they respond to major industrial demands. For instance, proteins are involved in a wide pannel of lucrative applications: enzymes and therapeutic antibodies represent respectively a market of 4 billion $ and of more than 100 billion $ [185, 186, 187, 188, 189]. Understanding evolutionary mechanisms, and applying them to the enhancement of proteins desired properties (enzymatic activity, stability, fitness to a specific environment, specificity to a substrate...) is thus a major industrial concern.

In this introduction, we first introduce studies on the origin of life and the use of directed evolution platforms in such perspectives. We particularly focus on two related biological applications that could benefit from droplet miniaturization. My contributions to both projects are limited to the physics part (design of chips, part of their microfabrication, data analysis) while the biological part is supported by Dany Chauvin (Simbad project) and Gabrielle Woronoff (EvoEvo project).

10.1 About the origin of life

Several theories are drawn on the origin of life. A consensual idea is that the apparition of complex organisms originates from adaptative processes through natural selection. Departing from simple RNA molecules, the evolution process enabled the apparition of complex cells with a metabolism (multiple proficient enzymes) and in which the genetic information is carried by DNA (translation factor). Taking the RNA world as the starting point, evolution must have

gone through several evolutionary steps, such as the compartmentalization of replicators into early protocells with a co-evolution of genome and membranes, the emergence of chromosomes that might have been driven by selection towards more specific enzymes, the transition from the RNA to the DNA world with the emergence of translation. Replication units - ribozymes in the RNA world, enzymes in the DNA world - are at the center of this evolution process. Ribozymes are RNA strands that are able to fold and form cavities that act as catalytic domains. An enzyme is a functional protein that is able to catalyze a chemical reaction at low concentration.

Historically, researchers on evolutionary processes only had access to fossil data and their comparison to current organisms, with sporadic informations on evolutionary intermediates, their genotypes or the conditions that prevailed the evolutionary trajectory. This observation led Richard Lenski to begin a long-term evolution experiment on the bacteria E. coli, that started 27 years ago and is still ongoing. Twelve initially identical populations of E. coli bacterias are studied in parallel, subjected to a low glucose growth medium. Lenski frozes a sample of each population of bactery every 500 generations to build a *frozen fossil record* that provides history of the evolution of each population, under a controlled environment. Several evolutionary assumptions could be verified by this evolutionary experiment; after 20,000 generations, parallel mutations were observed in all twelve populations, with a global increase of the bacterias fitness to their minimal growth medium[190]. This confirmed the hypothesis of an adaptative evolution process. However, they noticed that fitness at a given time does not ensure fitness at later times; some clones with lower fitness finally took over clones with higher beneficial mutations, because they had greater adaptive potential[191]. Lenski and co-workers also studied interactions between mutations[192] (some mutations have different effect if simultaneously or individually present, a process called *epistasis*) or dynamics of mutation apparitions. A review of their main findings can be found in [193].

A major drawback of Lenski's method is the time scale of micro-organisms evolution remains large, imposing extended experimental times (decades). In this context, directed evolution appears as an interesting strategy for laboratory evolution experiments, as evolutionary rates can be controlled. Directed evolution mimics the Darwinian evolution process in laboratory conditions: genetic mutations are imposed, the best mutants regarding an aimed phenotype are selected and the process is cycled. Mutation rates can be artificially controlled, thus varying the evolutionary time scale, and a variety of selection pressures can be applied, providing a wide convenience of study.

Directed evolution provides a platform for both the study of RNA and DNA evolutionary processes. Those two applications are detailed below.

10.2 RNA world evolutionary processes

10.2.1 The RNA world

Ribozymes are assumed to be the central unit of a prebiotic RNA world. The discovery of those RNA molecules that are able to both carry the genetic information and have a catalytic activity led researchers to envision a protocell world in which the RNA was the precursor of all biological functions.

Members of the LBC lab elaborated a model for protocell's in the early RNA world to be able to test some evolution assumptions (Figure 10.1.a). Ribozymes containing a replication domain are replicated by an enzyme, the Q_β replicase, into a complementary ribozyme that possesses a catalytic domain. Analysis of the ribozyme activity can be done by addition of a corresponding fluorogenic substrate.

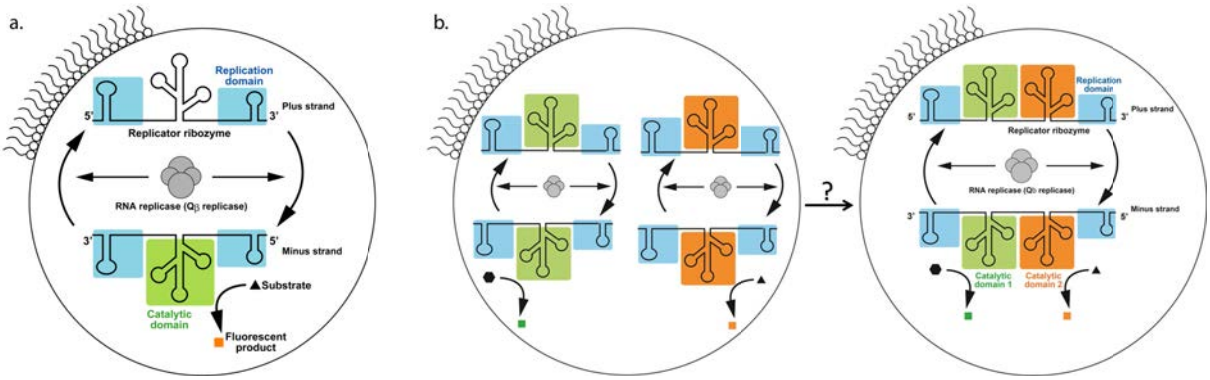

Figure 10.1 – a. Model of a protocell in the early RNA world. The ribozyme does not have a catalytic activity but it complementary strand has one. Ribozymes are replicated by an enzyme, the Q_β replicase, to obtain an efficient replication rate. b. By co-encapsulating two ribozymes with different catalytic activities and performing rounds of split and fuse, it is possible to investigate if and under which condition chromosomes emerge spontaneously. Figures by S. Matsumura.

Gabrielle Woronoff and co-workers investigate, notably, if chromosomes could spontaneously emerge in the RNA world, and which conditions prevailed their apparition. By co-encapsulating two different ribozymes with detectable catalytic activity (Figure 10.1.b) and by imposing varying selection pressures, it would be possible to test the spontaneous emerging of ribozymes containing the two replication domains, confirming the hypothesis of the spontaneous formation of chromosomes.

10.2.2 Problematic

The directed evolution platform provides tools to analyze droplets phenotypes and impose selection pressures, such as the presence of multiple genes in recovered droplets, and can be directly applied to ribozymes study.

To reproduce natural evolutionary processes, this experiment relies on multiple cell division/cell growth events. Unfortunately, the experiment requires different constraints on the number of RNA molecules before the cell division and during the cell growth. Before the cell division, concentrations of ribozymes must be high to enable fluorescence analysis and sorting of the droplets of interest. During the cell growth step, initial ribozymes concentrations must be low to obtain numerous replications of a limited number of RNA molecules. 1:1,000 dilution factors are necessary to obtain reasonable concentrations and correctly model protocell division with maintaining detectable levels of fluorescence in the workflow. The use of femtoliter droplets was envisioned to obtain such dilution factors.

10.3 DNA world evolutionary processes - enzyme engineering

Enzymes are involved in most of chemical transformations inside living organisms (digestive systems, muscle contraction) and present a diversity and a proficiency that exceed other chemical catalysts[18]. The structure of an enzyme is organized around an active site, containing itself a binding site matching the substrate, and a catalytic site, which is responsible for the acceleration of the chemical reaction. Protein functionality is highly coupled to its structure; the understanding of the relation between a protein structure and its function is still in its early developments, though there have been recent progress in protein engineering.

10.3.1 Strategies for the engineering of proteins

There are several strategies for engineering proteins (De novo design, rational redesign, directed evolution, combinations of the above). The de novo protein design refers to a computational method to predict the structure of the protein from its aminoacid (AA) sequence. This algorithmic process demands large computational resources and is thus restricted to small proteins. It has demonstrated its efficiency in some cases, and notably enabled the creation of new enzymes with functions not existing in nature[194, 195]. On rational redesign, changes in the AA sequence are induced at precise locations, based on a detailed knowledge of the protein structure. Though this method has demonstrated some successes [196], many attempts have failed because of the incomplete understanding of genotype/phenotype linkage.

In this context, directed evolution presents the advantage of not requiring information about the genotype/phentoype relation. The ability to test millions of genotypes in a single experiment opens access to the drawing of evolutionary maps, *i.e.* maps representing the relationship between genotype and phenotype under varying selection pressures.

10.3.2 Interest of miniaturization

The directed evolution workflow combines several steps (Figure 10.2).

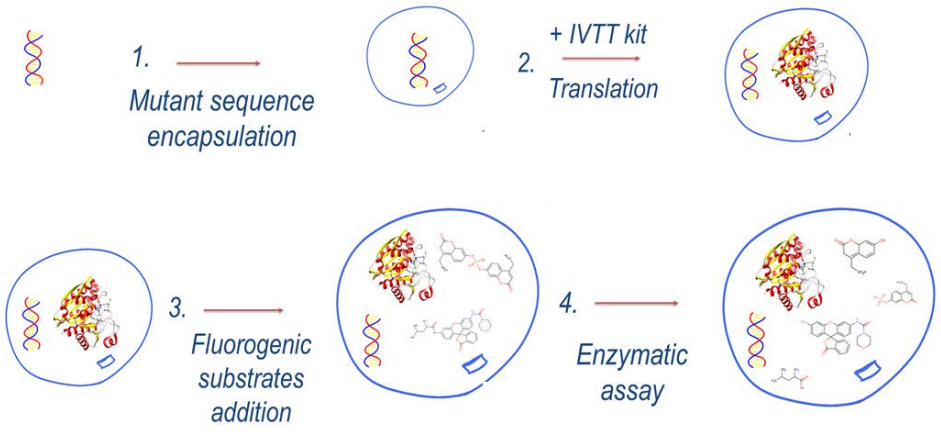

Figure 10.2 – Directed evolution worflow. A library of mutants is created, and each mutant is encapsulated in a single droplet (step 1.). The presence of the droplet interface links the genotype of the mutant to the phenotype it will generate. The In Vitro Translation kit is injected into each droplet (step 2.), either by pico-injection or by electrocoalescence. This step translates the genetic information into the corresponding enzyme. The fluorogenic substrates are added (step 3.), either by pico-injection or by electrocoalescence. The enzymatic assay is performed (step 4.) At the end of this workflow, the fluorescence of the droplet is directly linked to the efficiency of the enzyme it contains. Droplets can be sorted with imposition of a selection pressure by DEP sorting. A fluorescence threshold is chosen, above which droplets are recovered and the process is cycled.

- A library of mutants is created, and each mutant is encapsulated in a single droplet (step 1.). The presence of the droplet interface links the genotype of the mutant to the phenotype it will generate.

- The In Vitro Translation kit is injected into each droplet (step 2.), either by pico-injection or by electrocoalescence. This step translates the genetic information into the corresponding enzyme.

- The fluorogenic substrates are added (step 3.), either by pico-injection or by electrocoalescence.

- The enzymatic assay is performed (step 4.).

- The fluorescence of the droplet is directly linked to the efficiency of the enzyme it contains. A selection pressure is imposed by chosing a fluorescence threshold above which droplets are recovered by DEP sorting. Most efficient mutants are selected at this step and the process can be cycled through several rounds of selections.

Dany Chauvin and Clément Nizak work on an enzymatic genotype-phenotype mapping project and observed that consecutive steps tend to inhibit themselves. Those inhibitions can be limited by imposing 1:10 dilution factors between each step. However, this considerably increases droplets volume and limits the throughput of the final sorting step. We envisioned the use of femtoliter droplets to miniaturize the workflow and maintain high-throughputs.

Those two direct illustrations of the utility of femtoliter droplets were investigated; results are presented in the following chapter.

Chapter 11

Study of evolutionary processes with femtoliter droplets

Two direct applications of femtoliter droplets were found in the study of evolutionary processes. The first one focuses on the early origin of transcription in the RNA world; the aim is to study the origin of chromosomes and see if they emerge spontaneously and under which conditions. The second project investigates the genotype-phenotype mapping of the enzyme SGAP; the aim is to better understand the link between the genetic mutations, that can be selectively elected, and their consequences on the phenotype of the enzyme.

Interest of femtoliter droplets is here double. In the genotype-phenotype mapping experiments, introduction of femtoliter droplets enables the miniaturization of a complex workflow, the increase of throughputs and the obtention of reasonable experimental times. In the RNA world project, femtoliter droplets enable the extraction of a small quantity of reagents out of a picoliter droplet and the modeling of protocell division with keeping reasonable biomolecules concentrations (a few genes per droplet).

This chapter is constructed around these two approaches: we first focus on the RNA world project before studying genotype-phenotype mapping.

11.1 Early RNA world study - the origin of chromosomes

11.1.1 Description of the workflow

The experiment should comprise the following steps :

- Two different ribozymes and the Q_β replicase are co-encapsulated into droplets. The emulsion is incubated to replicate the ribozymes (*replication*) until disappearance of all dNTPs; this reaction creates $\sim 10^7$ replicates.

- Protocell division is modeled by the droplet splitting into daughter droplets (*cell splitting*).

- Daughter cells are merged with fresh droplets containing replication medium. Incubation is performed (*cell nursing*).

- The phenotypes are analyzed (two fluorogenic products) and droplets are sorted out (*cell survival*). Several selection pressures may be applied depending on the tested assumption. For the investigation of the apparition of chromosomes, only droplets containing the two catalytic activities are recovered.

- The process is cycled; recovered droplets are splitted and fused with fresh medium.

The high concentration of dNTPs enables the obtention of detectable levels of fluorescence for the phenotype analysis step and cannot be reduced. However, for the model to work, many replications must happen inside the fresh droplet; a split by two and the merging with a fresh droplet would enable ribozymes to be replicated only twice before dNTPs thin out. By using a split by 1,000, ribozymes can be replicated 1,000 times in the fresh droplet and the probability of observing recombination events is much higher.

This encouraged the development of a femtoliter-picoliter platform in which femtoliter droplets are extracted from picoliter droplets and merged with fresh picoliter droplets. This workflow demands the development of a picoliter to femtoliter splitting operation and of a picoliter-femtoliter electrocoalescence operation.

11.1.2 Splitting of picoliter droplets into multiple femtoliter droplets

Strategy Assymetric splitting is possible in the T-junction configuration by imposing a hydrodynamic resistance difference between the two arms of the junction[197, 198]. The ratio between the two daugther droplets is however limited to 95-5 % in the best case[198]. To obtain larger ratios, we designed a two-layer device comprising two thick flow channels (25 μm) linked by a thin channel (3 μm). Several thickness ratios were assessed : the thin channel layer varied from 1.5 to 4.5 μm at constant thick layer height (25 μm).

Protocol A 20 pL water-in-oil droplet emulsion is made with a droplet maker device and stored under mineral oil. The emulsion is reinjected into the splitting device using an MFCS pressure controller. In an early version of the device, the picoliter droplet library was sent towards an array of thin channels (Figure 11.1.a.). A later device comports a main flow channel that contains non-pressurized lateral thin channels, connected to deep reservoirs to avoid increasing the hydrodynamic resistance (Figure 11.1.b.). We denote h the height of thin channels. Experiments are recorded with a Photron fast camera.

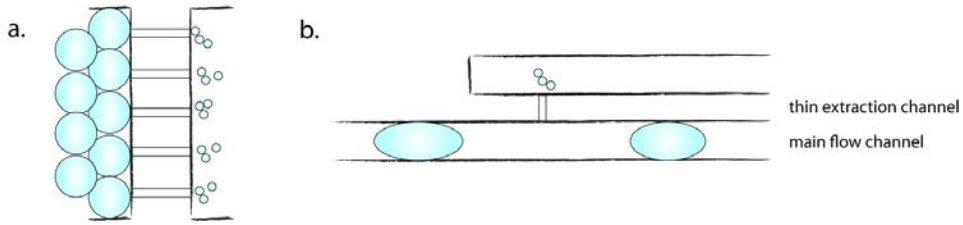

Figure 11.1 – Splitting of a picoliter droplet into femtoliter ones. a. Splitting of picoliter droplet in an array of thin channels. b. Extraction of femtoliter droplets out of a circulating picoliter droplet.

Results and discussion In the first version of the device, the picoliter emulsion was pushed through an array of thin channels. The close-packing of droplets introduced many coalescence events at the entrance of the splitters. Experiments were made trying to decrease the packing of droplets by vortexing the emulsion during its reinjection but did not completely suppress coalescence events.

A second version of the device was implemented, such as depicted in Figure 11.2. Extraction of femtoliter droplets from a picoliter library was only possible above a critical thickness $h > 2\mu m$. This can be understood by the presence of gutters when pL droplets travel inside a channel; if h is much lower than the gutter characteristic dimension, the droplet interface does not feel the depression and there is no split. This implies the existence of a minimal dimension of extracted femtoliter droplets, experimentally found at 120 fL with $h = 2\mu m$.

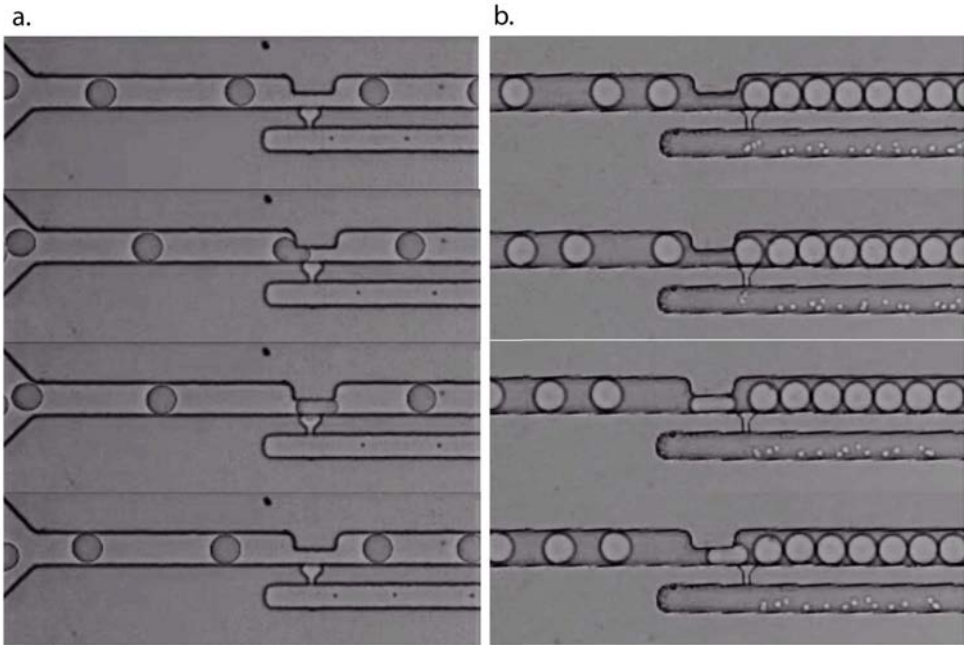

Figure 11.2 – Splitting of a picoliter droplet into femtoliter ones. a. Extraction of a single femtoliter droplet of 120 fL. b. Extraction of multiple femtoliter droplets (4 droplets of 700 fL in this case). Main flow channel width is 30 μm.

With $h = 3\mu m$, femtoliter droplets are reproducibly extracted from the library of 20 pL

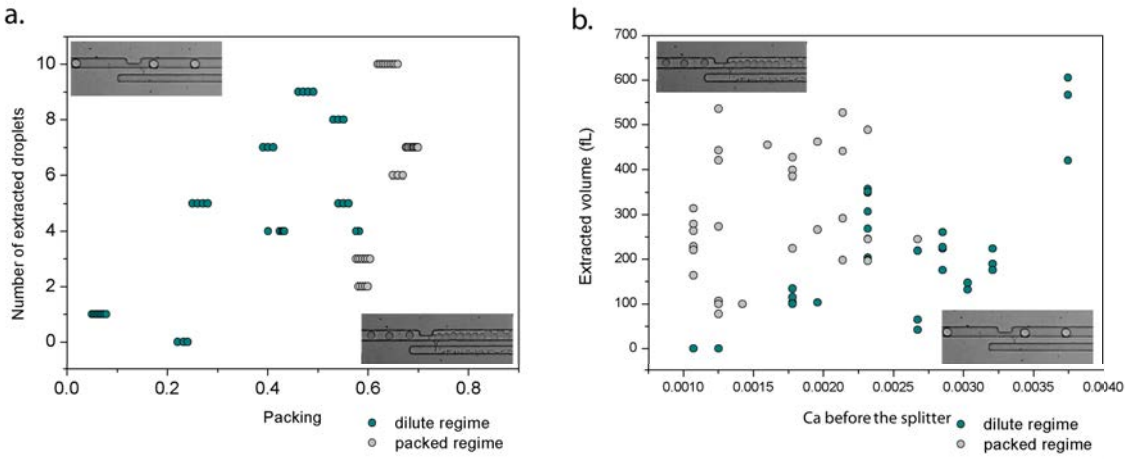

Figure 11.3 – Extraction of femtoliter droplets out of picoliter droplets. Two regimes are defined: in the *dilute regime*, the pL droplet leaves the splitter before the following droplet arrival. In the *packed regime*, displacement of the pL droplet out of the splitter is prompted by the arrival of the following droplet. a. Variation of the total extracted volume as a function of the Capillary number before the splitter. b. Number of extracted droplets as a function of the packing Φ.

droplets. The presence of the splitter also extracts part of the continuous phase which results in a significant slowing down of pL droplets after the splitter. Two regimes are defined: in the *dilute regime*, the pL droplet leaves the splitter before the arrival of the following droplet. In the *packed regime*, displacement of the pL droplet out of the splitter is prompted by the arrival of the following droplet.

The packing is characterized by Φ, the fraction of the channel occupied by droplets after the splitter, calculated by :

$$\Phi = \frac{\text{Area occupied by droplets after the splitter}}{\text{Area of the channel after the splitter}} \tag{11.1}$$

Transition from the dilute to the packed regime is experimentally found at $\Phi = 0.59$. The number of extracted droplets varies with the regime (Figure 11.3.a.). In the dilute regime, the number of extracted droplets increases with Φ while it is hardly predictible in the packed regime. Figure 11.3.b. represents the total extracted volume in fL as a function of the Capillary number calculated before the splitter. In the dilute regime, the extracted volume increases with Ca and varies from 100 to 600 fL. In the packed regime, there is no correlation between the extracted volume and the Capillary number. Volumes are globally higher than in the dilute regime.

Extraction of femtoliter droplets can be performed in the dilute regime of the designed system. The next step is the pairing and coalescence of extracted femtoliter droplets with fresh picoliter droplets.

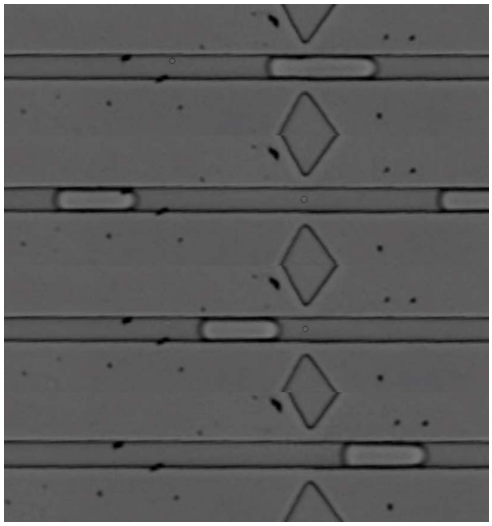

Figure 11.4 – Timelapse of the electrocoalescence of a femtoliter droplet and a fresh picoliter droplet. Voltage : 700V.

11.1.3 Pairing and coalescence with fresh picoliter droplets

Strategy In this application, a 1,000 dilution factor is aimed at; in such conditions, the relative size of femtoliter droplets and of the fresh picoliter droplet library is very large and hydrodynamic pairing is discarded according to Chapter 8.3.2. Similarly to the droplet printer, the pairing and coalescence is performed by DEP attraction and electrocoalescence between electrodes.

Protocol Side electrodes are filled with a conductive buffer (NaCl, 189 g/L, $\sigma = 41S/m$) and electrified through an Electrowell. Voltages are generated by an AM300 generator ($R\&S$) and amplified by a BOP1000M amplifier (KEPCO) with a gain of 100. Fluids are injected with an MFCS 7 bars (Fluigent).

Results Similarly to the case of the droplet printer device, efficient pairing and coalescence are operated in the electrocoalescence area. The femtoliter droplet is trapped between the electrodes by DEP attraction towards the positive electrode and reduction of the drag force close to the wall. It remains trapped until arrival of the following picoliter droplet (Figure 11.4).

A platform coupling picoliter and femtoliter droplets was successfully developped. Further results are awaiting biological experiments and should be carried out soon by project leaders.

11.2 Genotype-phenotype mapping of the enzyme SGAP

The SIMBAD project focuses on the genotype-phenotype mapping of the enzyme SGAP. Understanding the connections between the genotype and the phenotype would help the development

of protein engineering which has many industrial applications (pharmaceuticals, textiles, food processing, biofuel, ...). The realization of such a study requires a complex multi-step workflow. In a first section, we are going to describe this worklow and explain its drawbacks. Then, we will introduce the optimized workflow using femtoliter droplets.

11.2.1 A multistep directed evolution workflow

The directed evolution workflow comports the following steps. First the library of mutants is created by an error-prone PCR and encapsulated into individual droplets of 2 pL. Isolated mutants are amplified by PCR. Droplets are then merged to a droplet containing the IVTT kit to opere the translation. The fluorogenic substrate is added by electrocoalescence, incubation is performed and droplets are sorted by fluorescence-activated DEP sorting.

All these consecutive steps are mandatory: the IVTT kit needs to be injected after the PCR because of PCR high temperature cycling, the fluorogenic substrate needs to be injected shortly before droplet sorting because of leaking issues on longer periods of time. However, each electrocoalescence step increases the volume of the droplet which is detrimental to the throughput of the final sorting step. This problem is accentuated by inhibition effects between consecutive biological reactions that are studied thereafter.

Inhibition of the IVTT by the PCR product Experiments were carried out changing the relative concentration of PCR product and monitoring the SGAP activity (Figure 11.5). The following protocol is used: four different IVTT reactions are prepared, by mixing different volumes of PCR product and IVTT kit (1:1, 1:5, 1:10, 1:20). The reaction mixes are incubated at 37 $^\circ$ C for 3 hours. At the end of the reaction, 10 μL of each mix is deposited in a well along with the enzyme substrate and the enzyme buffer. Fluorescence intensity is measured as a function of time for the excitation / emission couple 488/525 nm, results are depicted in Figure 11.5.a.

For a low dilution factor of the PCR products (1:1), the enzyme activity is very low (Figure 11.5.a, orange curve). The enzyme activity increases with the dilution factor. To better characterize the effect of dilution, the linear part of each Figure 11.5.a curve is fitted with Origin; the slope corresponds to the enzymatic kinetics, expressed in fluorescence intensity per second. Figure 11.5.b summarizes the enzymatic activity for different dilution factors. The increase is significant between 1:1 and 1:5 and faints at larger dilutions. A negative test was also performed, without PCR product and shows the expected absence of enzymatic activity.

Above experiments led us to chose a 1:10 dilution factor for later experiments.

Inhibition of the enzymatic assay by the IVTT product Similar experiments were carried out changing the relative concentration of IVTT product and monitoring the SGAP

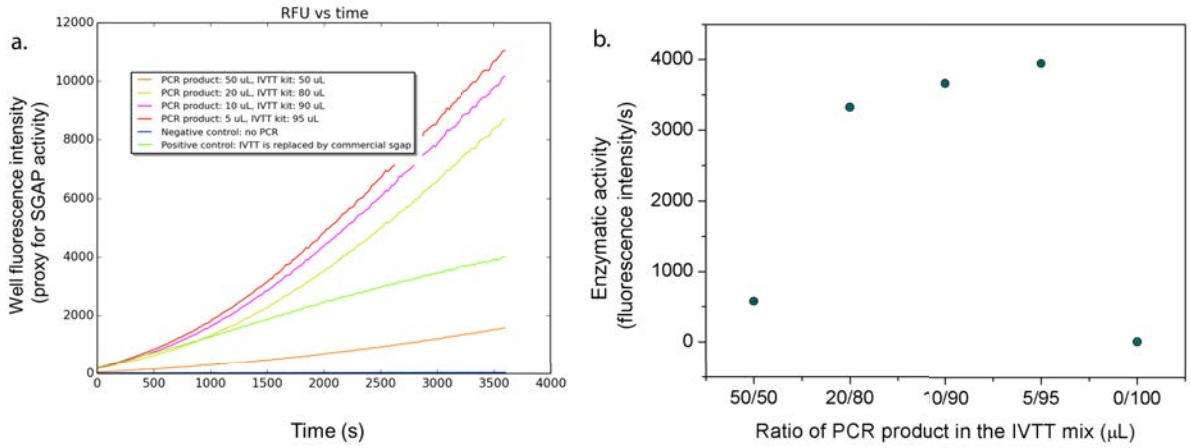

Figure 11.5 – a. SGAP activity as a function of time, with varying relative concentrations of PCR product and IVTT kit. For a low dilution factor of the PCR products (1:1), the enzyme activity is very low (orange graph). Several diltution factors have been tested: yellow 1:4, pink 1:10, red 1:20. The enzyme activity increases with the dilution factor. b. Kinetic parameters extracted from a. by linearly fitting the curve in OriginPro8 for t > 2500s. The increase is significant between 50:50 and 20:80 and faints at larger dilutions. Standard errors on the fitted slope are represented. The chosen dilution parameter for later experiments is a 1:10 ratio.

activity (Figure 11.6). The following protocol was used: the IVTT was performed with a 1:10 PCR / IVTT kit ratio, at 37 ° C for 5 hours. The product of this reaction was deposited in three wells, with volumes of 10, 50 and 89 μL. The enzyme substrate and buffer were added, at equal final concentrations in each well with a final volume of 100 μL. Fluorescence intensity is measured as a function of time for the excitation / emission couple 488/525 nm and represented in Figure 11.6.a.

At low dilution factors, the enzymatic activity is very low (pink curve). Decreasing the concentration of IVTT products enhances the enzymatic assay (orange curve). Enzyme kinetics were extracted from Figure 11.6.a. by fitting the linear part of the curves with Origin and extracting the slopes (Figure 11.6.b). The obtention of an appropriate enzymatic activity demands a minimal 1:10 dilution factor.

Consequence on the workflow The inhibition of each step of the workflow by the previous one demands large dilution factors between each step. Starting from 2 pL droplets for the mutant library encapsulation, the final droplet volume is 200 pL after the enzymatic assay. As demonstrated in Chapter 5.2, the sorting frequency varies inversely to the droplet radius. This limits the DEP sorting rate to a few 100 Hz, corresponding to large experimental times (typically 10 hours to sort a 10^7 library). By reducing the size of the initial emulsion, it is possible to limit the final droplets volume.

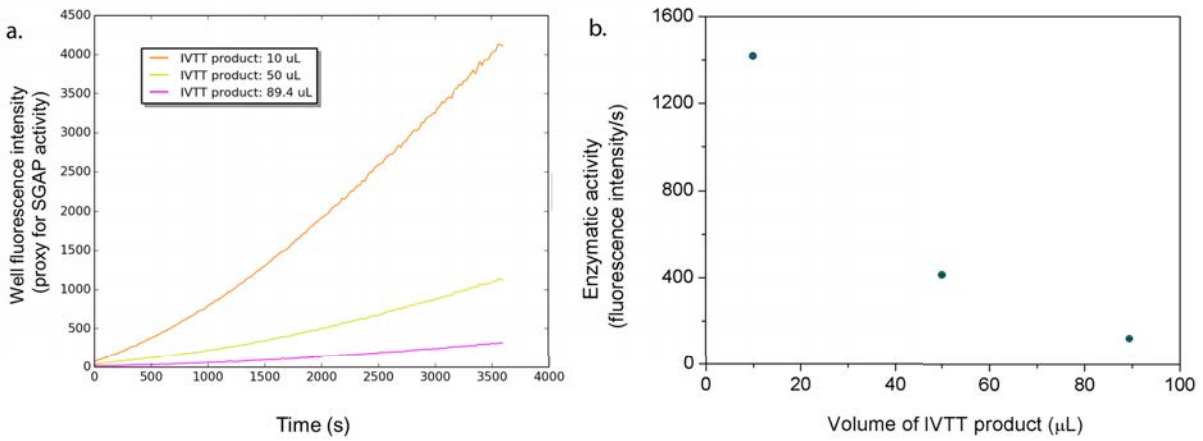

Figure 11.6 – a. SGAP activity as a function of time, with varying relative concentrations of IVTT products. For a low dilution factor of the IVTT products (9:10), the enzyme activity is very low (pink graph). Two other dilution factors have been tested: yellow 1:1 and orange 1:10. The enzyme activity increases with the dilution factor. b. Kinetic parameters extracted from a. by linearly fitting the curve in OriginPro8 for t > 2000s. The increase is significant between 9:10 and 1:10. Standard errors on the fitted slope are represented. The chosen dilution parameter for later experiments is a 1:10 ratio.

11.2.2 Production of 200 fL droplets

The encapsulation of the library of mutants into 200 fL droplets enables the miniaturization of the entire worflow.

Strategy To produce droplets of 200 fL (7.2 μm in diameter), the design of the step-emulsification device was adapted from Chapter 2.1.1. Li *et al.* model predicts the channel thickness has to be a third of the desired droplet size, here 2.3 μm. On the shallow part of the step-emulsification device, a 2D assumption must be verified to prevent the development of a Rayleigh-Plateau instability. The shallow part width is set to $w > 5b = 12\mu m$. A single-nozzle design was envisioned to obtain a better monodispersity.

Results The final production device is represented in Figure 11.7.a. Under such conditions, 200 fL droplets containing the library of mutants can be formed at kHz frequencies and stored off-chip.

11.2.3 Pairing and releasing of 200 fL droplets in 2 pL droplets

Strategy The difference in droplets size is small enough to consider hydrodynamic pairing. With a channel width of 20 μm, the expected R/a is of 0.4, enabling hydrodynamic pairing of fL droplets behind pL droplets according to Chapter 8.3.2. To obtain an efficient 1:1 pairing, a synchronization module was downscaled; 2 pL droplets are produced on-chip and their oil phase

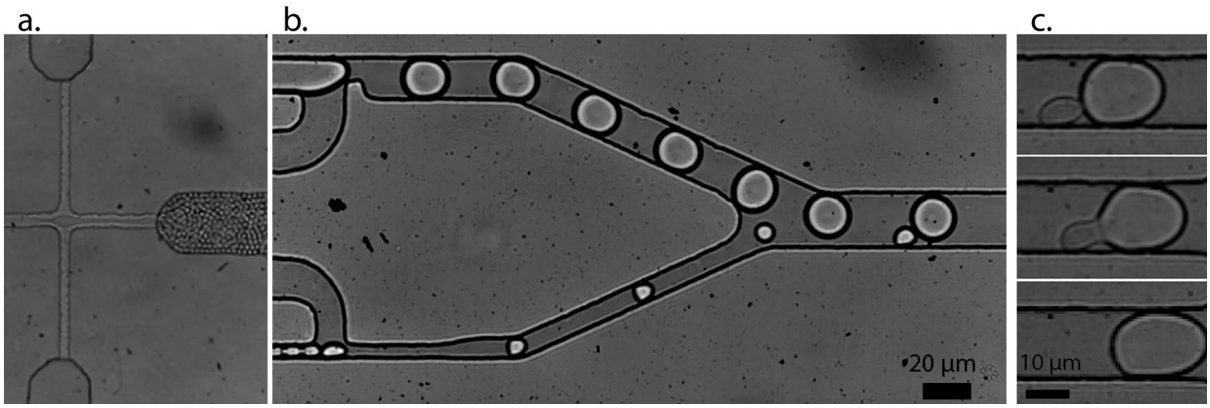

Figure 11.7 – New workflow for the SGAP genotype-phenotype mapping. a. 200 femtoliter droplet production in step-emulsification. b. Hydrodynamic pairing of picoliter and femtoliter droplets. c. Electrocoalescence of picoliter and femtoliter droplets.

input is coupled to the reinjection module of fL droplets. The production of a 2 pL droplet provokes a depression that triggers the injection of a 200 fL droplets. Electrodes are placed around the main channel to make pL and fL droplers merge together.

Results Figure 11.7.b represents the miniaturized synchronization module. Femtoliter droplets are correctly paired to picoliter droplets. Once in the main flow channel, fL droplets flow faster than pL ones; the speed ratio of droplets over slugs' is 1.4, in agreement with Chapter 8.3.2 for $R/a = 0.4$, $d/a = 0.47$. In such conditions, fL droplets robustly pair with the preceding pL droplet, after a travelling distance smaller than 75 μm (a few picoliter droplet width). Electrocoalescence is robustly performed between two low-melt solder electrodes (Figure 11.7.c). A ground electrode is added to shield the droplets at the output and avoid undesired coalescence events. Figure 11.8 summarizes the entire pairing and releasing process, with the synchronization area (Figure 11.8.b) and the electrocoalescence area (Figure 11.8.c). The imposition of the electric field (typically, 700V at 1.5 kHz) enables the droplets to merge. Droplets are recovered off-chip and incubated at 37 $^\circ$ C for 3 hours to perform the translation.

We developped a platform for the production of 200 fL droplets and their 1:1 merging with 2 pL droplets. The rest of the workflow uses already existing devices, such as an electrocoalescer for the merging of 2 pL to 20 pL and a 20 pL DEP sorter that are not described here for their lack of novelty. Final droplets volume is reduced by a factor 10, enabling kHz sorting frequencies and reasonable experimental times (2,5 hours for a 10^7 library). Biological experiments are now undergoing by the project leader.

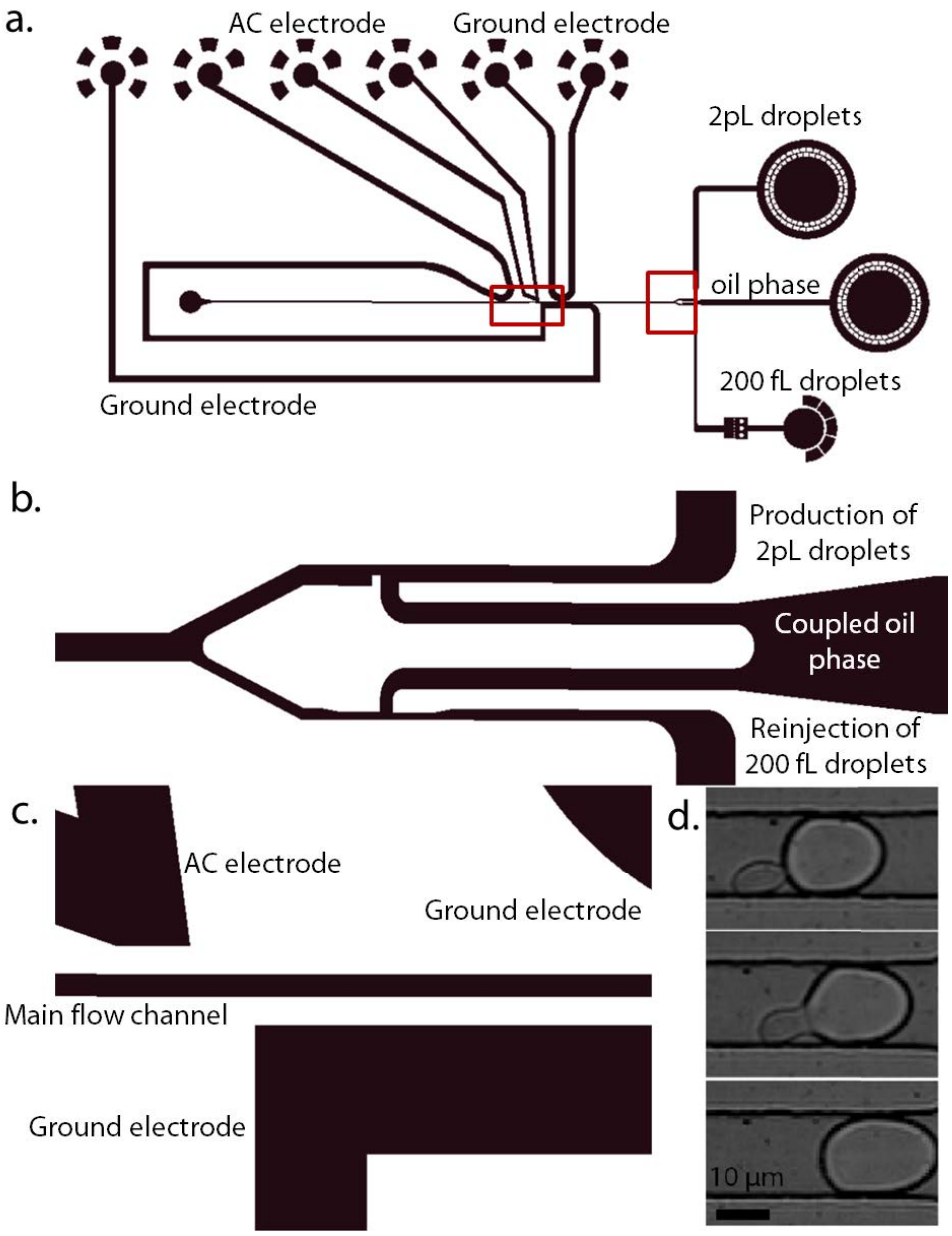

Figure 11.8 – Electrocoalescence of 200 fL and 2 pL droplets device. a. General view of the device. The system combines a module to synchronise the production of pL droplets and the reinjection of fL droplets and a main flow channel surrounded by low-melt solder electrodes. A ground electrode is added to shield the droplets at the output and avoid undesired coalescence events. b. Zoom on the synchronisation module. The oil phase couples the two droplet inputs; the formation of a 2 pL droplet provokes a depression that triggers the injection of a 200 fL droplet, favoring a 1:1 pairing. c. Electrocoalescence area. d. Time lapse of an electrocoalescence event. (700V, 1.5 kHz)

11.2.4 Perspectives - Towards a more complex genotype-phenotype mapping

The workflow presented in this chapter enables the imposition of a single selection pressure; a fluorescence threshold is defined above which droplets are recovered. This limits the potential of this method. Indeed, as demonstrated by Lenski's experiments (see Chapter 10.1), fitness at a given time is not proof of fitness at later times; some suppressed mutants could have higher adaptive potential and would have become remarkably efficient after several rounds of mutations, as represented graphically in Figure 11.9. The blue mutant would be suppressed at the first round of sorting but could become a better mutant after several rounds of mutations. The adaptation capabilities of mutants are not necessarily related to their enzymatic activity at a given time.

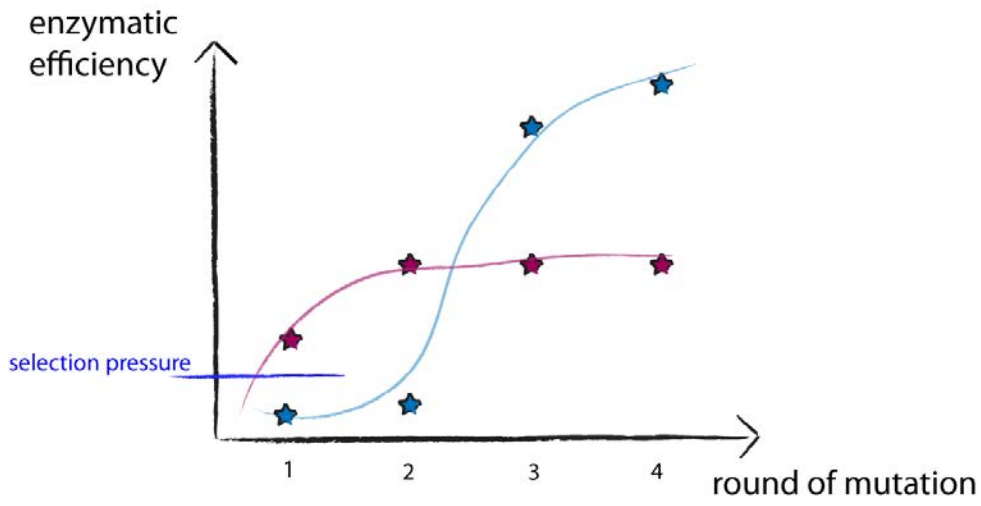

Figure 11.9 – A 2 binning sorting might suppress interesting mutants. After a first round of mutations, the imposition of a selection pressures suppresses a lot of mutants, that could have resulted in interesting phenotypes after several mutation rounds.

To better understand the link between genotype and phenotype, a more complex binning is necessary. Setting several fluorescence thresholds (typically, a 16 binning is envisioned) would enable the drawing of more complex evolutionary maps. A direct method to obtain such a binning is to use the droplet printer platform to encode the droplets after a fluorescence detection step. Thorough analysis of the genotype/phenotype mapping should be accessible with combining both projects.

Study of evolutionary processes with femtoliter droplets

✧ **Study of the emergence of chromosomes in the RNA world**

- A model prebiotic RNA world was developped in the LBC lab. It comprises originate replicators (ribozymes) carrying two different genes. Each gene possesses a catalytic activity enabling the assessment of its presence inside the droplet.
- By co-encapsulating two types of ribozymes and performing multiple protocell division cycles with imposing the presence of both genes inside selected droplets, the emergence of ribozymes containing both catalytic domains is forecast.
- A platform coupling picoliter and femtoliter droplets was developped to test this assumption. The use of femtoliter droplets enables the extraction of a limited number of ribozymes and a better modeling of protocell division.
- Biological experiments are undergoing.

✧ **SGAP enzyme genotype-phenotype mapping**

- Multiple steps are needed to perform the genotype-phenotype mapping of SGAP (library of mutants generation, addition of the IVTT kit, addition of fluorogenic substrates, enzymatic assay, DEP sorting).
- The IVTT is inhibited by PCR products remaining after the mutants library generation. The enzymatic assay is inhibited by IVTT products remaining after the translation step.
- Both inhibitions can be curtailed by imposing a 1:10 dilution factor between each step.
- The development of a platform coupling picoliter and femtoliter droplets limits the final droplet size and maintains reasonable experimental times for the final sorting step (a few hours).
- Combining the SGAP project to the droplet printer should provide access to thorough genotype/phenotype maps.

General conclusion on the scope of this work

This PhD work has extended the current handling of droplets down to femtoliter scale. By studying miniaturization laws and decreasing devices scales, we could successfully demonstrate that femtoliter droplets can be produced, continuously or on-demand, sorted by dielectrophoresis, merged by electrocoalescence, hydrodynamically splitted, incubated over days, and that they are suitable reservoirs for biochemical assays. Unprecedently low mixing times were demonstrated with droplet reactors. Miniaturization was performed with keeping the fast PDMS technology and remaining within standard soft lithography resolutions. This opens up multiple applications, from a simple improvement of existing picoliter assays to the development of new functionalities; typically, single-molecule studies should benefit from these developments.

Three biological applications were considered during this PhD work. The first one is the creation of a *droplet printer* device, a tool that enable the creation of DNA barcodes on-demand. Barcodes consist of elementary double strand DNA fragments that can be ligated one another, and that possess ends compatible with the Illumina sequencing technology. The possibility of constructing DNA barcodes on-demand was demonstrated. More complete results, including the final sequencing step, are under progress. This platform should become a competitor to existing barcoding technologies, and notably to the encapsulation of hydrogel beads, and enables binning considerations. Indeed, by analyzing the phenotype of the droplet and triggering a corresponding barcode injection, it is possible to create complex droplet sorters. 16 bins are already available in the current version of the device, with is enough for many applications (genotype-phenotype mapping for instance). The encoding of a library of 10^7 droplets by an *in situ* technique such as our does not demand millions of distinct barcodes; the number of barcodes is chosen in function of the aimed resolution of analysis.

Another application was found in the study of origin of chromosomes in the RNA world. Taking as a starting point an RNA world model developped in the LBC, a platform was created to test selection pressures that may have favoured the apparition of chromosomes. Femtoliter droplets are used here to extract a low amount of biomolecules (ribozymes), inject them into a fresh picoliter droplet and study repetitive cycles of protocell division/growth. Last, a third application focused on the genotype-phenotype mapping of the enzyme SGAP. The use of femtoliter

droplets enabled a miniaturization of this multistep complex workflow and the maintainment of kilohertz sorting rates at the end of the worflow. In both works, project leaders are now performing biological tests on the developped platform.

At the end of this PhD, several perspectives remain open. The development of a higher throughput droplet printer should be carried out, probably heading towards a miniaturized version of the pico-injector. The coupling of the encoding process to an analysis of fluorescence is also foreseen and should be easily achieved within LBC platforms. Last, several applications of the droplet printer are envisioned, such as its use on the genotype-phenotype mapping project.

Appendices

Appendix A

Multiple layer soft lithography

The complete procedure is summarized in Figure A.1.

- The first layer is spin-coated, soft-baked, exposed, and post-baked as in the classical procedure. The resist is then developed to make the alignment structures apparent.
- A hard bake is performed (200 $^\circ$C, 10 minutes). This step is not mandatory, but it improves the adhesion of the resist onto the wafer and prevents the alignment structures from getting ripped off by the tape.
- Tape pieces are glued onto the alignment structures. The tape must not hid any structure of interest.
- The second layer is spin-coated.
- The tape is removed using tweezers, making the alignment structures fully apparent, before proceeding to the soft bake. The tape must be removed before the soft bake to prevent it from sticking to the wafer.
- The alignment step is then performed very easily with the mask aligner.

Following steps (post-bake, development, hard bake) are carried out in the classical procedure. Multiple-layer lithographies are possible by repeating the process. The development of the first layer is recommended to enhance the visibility but not necessary.

Figure A.2.a. depict a picture of the wafer during the taping process. After the second layer deposition, the tape is removed, leaving a clean surface and completely visible alignment marks. Figure A.2.b-d. show the resulting alignment procedures in the case of the realization of the second layer without development of the first layer (Figure A.2.b.), and with intermediate development of the first layer (Fig A.2.c-d).

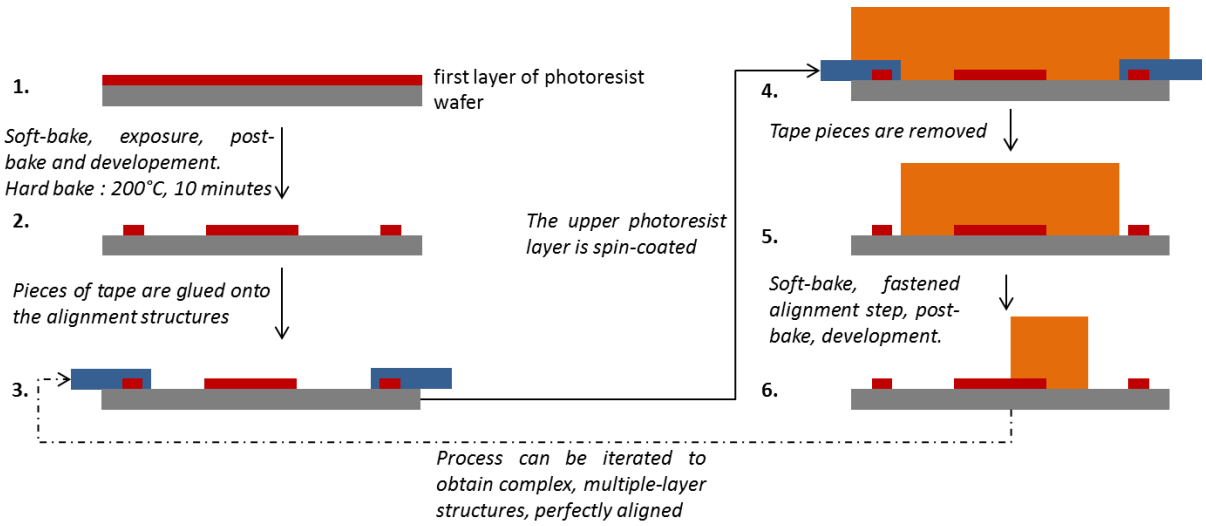

Figure A.1 – Protocol developed for a multiple layer soft lithography

The addition of tape onto the alignment structures generates an extra-thickness during the spin-coating process. To determine the extent of the non-uniform area, we measured the thickness of the upper SU8 layer after the soft bake, near the edge generated by tape removal. Figure A.3 depicts an example of the profiles obtained by the optical profiler, in the case of SU8 2035 resist. Because of the steep slope generated by the tape removal, the profiler can not resolve the fringes at the edge. The practical slope limit is typically 5 ° at a magnification of 5x. Consequently, profiles are not defined near the tape, and the precise tape position is taken at the location of the silica wafer fringes. (Figure A.3.a). The use of tape results in an extra-thickness of resist. Figure A.3.b represents the obtained profiles for five different resists (SU8 2010, 2025, 2035, 2050, 2075 and 2100) deposited at the same rotation speed (3000 rpm). In the case of SU8 2075 and 2100, profiles are measured with a mechanical profiler because the perturbed area is larger than the optical profiler field of view. From these profiles, we extract the distance of perturbation Δ, defined as the distance between the tape location and the return to the mean thickness, and the maximum extra-thickness δh. Figure A.3.c shows that Δ increases with the thickness of the deposited resist. However, its value remains quite low (maximum a few millimeters). Resists above SU8 2075 are known to induce planarization defects after the spin-coating, with, notably, the creation of an edge bead. The same phenomena amplifies the distance over which the film uniformity is disturbed by the tape in the case of thick resists. However, in all cases, the available area for constructing structures of interest is very large; we estimate that the tape pieces occupy an area of $150mm^2$, and the disturbed area is, in the worst case, $900mm^2$ which represents 10% of the area of a 4// wafer. For resists in the range SU8 2010 - SU8 2075, less than 5% of the wafer is disturbed by the tape. Figure A.3.d represents the maximum measured extra-thickness δh of resist near the edge, i.e. the difference between the maximum thickness and the mean thickness far from the tape. δh first increases within the SU8 series (SU8 2010 - 2035) but then decreases for film thicknesses of 49 and 66 μm. This can be explained by the fact the tape thickness is 60 μm; the deposition process is less disturbed when the tape is of

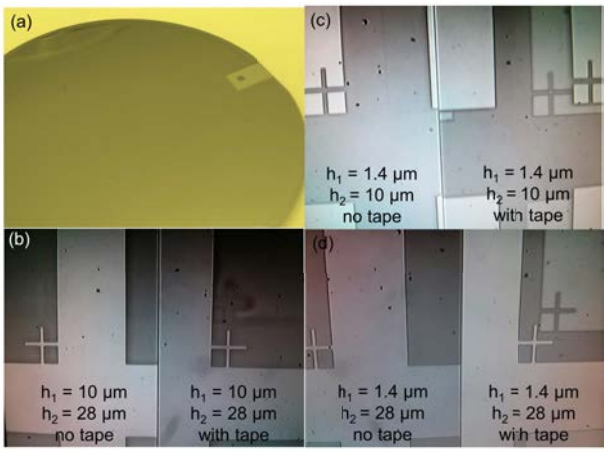

Figure A.2 – (a) Tape pieces are added onto the alignment structures, here after developing the first layer. (b) Picture of the alignment process. The first layer (SU8 2010 - 3000 rpm) is not developed prior to the second layer deposition (SU8 2025 - 3000 rpm). On the left, no tape was used and the alignment mark is faint. On the right side, tape was used to protect the structure, that is much more visible. (c) Picture of the alignment process. The first layer (SU8 2002 - 3000 rpm) is developed prior to the second layer deposition (SU8 2010 - 3000 rpm). On the left, no tape was used and one can see the faint mark bellow the mask. On the right, tape pieces were used and structures are fully visible. (d) Picture of the alignment process. Process B: the first layer (SU8 2002 - 3000 rpm) is developed prior to the second layer deposition (SU8 2025 - 3000 rpm). On the left, the alignment structures are completely hidden whereas they are fully visible on the right.

similar height. Higher thicknesses (SU8 2100) have a large δh, but this needs to be put into perspective, as the bead edge formed all around the wafer with such resists is high.

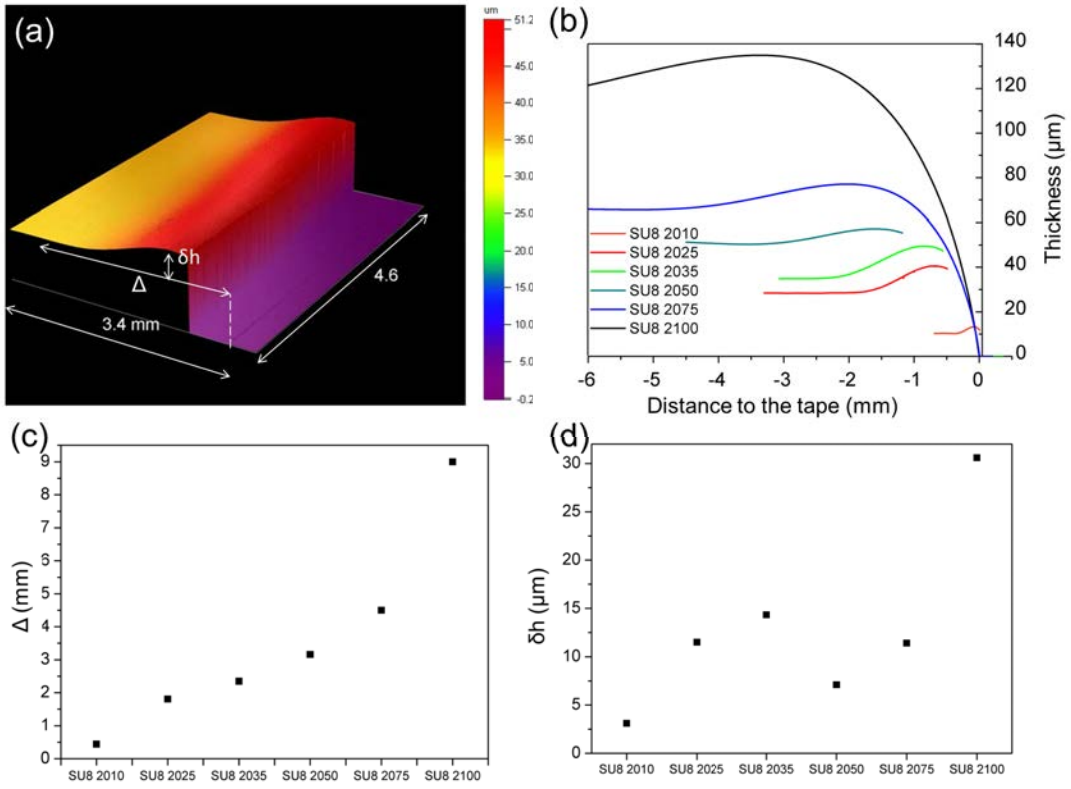

Figure A.3 – Characterization of the surface homogeneity near the tape edge. (a) Example of a surface profile obtained in the case of SU8 2035. Near the edge, the profilometer can not resolve the fringes because of the steep slope. The zero position is defined at the location of the silica wafer fringes. (b) Profiles extracted from optical profilometre surface profiles. In the case of SU8 2075 and SU8 2100, profiles are obtained by a Dektak mechanical profilometer because the disturbed region is larger than the field of view. (c) Distance between the edge and the return to mean thickness, Δ, as a function of the resist type. (d) Maximum extra-thickness near the edge as a function of the resist type.

Appendix B

Article : Droplet-based microfluidics at the femtoliter scale

Lab on a Chip

PAPER

View Article Online
View Journal

CrossMark click for updates

Cite this: DOI: 10.1039/c4lc01122h

Droplet-based microfluidics at the femtolitre scale†

Marie Leman,*[ab] Faris Abouakil,[a] Andrew D. Griffiths[b] and Patrick Tabeling[a]

We have built a toolbox of modules for droplet-based microfluidic operations on femtolitre volume droplets. We have demonstrated monodisperse production, sorting, coalescence, splitting, mixing, off-chip incubation and re-injection at high frequencies (up to 3 kHz). We describe the constraints and limitations under which satisfactory performances are obtained, and discuss the physics that controls each operation. For some operations, such as internal mixing, we obtained outstanding performances: for instance, in 75 fL droplets the mixing time was 45 μs, 35-fold faster than previously reported for a droplet microreactor. In practice, in all cases, a level of control comparable to nanolitre or picolitre droplet manipulation was obtained despite the 3 to 6 order of magnitude reduction in droplet volume. Remarkably, all the operations were performed using devices made using standard soft-lithography techniques and PDMS rapid prototyping. We show that femtolitre droplets can be used as microreactors for molecular biology with volumes one billion times smaller than conventional microtitre plate wells: in particular, the Polymerase Chain Reaction (PCR) was shown to work efficiently in 20 fL droplets.

Received 24th September 2014,
Accepted 19th November 2014

DOI: 10.1039/c4lc01122h

www.rsc.org/loc

Published on 27 November 2014. Downloaded on 05/12/2014 08:49:12.

Introduction

By using droplets as microreactors, droplet-based microfluidics[1–8] has allowed biological and chemical systems to be analyzed with high throughputs, small sample volumes, low costs, fast mixing,[9] and "digital" analysis of single compartmentalized molecules[10–14] or cells.[15,16] In the state-of-the-art, droplet volumes usually range from 2 pL to 4 nL (15 and 200 μm diameter), one thousand to one million times smaller than microtitre plate wells. Highly monodisperse droplets can be made and manipulated at kHz frequencies: a range of on-chip droplet manipulations such as mixing,[9,17,18] splitting,[19,20] fusing,[21–25] injecting,[26] incubating[27–29] and sorting[30–32] have been developed, that can be combined with off-chip incubations followed by re-injection.[16] These operations allow a wide range of processes and assays, some of which require complex, multi-step operations to be implemented in droplet-based microfluidic systems (see, for example ref. 33 and 34). This miniaturized technology has developed into a powerful tool for a number of applications[1,4,5,7] including synthesis of small molecules or particles,[17,35,36] screening of small molecule libraries,[37] screening of antibodies,[38,39] screening and directed evolution of enzymes,[40–42] targeted sequencing[43] and digital PCR.[10–13,44] Today, droplet-based microfluidic systems for targeted sequencing, next-generation sequencing and digital PCR are commercially available.

Further miniaturizing the droplets down to the femtolitre scale affords significant gains in terms of reduction in reagent consumption and cost, increased throughput, faster thermal transfer and higher mixing speeds. Moreover, there exist areas where use of very small droplets is either advantageous or essential. For example, drug delivery[45] (in which droplets must have volumes <65 fL to avoid embolism), or "digital biology" approaches based on analyzing single-cells or single-molecules, such as measurement of the activity of single enzyme molecules.[14,46,47] Last but not least, having the capability to generate droplets of colloidal size using microfluidics may open up interesting new avenues in the fields of diagnostics and colloidal materials.[48]

The first devices for producing femtolitre droplets at high throughput were demonstrated by Kobayashi.[49] Femtolitre droplets were produced using a step emulsification geometry, with kHz production rates and monodispersivities in the range of a few percent. Using a similar geometry, Malloggi *et al.*[50] extended this approach by demonstrating that complex droplets, such as Janus droplets, double emulsions, UV cured particles, and elementary clusters with volumes in the femtolitre range could be produced. More recently, novel

[a] *Microfluidics, MEMS and Nanostructures Laboratory (MMN), CNRS UMR 7083, École supérieure de physique et de chimie industrielles de la Ville de Paris (ESPCI ParisTech), 10, rue Vauquelin, 75231 Paris Cedex 05, France. E-mail: patrick.tabeling@espci.fr, marie.leman@espci.fr*

[b] *Laboratory of Biochemistry (LBC), CNRS UMR 8231, École supérieure de physique et de chimie industrielles de la Ville de Paris (ESPCI ParisTech), 10, rue Vauquelin, 75231 Paris Cedex 05, France. E-mail: andrew.griffiths@espci.fr*

† Electronic supplementary information (ESI) available: S1: mixing inside femtolitre droplets produced by step-emulsification, S2: mixing inside picolitre droplets produced by step-emulsification, S3: dielectrophoretic sorting of femtolitre droplets, S4: electrocoalescence of femtolitre droplets, S5: splitting of femtolitre droplets, S6: parallelized production of femtolitre droplets, S7: reinjection of femtolitre droplets. S8: fabrication of the molds by multiple-layer soft lithography. See DOI: 10.1039/c4lc01122h

Published on 27 November 2014. Downloaded on 05/12/2014 08:49:12.

methods of production/parallelization have been proposed,[51] enabling MHz production of femtolitre droplets.[14]

However, subsequent downstream manipulation of femtolitre droplets has so far been restricted to optical manipulation of individual droplets.[52,53] From a physical standpoint, high-throughput manipulation of femtolitre droplets is challenging due to unfavorable scaling of many operations. By reducing droplet volumes from the pL to fL scale, one considerably affects the balance of forces that governs the physics of the system. For example, picolitre droplets are traditionally sorted using dielectrophoresis.[30,31] By reducing droplet volume by a factor of 1000, dielectrophoretic forces[54] are reduced by three orders of magnitude while drag forces are decreased by one order of magnitude only. It is thus questionable whether dielectrophoretic forces can overcome drag forces to allow high-throughput dielectrophoretic sorting of fL droplets. Likewise, the destabilization and coalescence of pairs of droplets by an electric field[55] is disfavored by miniaturization as the capillary recovering force (linear in R) decreases more slowly than the competing electrostatic force (square dependence in R). Scaling difficulties are also encountered for droplet splitting[19,20] or droplet coalescence by hydrodynamic forcing,[56] as droplets must be confined, which poses problems when using standard microfabrication methods. Last but not least, the surface/volume (S/V) ratio increases on reducing droplet size ($S/V = 3/R$). Thus adsorption of reagents to surfaces risks to compromise chemical and biological reactions such as DNA amplification in fL droplets or other highly miniaturized systems.[57]

Here we demonstrate that, even though scaling laws look at first sight unfavorable in a number of cases, all the key operations of droplet-based microfluidics can be performed in a highly controlled manner with droplets of a few femtolitres in volume, at kHz rates. We have built up a modular femtolitre droplet toolbox of unit operations: high throughput monodisperse production, sorting, coalescence, splitting, mixing and production, off-chip incubation and re-injection. In certain cases (such as internal mixing), we obtain outstanding microfluidic performances, interesting in their own right.

Experimental section

Device fabrication

Microfluidic chips were fabricated using a classical soft lithography process.[58,59] Silica molds were fabricated with SU-8 negative photoresist (Micro Chem). In most cases, two-layer lithography was used: the silica wafer was first dehydrated at 200 °C, then the thin layer (900 nm to 3.6 μm depending on the design) was spin-coated, exposed, and developed. In order to prevent adhesion issues, the post bake time was extremely long (9 minutes) and a hard bake was performed before starting the second layer fabrication. To obtain a thick second layer without an intermediate step, pieces of tape (3M, Magic Scotch) were added onto the alignment structures before the second layer spin-coating. Alignment structures were then fully visible whatever the thickness of the second layer and optical aberrations were suppressed during the alignment procedure. The alignment process was thus very fast and accurate, and a typical ratio between the heights of the two layers of 35 : 1 was obtained without an intermediate step. The detailed protocol for fabrication of the molds is provided as ESI.† Poly-(dimethylsiloxane) (PDMS, Sylgard 184, Dow Corning) mixed with 10% (w/w) curing agent was poured over the mold to a depth of 4 mm and incubated at 65 °C for around 12 hours. The PDMS was peeled off the mold and the input and output ports were punched with a 0.5 mm-diameter Harris Uni-Core biopsy punch (Electron Microscopy Sciences). 150 μm thick glass slides were spin-coated with a 50 μm PDMS layer and cured. Devices were bonded to these slides with a PDC-002 oxygen plasma cleaner (Harrick Plasma). To obtain hydrophobic systems, bonded devices were then aged at 90 °C overnight to enable the PDMS to go back to its native hydrophobic state. Sometimes, the aging was accelerated by heating to 115 °C. For thin structures with aspect ratios higher than 10, hard PDMS was sometimes used, with a standard protocol.[60]

Apparatus

Unless mentioned, fluids were injected using an MFCS pressure controller (Fluigent) which can apply up to 7 bars. Usual working pressures were 1.5 to 4 bars. For applications where an electrical field was needed, channels were added in the lithographic process and filled with a conductive buffer (Na Cl, 189 g L^{-1}, σ = 41 S m^{-1}).[61,62] Electric voltages were produced by an AM300 generator (R&S) and amplified by a BOP1000M amplifier (KEPCO) with a gain of 100. The electric field was applied to the microfluidic device by an Electrowell (Fluigent) through Pt electrodes (Ø 300 μm) plunged into the conductive buffer. Experiments were observed using an inverted microscope (Zeiss, Observer A1), with a 40× or 100×, objective and recorded with a high-speed camera (Photron; Fastcam SA3). For fluorescence measurement, fluorescein was excited with an HBO 100 mercury vapor lamp (Zeiss) through an FITC filter (490 nm).

Formulation

Emulsions were formed using an aqueous phase and fluorinated oil (Novec HFE 7500) containing a non-ionic tri-block copolymer surfactant[63] with two perfluoropolyether (PFPE) tails (M_W ~ 6000 g mol^{-1}) and a polyethylene glycol (PEG) head group (M_W ~ 600 g mol^{-1}) at a concentration of 2% (w/w) as the carrier fluid. The interfacial tension between the Novec HFE 7500 oil containing 2% surfactant and DI water with 1% F68 pluronic was 5 mN m^{-1}, measured by the pendant drop method using a DSA 30 (Krüss GmbH). Experiments involving fluorescence were carried out with fluorescein sodium salt, whose dianionic form is highly fluorescent (quantum yield of 0.93) and whose bi-protonated form is non-fluorescent (pK_{a1} = 6.4, quantum yield of 0.37, pK_{a2} = 4.3,

 This journal is © The Royal Society of Chemistry 2014

Published on 27 November 2014. Downloaded on 05/12/2014 08:49:12.

non fluorescent). Conductimetry measurements were carried out with a CDM 210 (Radiometer Analytical S.A.).

Polymerase chain reaction (PCR)

PCR was performed on a 2660 bp pUC18 plasmid, out of which a 129 bp PCR product was amplified with M13 Forward and Reverse primers. The PCR mix consisted of DreamTaq Green Buffer (Thermoscientific, 5 μL/50 μL), M13 Forward and Reverse primers (Thermoscientific, 0.4 μM), dNTPs (Thermoscientific, 200 μM), DreamTaq polymerase (Thermoscientific, 1 μL/50 μL), F68 pluronic (0.02%) and drosophila total RNA (340 pg μL^{-1}). DNA concentration was varied from 10 pg μL^{-1} to 200 pg μL^{-1}. 25 to 65 fL droplets containing the above mix were produced by step emulsification.[50] The droplets were collected in a 200 μL Eppendorf tube and covered with heavy mineral oil to avoid evaporation. PCR was performed in a thermocycler (MJ Research PTC-200) off-chip. The amplification program comprised the following steps; initial denaturation at 94 °C for 2 minutes, 35 cycles consisting of DNA denaturation at 94 °C for 15 s, primer annealing at 62 °C for 30 s, extension at 72 °C for 30 s, and final elongation at 72 °C for 5 min. After thermocycling, the emulsion was broken by adding 30 to 60 μL of perfluorooctanol (approximately three to six times the emulsion volume), and analyzed by electrophoresis on 2% agarose gels in 0.5× TBE buffer containing 0.05 μL mL^{-1} of ethidium bromide.

Image analysis

Image analyses were performed using Image J (NIH). To estimate droplet sizes, images were thresholded, skeletonized and the analyze particle function used to provide quantitative information on the droplet area and position. Size distributions were also determined in the same way.

To estimate the fraction of coalescence events in a packed emulsion, we identified coalesced droplets by their size and measured the total area of coalesced droplets a_c, the total area occupied by uncoalesced droplets a_u and the total number of uncoalesced droplets n_u. The fraction of coalesced droplets is $C = (a_c/a_u n_u)/(n_u + a_c/a_u n_u)$.

For fluorescence experiments, the IntDen function was used. It allows the product of the mean gray value times the droplet area to be computed. In some cases, image averaging was carried out to enhance the signal to noise ratio.

Results and discussion

Mixing inside droplets

Droplets function as individual reactors of small volume in which dispersion of the reagents is suppressed by the presence of the droplet interface. Thanks to a number of favorable mechanisms (internal recirculations, chaotic regimes), mixing times down to 2 ms have been achieved in μL to pL droplets.[9,17] Here we asked whether, by reducing droplet sizes to femtolitre volumes, faster internal mixing can be obtained.

To investigate this question, we used the diffusion-limited acid base reaction between fluorescein (50 mM) at pH 4 and a basic buffer at pH 9 (30 mM Tris-base), which is much faster than the mixing times considered hereafter. Protonated fluorescein has a very low fluorescence, while its dianionic form is highly fluorescent. An intercalating stream of acid buffer (10 mM Tris-HCl pH 4) separated the two reagents to prevent prior contact. The three laminar streams flowed side by side (Fig. 1a) and were pinched between two streams of fluorinated oil containing fluorosurfactant.

Owing to the shallow geometry (1.7 μm height, 25 μm width), no droplets were formed at this stage. On reaching the step, where the channel increased to 40 μm in height and broadened to 100 μm in width, droplet precursors began to form at the step and grew until droplets were generated.[64] Droplets of 75 fL (5.2 μm diameter) were produced at a frequency of 10.7 kHz in the step-emulsification regime. The increase of fluorescence intensity I_f was monitored during droplet production and time-position equivalence was used to replace the position coordinate by time.

Low fluorescence emission and high speeds did not allow femtolitre droplets to be tracked individually in real time. We thus exploited image averaging to enhance the signal to noise ratio to obtain profiles like the one depicted in Fig. 1b, in which space has been converted to time by using the relation $t = y/U$ (with U the aqueous phase speed). Additional experiments carried out with 1.1 picolitre droplets (13 μm diameter) produced at a lower frequency (2.8 kHz) using a step emulsification regime (Fig. 1c) enlightened the hydrodynamics of mixing. In this case, individual droplets could be imaged and tracked after their production and the increase in fluorescence measured by image analysis.

Before the step, the contact time $\tau_{contact}$ between the fluids was short enough to exclude the possibility of diffusive mixing as the fluids flow side by side. The contact time was 3 to 500 times smaller than the characteristic diffusion time τ_{diff} for H^+ and OH^- ions in water, calculated over the width w of the water stream (Fig. 1a). At infinite dilution, $D_{H^+} = 9.31 \times 10^{-5}$ cm^2 s^{-1}, $D_{OH^-} = 5.30 \times 10^{-5}$ cm^2 s^{-1}.[65] For the 75 fL droplets: w = 3 μm, τ_{diff} = 480 μs, $\tau_{contact}$ = 160 μs. For the 1.1 pL droplets: w = 18 μm, τ_{diff} = 17 ms, $\tau_{contact}$ = 60 μs. Calculated diffusion times are overestimated as diffusion coefficients are smaller at finite dilution.

Fig. 1d depicts the renormalized fluorescence measurements in the femtolitre case (●) and in the picolitre case (□). Owing to the different time scales, the femtolitre fluorescence intensity measurement is replotted in Fig. 1e. Experimental data was fitted to an exponential evolution with Matlab (lines in Fig. 1d and e). Corresponding mixing times are 330 μs in 1.1 pL droplets and 45 μs in 75 fL droplets. The latter result is the shortest time reported to date for a droplet microreactor, 35-fold smaller than fastest time previously reported (2 ms).[18] We thus demonstrate that miniaturizing droplets to the femtolitre scale allows unprecedented fast mixing times (45 μs).

Published on 27 November 2014. Downloaded on 05/12/2014 08:49:12.

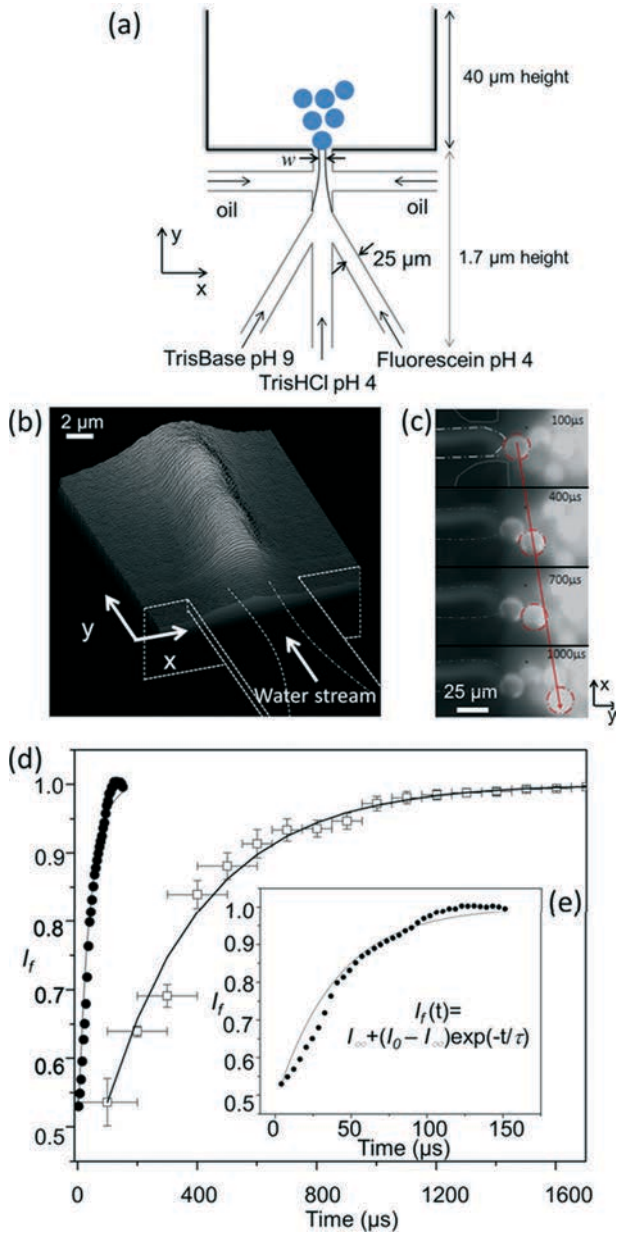

Fig. 1 (a) Droplet production and mixing in the step emulsification regime. The increase in fluorescence resulting from fluorescein deprotonation was used to determine the mixing time. Dimensions are indicated for the fL experiments. (b) Surface profile of 75 fL droplet production, with an exposure time of 500 ms. At the step, the fluorescence emission was low then increased along the streamwise direction (*y* axis). A movie of droplet production can be found in the ESI† (Movie S1). (c) Example of 1 pL droplet production. The location of a selected droplet in successive images is indicated by a red circle. A movie of droplet production can be found in the ESI† (Movie S2). (d) pL droplet fluorescence was measured using Image J, integrating the fluorescence over the entire drop. The fluorescence intensity $I_f(t)$ (□) was renormalized and averaged over 8 droplets, then fitted to an exponential evolution to obtain the characteristic time, τ_{pico} = 330 μs. The fluorescence intensity extracted from surface profiles of 75 fL droplets production is plotted on the same graph (●). (e) Average fluorescence intensity I_f of 75 fL droplets was determined as a function of the distance to the step and the time-position equivalence was used to determine the time. The fluorescence intensity was renormalized and fitted to an exponential evolution $I_f(t) = I_\infty + (I_0 - I_\infty)\exp(-t/\tau)$ with Matlab to obtain the characteristic time, τ_{femto} = 45 μs.

Dielectrophoretic (DEP) droplet sorting

When driven towards a junction containing two paths of unequal hydrodynamic resistance, droplets (or cells, or particles) choose the hydrodynamic path of least resistance (Fig. 2a). However, when subjected to a non-uniform electric field, droplets become electrically polarized and a dielectrophoretic (DEP) force can drive the droplets into the channel of highest resistance.[30] This is how active sorting of droplets is classically achieved. However, DEP forces are expected to decrease with the volume of the droplet,[54] and we may wonder whether miniaturization will jeopardize DEP sorting.

In our experiments, droplets are sent towards a Y junction (Fig. 2a), and completely obstruct the channel prior to the bifurcation. In such conditions, the pressure drop across a plug is given by:[66]

$$\Delta P = R_h l u \sim \frac{\eta}{wh} l u \quad (1)$$

where R_h is the fluidic resistivity, u the droplet speed (close to the flow speed U_c at low capillary numbers[66]), η the droplet viscosity, w the width of the channel, h its height, and l the plug length. The resulting force F_h that drives the plug downstream is thus given by:

$$F_h = \Delta P^* S \sim \eta l u \quad (2)$$

in which $S \sim wh$ is the droplet area (projected normally to the mean flow) on which the pressure field applies. When the obstructing droplet arrives at the junction, if the difference between the hydrodynamic resistances of the two paths is large, the droplet will be driven into the least resistive branch with, in terms of order of magnitude, the same force F_h. In the presence of a non-uniform electric field, the droplet will be attracted towards the more resistive channel by DEP forces. In order to achieve sorting, these forces must overcome F_h. The DEP force is proportional to the volume of the droplet whl and to the product the electric field times its gradient:[54]

$$F_{DEP} \sim \varepsilon_0 \varepsilon_c whl E \cdot \nabla E \quad (3)$$

where ε_0 is the vacuum permittivity, ε_c is the permittivity of the carrier fluid. The critical electric field E that must be applied to overcome the hydrodynamic drag is thus given by the expression:

$$\eta l u \sim \varepsilon_0 \varepsilon_c whl E \cdot \nabla E \quad (4)$$

Eqn (4) implies the existence of a threshold speed, $u_{thresh}(E)$, above which sorting cannot be achieved:

$$u_{thresh}(E) = \alpha \frac{1}{\eta} \varepsilon_0 \varepsilon_c whE \cdot \nabla E \quad (5)$$

This journal is © The Royal Society of Chemistry 2014

Published on 27 November 2014. Downloaded on 05/12/2014 08:49:12.

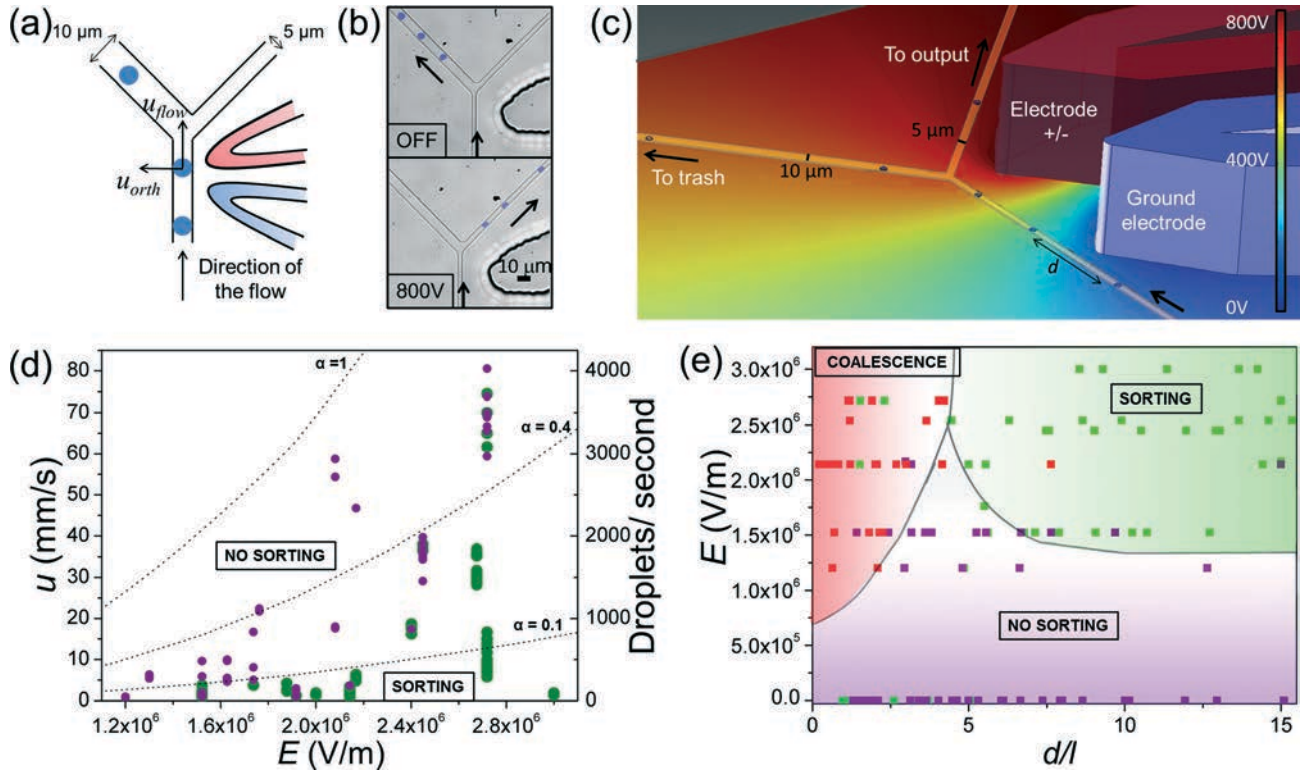

Fig. 2 DEP sorting. (a) Droplets are driven towards a y-shaped junction comprising two channels of unequal hydrodynamic resistance. (b) In the absence of an electric field all the droplets pass into the wider channel. Application of an electric field gradient steers droplets by DEP into the narrower channel. A movie of droplet sorting can be found in the ESI† (Movie S3). (c) Perspective representation of the sorting area. COMSOL calculated electric potentials are indicated. (d) Speed of isolated droplets *vs.* the applied electric field. Green dots: droplets directed towards the narrow channel. Purple dots: droplets directed towards the wide channel. The dotted line represents the theoretical maximum speed that enables DEP actuation calculated using eqn (5), with α = 0.1, 0.4 and 1. The corresponding number of droplets per second are calculated assuming a distance of 5*l* between 20 fL consecutive droplets. (e) Phase diagram of the femtolitre DEP sorter. Green: sorted, purple: unsorted, red: undesired coalescence events. The DEP force becomes strong enough to direct droplets at applied fields larger than 1.5 × 10^6 V m^{-1}. Droplets speed were limited to 0, 6–9 mm s^{-1}. Under a critical distance *d*/*l* = 5, droplets coalesce in this device.

where α is a numerical prefactor determined empirically. In practice, the maximum electric field E_{max} that can be applied is limited by electrosplitting:[67]

$$E_{max} \sim \sqrt{\frac{\gamma}{\varepsilon_0 \varepsilon_c w}} \quad (6)$$

where γ is the surface tension. As $\nabla E \sim E/\delta$, where δ is the distance between the electrodes, combining (5) and (6), one obtains a critical droplet speed u^* above which no sorting can be achieved:

$$u^* \sim \frac{\alpha h \gamma}{\eta \delta} \quad (7)$$

Assuming further that the minimal distance d_{min} between consecutive droplets is in the order of a few droplet lengths l, one obtains the maximum droplet sorting frequency f_{max}, from the following relation:

$$f_{max} = \frac{u^*}{d_{min}} \sim \frac{\alpha h \gamma}{l \eta \delta} \quad (8)$$

This formula shows that miniaturization should favor higher sorting frequencies, since h, l and δ scale down with the same factor, implying that f_{max} is inversely proportional to the device characteristic dimension.

In our experiments, embedded electrodes were added next to the Y junction during the lithographic process; this guaranteed that the electrodes were aligned with the microfluidic channel with micrometric precision, and they were close enough to generate large electric field gradients (Fig. 2a). The applied AC electric fields were generated by applying between 400 and 1000 V through Pt electrodes plunged in the conductive buffer, at a frequency of 1.5 kHz. Modeling of the electric field distribution was obtained through a finite element analysis with COMSOL multi-physics, considering the 3D system and the electrical parameters of the PDMS and the fluids involved (Fig. 2c). Local fields at the junction were found to vary from 1.1 × 10^6 to 3 × 10^6 V m^{-1} and are close to the theoretical limit E_{max} for femtolitre droplet splitting (3.1 × 10^6 V m^{-1} for 40 fL droplets).[67] Such fields would not be admissible for picolitre droplets, because that they are above the critical field producing droplet breakup at rest (E_{max} = 1.2 × 10^6 V m^{-1} for 15 pL (30 μm diameter) droplets).

Droplets of 20 to 50 fL volume containing deionized water with 1% pluronic were produced on-chip with a step-emulsification process and driven towards a Y-shaped

Published on 27 November 2014. Downloaded on 05/12/2014 08:49:12.

junction, with a hydrodynamic resistance ratio κ = 1.6 between the two paths. With κ = 1.6, the wide channel can contain up to 14 circulating droplets without substantially perturbing the main channel resistance.[68] The sorter was tested with trains of droplets travelling at velocities, u, ranging from 0.6 to 90 mm s^{-1}, varying the applied voltage V and the spacing d between the droplets. This corresponds to 8 to 9000 droplets s^{-1}, depending on u and d. Image processing was used to determine the droplet length l parallel with the flow, the distance d to the preceding droplet and the droplet trajectory.

In the absence of an electric field, all droplets passed into the low resistance channel, but by applying a voltage to the electrodes, it was possible to direct the stream of droplets into the high resistance channel (Fig. 2b). As predicted by the above theory, DEP sorting was possible only below a threshold velocity. Fig. 2d shows that well spaced droplets ($d/l \geq 15$) were correctly driven towards the narrow channel at low speeds (green dots), but they flow into the large channel in the presence of an electric field above a critical speed u_{thresh} (E) (purple dots). Experimentally, below $E = 1.5 \times 10^6$ V m^{-1}, no speeds were found to enable DEP actuation, implying the threshold speed is lower than 0.6 mm s^{-1} in such conditions. The dotted lines represent the theoretical threshold speed, calculated using eqn (5) and electric field gradients computed with COMSOL, for α = 0.1, 0.4 and 1. One sees that α = 0.1 describes correctly the experimental trend at low electric fields, but α = 0.4 better matches the experimental data at high fields. The discrepancy between theory and experiment most likely comes from the simplicity of our model; at high electric fields, droplets tend to deform, a parameter discarded from the discussion. A more accurate assessment would need to take into account the detailed shape of the droplet, its dynamical evolution during the sorting process, but also the presence of surfactants and the precise flow geometry at the junction, which is beyond the scope of this paper.

Fig. 2e shows an overview of the regimes of sorting found for various applied electric fields and distances between consecutive droplets, d (expressed as the ratio d/l) with u = 0.6–9 mm s^{-1}. Three regimes were observed, which are color-coded in Fig. 2d: droplets passing into the wide channel (purple), droplets passing into the narrow channel (green), and droplets electrocoalescing (red). In the absence of an electric field (0 V), with $d/l > 5$, all 716 analyzed droplets passed into the wide channel. In the presence of a low electric field, in agreement with the study of well spaced droplets (Fig. 2d), no droplets were correctly sorted. Above $E = 1.5 \times 10^6$ V m^{-1}, sorting was possible. In such conditions, droplets were correctly sorted as long as they were not perturbed by the preceding droplet. Fig. 2e indicates that the distance between consecutive droplets has to be above $d/l \approx$ 5–6 to enable efficient sorting, without sorting errors or coalescence events caused by the proximity of the preceding droplet. The maximum sorting frequency obtained experimentally was 3 kHz for 20 fL droplets, which is an improvement compared to maximum sorting rates observed for picolitre droplets (2 kHz).[31,41] To assess the theoretical maximum frequency at the electrosplitting limit, we assumed α was close to 0.4, and assessed the term $E \cdot \nabla E$ in COMSOL at the theoretical limit $E_{max} = 3.5 \times 10^6$ V m^{-1} for 20 fL droplet splitting. Eqn (5) then gives u_{thresh} (E_{max}) = 203 mm s^{-1}, and f_{max} = 8 kHz. It may be possible, therefore, to further improve the sorting speed by increasing the applied electric field.

To summarize, we have shown that sorting of streams of femtolitre droplets under high throughput conditions is feasible. This operation is achieved by increasing the electric field, which is possible owing to the fact that electrosplitting of droplets is inhibited by miniaturization.

Pairwise electrocoalescence

When subjected to a uniform electric field, water droplets in a dielectric phase get polarized and an attractive force operates between each dipole droplet;[69] as droplets approach, the film that separates them thins out and eventually breaks up, leading to coalescence. Furthermore, each droplet dipole locally increases the electric field as they get closer,[69] thus deforming the interfaces and enhancing the coalescence process. The physics that underlies this process can be described by two dimensionless parameters:[55,70,71] i) the Bond electrical number, $B_e = \varepsilon_0 \varepsilon_c E^2 R/\gamma$, represents the ratio of the electrical force that tends to deform the droplets over the restoring capillary force. Here E is the field quadratic mean and R is the droplet radius; ii) the ratio of the initial distance between droplets over their radius d/R, which is related to the intensity of the interaction between droplet dipoles.

In the literature, it is well established that coalescence occurs at Bond numbers below unity (typically B_e = 0.2–0.5). This implies that, as droplet radius, R, decreases by a factor of ten, electric fields needed to induce coalescence are increased by a factor of $\sim 3\left(\sqrt{10}\right)$. The question is whether this is feasible.

In the experiments, electrodes were added close to the coalescence zone during the soft lithography process in order to obtain high electric fields. Two sets of 20 to 30 fL aqueous droplets were generated at 3 kHz using an on-chip step emulsification process, and brought together just upstream of the coalescence zone (Fig. 3a). The coalescence zone was designed to favor the pairing of droplets and to assist the electrocoalescence process through decompression of the droplet-pairs at the restriction at the exit of the coalescence chamber.[56] Electrodes were positioned slightly asymmetrically around the channel to ensure that the highest electric field was located at the restriction. To assess the electric field effectively applied in the channel, 3D COMSOL Multiphysics simulations were performed, taking into account the material's electrical characteristics (Fig. 3b).

Droplets entered the coalescence chamber at speeds ranging from 2 to 22 mm s^{-1} and the coalescence process was tracked by analysing images taken with a high-speed camera. An example of coalescence of two droplets, containing

 This journal is © The Royal Society of Chemistry 2014

Published on 27 November 2014. Downloaded on 05/12/2014 08:49:12.

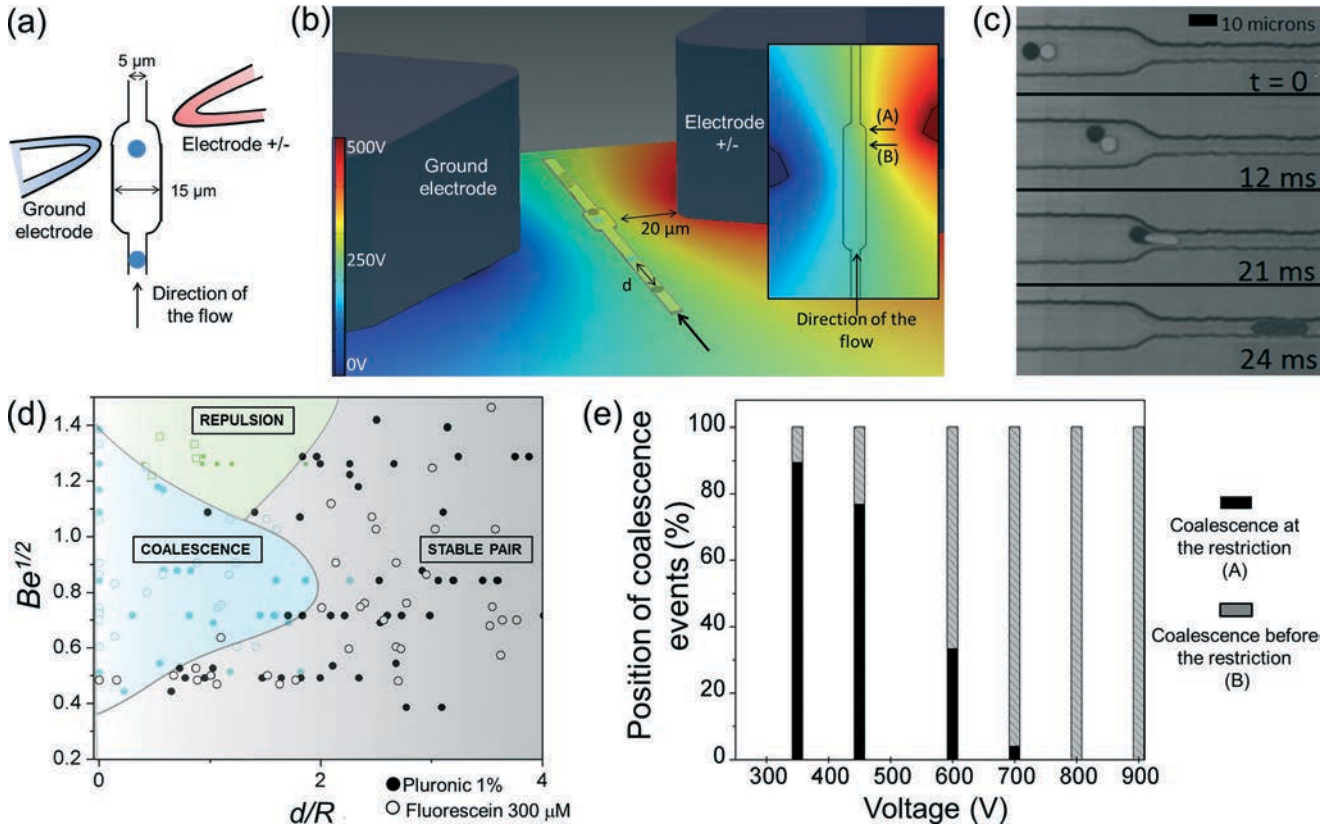

Fig. 3 Electrocoalescence. (a) Electrocoalescence device. Droplets of 25 fL volume, generated by two drop makers, were brought together and enter a coalescence zone designed to favor droplet pairing and coalescence. Electrodes were added around this zone to ensure efficient electrocoalescence of the droplet pairs. (b) Perspective representation of the coalescence region, with the electric potential calculated by COMSOL. The inset represent in more details the coalescence area. Electrodes are positioned slightly asymmetrically to ensure that the highest electric field (position B) is located near the restriction (position A). (c) Example of a coalescence event for 25 fL droplets colored with brilliant black (2%) and fluorescein (1%), respectively. The applied voltage was 450 V. Droplets reorient along the field (t = 12 ms) and then coalesce at the restriction (t = 21 ms). The channel height is 1 µm. A movie of droplet coalescence can be found in the ESI† (Movie S4). (d) Phase diagram of the system. Blue area: coalescence. Gray: stable pair. Green: repulsion. Experiments were carried out using droplets containing (o) 300 µM fluorescein and (●) 1% pluronic F68, without observable differences between the two solutions. (e) Percentage of droplets coalescing in position A (black) or position B (gray), as a function of the voltage applied.

brilliant black (2%) and fluorescein (1%) is shown in Fig. 3c. Phase diagrams were drawn for two solutions of different conductivity: deionised water with F68 pluronic (1%) and deionised water with fluorescein (300 µM) (Fig. 3d). Their conductivities were, respectively, 10^{-3} S m^{-1} and 10^{-1} S m^{-1}. When subjected to the electric field, droplet free charges move with a time constant $\tau = \varepsilon_0\varepsilon_d/\sigma$, where ε_d is the permittivity of the dispersed phase, ε_0 the vacuum permittivity, and σ the dispersed phase conductivity. This time constant is much smaller than the excitation period in both cases ($\tau = 10^{-7}$ s and 10^{-9} s $\ll \tau_{ex}$ = 0.7 ms) which guarantees that droplets get polarized instantly and act as charged conductors.

We measured the radius R and the distance between paired droplets, d, at the entrance of the coalescence area. The distance between consecutive droplet pairs was maintained above $4R$ to avoid droplet–droplet interactions.[55] Under this condition, the maximum coalescence throughput of the device was 1.1 kHz.

Similarly to picolitre droplets,[55] three regimes were observed depending on the field strength and on the initial separation d between successive droplets: droplet coalescence (Fig. 3c blue area), stable droplet pairs (Fig. 3c grey area), and repulsion between droplets (Fig. 3c green area).[72,73] No difference in behavior was observed between the two solutions of different conductivities. The phase diagram (Fig. 3d) has a structure similar to that established for picolitre droplets,[55] with a triple point separating the three regimes. However, on analysing in more detail the phase diagram, one sees that droplets coalesce up to an initial separation distance of $2R$, compared to $0.7R$ usually found for picolitre droplets. This is presumably due to the geometry: droplets need to deform to enter the restriction which causes their average speed to be slowed down by 50% just before the restriction. This eases the synchronization of droplets in the coalescence area. The position of coalescence events was highly dependent on the electric field (Fig. 3e). Above 800 V, all coalescence events happened before the constriction (position B), whereas droplets coalesced at the restriction at lower fields (position A). This can be explained by the fact that the mechanism of coalescence depends on the voltage: at high fields, only electric

Published on 27 November 2014. Downloaded on 05/12/2014 08:49:12.

stresses are at play, whereas at lower voltages, droplet coalescence results from both electric stress and hydrodynamic decompression at the restriction.

To summarize, we demonstrate here that controlled electrocoalescence of femtolitre droplets can be achieved in a microfluidic environment, at the expense of applying larger electric fields than for picolitre droplets. The coalescence chamber design favors droplet pairing at larger initial distance and helps destabilization of the pair at the restriction.

Splitting

When droplets are driven towards a T-junction at high speeds, they may either breakup or flow along one of the arms of the T. Mechanical splitting is controlled by the geometry, the viscosity ratio of the continuous and dispersed phase $\lambda = \mu_c/\mu_d$ and the Capillary number, defined by $Ca = \mu_c u/\gamma$. It has been shown that two regimes of splitting are possible, one in which droplets occupy only a fraction of the channel width (non obstructed regime), and the other in which droplets completely obstruct the channel (break up with complete obstruction of the channel).[21,22] The former necessitates moderately low Ca, while the latter, being mostly controlled by the geometry, occurs almost independently of Ca.[20,74] Since the capillary numbers for fL droplets are typically small (below 10^{-2}), it is difficult in practice to achieve break up in the non obstructed regime: the underlying reason is that the geometries needed to handle fL droplets result in channels with high hydrodynamic resistance, which limits droplet speeds and typically results in small Capillary numbers.

In our case, 25 to 135 fL droplets were generated by on-chip step emulsification and driven toward a 1 μm high, 5 μm width T-junction (Fig. 4a). The viscosity ratio between the oil and the water phase is $\lambda = 1.43$. Droplets were driven towards the junction and experiments were recorded by a high-speed camera (Fig. 5b). Droplet speeds and droplet lengths l, were measured by image analysis. The channel width w was also measured *in situ*, so as to take into account the PDMS deformation.

Throughout the experiments, we spanned a range of inlet pressures from 1.5 to 6 bars. Because of the geometry (long thin channels), the corresponding speeds were low – between 5 and 50 mm s^{-1}. Attempts to achieve higher flow rates were made with a neMESYS syringe pumps, but the glass slides could not withstand the corresponding applied pressures. To avoid unwanted interactions, the distance between successive droplets was kept above $4l$, limiting the frequency to 850 Hz at the maximum speed of 50 mm s^{-1}.

As expected from the low Capillary number of the system, breakup was only observed in the complete obstruction regime. Fig. 4c shows that the critical ratio l/w upon which breakup is obtained does not depend on the Capillary number, consistent with theory, but is mostly controlled by the geometry. According to the model described in ref. 74, the breakup with tunnels regime could only be achieved at capillary numbers of 10^{-2}, a range that is difficult to achieve in our device.

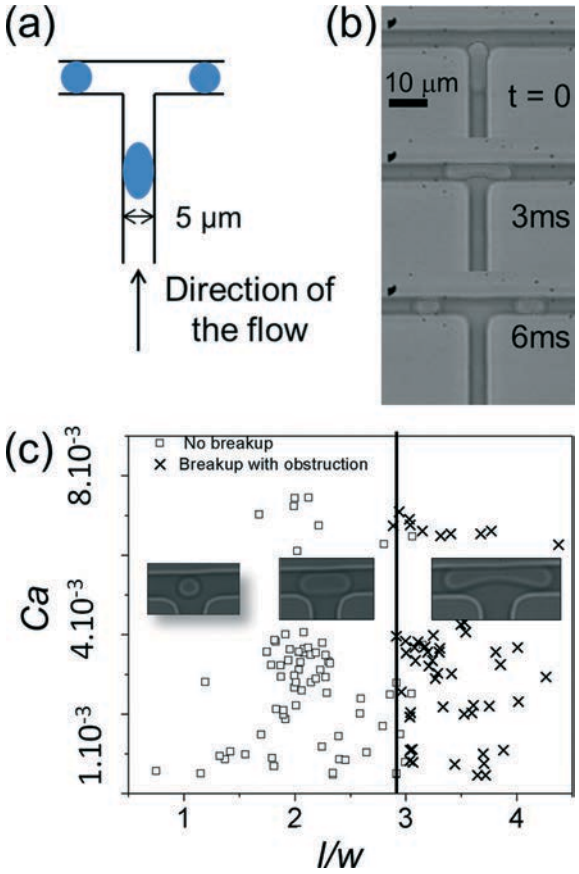

Fig. 4 Droplet splitting. (a) Splitting device. Droplets flow towards a T junction. The height of the channel was 1 μm to favor obstruction and enhance the splitting process. (b) Time series of micrographs showing a 75 fL droplet splitting. A movie of droplet splitting can be found in the ESI† (Movie S5). (c) Phase diagram of the splitting of 25 to 135 fL droplets. Only two regimes were observed: (o) non breakup, and (x) breakup with obstruction (at $l/w \geq 3$). This corresponds to a droplet volume of 75 to 130 fL in our geometry, depending on the PDMS pressure related deformation.

To summarize, we demonstrate here that femtolitre droplets splitting is achievable in T junctions in obstructed regimes, with a minimal volume of 75 fL (daughter droplets of 32 fL each) and a maximum frequency of 850 Hz. To split smaller droplets would require either smaller features, beyond the scope of standard soft-lithography techniques, or higher Capillary numbers, thereby higher pressures, which were out of reach with our device.

Droplet stability

The question we address here concerns the thermodynamic stability of femtolitre droplets, stability being a pre-requisite if such droplets are to be used as microreactors for chemical or biological reactions. According to the Epstein–Plesset dissolution model, established for gas bubbles in a liquid solution[75] and later extended to liquid microdroplets dissolution,[76] the miniaturization increases the shrinking rate of droplets, by driving faster mass exchanges between them and the

This journal is © The Royal Society of Chemistry 2014

Published on 27 November 2014. Downloaded on 05/12/2014 08:49:12.

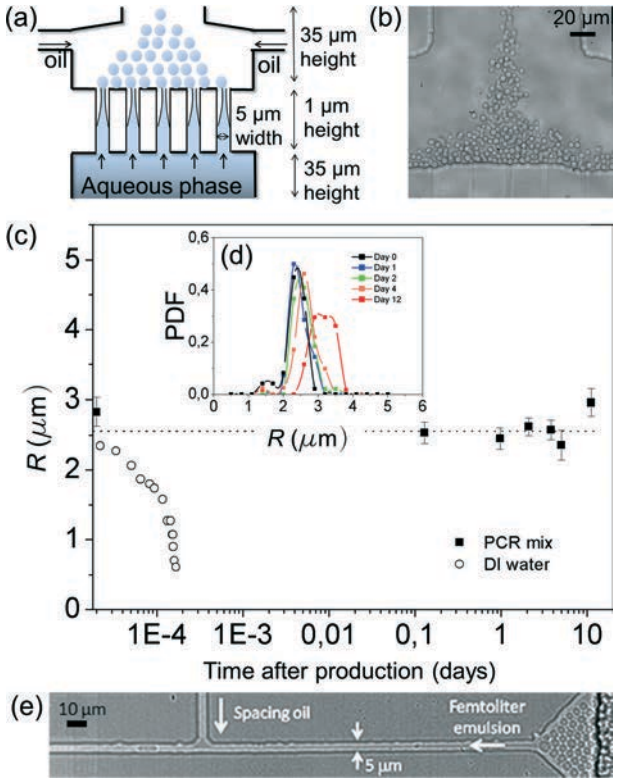

Fig. 5 Off-chip droplet incubation and reinjection. (a) Diagram of the parallelized femtolitre droplet maker. (b) Micrograph of a parallelized femtolitre droplet maker. A movie of the production of 65 fL droplets can be found in ESI† (Movie S6). (c) Evolution of the average radius of 65 fL droplets containing DI water (○) or PCR reagents (■) after droplet production and during storage at room temperature under mineral oil. (d) Evolution of the probability density function (PDF). Black: day 0, dark blue: day 1, green: day 2, orange: day 4, red: day 12. The monodispersity remained high during the first two days (coefficient of variation (CV) 0.02) and started to decrease after 4 days of incubation at room temperature (CV 0.16 at day 12). (e) Reinjection of a femtolitre emulsion. The channel was 1 μm high, increasing the apparent radius of droplets and enabling one-to-one injection without leaving standard soft lithography processes. A movie of emulsion reinjection can be found in ESI† (Movie S7).

continuous phase. On the other hand, the process is known to be inhibited by the addition of solutes.[77–79] In these papers, the solutes are assumed to be insoluble in the continuous phase. Let us denote the subscripts α for the droplet and β for the surrounding phase, 1 for water, 2 for oil and 3 for the solutes. The oil reservoir is assumed to be infinite. At equilibrium, water chemical potentials in the droplet and in the surrounding phase are equal:

$$\mu_{1,\alpha}(T,P_\alpha) = \mu_{1,\beta}(T,P_\beta) \tag{9}$$

The equilibrium is stable under the condition:[77]

$$\left[\frac{\partial\left(\mu_{1,\alpha}\left(T,P_\alpha\right)-\mu_{1,\beta}\left(T,P_\beta\right)\right)}{\partial R}\right]_{eq} > 0 \tag{10}$$

On the other hand, there is a relation between the fraction of water in the dispersed phase $x_{1,\alpha}$, the continuous phase $x_{1,\beta}$, and the Laplacian pressure term across the droplet interface:[72]

$$v_{m1}\frac{2\gamma}{R_{eq}} + RT\ln\left(x_{1,\alpha}\right) = RT\ln\left(x_{1,\beta}\right) \tag{11}$$

where v_{m1} is the molar volume of water and R_{eq} is the radius of the droplet at equilibrium.

Inside the droplet, $x_{1,\alpha} = 1 - x_{3,\alpha}$, where $x_{3,\alpha}$ is the fraction of solutes in the droplet at equilibrium; $\ln(1 - x_{3,\alpha})$ can be developed at first order in the vicinity $x_{3,\alpha} \ll 1$. The fraction of solutes in the droplet at equilibrium $x_{3,\alpha}$ is increased by a factor $(R_0/R_{eq})^3$ as droplets shrink:

$$v_{m1}\frac{2\gamma}{RT\ R_{eq}} - x_{3,\alpha,0}\left(R_0/R_{eq}\right)^3 = \ln\left(x_{1,\beta}\right) \tag{12}$$

where R_0 is the initial droplet radius and $x_{3,\alpha,0}$ is the initial fraction of solutes in the droplet. The application of condition (10) to eqn (12) gives the minimal fraction of solutes $x_{3,\alpha,0}^*$, and hence the minimal concentration of solutes $c_{3,\alpha,0}^*$, under which droplets are stable:

$$x_{3,\alpha,0} > x_{3,\alpha,0}^* = \frac{2\gamma v_{m1}}{3RTR_0} \tag{13}$$

$$c_{3,\alpha,0} > c_{3,\alpha,0}^* = \frac{2\gamma v_{m1}\rho_1}{3RTR_0 M_{solute}} \tag{14}$$

where ρ_1 is the volumic mass of water and M_{solute} is the molar mass of the solute. With droplet miniaturization, higher solute concentrations are needed to obtain stable droplets. For a typical M_{solute} = 300 g mol^{-1}, the minimum solute concentration as a function of droplet volume is presented in Table 1. Despite the increase in $c_{3,\alpha,0}^*$ on miniaturization, the values remain accessible experimentally, and femtolitre emulsions can easily be stabilized with proper formulation. We recall that the theory corresponds to an infinite reservoir of the continuous phase. However, in reality, the emulsion reservoir is finite, and shrinkage is expected to stop once the continuous phase is saturated with water and the chemical potentials in the droplet and in the surrounding phase are equal. In this case, the minimum initial solute concentrations required for stability, will be lower than those in Table 1.

In our experiments, droplets of 65 fL volume were produced using a parallelized step-emulsification device (Fig. 5a–b). The aqueous phase flows through an array of 37 narrow channels (1 μm high, 5 μm wide), and falls into a deep

Table 1 Minimum initial solute concentration $c_{3,\alpha,0}^*$ to obtain stable droplets, for several values of droplet volume, and M_{solute} = 300 g mol^{-1}

Droplet volume	4 fL	60 fL	500 fL	5 pL
Minimum solute concentration $c_{3,\alpha,0}^*$	80 μM	28 μM	14 μM	6 μM

Published on 27 November 2014. Downloaded on 05/12/2014 08:49:12.

reservoir of oil (35 μm deep), giving a total droplet production frequency of ~10 kHz. When composed of DI water ($c_{3,\alpha,0} = 0$), droplets disappeared in a few seconds (Fig. 5c, ○) in agreement with the theory. Droplets containing high solute concentration (for instance, PCR reagents, with $c_{3,\alpha,0}$ over ~2 mM) demonstrated a better stability. To go deeper, we measured the droplet size distribution by injecting an emulsion comprising 65 fL droplets containing PCR reagents between two glass slides and carried out image analysis (Fig. 5c–d). Just after their production, droplets shrunk slightly towards their radius of equilibrium (0.1 days). Then, the mean radius remained constant over 5 days, before increasing towards higher radii (12 days after the production). The variance in radius (Fig. 5d) remained small at short times (up to 2 days) and slightly increased at longer times (12 days).

The slight initial shrinking is most likely caused by the low but non-zero solubility of solutes in oil. In this case, size distribution depends on the diffusion rates of the solutes and is expected to decrease slightly in the case $c_{3,\alpha,0} \gg c_{3,\alpha,0}^*$, $c_{3,\beta,0} = 0$.[79] The increase in size distribution observed at long time scales most likely results from coalescence events rather than Ostwald ripening because the average droplet volume increases.

When performing chemical or biological reactions in droplets, many studies focus on performing incubation steps on-chip, but this is associated with a variety of technological issues, notably related to evaporation due to the porosity of PDMS. A way to avoid these issues is to recover the emulsion off-chip, incubate off-chip, and reinject the emulsion into another chip for analysis.

After overnight incubation at room temperature, the 65 fL droplets containing PCR reagents were reinjected and spaced with fluorinated oil with 2% fluorosurfactant. Regular spacing of droplets demands a nozzle as narrow as the droplet diameter, to allow just one droplet to be separated by spacer oil at a time. To obtain such characteristics with 65 fL droplets, the channel height was lowered to 1 μm. The squeezed micrometric droplets have an increased effective radius and could be reinjected in a controlled way in 5 μm width channels accessible by standard soft lithography process with a chrome mask. (Fig. 5e).

To summarize, aqueous femtolitre droplets are thermodynamically stable, provided the aqueous phase contains a low concentration of solute. Under these conditions femtolitre droplets can be incubated for a few days off chip and reinjected on-chip for further analysis. This stability ensures that incubation of biochemical reactions can be performed inside femtolitre droplets, as presented below.

Polymerase chain reaction (PCR) in femtolitre droplets

The Polymerase chain reaction (PCR) is one of the most important biochemical reactions, allowing exponential amplification of target DNA *via* cycles of enzymatic polymerisation with temperature cycling. However, one can question the impact of droplet miniaturization on the amplification yield, since the surface to volume ratio varies inversely to the droplet radius, and surface effects are expected to become increasingly important.

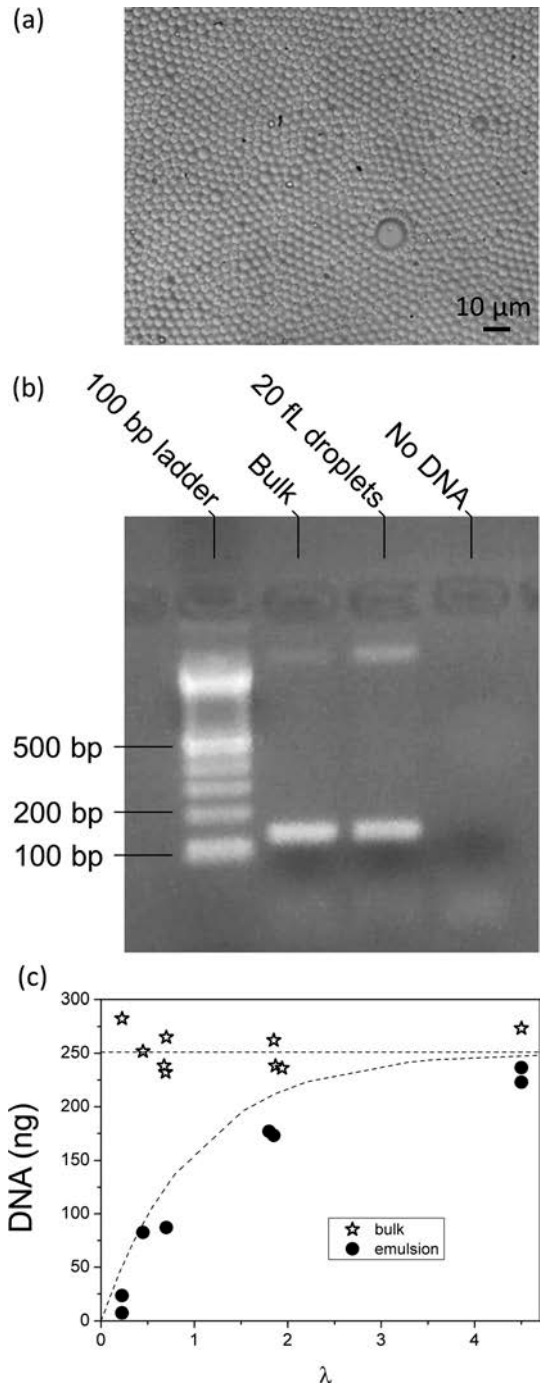

Fig. 6 PCR in droplets. (a). Picture of a PCR emulsion after thermocycling. (b) Example of analysis by agarose gel electrophoresis of PCR in 20 fL droplets, mean number of template DNA molecules per droplet $\lambda = 1.85$. (c) Final yield of DNA after PCR *versus* the mean number of template DNA molecules, λ, per 65 fL reaction volume in bulk (stars), and in 65 fL droplets (dots). Dotted lines represent the mean amplification in bulk, and the expected Poisson distribution in emulsion.

This journal is © The Royal Society of Chemistry 2014

Appendix C

Article : Dynamics of a small number of droplets in microfluidic Hele-Shaw cells

Exp Fluids (2014) 55:1728
DOI 10.1007/s00348-014-1728-2

RESEARCH ARTICLE

Dynamics of a small number of droplets in microfluidic Hele–Shaw cells

B. Shen · M. Leman · M. Reyssat · P. Tabeling

Received: 12 September 2013 / Revised: 8 April 2014 / Accepted: 10 April 2014 / Published online: 1 May 2014
© Springer-Verlag Berlin Heidelberg 2014

Abstract We investigate the dynamics of a small number of droplets ($N = 1, 2, 3$) in microfluidic Hele–Shaw cells. We study the cases $N = 1$, 2, and 3 droplets and analyze the influence of the side walls. In the course of the study, we observe spontaneous alignment of droplet pairs, pair exchanges, droplet escape, multiple reflections between walls, i.e., a number of phenomena that have not been reported yet. As a whole, using pairwise far-field dipolar interactions between droplets, along with treating the walls as mirrors, allows to reproduce the observations, even though limitations in the predictability of the model are pointed out in a few cases. From a more practical prospective, the work shows that the behavior of elementary droplet assemblies can be put under acceptable experimental control in a wide variety of situations, a feature potentially interesting for self-assembly, mixing, or transport of particles in microfluidic environments.

1 Introduction

Recent studies have revealed the rich dynamics of systems of droplets and particles (cylindrical and spherical) confined in shallow microfluidic systems, i.e., in micro Hele–Shaw cells. Small amplitude longitudinal and transverse waves (Beatus et al. 2006), along with shock waves induced by localized jams (Champagne et al. 2011), have been observed in droplet lines. Shocks, pattern formation, and dislocations have been observed in 2D populations of droplets (Beatus et al. 2007, 2012; Baron et al. 2008). In the presence of side walls, oscillatory and chaotic regimes have been calculated and observed (Uspal and Doyle 2012a). Studies of small clusters have revealed the existence of stable and metastable configurations (Uspal and Doyle 2012b).

The underlying physics of these systems is the following: Flattened droplets or particles, confined in Hele–Shaw cells, and subjected to a steady flow, are advected downstream. These droplets, being slowed down by the walls, move at speeds smaller than the upstream velocity. In such circumstances, each droplet generates, in its own frame of reference, multipolar interactions with its neighbors. These interactions give rise to the dynamics revealed in the above references (Happel and Brenner 1965; Evans and Sackmann 1988; Guyon et al. 2001; Cui et al. 2004; Bhattacharya et al. 2006; Diamant 2009).

Owing to the complexity of the problem, simplifications are currently made in the literature. Most often, the problem is viewed as two-dimensional, and the interactions are treated as dipolar and pairwise (Beatus et al. 2012). The extent to which these approximations are acceptable for describing experimental situations can be questioned. Higher-order interactions may come into play. Lubricating films, flows driven by gradients of curvature, and boundary layers close to the walls and in the vicinity of the droplets boundaries may also play a role by conveying 3D perturbations. The goal of the present experiment is to carry out a quantitative analysis of the dynamics of populations

B. Shen and M. Leman have contributed equally to this paper.

Electronic supplementary material The online version of this article (doi:10.1007/s00348-014-1728-2) contains supplementary material, which is available to authorized users.

B. Shen · M. Leman · M. Reyssat · P. Tabeling (✉)
MMN, Gulliver, ESPCI ParisTech, 10 Rue Vauquelin, Paris 75005, France
e-mail: patrick.tabeling@espci.fr

M. Leman
e-mail: marie.leman@espci.fr

including up to three droplets in micro Hele–Shaw cells and compare the results to the current approximate theoretical modeling. As a whole, the present work shows that the behavior of elementary droplet assemblies is well described by assuming 2D pairwise dipolar far-field interactions. Despite this approximation must be taken cautiously, we demonstrate that the behavior of small clusters is predictable within this model when droplets enclose, or even touch each other, at the expense of reasonable discrepancies. The present work suggests that developing strategies of self-assembly, mixing, or transport in microfluidic devices, based on the controlled dynamics of a few interacting particles or droplets, may be envisageable.

2 Experimental system

Soft lithography technique is used to fabricate the microfluidic devices. In almost all cases (i.e., droplet pairs and triplets), the systems are composed of two T junctions connected to a long shallow channel defining our micro Hele–Shaw cell (Fig. 1). For isolated droplet studies, the two T junctions are replaced by a single one, injecting droplets at the center of the micro Hele–Shaw cell. To avoid couplings between two parallelized T junctions studied earlier (Barbier et al. 2006) and better monitor the production, the two T junctions are filled independently. Oil droplets are independently formed at the T junctions and are driven into the micro Hele–Shaw cell, at controlled

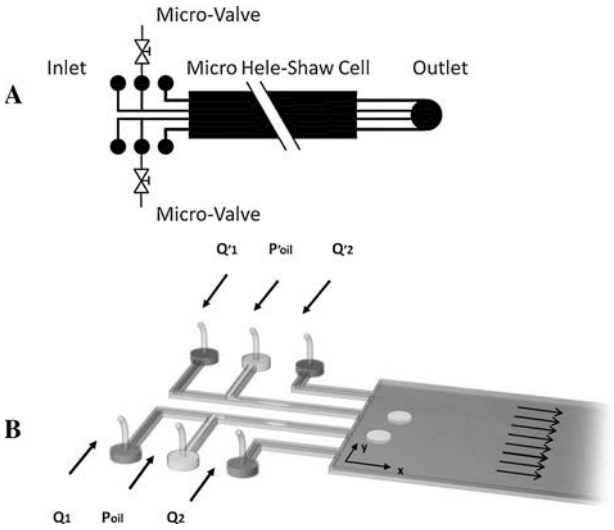

Fig. 1 **A** Sketch of the microfluidic device. Two independent externalized valves are connected to the oil inlets to regulate the droplet production. **B** Sketch of the experimental device showing how it operates: Oil droplets (*white*) are formed at two T junctions and injected into the micro Hele–Shaw cell. Two entries are added to the micro Hele–Shaw cell, in order to favor flow uniformity of the continuous phase (*gray*)

times. Two additional inputs of water allow to improving the cross-stream homogeneity of the outer phase flow conditions. Should these inputs be absent, the droplets would systematically drift laterally and small initial separations between them would be impossible to obtain.

Oil and water are injected at the T junctions under controlled pressure conditions, using a MFCS Fluigent controller. By using an integrated flowmeter, we measure the corresponding water flow rates (Q_1 and Q'_1). The water entries that homogenize the flow structure in the Hele–Shaw cell (see Fig. 1) are controlled by two syringe pumps NEMESYS, providing Q_2 and Q'_2. The total flow rate of the water in the Hele–Shaw cell is thus $Q_T = Q_1 + Q'_1 + Q_2 + Q'_2$. The corresponding speed at infinity U_∞ is obtained by dividing the total flow rate Q_T by the micro Hele–Shaw cross-sectional area.

In practice, the Hele–Shaw cells heights h vary from 18 to 48 μm, the width of the T junctions is 200 μm, the widths of Hele–Shaw cells vary from 500 to 3,000 μm, and their lengths l range between 1 and 3 cm. In the micro Hele–Shaw cell, the aspect ratio height over width therefore ranges from 0.006 to 0.1, a range acceptable for applying the lubrication approximation.

Concerning the microfabrication, we use PDMS (Dow Corning SYLGARD 184, 1/9 ratio of curing agent to bulk material) or NOA (Norland Optical Adhesive 81). The advantage of using NOA is to suppress any mechanical deformation in the micro Hele–Shaw cell that would affect the droplet trajectories. In the case of PDMS, standard soft lithography is used (Tabeling 2005). Thereafter, we close the system by binding thermally cured PDMS to a glass slide, after exposing the surfaces to oxygen plasma and bringing them into contact. In the case of NOA, we follow the protocol described by Bartolo et al. (2008).

All the experiments employ fluorinated oil (FC 3283, viscosity $\mu = 1.4$ mPa.s) as the dispersed phase and DI water with 1 % w/w sodium dodecyl sulfate (SDS) surfactant as the continuous phase (interfacial tension 18 mN m^{-1}). The sizes of the droplets and the separation distances between two successive droplets in each T junctions are tuned by using externalized pneumatic valves, monitored by a Labview program, using a technique described previously (Goulpeau et al. 2005; Galas et al. 2009). These externalized valves operate with a small dead volume ($\sim$10 nL), a small displaced volume (<1 nL), and a fast response time ($\sim$10 ms). These characteristics guarantee a precise control over the droplet production. Droplets can thus be produced on demand, in an accurate manner. Typical droplet radii of the pancake-like droplets range between 100 and 200 μm.

Throughout the experiments, the water flow rate varies from 2 to 30 μL mn^{-1}. The capillary number $Ca = \mu U/\gamma$ ranges between 2.5×10^{-6} and 3.7×10^{-5}, and the

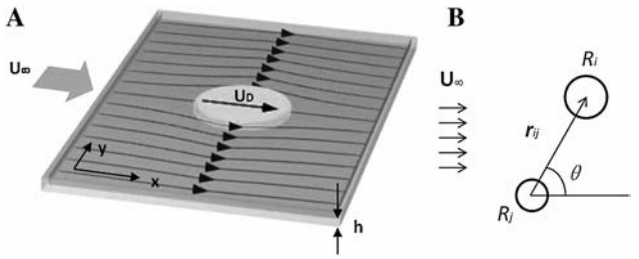

Fig. 2 **A** Sketch of the streamlines around an isolated disk-like droplet confined between the channel "floor" and "ceiling," in a Hele–Shaw cell. **B** Sketch of the general case where the droplets are different

Reynolds number $Re = \rho UL/\mu$ varies between 2.2×10^{-3} and 3.4×10^{-2}.

The droplet motions are recorded with a fast camera (Photron) through an inverted microscope (5×, Zeiss). Image processing is used to extract the droplets characteristics such as their radius R, the distance between droplets r, the orientation angle θ with respect to the upstream flow direction, and their longitudinal and transverse velocities U_x and U_y.

3 Theoretical modeling

In the case of a single droplet, the geometry of the system, along with the axes, is illustrated in Fig. 2.

An isolated droplet immersed in a uniform flow $\mathbf{U}_\infty$ in a Hele–Shaw cell experiences a drag force that conveys it downstream (see Fig. 2A). The droplet motion $\mathbf{U_D}$ has an amplitude smaller than the upstream speed $\mathbf{U}_\infty$, owing to the friction exerted by the walls onto the droplet. In an infinite medium, we may assume the following relation: (Beatus et al. 2012)

$$\mathbf{U}_D = \beta \mathbf{U}_\infty \tag{1}$$

where β is a parameter depending, in the small Reynolds number limit, for incompressible Newtonian fluids and in an infinite medium, on three-dimensionless numbers: the radius over the channel height and the viscosity ratio between the two fluids along with the capillary number. To the best of our knowledge, although work has been done on related topics (Diamant 2009; Eri and Okumura 2011), no systematic calculation of β is available in the literature. For the sake of simplicity, and in good consistency with the experimental literature (Beatus et al. 2012), we will assume that β is independent of the flow conditions, an assumption that will be confirmed empirically in Sect. 4 within the range of experimental conditions we investigated.

When several droplets move in the Hele–Shaw cell, the current approach consists in considering that the interactions are pairwise, dipolar, and far-field. Under these assumptions, the expression for the speed of droplet i, subjected to the mean flow and the action of the other droplets, reads (Beatus et al. 2012; Uspal and Doyle 2012a, b):

$$\mathbf{U}_i = \beta_i \left(\mathbf{U}_\infty + \sum_{j \neq i} \mathbf{v}^{(ij)} \right) \tag{2}$$

where $\mathbf{v}^{(ij)}$ is defined by

$$\mathbf{v}^{(ij)} = \frac{2\mathbf{r}_{ij}}{r_{ij}^4} \left(\mathbf{r}_{ij} \cdot \mathbf{p}_j \right) - \frac{\mathbf{p}_j}{r_{ij}^2} \tag{3}$$

in which one has

$$\begin{aligned} \mathbf{p}_j &= R_j^2 \left(\mathbf{U}_j - \mathbf{U}_{\text{jext}} \right) \\ \mathbf{r}_{ij} &= \mathbf{r}_i - \mathbf{r}_j \end{aligned} \tag{4}$$

in which $\mathbf{U}_{\text{jext}} = \mathbf{U}_j/\beta_j$ is the local upstream flow droplet j is subjected to. The differences in the droplet sizes are expressed through the radius R_j and the factor β_j, which may differ from one droplet to the other.

The system is linear in $\mathbf{U}_i$. It must be solved to determine the droplet speed at each point. Thereafter, the droplet position can be calculated. The process must be iterated to obtain the trajectories of all the droplets. Nonetheless, in the far-field limit, the ratio of the typical radius over the typical intradroplet distance is small, and $\mathbf{U}_{\text{jext}}$ can be replaced by $\mathbf{U}_\infty$, so that system (2) can be simplified into the following:

$$\mathbf{U}_i = \beta_i \left(\mathbf{U}_\infty + \sum_{j \neq i} (1 - \beta_j) \left(\frac{R_j^2}{r_{ij}^2} \mathbf{U}_\infty - \frac{2R_j^2 \mathbf{r}_{ij}}{r_{ij}^4} \left(\mathbf{r}_{ij} \cdot \mathbf{U}_\infty \right) \right) \right) \tag{5}$$

Equation (5) can be brought to a more convenient form by working in a system of coordinates in which U_∞ lies along x (as shown in Fig. 2) i.e.,:

$$\mathbf{U}_\infty = U_\infty \hat{\boldsymbol{x}} \tag{6}$$

(in which $\hat{\boldsymbol{x}}$ is the unit vector along x). In such a system, one obtains the following equations:

$$\begin{aligned} U_{ix}^{(0)} &= \frac{\mathrm{d}x_i}{\mathrm{d}t} = \beta U_\infty \left(1 + \sum_{j \neq i} \frac{(1 - \beta_j) R_j^2 \left(r_{ijy}^2 - r_{ijx}^2 \right)}{r_{ij}^4} \right) \\ U_{iy}^{(0)} &= \frac{\mathrm{d}y_i}{\mathrm{d}t} = \beta U_\infty \sum_{j \neq i} \frac{-2(1 - \beta_j) R_j^2 r_{ijx} r_{ijy}}{r_{ij}^4} \end{aligned} \tag{7}$$

in which

$$r_{ijx} = x_i - x_j \text{ and } r_{ijy} = y_i - y_j \tag{8}$$

defines a dynamical system that can be integrated by using standard MatLab routines. We used this formulation to compare theory with experiment.

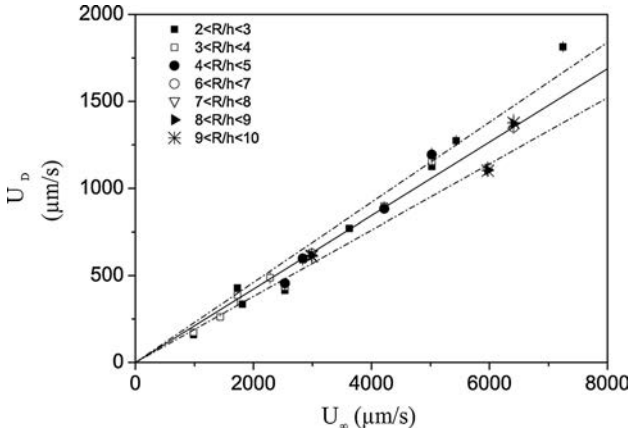

Fig. 3 Measurements of the velocity of an isolated droplet U_D as a function of the velocity U_∞, regrouped by values of *R*/*h*. The *solid line* is a linear fit of the data, with a slope equal to 0.21. The *error bars* are the min and max values obtained, for each *R*/*h*, by varying the droplet radius and the channel height. *Error bars* are sometimes not visible, being smaller than the points. Within the *error bar*, β does not depend on *R*/*h* and its mean value is 0.21 ± 0.02 (*solid line*)

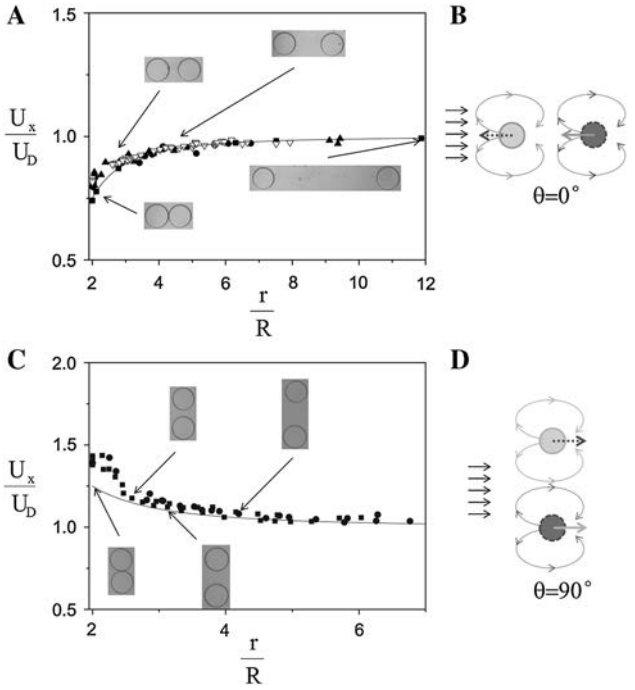

Fig. 4 Velocity of droplet pairs, normalized by the velocity of an isolated droplet, as a function of their distances normalized by their radii. The velocity of isolated droplets was measured in situ. **A** Pairs of droplets oriented in the streamwise direction, $\theta = 0°$, (*inverted triangle*) PDMS system, $h = 18$ μm, $w_2 = 3{,}000$ μm, $U_D = 612$ μm s^{-1}, (*filled square box*) NOA system, $h = 37$ μm, $w_2 = 3{,}000$ μm, $U_D = 680$ μm s^{-1}, (*filled circle*) PDMS system, $h = 48$ μm, $w_2 = 3{,}000$ μm, $U_D = 1{,}485$ μm s^{-1}, (*filled triangle*) PDMS system, $h = 48$ μm, $w_2 = 3{,}000$ μm, $U_D = 1{,}700$ μm s^{-1}. **B** Representation of the recirculations generated by each droplet in the *horizontal* position. The dark droplet generates a force on the clear droplet, represented by a *dark dotted arrow*. Respectively, the force generated by the clear arrow on the dark one is represented by a clear *solid arrow*. **C** Pairs of droplets oriented perpendicularly to the direction of the flow, $\theta = 90°$, (*filled square box*) NOA system, $h = 37$ μm, $w_2 = 3{,}000$ μm, $U_D = 322$ μm s^{-1}, (*filled circle*) NOA system, $h = 37$ μm, $w_2 = 3{,}000$ μm, $U_D = 462$ μm s^{-1}. Droplet radius varies between 100 and 200 μm. The *solid lines* show the theoretical results based on Eq. (10). **D** Representation of the recirculations generated by each droplet in the *vertical position*. Forces generated by each droplet are represented by *arrows* of the droplet color

4 Results and discussion

4.1 The case $N = 1$ (isolated droplets)

We first investigate the case of a single droplet moving along the micro Hele–Shaw cell. In this case, the system contains a single T junction along with the two diluting inlets; a single droplet penetrates the micro Hele–Shaw cell. In all cases, for a fixed channel geometry, we obtain a linear relation between the droplet speed U_D and the upstream flow velocity U_∞ (Fig. 3). Within the experimental error, the relation we obtain experimentally can thus be expressed in the form:

$$\mathbf{U}_D = \beta \mathbf{U}_\infty \tag{9}$$

in which β is the proportionality factor, independent of U_∞, in agreement with the theory (1).

Experiments at different *R*/*h* are carried out, varying both the radius *R* (100–290 μm) and the height *h* (18–48 μm). Widths vary from 1,000 to 3,000 μm, and we make sure that the minimal distance to the wall is 3R to avoid confinement effects. Figure 3 shows that within ±10 %, the slope β does not depend on the ratio *R*/*h*. Its averaged value is 0.21 ± 0.02. Arguments shown later will confirm this conclusion, by indicating that the variations of β with the droplet size are on the order of 10^{-3}.

4.2 The case $N = 2$ (pairs of droplets)

4.2.1 The case of identical droplets

We start here with the case where droplets have the same size. Figure 4A shows the evolution of a droplet pair aligned with the streamwise direction, for different separation distances. As shown in Fig. 4A, the pair speed increases with the separation, up to a point when the droplets cease to interact and consequently move as isolated droplets.

An important observation is that, as shown in Fig. 4A, the ratio of the pair speed U_x over U_D does not vary with the parameter *R*/*h*. In this plot, *R*/*h* has been varied between 2.5 and 10, and the data collapse onto a single curve, function of *r*/*R*. From dimensional grounds, within the small Reynolds numbers limit, one may conclude that the speed ratio depends on *r*/*R* only. The measurements agree well with the model, which yields to the following expressions: (see Appendix 1.a of ESM)

$$U_x = \beta U_\infty \left(1 - (1-\beta)\frac{R^2}{r^2}\cos 2\theta\right)$$
$$U_y = -(1-\beta)\beta U_\infty \frac{R^2}{r^2}\sin 2\theta \quad (10)$$

in which r is the initial pair separation and θ (mod. π) is the angle between the line joining the droplets centers and the Ox axis (see Fig. 2B). Equation (10) shows that droplet pairs displace at an angle equal to 2θ with respect to the x axis. Droplet pairs normal to the x axis move faster than isolated droplets. On the other hand, isolated droplets move faster than droplet pairs aligned along x (so-called peloton effect, Beatus et al. 2006).

The solutions (10) are represented as solid lines in Fig. 4. It agrees well with the experiment down to $r/R = 2$, where deviations do not exceed 20 %. This deviation is surprisingly low if we take into account that the far-field approximation is no longer valid in this region.

Theory (10) and experiment agree well also in the case where the pair is oriented normally to the upstream velocity (see Fig. 4C). In this case, the doublet moves faster than an isolated droplet. This can be called an "antipeloton" effect, because here the drag developed by the upstream flow appears larger than for isolated droplets. This can be explained by noting that the presence of the droplet pair deviates the incoming streamlines more importantly than in the isolated case. Thereby, larger local speeds and larger drags can be expected. More specifically, each droplet generates dipolar motions (Fig. 4B, D) that exert drag forces on neighboring droplets. In the horizontal case, those forces are directed oppositely to the flow direction as pictured in Fig. 4B, while they are directed along the flow in the vertical case (Fig. 4D). As a consequence, dipolar interactions result, respectively, in a reduction/increase of the drag in the horizontal/vertical case; horizontal pairs are slowed down and vertical pairs fastened.

The acceptable agreement between theory and experiment is further confirmed by investigating the behavior of droplets pairs oriented by angle θ with respect to the upstream velocity. The pair speeds along the x and y directions, measured for different angles θ, are shown in Fig. 5. Here, the droplets touch each other ($r/R = 2$). We obtain, as expected theoretically from formulas (10), that the pair speeds develop sine-like behaviors with respect to 2θ. The theory, represented by full lines, agrees well with the x speed component of the droplet pair, without any fitting parameter, despite the long-range hypothesis is not valid here. This agreement does not appear in the transverse component that is overestimated by the theory by 30 %. The transversal speed variation is only qualitatively predicted by the model.

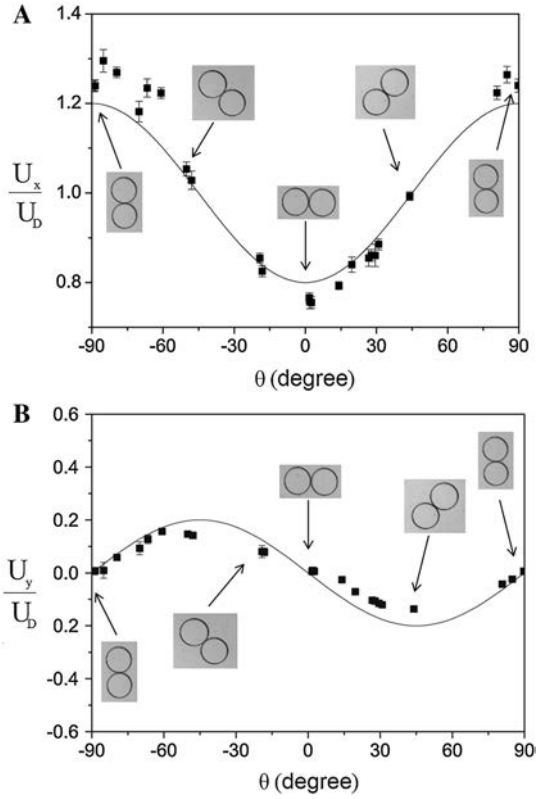

Fig. 5 Velocity of contacting droplet pairs ($r/R = 2$) normalized by the velocity of an isolated droplet, as a function of the angle of orientation θ. The isolated droplet velocity was $U_D = 1{,}100$ μm s^{-1}. PDMS system, $h = 46$ μm, $w_2 = 3{,}000$ μm. **A** Measurements along x. Note that in this set of experiments, when the pair is *vertical*, the ratio U_x/U_D is smaller than on Fig. 4C. This variability is compatible with the standard type deviation we obtain experimentally over a set of experiments conduced in the same conditions. **B** Measurements of the speed component along y. The *solid lines* show the theoretical results given by Eq. (10)

4.2.2 *The case of droplets of different sizes initially aligned along the downstream direction*

We consider here the case of droplets of different sizes initially aligned along the downstream direction. We monitor the distance between the droplet centers $\delta(t) = x_2(t) - x_1(t)$ in three different cases (Fig. 6): a small droplet moving behind a large one (a), a large droplet moving behind a small one (c), and for the sake of comparison, two identical droplets placed one behind the other (b). Droplets initially lie parallel to the centerline of the micro Hele–Shaw cell ("horizontal" line). Their disalignement being at most of 10° can be neglected. The conclusion is suggested by the inspection of Fig. 5 and supported by the evidence that there is no pair rotation (see Sect. 4.2.3). In all these experiments, droplets cover a distance larger than 30 times their radius. For identical droplets, we recover the result, shown previously, that their

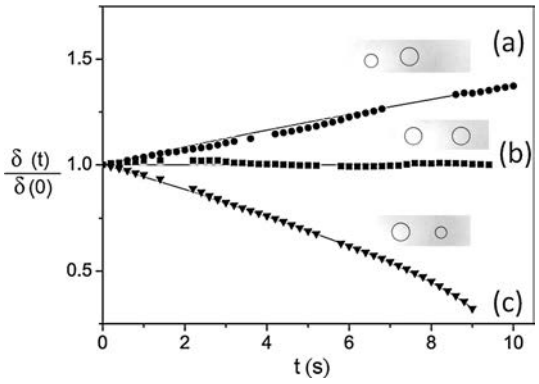

Fig. 6 Evolution of the distance between droplets as a function of time. *Solid lines* depict the theoretical model using an adjustment of the parameter $\Delta\beta = \beta_2 - \beta_1$. PDMS system, $h = 48$ μm, $w_2 = 3{,}000$ μm. *a* $R_2 = 209$ μm, $R_1 = 155$ μm, $\Delta\beta = 0.0055$. *b* $R_2 = 206$ μm, $R_1 = 201$ μm. *c* $R_2 = 131$ μm, $R_1 = 205$ μm, $\Delta\beta = -0.0157$. For identical droplets (case *b*), theory predicts that their separation remains constant (*horizontal solid line*)

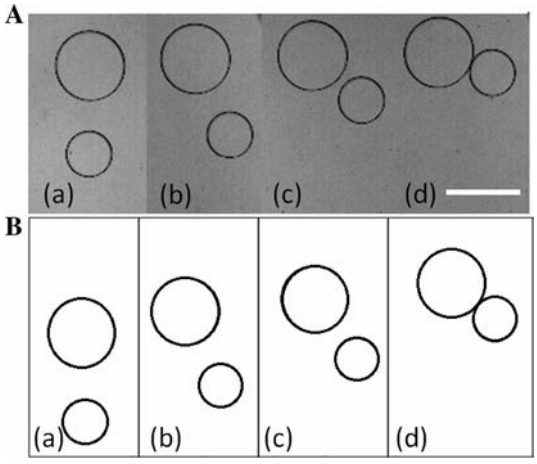

Fig. 7 **A** Evolution of a pair of droplets with different size ($R = 250$ and 167 μm, respectively) oriented normally to the upstream velocity $U_\infty = 6{,}105$ μm s^{-1}. PDMS system, $h = 48$ μm, $w_2 = 3{,}000$ μm. *a* $t = 0$ s; *b* $t = 1.6$ s; *c* $t = 3.2$ s; *d* $t = 4$ s. The external phase flows from *left* to *right*. **B** The same situation calculated by using Eq. (7) with the parameters of Figure **A** (U_∞, radii, initial positions, $\beta = 0.2$) *a* $t = 0$ s; *b* $t = 2.97$ s; *c* $t = 4.06$ s; *d* $t = 5$ s. A *vertical* drift on the order of 50 μm s^{-1} is found in the simulation, which is higher than the experimental drift. The *scale bar* corresponds to 500 μm

separation does not change with time, within a 5 % experimental uncertainty. As droplets are different, there is no more steady state: The separation diverges in case (a), while it contracts in case (c).

The long-time behavior of the "repelling" case (a) indicates that the factor β, introduced in Eq. (1), must slightly increase with the droplet size, in a way undetectable by measurements made on isolated droplets, owing to experimental uncertainty, as pictured in Sect. 4.1. We thus compared the observations with the theory by introducing a free parameter $\Delta\beta = \beta_2 - \beta_1$, which takes the variation of β with the droplet size into account. With this adjustable parameter, the theoretical predictions is given by the following equation: (see Appendix 1.b of ESM)

$$\frac{\mathrm{d}\delta}{\mathrm{d}t} = (\beta_2 - \beta_1)U_\infty + \frac{(1-\beta_2)\beta_1 R_2^2 - (1-\beta_1)\beta_2 R_1^2}{\delta^2} U_\infty \tag{11}$$

The solid lines, representing the above formula, agree well with the experiment.

From these experiments, we can provide an estimate for the variations of β with the droplet radius R, for a range of R/h varying between 2.5 and 5.

$$\frac{\Delta\beta}{\Delta R} \approx 1.6 \times 10^{-4} \pm 0.5 \times 10^{-4}\ \mu\mathrm{m}^{-1}$$

The very low value of the $\frac{\Delta\beta}{\Delta R}$ explains that those variations were not detectable for isolated droplets in Sect. 4.1. It is remarkable that such small variations control the dynamics of droplet pairs, in the case where droplets are unequal. This point must be taken seriously in studies attempting to model the dynamics of populations with droplets of different sizes.

4.2.3 *Spontaneous pair alignment along the downstream direction*

We observed an interesting phenomenon with unequal droplet pairs placed normally to the upstream direction. Their trajectory is shown in Fig. 7A. The pair rotates up to a point where it almost aligns with the downstream direction. In the meantime, the droplets approach each other and cluster. Eventually, the pair moves steadily downstream (not shown). The physical origin of the rotation comes from the fact that the large droplet develops vigorous recirculations that advect its small partner around it. The effect cancels out when the droplets are identical.

Figure 7B shows calculations based on Eq. (7), without fitting parameter. The approximate theory reproduces well the internal evolution of the pair (rotation and mutual approach), prior to the collision. Beyond the collision time, the calculation indicates that the droplets interpenetrate, which is nonphysical. We thus stopped the calculation after the droplets come into contact.

4.3 The case $N = 3$: pair exchange

For the case $N = 3$, we analyzed a number of different situations and figured out typical behaviors. We found a phenomenon that is well known in vortex dynamics, called "pair exchange" [a similar effect is known in the field of sedimentation (Guazzelli and Morris 2012)]. The phenomenon is shown in Fig. 8, for two different initial conditions. In Fig. 8A, the three droplets initially lie along the streamwise

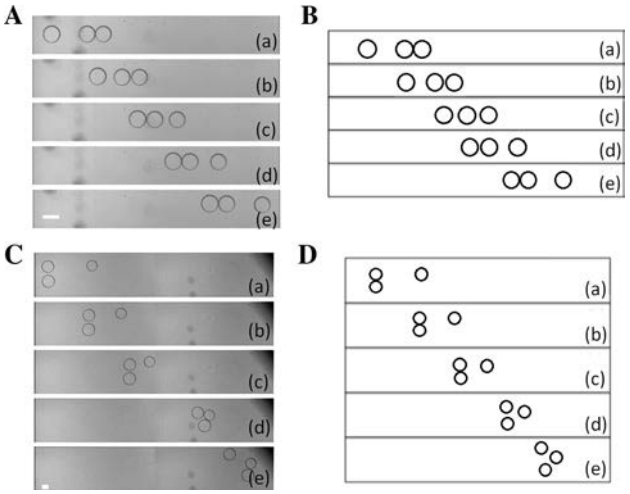

Fig. 8 Image sequences of triplets of droplets moving from *left* to *right* in a Hele–Shaw cell. **A** An isolated droplet catches up with a "horizontal" pair; then, the droplet ahead is released ($R = 99$, 94 and 94 μm, respectively). PDMS system, $h = 48$ μm, $w_2 = 1{,}300$ μm; flow velocity is $U_\infty = 2{,}352$ μm s^{-1}. *a* $t = 0$ s; *b* $t = 1.2$ s; *c* $t = 2.4$ s; *d* $t = 3.6$ s; *e* $t = 4.8$ s. **B** Numerical simulation with the parameters of Figure **A**: U_∞, initial positions, $\beta = 0.2$. Here, the droplets radii are assumed to be identical and equal to the mean radius ($R = 96$ μm). *a* $t = 0$ s; *b* $t = 1.56$ s; *c* $t = 2.5$ s; *d* $t = 3.75$ s; *e* $t = 5.93$ s. **C** A "vertical" pair catches up with an isolated droplet and then moves downstream, abandoning its former partner ($R = 165$, 172, and 150 μm, respectively). PDMS system, $h = 48$ μm, $w_2 = 1{,}300$ μm; flow velocity is $U_\infty = 3{,}450$ μm s^{-1}. *a* $t = 0$ s; *b* $t = 1.2$ s; *c* $t = 2.4$ s; *d* $t = 3.6$ s; *e* $t = 4.8$ s. **D** Numerical simulation with the parameters of Figure **C**: U_∞, initial positions, $\beta = 0.2$. Here, the droplets radii are assumed to be identical and equal to the mean radius ($R = 162$ μm). *a* $t = 0$ s; *b* $t = 1.4$ s; *c* $t = 2.66$ s; *d* $t = 7.03$ s; *e* $t = 10$ s. The *scale bars* correspond to 200 μm

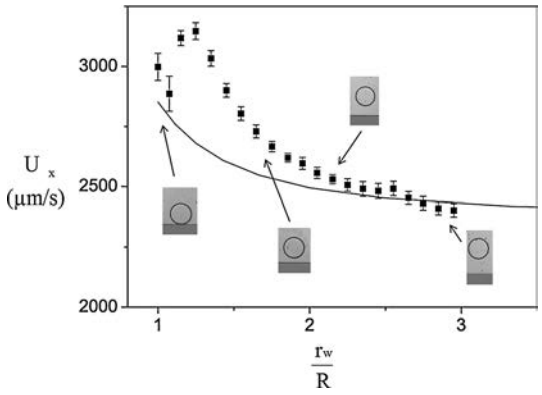

Fig. 9 Speed of a single droplet moving along a wall plotted versus the distance between the droplet center and the wall r_w over the droplet radius R. The system is made in PDMS ($h = 46$ μm, $w_2 = 1{,}300$ μm). The radius of the droplet is $R = 140$ μm. The speed of the continuous phase U_∞ is 10,800 μm s^{-1}. It is measured in situ by seeding the flow with micrometric particles. The side wall is shown in *dark gray*. In the single-image approach, the droplet and its image form a "vertical" pair whose speed can be calculated by using Eq. (10)

direction, one pair standing ahead of their third partner. Since the isolated droplet moves faster than the pair, it will approach the pair. Eventually, the droplet located at the front detaches and gradually escapes the new pair formed by two other droplets. We thus obtain a horizontal "exchange." This horizontal exchange is the three-body version of the shock-wave phenomenon discussed in previous work (Beatus et al. 2006; Champagne et al. 2011).

In another situation (Fig. 8C), a "vertical" pair (i.e., normal to the streamwise direction) stands behind an isolated droplet. In this case, the pair moves faster and thus will come closer to the isolated droplet. We observe that as the pair approaches their partner, a droplet detaches from the triplet newly formed; eventually, the droplet is left behind, while the new vertical pair formed with its former partner moves downstream at larger speed and consequently escapes away from it.

The two phenomena are correctly reproduced by Eq. (7). This is especially true for the horizontal exchange (Fig. 8B), where a semi-quantitative agreement is obtained, again without fitting parameter. Figure 8D shows a more complicated situation: The approach of the vertical pair is well reproduced by Eq. (7), as is the outcome of the exchange, but there is a discrepancy between the experiment and the theory concerning the duration of the exchange process. In the experiment, full exchange is observed at 4.8 s, while in the simulation, we need larger times (beyond 10 s) to reach a state where the exchange can be considered as completed. The reason for this discrepancy is due to the fact that as the droplets get close to each other (See Fig. 8A, d, C, d), Eq. (7) becomes inaccurate. The inaccuracies propagate at later times, reaching substantial levels. Calculations nonetheless show that Eq. (7) still represents qualitatively well the evolution of the system at late times in this particular case.

4.4 Interactions with the walls

4.4.1 A single droplet moving along a wall

In these series of experiments, we drive a single droplet along a wall and measure its speed as a function of its distance to the wall r_w (see Fig. 9). The other wall is located at a distance at least about 800 μm (around 6R) so that its influence may be neglected. We observe that the speed of a droplet increases as its distance to the wall decreases. This is consistent with the idea that the lateral wall acts as a mirror and consequently develops an image that forms a pair with the droplet, oriented normally with respect to the streamwise direction. The "vertical" pair (formed by the droplet and its image) moves therefore faster than the isolated droplet.

At a quantitative level, we compared the droplet speed with the theory (solid line), again without fitting parameter,

taking the wall as a mirror and the droplet as pointwise. The distance to the wall is r_w, so that the distance to the droplet image is $r = 2\ r_w$. We found good agreement between the theory and the experiment for $r_w/R > 1.8$. For short distances ($r_w/R < 1.8$), the evolution seems more complicated: The measured speed is substantially higher than expected close in a range of r_w/R lying between 1.25 and 1.8. Surprisingly, the discrepancy decreases as the droplet approaches the wall further. The discrepancy observed between 1.25 and 1.8 is probably due to the fact that the far-field assumption becomes inaccurate.

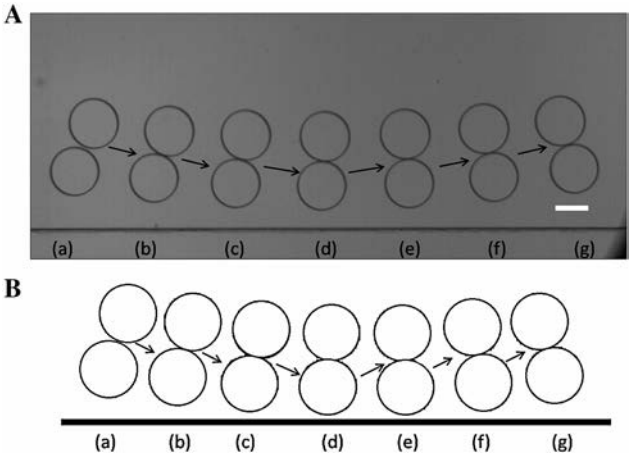

Fig. 10 **A** Evolution of a pair of droplets approaching the side wall ($R = 146$ and 142 μm, respectively) at an incident angle equal to 21°. The external phase flows from *left* to *right*. PDMS system, $h = 48$ μm, $w_2 = 1{,}300$ μm, flow velocity $U_\infty = 4{,}098$ μm s^{-1}. *a* $t = 0$ s; *b* $t = 0.4$ s; *c* $t = 0.8$ s; *d* $t = 1.2$ s; *e* $t = 1.6$ s; *f* $t = 2$ s; *g* $t = 2.4$ s. The *scale bar* corresponds to 200 μm. **B** Numerical simulation with the parameters of Figure **A** (U_∞, $R = 144$ μm, initial positions provided by the experiment, $\beta = 0.2$). *a* $t = 0$ s; *b* $t = 0.38$ s; *c* $t = 0.75$ s; *d* $t = 1.13$ s; *e* $t = 1.5$ s; *f* $t = 2.25$ s; *g* $t = 2.38$ s

Regarding the decrease in the droplet speed as the wall is approached further, a possible explanation bears on the idea that the width of the boundary layer located at the wall is around 50 μm (Bruus 2008). Therefore, for $r_w/R \sim 1$, the droplet stands partially in the boundary layer, and consequently, its speed is slowed down. The fact that the model reproduces the experiment in this case is thus fortuitous.

4.4.2 Droplet pair reflecting against a wall

The stream lines in a Hele–Shaw cell move parallel to the flow. It is thus impossible to study the reflection phenomena with a single droplet, as it moves parallel to the wall. We used the dipolar interaction discussed earlier to send droplet pairs toward the wall and study reflection laws.

We observed different situations. The first one is shown in Fig. 10A. In this situation, the pair moves toward the wall at a small incident angle (21°, measured with respect to the wall), deviates, avoids it, and eventually moves away from the wall. The pair keeps its integrity, and the reflection angle is equal to the incident angle. We thus have pure symmetric reflection.

A second case is shown in Fig. 11A. Here, the incidence angle is larger (61°). The two droplets first come into (apparent) contact with the wall. Later, the droplet ahead of the pair moves along the wall, while its partner separates from the wall. The droplet located ahead moves faster so that as time grows, the distance between them increases. Eventually, the droplets are far apart, and the pair is destroyed.

A third case is shown in Fig. 12A. In this case, the pair moves in a strongly confined space—the distance between the walls is twice the droplet diameter. The pair undergoes a sequence of events, including contact with the wall, rotation, and drift toward the opposite wall. The process

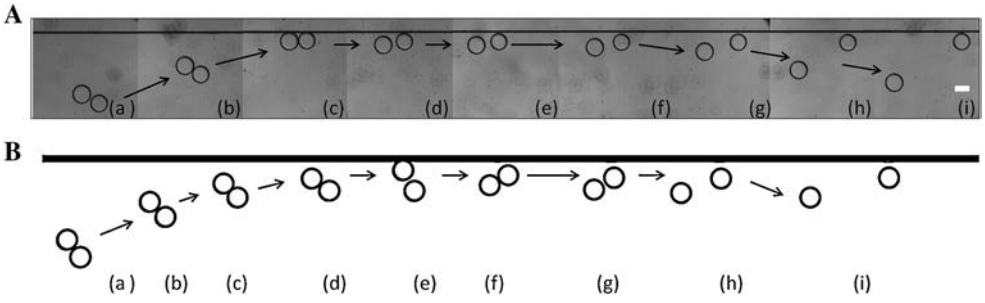

Fig. 11 **A** Evolution of a pair of droplets approaching the side wall ($R = 120$ and 113 μm, respectively). The flow is from *left* to *right*. The flow velocity $U_\infty = 3{,}465$ μm s^{-1}. PDMS system with h = 48 μm, $w_2 = 3{,}000$ μm. *a* $t = 0$ s; *b* $t = 2$ s; *c* $t = 4$ s; *d* $t = 12$ s; *e* $t = 14$ s; *f* $t = 16$ s; *g* $t = 18$ s; *h* $t = 20$ s; *i* $t = 22$ s. The *scale bar* corresponds to 200 μm. **B** Numerical simulation with parameters close to those of Figure **A** $U_\infty = 3{,}465$ - μm s^{-1} and $R = 116$ μm. The initial angle had to be slightly changed to reproduce this escape phenomenon. *a* $t = 0$ s; *b* $t = 1.28$ s; *c* $t = 2.07$ s; *d* $t = 2.25$ s; *e* $t = 2.31$ s; *f* $t = 2.34$ s; *g* $t = 2.41$ s; *h* $t = 2.84$ s; *i* $t = 3.55$ s

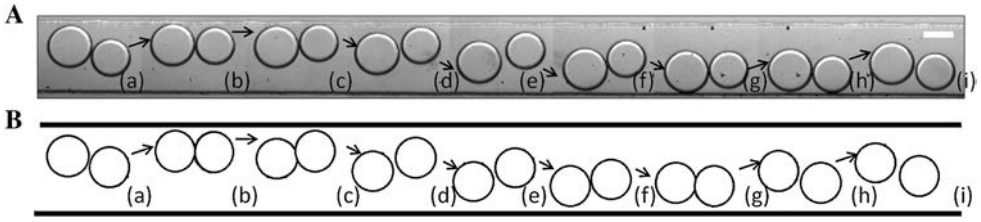

Fig. 12 **A** Bouncing of a pair of droplets in confined conditions ($R = 133$ and 120 μm, respectively). PDMS system, $h = 41$ μm, $w_2 = 500$ μm. The external phase flows from *left* to *right*. *a* $t = 0$ s; *b* $t = 0.1$ s; *c* $t = 0.2$ s; *d* $t = 0.3$ s; *e* $t = 0.4$ s; *f* $t = 0.5$ s; *g* $t = 0.6$ s; *h* $t = 0.7$ s; *i* $t = 0.8$ s. The scale bar corresponds to 200 μm. **B** Numerical simulation showing (qualitatively) the same phenomenon, using the same conditions as the experiment. *a* $t = 0$ s; *b* $t = 1.17$ s; *c* $t = 2.28$ s; *d* $t = 3.36$ s; *e* $t = 4.47$ s; *f* $t = 5.55$ s; *g* $t = 6.66$ s; *h* $t = 7.73$ s; *i* $t = 8.66$ s

repeats periodically. We have observed up to five cycles in a long narrow channel.

Equation (7) quantitatively reproduces the experimental behavior observed in the case of pair reflection against the wall (see Fig. 10B). The good agreement may originate from the fact that at all times, the pair remains substantially distant from the wall. This is an interesting outcome, which indicates that in practice, walls can be considered as mirrors, and higher-order reflections can be neglected as long as pairs remain distant from the wall.

The quantitative agreement gets worse as pairs approach the wall. One example is the escape shown in Fig. 11B. Here, the behavior observed experimentally is reproduced only qualitatively, and only after adjusting the initial angle between the droplet. Numerically, there is sensitivity to the initial conditions, while experimentally the escape regime appears robust with respect to slight changes in the experimental conditions. The existence of various regimes (reflection, escape) that we found, both experimentally and numerically, appears consistent with the analysis of Uspal and Doyle (2012a, b).

The last situation (Fig. 12) is well reproduced by the single-image theory. The details of the rebound (contact with the wall, rotation, and drift toward the opposite wall) are well obtained numerically. However, we observed a discrepancy regarding the times at which the reflection events occur (see Fig. 12A, B). This is mainly due to the fact that in the experiment, we operated at fixed pressure, and consequently, the upstream velocity U_∞ is not imposed. In this particular set of experiment, U_∞ must be taken as a free parameter. When this remark is taken into account, agreement between the theory and experiment is found to be good (albeit at the expense of a free parameter).

5 Conclusion

In this paper, we investigated the behavior of droplets conveyed by a mean flow and confined in micro Hele–Shaw cells. We analyzed the case $N = 1$, 2, and 3 in detail. For $N = 3$, we observe several phenomena (rebounds, pair exchange) that have not been reported yet. We moreover show that the side walls generate a rich dynamics (escape, simple and multiple reflections).

As a whole, the dipolar interaction model (far field, limited to nearest neighbors) provides an accurate picture as long as the droplet boundaries are distant by more than one radius from its neighbor or from the wall. Below this critical distance, the far-field approximation is no longer valid, but theory still describes well most of the observed phenomena (speed of a pair of droplets, pair exchange, pair rotation, speed of a droplet close to a wall, rebounds); the agreement is surprisingly good in purely longitudinal studies. Whatever the distance between particles and the number of droplets involved ($N = 1$, 2, 3), the dipolar interaction model gives good qualitative predictions, with easy to compute equations, and without fitting parameters.

The capacity of predicting the movement of small assemblies of droplets opens the possibility of devising self-assembly strategies based on hydrodynamic interactions between particles and droplets. It more generally suggests that controlling small populations of particles in microchannels, to mix or transport entities, seems feasible.

Acknowledgments We gratefully acknowledge Ministry of Research, ESPCI, and CNRS for their support of this work. We benefited from discussions with P. Doyle, A. Leshansky, D. Bartolo, M. Nagel, E. Guazzelli, A. Huerre, and M-C. Jullien. We thank F. Monti for his technical help.

References

Barbier V, Willaime H, Tabeling P, Jousse F (2006) Producing droplets in parallel microfluidic systems. Phys Rev E 74:046306

Baron M, Blawzdziewicz J, Wajnryb E (2008) Hydrodynamic crystals: collective dynamics of regular arrays of spherical particles in a parallel-wall channel. Phys Rev Lett 100:174502

Bartolo D, Degré G, Nghe P, Studer V (2008) Microfluidic stickers. Lab Chip 8:274

Beatus T, Tlusty T, Bar-ziv R (2006) Phonons in a one-dimensional microfluidic crystal. Nat Phys 2:743

Beatus T, Tlusty T, Bar-ziv R (2007) Anomalous microfluidic phonons induced by the interplay of hydrodynamic screening and incompressibility. Phys Rev Lett 99:124502

Beatus T, Tlusty T, Bar-ziv R (2012) The physics of 2D microfluidic droplet ensembles. Phys Rep 516:103

Bhattacharya S, Blawzdziewicz J, Wajnryb E (2006) Far field approximation for hydrodynamic interactions in parallel-wall geometry. J Comput Phys 212:718–738

Bruus H (2008) Theoretical microfluidics. Oxford University Press, Oxford

Champagne N, Lauga E, Bartolo D (2011) Stability and non-linear response of 1D microfluidic-particle streams. Soft Matter 7:11082

Cui B, Diamant H, Lin B, Rice SA (2004) Anomalous hydrodynamic interaction in a quasi-two-dimensional suspension. Phys Rev Lett 92:258301

Diamant H (2009) Hydrodynamic interaction in confined geometries. Phys Soft Condens Matter 78:041002

Eri A, Okumura K (2011) Viscous drag friction acting on a fluid drop confined in between two plates. Soft Matter 7:5648

Evans E, Sackmann E (1988) Translational and rotational drag coefficients for a disk moving in a liquid membrane associated with a rigid substrated. J Fluid Mech 194:553

Galas JC, Bartolo D, Studer V (2009) Active connectors for microfluidic drops on demand. New J Phys 11:075027

Goulpeau J, Trouchet D, Ajdari A, Tabeling P (2005) Experimental study and modeling of polydimethylsiloxane peristaltic micropumps. J Appl Phys 98:044914

Guazzelli E, Morris JF (2012) A physical introduction to suspension dynamics. Cambridge University Press, Cambridge

Guyon E, Hulin JP, Petit L (2001) Hydrodynamique physique. EDP Sciences, Les Ulis

Happel J, Brenner H (1965) Low Reynolds number hydrodynamics: with special applications to particulate media. Kluwer, Boston

Tabeling P (2005) Introduction to microfluidics. Oxford University Press, Oxford

Uspal WE, Doyle PS (2012a) Scattering and nonlinear bound states of hydrodynamically coupled particles in a narrow channel. Phys Rev E 85:016325

Uspal WE, Doyle PS (2012b) Collective dynamics of small clusters of particles flowing in a quasi-two-dimensional microchannel. Soft Matter 8:10676

Appendix D

Elementary DNA units sequences

Table of elementary DNA sequences

Elementary units	**Sequence**
$A_{0,bot}$	$5' - /5Phos/CGAAACAGATATCCACAGATATCC - 3'$
$A_{0,top}$	$5' - /5Phos/CAGAGGATATCTGTGGATATCTGT - 3'$
$A_{1,bot}$	$5' - /5Phos/CGAAACAGATATCCACAGATATCC - 3'$
$A_{1,top}$	$5' - /5Phos/CAGAGGCTGCCATAGGCTGCCATA - 3'$
$B_{0,bot}$	$5' - /5Phos/GTCAGCAACCAAGCGCAACCAAGC - 3'$
$B_{0,top}$	$5' - /5Phos/TTCGGCTTGGTTGCGCTTGGTTGC - 3'$
$B_{1,bot}$	$5' - /5Phos/GTCAGAACCACTCCGAACCACTCC - 3'$
$B_{1,top}$	$5' - /5Phos/TTCGGGAGTGGTTCGGAGTGGTTC - 3'$
$C_{0,bot}$	$5' - /5Phos/GGGAAGCGCCAAGTAGCGCGAAGT - 3'$
$C_{0,top}$	$5' - /5Phos/TGACACTTGGCGCTACTTGGCGCT - 3'$
$C_{1,bot}$	$5' - /5Phos/GGGAGGAGCGTTCTGGAGCGTTCT - 3'$
$C_{1,top}$	$5' - /5Phos/TGACAGAACGCTCCAGAACGCTCC - 3'$
$D_{0,bot}$	$5' - /5Phos/GTTGGTCCAATGGCGTCCAATGGC - 3'$
$D_{0,top}$	$5' - /5Phos/TCCCGCCATTGGACGCCATTGGAC - 3'$
$D_{1,bot}$	$5' - /5Phos/GTTGAGGATTCGGCAGGATTCGGC - 3'$
$D_{1,top}$	$5' - /5Phos/TCCCGCCGAATCCTGCCGAATCCT - 3'$

P5: 5' AAT GAT ACG GCG ACC ACC GA 3'

P7: 5' CAA GCA GAA GAC GGC ATA CGA GAT 3'

SBS3 : 5' ACA CTC TTT CCC TAC ACG ACG CTC TTC CGA TCT

SBS12: 5' P- GAT CGG AAG AGC TCG TAT GCC GTC TTC TGC TTG

Bibliography

[1] Michael Weber, Lalitha Muthusubramaniam, Justin Murray, Ed Hudak, Oleg Kornienko, Eric N. Johnson, Berta Strulovici, and Priya Kunapuli. Ultra-High-Throughput Screening for Antagonists of A Gi-Coupled Receptor in A 3,456-Well Plate Format CyclicAMP Assay. Assay and drug development technologies, 5(1):117–126, 2007.

[2] Kevin R. Oldenburg, Ji-Hu Zhang, Tongming Chen, Anthony Maffia, Karl F. Blom, Andrew P. Combs, and Thomas DY Chung. Assay miniaturization for ultra-high throughput screening of combinatorial and discrete compound libraries: a 9600-well (0.2 microliter) assay system. Journal of Biomolecular Screening, 3(1):55–62, 1998.

[3] Michael Berg, Katrin Undisz, Ralf Thiericke, Peter Zimmermann, Thomas Moore, and Clemens Posten. Evaluation of liquid handling conditions in microplates. Journal of biomolecular screening, 6(1):47–56, 2001.

[4] Najeeb Halabi, Olivier Rivoire, Stanislas Leibler, and Rama Ranganathan. Protein Sectors: Evolutionary Units of Three-Dimensional Structure. Cell, 138(4):774–786, August 2009.

[5] J. Orskov. Method for the Isolation of Bacteria in Pure Culture from Single Cells and Procedure for the Direct Tracing of Bacterial Growth on a Solid Medium. Journal of Bacteriology, 7(6):537–549, November 1922.

[6] E. M. Hildebrand. Techniques for the isolation of single microorganisms. The Botanical Review, 4(12):627–664, December 1938.

[7] E. M. Hildebrand. Techniques for the isolation of single microorganisms. II. The Botanical Review, 16(4):181–207, April 1950.

[8] Joshua Lederberg. A simple method for isolating individual microbes. Journal of Bacteriology, 68(2):258–259, August 1954.

[9] G. J. V. Nossal. Antibody Production by Single Cells. British Journal of Experimental Pathology, 39(5):544–551, October 1958.

[10] Dan S. Tawfik and Andrew D. Griffiths. Man-made cell-like compartments for molecular evolution. Nature biotechnology, 16(7):652–6, 1998.

[11] Michihiko Nakano, Jun Komatsu, Shun-ichi Matsuura, Kazunori Takashima, Shinji Katsura, and Akira Mizuno. Single-molecule PCR using water-in-oil emulsion. Journal of Biotechnology, pages 117–124, 2003.

[12] Anna Musyanovych, Volker Mailander, and Katharina Landfester. Miniemulsion Droplets as Single Molecule Nanoreactors for Polymerase Chain Reaction. Biomacromolecules, 6(4):1824–1828, July 2005.

[13] Richard Williams, Sergio G. Peisajovich, Oliver J. Miller, Shlomo Magdassi, Dan S. Tawfik, and Andrew D. Griffiths. Amplification of complex gene libraries by emulsion PCR. Nature Methods, 3(7):545–550, July 2006.

[14] Machiko Hori, Hajime Fukano, and Yosuke Suzuki. Uniform amplification of multiple DNAs by emulsion PCR. Biochemical and Biophysical Research Communications, 352(2):323–328, January 2007.

[15] Carl T. Wittwer, G. Chris Fillmore, and David J. Garling. Minimizing the time required for DNA amplification by efficient heat transfer to small samples. Analytical Biochemistry, 186(2):328–331, May 1990.

[16] Liat Rosenfeld, Tiras Lin, Ratmir Derda, and Sindy K. Y. Tang. Review and analysis of performance metrics of droplet microfluidics systems. Microfluidics and Nanofluidics, 16(5):921–939, January 2014.

[17] Andrew D. Griffiths and Dan S. Tawfik. Man-made enzymes, from design to in vitro compartmentalisation. Current Opinion in Biotechnology, 11(4):338–353, August 2000.

[18] Andrew D. Griffiths and Dan S. Tawfik. Miniaturising the laboratory in emulsion droplets. Trends in Biotechnology, 24(9):395–402, September 2006.

[19] Valerie Taly, Bernard T. Kelly, and Andrew D. Griffiths. Droplets as Microreactors for High-Throughput Biology. ChemBioChem, pages 263–272, 2007.

[20] N. Fraysse, M. P. Valignat, A. M. Cazabat, F. Heslot, and P. Levinson. The Spreading of Layered Microdroplets. Journal of Colloid and Interface Science, 158(1):27–32, June 1993.

[21] Todd Thorsen, Richard W. Roberts, Frances H. Arnold, and Stephen R. Quake. Dynamic Pattern Formation in a Vesicle-Generating Microfluidic Device. Physical Review Letters, 2001.

[22] Shelley L. Anna, Nathalie Bontoux, and Howard A. Stone. Formation of dispersions using flow focusing in microchannels. Applied Physics Letters, page 364, 2003.

[23] Liang-Yin Chu, Andrew S. Utada, Rhutesh K. Shah, Jin-Woong Kim, and David A. Weitz. Controllable monodisperse multiple emulsions. Angewandte Chemie International Edition, pages 8970–8974, 2007.

[24] Florent Malloggi, Nicolas Pannacci, Rafaele Attia, Fabrice Monti, Pascaline Mary, Herve Willaime, Patrick Tabeling, Bernard Cabane, and Pascal Poncet. Monodisperse Colloids Synthesized with Nanofluidic Technology. Langmuir, pages 2369–2373, 2010.

[25] Marc A. Unger, Hou-Pu Chou, Todd Thorsen, Axel Scherer, and Stephen R. Quake. Monolithic Microfabricated Valves and Pumps by Multilayer Soft Lithography. Science, 288(5463):113–116, April 2000.

[26] Jean-Christophe Galas, Denis Bartolo, and Vincent Studer. Active connectors for microfluidic drops on demand. New Journal of Physics, 11(7):075027, July 2009.

[27] Xuefei Sun, Keqi Tang, Richard D. Smith, and Ryan T. Kelly. Controlled dispensing and mixing of pico- to nanoliter volumes using on-demand droplet-based microfluidics. Microfluidics and Nanofluidics, 15(1):117–126, July 2013.

[28] Todd Thorsen, Sebastian J. Maerkl, and Stephen R. Quake. Microfluidic large-scale integration. Science, 298(5593):580–584, 2002.

[29] Jie Xu and Daniel Attinger. Drop on demand in a microfluidic chip. Journal of Micromechanics and Microengineering, 18(6):065020, 2008.

[30] Avishay Bransky, Natanel Korin, Maria Khoury, and Shulamit Levenberg. A microfluidic droplet generator based on a piezoelectric actuator. Lab Chip, 9(4):516–520, 2009.

[31] P.-H. Cazorla, O. Fuchs, M. Cochet, S. Maubert, G. Le Rhun, P. Robert, Y. Fouillet, and E. Defay. Piezoelectric Micro-pump with PZT Thin Film for Low Consumption Microfluidic Devices. Procedia Engineering, 87:488–491, 2014.

[32] Nam-Trung Nguyen, Teck-Hui Ting, Yit-Fatt Yap, Teck-Neng Wong, John Chee-Kiong Chai, Wee-Liat Ong, Junlong Zhou, Say-Hwa Tan, and Levent Yobas. Thermally mediated droplet formation in microchannels. Applied Physics Letters, 91(8):084102, August 2007.

[33] Charles N. Baroud, Matthieu Robert de Saint Vincent, and Jean-Pierre Delville. An optical toolbox for total control of droplet microfluidics. Lab on a Chip, 7(8):1029, 2007.

[34] Masumi Yamada and Minoru Seki. Nanoliter-sized liquid dispenser array for multiple biochemical analysis in microfluidic devices. Analytical chemistry, 76(4):895–899, 2004.

[35] David J. Collins, Tuncay Alan, Kristian Helmerson, and Adrian Neild. Surface acoustic waves for on-demand production of picoliter droplets and particle encapsulation. Lab on a Chip, 13(16):3225, 2013.

[36] William C. Jackson, Hy D. Tran, Michael J. OBrien, Emmanuil Rabinovich, and Gabriel P. Lopez. Rapid prototyping of active microfluidic components based on magnetically modified elastomeric materials. Journal of Vacuum Science & Technology B, 19(2):596–599, March 2001.

[37] Mingyan He, Jason S. Kuo, and Daniel T. Chiu. Electro-generation of single femtoliter- and picoliter-volume aqueous droplets in microfluidic systems. Applied Physics Letters, 87(3):031916, July 2005.

[38] Yung-Chieh Tan, Jeffrey S. Fisher, Alan I. Lee, Vittorio Cristini, and Abraham Phillip Lee. Design of microfluidic channel geometries for the control of droplet volume, chemical concentration, and sorting. Lab on a Chip, 4(4):292–298, July 2004.

[39] Xize Niu, Shelly Gulati, Joshua B. Edel, and Andrew J. deMello. Pillar-induced droplet merging in microfluidic circuits. Lab on a Chip, 8(11):1837–1841, November 2008.

[40] Nicolas Bremond, Abdou R. Thiam, and Jerome Bibette. Decompressing Emulsion Droplets Favors Coalescence. Physical Review Letters, 100(2):024501, January 2008.

[41] Eujin Um and Je-Kyun Park. A microfluidic abacus channel for controlling the addition of droplets. Lab on a Chip, 9(2):207–212, January 2009.

[42] Piotr Korczyk, Ladislav Derzsi, Slawomir Jakiela, and Piotr Garstecki. Microfluidic traps for hard-wired operations on droplets. Lab on a Chip, 13(20):4096, 2013.

[43] Luis M. Fidalgo, Chris Abell, and Wilhelm T. S. Huck. Surface-induced droplet fusion in microfluidic devices. Lab on a Chip, 7(8):984, 2007.

[44] Ying Liu and Rustem F. Ismagilov. Dynamics of Coalescence of Plugs with a Hydrophilic Wetting Layer Induced by Flow in a Microfluidic Chemistrode. Langmuir, 25(5):2854–2859, March 2009.

[45] Linas Mazutis and Andrew D. Griffiths. Selective droplet coalescence using microfluidic systems. Lab on a Chip, 12(10):1800, 2012.

[46] J. E. Reiner, A. M. Crawford, R. B. Kishore, Lori S. Goldner, K. Helmerson, and M. K. Gilson. Optically trapped aqueous droplets for single molecule studies. Applied Physics Letters, 89(1):013904, July 2006.

[47] Robert M. Lorenz, J. Scott Edgar, Gavin D. M. Jeffries, and Daniel T. Chiu. Microfluidic and Optical Systems for the On-Demand Generation and Manipulation of Single Femtoliter-Volume Aqueous Droplets. Analytical Chemistry, 78(18):6433–6439, September 2006.

[48] Abdou R. Thiam, Nicolas Bremond, and Jerome Bibette. Breaking of an Emulsion under an ac Electric Field. Physical Review Letters, 102(18):188304, May 2009.

[49] Craig Priest, Stephan Herminghaus, and Ralf Seemann. Controlled electrocoalescence in microfluidics: Targeting a single lamella. Applied Physics Letters, 89(13):134101, September 2006.

[50] Darren R. Link, Erwan Grasland-Mongrain, Agnes Duri, Flavie Sarrazin, Zhengdong Cheng, Galder Cristobal, Manuel Marquez, and David A. Weitz. Electric Control of Droplets in Microfluidic Devices. Angewandte Chemie International Edition, 45(16):2556–2560, April 2006.

[51] Max Chabert, Kevin D. Dorfman, and Jean-Louis Viovy. Droplet fusion by alternating current (AC) field electrocoalescence in microchannels. ELECTROPHORESIS, 26(19):3706–3715, 2005.

[52] Wei-Heong Tan and Shoji Takeuchi. Timing controllable electrofusion device for aqueous droplet-based microreactors. Lab on a Chip, 6(6):757, 2006.

[53] Keunho Ahn, Jeremy Agresti, Henry Chong, Manuel Marquez, and D. A. Weitz. Electrocoalescence of drops synchronized by size-dependent flow in microfluidic channels. Applied Physics Letters, 88(26):264105, June 2006.

[54] Michele Zagnoni and Jonathan M. Cooper. On-chip electrocoalescence of microdroplets as a function of voltage, frequency and droplet size. Lab on a Chip, 9(18):2652–2658, September 2009.

[55] Wei Wang, Chun Yang, and Chang Ming Li. Efficient On-Demand Compound Droplet Formation: From Microfluidics to Microdroplets as Miniaturized Laboratories. Small, 5(10):1149–1152, May 2009.

[56] Adam R. Abate, Tony Hung, Pascaline Mary, Jeremy J. Agresti, and David A. Weitz. High-throughput injection with microfluidics using picoinjectors. Proceedings of the National Academy of Sciences, 107(45):19163–19166, November 2010.

[57] Liang Li, James Q. Boedicker, and Rustem F. Ismagilov. Using a Multijunction Microfluidic Device To Inject Substrate into an Array of Preformed Plugs without Cross Contamination. Comparing Theory and Experiments. Analytical Chemistry, 79(7):2756–2761, April 2007.

[58] Yung-Chieh Tan, Yao Li Ho, and Abraham Phillip Lee. Microfluidic sorting of droplets by size. Microfluidics and Nanofluidics, 4(4):343–348, June 2007.

[59] Linas Mazutis and Andrew D. Griffiths. Preparation of monodisperse emulsions by hydrodynamic size fractionation. Applied Physics Letters, 95(20):204103, November 2009.

[60] Masumi Yamada, Megumi Nakashima, and Minoru Seki. Pinched Flow Fractionation Continuous Size Separation of Particles Utilizing a Laminar Flow Profile in a Pinched Microchannel. Analytical Chemistry, 76(18):5465–5471, September 2004.

[61] Hirosuke Maenaka, Masumi Yamada, Masahiro Yasuda, and Minoru Seki. Continuous and Size-Dependent Sorting of Emulsion Droplets Using Hydrodynamics in Pinched Microchannels. Langmuir, 24(8):4405–4410, April 2008.

[62] Jae-Sung Park, Suk-Heung Song, and Hyo-Il Jung. Continuous focusing of microparticles using inertial lift force and vorticity via multi-orifice microfluidic channels. Lab Chip, 9(7):939–948, 2009.

[63] Haakan N. Joensson, Mathias Uhlan, and Helene Andersson Svahn. Droplet size based separation by deterministic lateral displacement. Separating droplets by cell-induced shrinking. Lab on a Chip, 11(7):1305, 2011.

[64] Yi Dong, Alison M. Skelley, Keith D. Merdek, Kam M. Sprott, Chunsheng Jiang, William E. Pierceall, Jessie Lin, Michael Stocum, Walter P. Carney, and Denis A. Smirnov. Microfluidics and Circulating Tumor Cells. The Journal of Molecular Diagnostics, 15(2):149–157, March 2013.

[65] G.K. Kurup and Amar Basu. Passive, label-free droplet sorting by chemical composition using tensiophoresis. 16th International Conference on Miniaturized Systems for Chemistry and Life Sciences, 2012.

[66] Max Chabert and Jean-Louis Viovy. Microfluidic high-throughput encapsulation and hydrodynamic self-sorting of single cells. Proceedings of the National Academy of Sciences of the United States of America, 105(9):3191–3196, March 2008.

[67] Ting-Hsiang Wu, Yue Chen, Sung-Yong Park, Jason Hong, Tara Teslaa, Jiang F. Zhong, Dino Di Carlo, Michael A. Teitell, and Pei-Yu Chiou. Pulsed laser triggered high speed microfluidic fluorescence activated cell sorter. Lab on a Chip, 12(7):1378–1383, April 2012.

[68] Thomas Franke, Adam R. Abate, David A. Weitz, and Achim Wixforth. Surface acoustic wave (SAW) directed droplet flow in microfluidics for PDMS devices. Lab on a Chip, 9(18):2625, 2009.

[69] Jeremy J. Agresti, Eugene Antipov, Adam R. Abate, Keunho Ahn, Amy C. Rowat, Jean-Christophe Baret, Manuel Marquez, Alexander M. Klibanov, Andrew D. Griffiths, and David A. Weitz. Ultrahigh-throughput screening in drop-based microfluidics for directed evolution. Proceedings of the National Academy of Sciences, 107(9):4004–4009, March 2010.

[70] Petra S. Dittrich and Petra Schwille. An Integrated Microfluidic System for Reaction, High-Sensitivity Detection, and Sorting of Fluorescent Cells and Particles. Analytical Chemistry, 75(21):5767–5774, November 2003.

[71] Anne Y. Fu, Hou-Pu Chou, Charles Spence, Frances H. Arnold, and Stephen R. Quake. An Integrated Microfabricated Cell Sorter. Analytical Chemistry, 74(11):2451–2457, June 2002.

[72] Mark M. Wang, Eugene Tu, Daniel E. Raymond, Joon Mo Yang, Haichuan Zhang, Norbert Hagen, Bob Dees, Elinore M. Mercer, Anita H. Forster, Ilona Kariv, Philippe J. Marchand, and William F. Butler. Microfluidic sorting of mammalian cells by optical force switching. Nature Biotechnology, 23(1):83–87, January 2005.

[73] Hakho Lee, Yong Liu, Donhee Ham, and Robert M. Westervelt. Integrated cell manipulation system CMOS/microfluidic hybrid. Lab on a Chip, 7(3):331, 2007.

[74] Ahn, C. Kerbage, T. P. Hunt, R. M. Westervelt, D. R. Link, and D. A. Weitz. Dielectrophoretic manipulation of drops for high-speed microfluidic sorting devices. Applied Physics Letters, 88, 2006.

[75] Yue Chen, Aram J. Chung, Ting-Hsiang Wu, Michael A. Teitell, Dino Di Carlo, and Pei-Yu Chiou. Pulsed Laser Activated Cell Sorting with Three Dimensional Sheathless Inertial Focusing. Small, 10(9):1746–1751, May 2014.

[76] Lothar Schmid, David A. Weitz, and Thomas Franke. Sorting drops and cells with acoustics: acoustic microfluidic fluorescence-activated cell sorter. Lab on a Chip, 14(19):3710, June 2014.

[77] Sherrif F Ibrahim and Ger van den Engh. High-speed cell sorting: fundamentals and recent advances. Current Opinion in Biotechnology, 14(1):5–12, February 2003.

[78] James F. Leary. Ultra high-speed sorting. Cytometry Part A, 67(2):76–85, 2005.

[79] Maria B. Dainiak, Ashok Kumar, Igor Yu Galaev, and Bo Mattiasson. Methods in Cell Separations. In Ashok Kumar, Igor Yu Galaev, and Bo Mattiasson, editors, Cell Separation, number 106 in Advances in Biochemical Engineering/Biotechnology, pages 1–18. Springer Berlin Heidelberg, 2007.

[80] Jean-Christophe Baret, Oliver J. Miller, Valerie Taly, Michael Ryckelynck, Abdeslam El-Harrak, Lucas Frenz, Christian Rick, Michael L. Samuels, J. Brian Hutchison, Jeremy J. Agresti, Darren R. Link, David A. Weitz, and Andrew D. Griffiths. Fluorescence-activated droplet sorting (FADS): efficient microfluidic cell sorting based on enzymatic activity. Lab on a Chip, 9(13):1850, 2009.

[81] Linas Mazutis, John Gilbert, W. Lloyd Ung, David A. Weitz, Andrew D. Griffiths, and John A. Heyman. Single-cell analysis and sorting using droplet-based microfluidics. Nature Protocols, 8(5):870–891, May 2013.

[82] Adam Sciambi and Adam R. Abate. Accurate microfluidic sorting of droplets at 30 kHz. Lab Chip, 15(1):47–51, 2015.

[83] S. Protiere, M. Z. Bazant, D. A. Weitz, and H. A. Stone. Droplet breakup in flow past an obstacle: A capillary instability due to permeability variations. EPL (Europhysics Letters), 92(5):54002, December 2010.

[84] D. R. Link, S. L. Anna, D. A. Weitz, and H. A. Stone. Geometrically Mediated Breakup of Drops in Microfluidic Devices. Physical Review Letters, 92(5):054503, February 2004.

[85] A. M. Leshansky, S. Afkhami, M.-C. Jullien, and P. Tabeling. Obstructed Breakup of Slender Drops in a Microfluidic T Junction. Physical Review Letters, 108(26):264502, June 2012.

[86] Vincent Miralles, Axel Huerre, Hannah Williams, Bastien FourniÃ©, and Marie-Caroline Jullien. A versatile technology for droplet-based microfluidics: thermomechanical actuation. Lab Chip, 15(9):2133–2139, 2015.

[87] Geoffrey Taylor. Disintegration of Water Drops in an Electric Field. Proceedings of the Royal Society of London. Series A, Mathematical and Physical Sciences, 280(1382):383–397, July 1964.

[88] M.-C. Jullien, M.-J. Tsang Mui Ching, C. Cohen, L. Menetrier, and P. Tabeling. Droplet breakup in microfluidic T-junctions at small capillary numbers. Physics of Fluids (1994-present), 21(7):072001, July 2009.

[89] Lucas Frenz, Kerstin Blank, Eric Brouzes, and Andrew D. Griffiths. Reliable microfluidic on-chip incubation of droplets in delay-lines. Lab on a Chip, 9(10):1344–1348, May 2009.

[90] Linas Mazutis, Ali Fallah Araghi, Oliver J Miller, Jean-Christophe Baret, Lucas Frenz, Agnes Janoshazi, Valerie Taly, Benjamin J Miller, J. Brian Hutchison, Darren Link, Andrew D. Griffiths, and Michael Ryckelynck. Droplet-Based Microfluidic Systems for High-Throughput Single DNA Molecule Isothermal Amplification and Analysis. Anal. Chem, pages 4813–4821, 2009.

[91] Marie Leman, Faris Abouakil, Andrew D. Griffiths, and Patrick Tabeling. Droplet-based microfluidics at the femtolitre scale. Lab Chip, 15(3):753–765, 2015.

[92] Hans Gorris and David Walt. Analytical Chemistry on the Femtoliter Scale. Angewandte Chemie International Edition, 49(23):3880–3895, May 2010.

[93] Kenneth A. Johnson and Roger S. Goody. The Original Michaelis Constant: Translation of the 1913 MichaelisMenten Paper. Biochemistry, 50(39):8264–8269, October 2011.

[94] Ali Fallah-Araghi, Kamel Meguellati, Jean-Christophe Baret, Abdeslam El Harrak, Thomas Mangeat, Martin Karplus, Sylvain Ladame, Carlos M. Marques, and Andrew D. Griffiths. Enhanced Chemical Synthesis at Soft Interfaces: A Universal Reaction-Adsorption Mechanism in Microcompartments. Physical Review Letters, 112(2):028301, January 2014.

[95] Ethan Schonbrun, Adam R. Abate, Paul E. Steinvurzel, David. A. Weitz, and Kenneth B. Crozier. High-throughput fluorescence detection using an integrated zone-plate array. Lab on a Chip, 10(7):852, 2010.

[96] Jiseok Lim, Philipp Gruner, Manfred Konrad, and Jean-Christophe Baret. Micro-optical lens array for fluorescence detection in droplet-based microfluidics. Lab on a Chip, 13(8):1472, 2013.

[97] Boris Rotman. Measurement of activity of single molecules of β-d-galactosidase. Proceedings of the National Academy of Sciences of the United States of America, 47(12):1981–1991, December 1961.

[98] Martin Bohmer and Jorg Enderlein. Fluorescence Spectroscopy of Single Molecules under Ambient Conditions: Methodology and Technology. ChemPhysChem, 4(8):792–808, August 2003.

[99] Fainerman V. B. Makievski A. V. Krugel J. Grigoriev D. O. Kazakov V. N. Miller, R. and O. V. Sinyachenko. Dynamics of protein and mixed protein/surfactant adsorption layers at the water/fluid interface. Advances in Colloid and Interface Science, 86(1, 2):39–82, May 2000.

[100] L. Spencer Roach, Helen Song, and Rustem F. Ismagilov. Controlling Nonspecific Protein Adsorption in a Plug-Based Microfluidic System by Controlling Interfacial Chemistry Using Fluorous-Phase Surfactants. Analytical Chemistry, 77(3):785–796, February 2005.

[101] Craig Priest, Stephan Herminghaus, and Ralf Seemann. Generation of monodisperse gel emulsions in a microfluidic device. Applied Physics Letters, 88(2):024106, January 2006.

[102] Isao Kobayashi, Sukekuni Mukataka, and Mitsutoshi Nakajima. Production of Monodisperse Oil-in-Water Emulsions Using a Large Silicon Straight-Through Microchannel Plate. Industrial & Engineering Chemistry Research, 44(15):5852–5856, July 2005.

[103] Zhenzhen Li, A.M. Leshansky, L.M. Pismen, and Patrick Tabeling. Step-emulsification in nanofluidic device. 2014.

[104] Jean-Christophe Baret, Felix Kleinschmidt, Abdeslam El Harrak, and Andrew D. Griffiths. Kinetic Aspects of Emulsion Stabilization by Surfactants: A Microfluidic Analysis. pages 6088–6093, 2009.

[105] Jessamine Ng Lee, Cheolmin Park, and George M. Whitesides. Solvent compatibility of poly(dimethylsiloxane)-based microfluidic devices. Analytical Chemistry, 75(23):6544–6554, December 2003.

[106] C. Holtze, A. C. Rowat, J. J. Agresti, J. B. Hutchison, F. E. Angila, C. H. J. Schmitz, S. Koster, H. Duan, K. J. Humphry, R. A. Scanga, J. S. Johnson, D. Pisignano, and D. A. Weitz. Biocompatible surfactants for water-in-fluorocarbon emulsions. Lab on a Chip, 8(10):1632–1639, October 2008.

[107] Alvaro Mata, Aaron J. Fleischman, and Shuvo Roy. Fabrication of multi-layer SU-8 microstructures. Journal of Micromechanics and Microengineering, 16(2):276, February 2006.

[108] Stanford. Designing Your Own Device: Multi-Height Molds. 2015.

[109] M. Heymann, S. Fraden, and Dongshin Kim. Multi-Height Precision Alignment With Selectively Developed Alignment Marks. Journal of Microelectromechanical Systems, 23(2):424–427, April 2014.

[110] David C. Duffy, J. Cooper McDonald, Olivier J. A. Schueller, and George M. Whitesides. Rapid Prototyping of Microfluidic Systems in Poly(dimethylsiloxane). Analytical Chemistry, 70(23):4974–4984, December 1998.

[111] Teri W. Odom, J. Christopher Love, Daniel B. Wolfe, Kateri E. Paul, and George M. Whitesides. Improved Pattern Transfer in Soft Lithography Using Composite Stamps. Langmuir, 18(13):5314–5320, June 2002.

[112] M Morra, E Occhiello, R Marola, F Garbassi, P Humphrey, and D Johnson. On the aging of oxygen plasma-treated polydimethylsiloxane surfaces. Journal of Colloid and Interface Science, 137(1):11–24, June 1990.

[113] Chen and Lindner. The Stability of Radio-Frequency Plasma-Treated Polydimethylsiloxane Surfaces. Langmuir, 23(6):3118–3122, March 2007.

[114] Jongsoo Kim, Manoj K. Chaudhury, and Michael J. Owen. Modeling hydrophobic recovery of electrically discharged polydimethylsiloxane elastomers. Journal of Colloid and Interface Science, 293(2):364–375, January 2006.

[115] Tatsunosuke Murakami, Shin-ichi Kuroda, and Zenjiro Osawa. Dynamics of Polymeric Solid Surfaces Treated with Oxygen Plasma: Effect of Aging Media after Plasma Treatment. Journal of Colloid and Interface Science, 202(1):37–44, June 1998.

[116] Christel Martin. Developpement, par une approche mixte Top-down / Bottom-up, de dispositifs planaires pour la nanoelectronique, 2005.

[117] Seok Woo Lee and Seung S. Lee. Shrinkage ratio of PDMS and its alignment method for the wafer level process. Microsystem Technologies, 14(2):205–208, May 2007.

[118] Jacques Goulpeau, Daniel Trouchet, Armand Ajdari, and Patrick Tabeling. Experimental study and modeling of polydimethylsiloxane peristaltic micropumps. Journal of Applied Physics, 98(4):044914, August 2005.

[119] M.D. Paine, M.S. Alexander, K.L. Smith, M. Wang, and J.P.W. Stark. Controlled electrospray pulsation for deposition of femtoliter fluid droplets onto surfaces. Journal of Aerosol Science, 38(3):315–324, March 2007.

[120] Ri Li, Nasser Ashgriz, and Sanjeev Chandra. Droplet generation from pulsed micro-jets. Experimental Thermal and Fluid Science, 32(8):1679–1686, September 2008.

[121] Pratikkumar Vikramark Raje and Naresh Chandra Murmu. A Review on Electrohydrodynamic-inkjet Printing Technology. 2008.

[122] Brian O'Donovan, Dennis J. Eastburn, and Adam R. Abate. Electrode-free picoinjection of microfluidic drops. Lab on a Chip, 12(20):4029, 2012.

[123] Ronald E. Pelrine, Roy D. Kornbluh, and Jose P. Joseph. Electrostriction of polymer dielectrics with compliant electrodes as a means of actuation. Sensors and Actuators A: Physical, 64(1):77–85, January 1998.

[124] A. Pimpin, Y. Suzuki, and N. Kasagi. Microelectrostrictive Actuator With Large Out-of-Plane Deformation for Flow-Control Application. Journal of Microelectromechanical Systems, 16(3):753–764, June 2007.

[125] Samuel Rosset, Muhamed Niklaus, Philippe Dubois, and Herbert R. Shea. Large-stroke dielectric elastomer actuators with ion-implanted electrodes. Microelectromechanical Systems, Journal of, 18(6):1300–1308, 2009.

[126] helene song, Delai L. chen, and rustem F. ismagilov. Reactions in Droplets in Microfluidic Channels. Angewandte Chemie International Edition, pages 7336–7356, 2006.

[127] T. Schindler, M. Herrler, M. A. Marahiel, and F. X. Schmid. Extremely rapid protein folding in the absence of intermediates. Nature Structural Biology, 2(8):663–673, August 1995.

[128] Chi-Kin Chan, Yi Hu, Satoshi Takahashi, Denis L. Rousseau, William A. Eaton, and James Hofrichter. Submillisecond protein folding kinetics studied by ultrarapid mixing. Proceedings of the National Academy of Sciences of the United States of America, 94(5):1779–1784, March 1997.

[129] M C Shastry, S D Luck, and H Roder. A continuous-flow capillary mixing method to monitor reactions on the microsecond time scale. Biophysical Journal, 74(5):2714–2721, May 1998.

[130] James B. Knight, Ashvin Vishwanath, James P. Brody, and Robert H. Austin. Hydrodynamic Focusing on a Silicon Chip: Mixing Nanoliters in Microseconds. Physical Review Letters, 80(17):3863–3866, April 1998.

[131] Charles N. Baroud, Francois Gallaire, and RÃ©mi Dangla. Dynamics of microfluidic droplets. Lab on a Chip, 10(16):2032, 2010.

[132] Joshua D. Tice, Helen Song, Adam D. Lyon, and Rustem F. Ismagilov. Formation of droplets and mixing in multiphase microfluidics at low values of the Reynolds and the capillary numbers. Langmuir, 19(22):9127–9133, 2003.

[133] Shia-Yen Teh, Robert Lin, Lung-Hsin Hung, and Abraham P. Lee. Droplet microfluidics. Lab on a Chip, 8(2):198, 2008.

[134] Jung-uk Shim, Rohan T. Ranasinghe, Clive A. Smith, Shehu M. Ibrahim, Florian Hollfelder, Wilhelm T. S. Huck, David Klenerman, and Chris Abell. Ultrarapid Generation of Femtoliter Microfluidic Droplets for Single-Molecule-Counting Immunoassays. ACS Nano, 7(7):5955–5964, 2013.

[135] J. C. Baygents, N. J. Rivette, and H. A. Stone. Electrohydrodynamic deformation and interaction of drop pairs. Journal of Fluid Mechanics, 368:359–375, 1998.

[136] T. B. Jones, K.-L. Wang, and D.-J. Yao. Frequency-Dependent Electromechanics of Aqueous Liquids: Electrowetting and Dielectrophoresis. Langmuir, 20(7):2813–2818, March 2004.

[137] Laars Lundgaard, Gunnard Berg, Stian Ingebrigtsen, and Pierre Atten. Emulsions and Emulsion Stability: Surfactant Science Series, Chapter 15. Johann Sjoblom, Boca Raton, crc press edition, 2006.

[138] Laure Menetrier-Deremble. Gouttes et champs electriques dans un systeme microfluidique, 2007.

[139] W. A. Macky. Some Investigations on the Deformation and Breaking of Water Drops in Strong Electric Fields. Proceedings of the Royal Society of London. Series A, Containing Papers of a Mathematical and Physical Character, 133(822):565–587, October 1931.

[140] J. D. Sherwood. Breakup of fluid droplets in electric and magnetic fields. Journal of Fluid Mechanics, 188:133–146, March 1988.

[141] Herbert Ackland Pohl. Some Effects of Nonuniform Fields on Dielectrics. Journal of Applied Physics, 29(8):1182–1188, August 1958.

[142] L.C. Waterman. Electrical coalescers. pages 51–57, 1965.

[143] D. J. Klingenberg, Frank van Swol, and C. F. Zukoski. Dynamic simulation of electrorheological suspensions. The Journal of Chemical Physics, 91(12):7888–7895, December 1989.

[144] R. Tao and J. M. Sun. Three-dimensional structure of induced electrorheological solid. Physical Review Letters, 67(3):398–401, July 1991.

[145] D. J. Klingenberg, Frank van Swol, and C. F. Zukoski. The small shear rate response of electrorheological suspensions. II. Extension beyond the point dipole limit. The Journal of Chemical Physics, 94(9):6170–6178, May 1991.

[146] K. W. Yu and Jones T. K. Wan. Interparticle force in polydisperse electrorheological fluids. Computer Physics Communications, 129:177–184, July 2000.

[147] M. Davis. Two Charged Spherical Conductors in a Uniform Electric Field, 1964.

[148] John S. Eow and Mojtaba Ghadiri. Dropâdrop coalescence in an electric field: the effects of applied electric field and electrode geometry. Colloids and Surfaces A: Physicochemical and Engineering Aspects, 219(1â3):253–279, June 2003.

[149] James C. Bird, William D. Ristenpart, Andrew Belmonte, and Howard A. Stone. Critical Angle for Electrically Driven Coalescence of Two Conical Droplets. Physical Review Letters, 103(16):164502, October 2009.

[150] Vincent Labrot, Michael Schindler, Pierre Guillot, Annie Colin, and Mathieu Joanicot. Extracting the hydrodynamic resistance of droplets from their behavior in microchannel networks. Biomicrofluidics, 3(1):012804, March 2009.

[151] A. Vrij and J. Th. G. Overbeek. Rupture of thin liquid films due to spontaneous fluctuations in thickness. Journal of the American Chemical Society, 90(12):3074–3078, June 1968.

[152] Ivan Ivanov. Thin Liquid Films. CRC Press, August 1988.

[153] Dimitrina S. Valkovska, Krassimir D. Danov, and Ivan B. Ivanov. Stability of draining plane-parallel films containing surfactants. Advances in colloid and interface science, 96(1):101–129, 2002.

[154] Timothy C. Scott, Osman A. Basaran, and Charles H. Byers. Characteristics of electric-field-induced oscillations of translating liquid droplets. Industrial & Engineering Chemistry Research, 29(5):901–909, May 1990.

[155] A. M. Leshansky and L. M. Pismen. Breakup of drops in a microfluidic T junction. Physics of Fluids (1994-present), 21(2):023303, 2009.

[156] P.S. Epstein and M.S. Plesset. On the Stability of Gas Bubbles in Liquid-Gas Solutions. Journal of Chemical Physics, pages 1505–1509, 1950.

[157] P. Brent Duncan and David Needham. Microdroplet dissolution into a second-phase solvent using a micropipet technique: test of the Epstein-Plesset model for an aniline-water system. Langmuir: the ACS journal of surfaces and colloids, 22(9):4190–4197, April 2006.

[158] A. S. Kabal'nov, A. V. Pertzov, and E. D. Shchukin. Ostwald ripening in two-component disperse phase systems: Application to emulsion stability. Colloids and Surfaces, 24(1):19–32, May 1987.

[159] Amy Q. Shen, Danhong Wang, and Patrick T. Spicer. Kinetics of Colloidal Templating Using Emulsion Drop Consolidation. Langmuir, 23(26):12821–12826, December 2007.

[160] Tianzhun Wu, Katsuki Hirata, Hiroaki Suzuki, Rong Xiang, Zikang Tang, and Tetsuya Yomo. Shrunk to femtolitre: Tuning high-throughput monodisperse water-in-oil droplet arrays for ultra-small micro-reactors. Applied Physics Letters, 101(7):074108, August 2012.

[161] Jeffrey M Levsky and Robert H Singer. Gene expression and the myth of the average cell. Trends in Cell Biology, 13(1):4–6, January 2003.

[162] David A. Hinkle and James H. Eberwine. Single-cell molecular biology: implications for diagnosis and treatment of neurologic disease. Biological psychiatry, 54(4):413–417, 2003.

[163] Christoph A. Klein, Thomas JF Blankenstein, Oleg Schmidt-Kittler, Marco Petronio, Bernhard Polzer, Nikolas H. Stoecklein, and Gert RiethmÃ$\frac{1}{4}$ller. Genetic heterogeneity of single disseminated tumour cells in minimal residual cancer. The Lancet, 360(9334):683–689, 2002.

[164] Allon M. Klein, Linas Mazutis, Ilke Akartuna, Naren Tallapragada, Adrian Veres, Victor Li, Leonid Peshkin, David A. Weitz, and Marc W. Kirschner. Droplet Barcoding for Single-Cell Transcriptomics Applied to Embryonic Stem Cells. Cell, 161(5):1187–1201, 2015.

[165] Valerie Taly, Deniz Pekin, Leonor Benhaim, Steve K. Kotsopoulos, Delphine Le Corre, Xinyu Li, Ivan Atochin, Darren R. Link, Andrew D. Griffiths, Karine Pallier, HÃ©lÃ¨ne Blons, Olivier BouchÃ©, Bruno Landi, J. Brian Hutchison, and Pierre Laurent-Puig. Multiplex Picodroplet Digital PCR to Detect KRAS Mutations in Circulating DNA from the Plasma of Colorectal Cancer Patients. Clinical Chemistry, 59(12):1722–1731, December 2013.

[166] Saiful Islam, Amit Zeisel, Simon Joost, Gioele La Manno, Pawel Zajac, Maria Kasper, Peter Lonnerberg, and Sten Linnarsson. Quantitative single-cell RNA-seq with unique molecular identifiers. Nature Methods, 11(2):163–166, February 2014.

[167] Guoji Guo, Mikael Huss, Guo Qing Tong, Chaoyang Wang, Li Li Sun, Neil D. Clarke, and Paul Robson. Resolution of cell fate decisions revealed by single-cell gene expression analysis from zygote to blastocyst. Developmental cell, 18(4):675–685, 2010.

[168] Angela R. Wu, Norma F. Neff, Tomer Kalisky, Piero Dalerba, Barbara Treutlein, Michael E. Rothenberg, Francis M. Mburu, Gary L. Mantalas, Sopheak Sim, Michael F. Clarke, and others. Quantitative assessment of single-cell RNA-sequencing methods. Nature methods, 11(1):41–46, 2014.

[169] Mira T. Guo, Assaf Rotem, John A. Heyman, and David A. Weitz. Droplet microfluidics for high-throughput biological assays. Lab on a Chip, 12(12):2146–2155, 2012.

[170] Xiaohu Gao, Warren C. W. Chan, and Shuming Nie. Quantum-dot nanocrystals for ultrasensitive biological labeling and multicolor optical encoding. Journal of Biomedical Optics, 7(4):532–537, 2002.

[171] Sheila R. Nicewarner-Pena, R. Griffith Freeman, Brian D. Reiss, Lin He, David J. Pena, Ian D. Walton, Remy Cromer, Christine D. Keating, and Michael J. Natan. Submicrometer Metallic Barcodes. Science, 294(5540):137–141, October 2001.

[172] Daniel C. Pregibon, Mehmet Toner, and Patrick S. Doyle. Multifunctional Encoded Particles for High-Throughput Biomolecule Analysis. Science, 315(5817):1393–1396, March 2007.

[173] Hicham Fenniri, Sangki Chun, Lunhan Ding, Yegor Zyrianov, and Klaas Hallenga. Preparation, Physical Properties, On-Bead Binding Assay and Spectroscopic Reliability of 25 Barcoded Polystyrene Poly(ethylene glycol) Graft Copolymers. Journal of the American Chemical Society, 125(35):10546–10560, September 2003.

[174] K. C. Nicolaou, Xiao-Yi Xiao, Zahra Parandoosh, Andrew Senyei, and Michael P. Nova. Radiofrequency Encoded Combinatorial Chemistry. Angewandte Chemie International Edition in English, 34(20):2289–2291, November 1995.

[175] Andrew R. Vaino and Kim D. Janda. Euclidean shape-encoded combinatorial chemical libraries. Proceedings of the National Academy of Sciences, 97(14):7692–7696, July 2000.

[176] Evan Z. Macosko, Anindita Basu, Rahul Satija, James Nemesh, Karthik Shekhar, Melissa Goldman, Itay Tirosh, Allison R. Bialas, Nolan Kamitaki, Emily M. Martersteck, John J. Trombetta, David A. Weitz, Joshua R. Sanes, Alex K. Shalek, Aviv Regev, and Steven A. McCarroll. Highly Parallel Genome-wide Expression Profiling of Individual Cells Using Nanoliter Droplets. Cell, 161(5):1202–1214, May 2015.

[177] F. Sanger, S. Nicklen, and A. R. Coulson. DNA sequencing with chain-terminating inhibitors. Proceedings of the National Academy of Sciences, 74(12):5463–5467, December 1977.

[178] Harris Wong, C. J. Radke, and S. Morris. The motion of long bubbles in polygonal capillaries. Part 2. Drag, fluid pressure and fluid flow. Journal of Fluid Mechanics, 292:95–110, June 1995.

[179] Fabien Jousse, Guoping Lian, Ruth Janes, and John Melrose. Compact model for multiphase liquid liquid flows in micro-fluidic devices. Lab on a Chip, 5(6):646–656, May 2005.

[180] Adam R. Abate, Chia-Hung Chen, Jeremy J. Agresti, and David A. Weitz. Beating Poisson encapsulation statistics using close-packed ordering. Lab on a Chip, 9(18):2628–2631, September 2009.

[181] Filip Beunis, Filip Strubbe, Masoumeh Karvar, Oksana Drobchak, Toon Brans, and Kristiaan Neyts. Inverse micelles as charge carriers in nonpolar liquids: Characterization with current measurements. Current Opinion in Colloid & Interface Science, 18(2):129–136, April 2013.

[182] Filip Strubbe, Manoj Prasad, and Filip Beunis. Characterizing Generated Charged Inverse Micelles with Transient Current Measurements. The Journal of Physical Chemistry B, 119(5):1957–1965, February 2015.

[183] Filip Strubbe, Alwin R. M. Verschueren, Luc J. M. Schlangen, Filip Beunis, and Kristiaan Neyts. Generation current of charged micelles in nonaqueous liquids: Measurements and simulations. Journal of Colloid and Interface Science, 300(1):396–403, August 2006.

[184] Zhishan Hua, Yongmei Xia, Onnop Srivannavit, Jean-Marie Rouillard, Xiaochuan Zhou, Xiaolian Gao, and Erdogan Gulari. A versatile microreactor platform featuring a chemical-resistant microvalve array for addressable multiplex syntheses and assays. Journal of Micromechanics and Microengineering, 16(8):1433, 2006.

[185] O Kirk, T.V. Borchert, and C.C. Fuglsang. Industrial enzyme applications. Current opinion in biotechnology, pages 345–351, 2002.

[186] C.J. Yeoman. Thermostable enzymes as biocatalysts in the biofuel industry. In Advances in Applied microbiology, pages 1–55. Academic press edition, 2010.

[187] P. Demarche. Harnessing the power of enzymes for environmental stewardship. pages 933–953, 2012.

[188] J.P. Rasor and E. Voss. Enzyme-catalyzed processes in pharmaceutical industry. Applied catalysis A: General, pages 145–158, 2001.

[189] C.R. Ispas, G. Crivat, and S. Andreescu. Review: recent developments in enzyme-based biosensors for biomedical analysis. Analytical letters, pages 168–186, 2012.

[190] Tim F. Cooper, Daniel E. Rozen, and Richard E. Lenski. Parallel changes in gene expression after 20,000 generations of evolution in Escherichia coli. Proceedings of the National Academy of Sciences, 100(3):1072–1077, February 2003.

[191] Robert J. Woods, Jeffrey E. Barrick, Tim F. Cooper, Utpala Shrestha, Mark R. Kauth, and Richard E. Lenski. Second-Order Selection for Evolvability in a Large Escherichia coli Population. Science, 331(6023):1433–1436, March 2011.

[192] Aisha I. Khan, Duy M. Dinh, Dominique Schneider, Richard E. Lenski, and Tim F. Cooper. Negative Epistasis Between Beneficial Mutations in an Evolving Bacterial Population. Science, 332(6034):1193–1196, June 2011.

[193] Jeffrey E. Barrick and Richard E. Lenski. Genome dynamics during experimental evolution. Nature Reviews Genetics, 14(12):827–839, October 2013.

[194] Justin B. Siegel, Alexandre Zanghellini, Helena M. Lovick, Gert Kiss, Abigail R. Lambert, Jennifer L. St.Clair, Jasmine L. Gallaher, Donald Hilvert, Michael H. Gelb, Barry L. Stoddard, Kendall N. Houk, Forrest E. Michael, and David Baker. Computational design of an enzyme catalyst for a stereoselective bimolecular Diels-Alder reaction. Science (New York, N.Y.), 329(5989):309–313, July 2010.

[195] Christine E. Tinberg, Sagar D. Khare, Jiayi Dou, Lindsey Doyle, Jorgen W. Nelson, Alberto Schena, Wojciech Jankowski, Charalampos G. Kalodimos, Kai Johnsson, Barry L. Stoddard, and David Baker. Computational design of ligand-binding proteins with high affinity and selectivity. Nature, 501(7466):212–216, September 2013.

[196] Elizabeth D. Getzoff, Diane E. Cabelli, Cindy L. Fisher, Hans E. Parge, Maria Silvia Viezzoli, Lucia Banci, and Robert A. Hallewell. Faster superoxide dismutase mutants designed by enhancing electrostatic guidance. Nature, 358(6384):347–351, July 1992.

[197] Jing Nie and Robert T. Kennedy. Sampling from Nanoliter Plugs via Asymmetrical Splitting of Segmented Flow. Analytical Chemistry, 82(18):7852–7856, September 2010.

[198] Bert Verbruggen, Tamara Toth, Yegermal Tesfaw Atalay, Frederik Ceyssens, Pieter Verboven, Robert Puers, Bart Nicolai, and Jeroen Lammertyn. Design of a flow-controlled asymmetric droplet splitter using computational fluid dynamics. Microfluidics and Nanofluidics, 15(2):243–252, January 2013.

Résumé en français du travail de thèse

La microfluidique en gouttes permet l'analyse de systèmes biochimiques à grand débit, en utilisant de faibles volumes réactionnels, à faible coût. Dans l'état de l'art, le volume des gouttes varie entre 2 pL et 4 nL, un millier à million de fois inférieur au volume d'un puit de microplaque. Miniaturiser d'avantage les volumes réactionnels permettrait d'augmenter encore les débits d'analyse, de d'avantage réduire les coûts et ouvre également l'accès à de nouvelles études, telles que les études sur molécule unique ou la délivrance de médicaments.

La première partie de ce travail de thèse concerne la miniaturisation des opérations classiques de la microfluidique en gouttes à l'échelle femtolitrique: production, stabilité, biocompatibilité, mélange en gouttes, coalescence, tri, division de gouttes, production à la demande ont été démontrés avec succès sur des gouttelettes femtolitriques. Le tout a été permis en restant dans les limites de la technologie PDMS et des standards classiques de la lithographie.

La seconde partie s'intéresse à certaines applications biologiques issues du couplage de gouttelettes picolitriques et femtolitriques. Une plateforme permettant l'encodage *in situ* de gouttes à l'aide de codes barres d'ADN lisibles par séquençage a été construite. Deux autres applications ont été envisagées: un projet concernant l'émergence des chromosomes dans un monde prébiotique qui nécessitait des facteurs de dilution de l'ordre de 1:1000 et un projet de cartographie génotype-phénotype sur une enzyme qui nécessitait deux dilutions par 10 ont bénéficié de la miniaturisation à l'échelle femtolitrique.

Abstract of this manuscript

Droplet-based microfluidics has demonstrated its multiple advantage over standard microtitre plates technologies by increasing analysis throughputs, decreasing costs and enabling the encapsulation of single cells into individual reservoirs. In the state-of-the-art, droplet volumes usually range from 2 pL to 4nL, one thousand to one million times smaller than microtitre plate wells. This PhD work focuses on the miniaturization of biological reservoirs down to the femtoliter scale which would enable an increase of throughputs of analysis and open up access to new studies, such as single-molecule studies or drug delivery.

The first part of this manuscript concentrates on the miniaturization of elementary operations of droplet-based microfluidics down to the femtoliter scale. Production, mixing, electrocoalescence, DEP sorting, splitting, drop-on-demand, stability, biocompatibility were successfully demonstrated on droplets of a few micrometers diameter.

The second part of this manuscript focuses on some biological applications that were developped with the LBC. A platform for the *in situ* encoding of droplets with DNA barcodes readable per sequencing was developped. Two other applications were envisioned: a project studying the conditions that prevailed the apparition of chromosomes in an early RNA world and a genotype-phenotype mapping project benefited from downscaling to the femtoliter scale.